Sergey Vyazovkin

Isoconversional Kinetics of Thermally Stimulated Processes

Springer

Isoconversional Kinetics of Thermally Stimulated Processes

Sergey Vyazovkin

Isoconversional Kinetics of Thermally Stimulated Processes

Springer

Sergey Vyazovkin
Department of Chemistry
University of Alabama at Birmingham
Birmingham
Alabama
USA

ISBN 978-3-319-14174-9 ISBN 978-3-319-14175-6 (eBook)
DOI 10.1007/978-3-319-14175-6

Library of Congress Control Number: 2015930832

Springer Cham Heidelberg New York Dordrecht London

Printed on acid-free paper

Springer is part of Springer Science+Business Media (www.springer.com)

To those who believe in the success
of hopeless enterprises

Prologue

The beginning of philosophy is to know the condition of one's own mind

Epictetus, Golden Sayings: XLVI

I have been developing and using isoconversional kinetics for about 25 years. A little over a decade ago, I started thinking about writing a book on this fascinating topic. However, it was only a year ago that I finally decided to invest my time and effort in actually doing it. My decision was spurred by a dramatic growth of interest in isoconversional kinetics and thus, of the potential audience for this book. In the past three years, (2012–2014) there have been around 2000 publications that use isoconversional methods for kinetic analysis. Barely one third of that number of such papers was published for the same period 10 years ago (2002–2004). That is why now seems like the opportune time for such a book to appear and make an impact.

I discovered isoconversional methods in the late 1980s when I was a graduate student. "Discovered" is really the right word here. Back then, the field of thermal analysis kinetics was ruled by single heating rate methods, and the method of Coats and Redfern was probably an uncrowned king. Like most workers at that time, I followed suit and started working with these methods. It seemed to me that by improving the computational and statistical aspects I could make the single heating rate methods produce unique and reliable kinetic triplets. Ironically, however, the computational and statistical refinement of the methods was making things worse. At that point I realized that the single heating rate methods are flawed beyond repair. The time spent was not entirely wasted, because in the process I learned a great deal of statistical and numerical techniques that I used later in developing isoconversional methodology. The major reason I recognized the fault of the single heating rate methods sooner than many others, was that I did not have the luxury of doing kinetics in the "*l'art pour l'art*" style. I was given a pragmatic task of finding a way of using thermal decomposition data for kinetic predictions, and the single heating rate methods were systematically failing to make sensible predictions.

The first multiple heating rate method I used was the isoconversional method of Kissinger, Akahira, and Sunose. To my shame, I did not know about the existence of this method. I simply rearranged the Coats-Redfern equation to the isoconversional form and went ahead. While in graduate school, I developed a technique for making isoconversional predictions without estimating the preexponential factor and

reaction model. I will never forget the sense of wonder when I saw these predictions work! In the early 1990s, I worked out the techniques for isoconversional evaluation of both the preexponential factor and the reaction model. These two techniques completed the computational core of isoconversional kinetics.

Over the years, I and other researchers have done a lot of work on improving the computational tools of isoconversional kinetics. Nevertheless, the main point of my interest has always been finding the link between the dependence of the effective activation energy and the process mechanism. Sometimes this link can be pretty straightforward; at other times it can be very convoluted. However, searching for it is exciting and illuminating every single time. Admittedly, I have learned a great deal of mechanisms and kinetics while trying to understand all kinds of variations in the activation energy. Much of that experience is described in this book.

The book has five chapters. It was my intention to make the book readily accessible to anyone who is familiar with basic (undergraduate) kinetics and thermodynamics. Chapter 1 was written to absorb some of "culture shock" that one may experience on transition from the classical homogenous kinetics to the kinetics of heterogeneous systems studied by the methods of thermal analysis. It provides some basics necessary for comprehension and interpretation of isoconversional kinetics. It also has some practical advice about obtaining computation worthy data.

Chapter 2 describes the computational tools of isoconversional kinetics. The chapter presents the evolution of the methods of estimating activation energy. It emphasizes an important difference between rigid and flexible integral methods. Although implementation of better methods may require significant computational efforts, it is shown that in both, the rigid and flexible categories, there are sufficiently accurate methods that are reducible to the standard linear regression. The chapter also discusses computational techniques for making isoconversional predictions as well as for evaluating the preexponential factors and reaction models.

Chapters 3 and 4 are devoted to the practical application of isoconversional methods to physical and chemical processes respectively. Individual processes are discussed in particular sections of the chapters. The sections are divided into subsections that provide some theoretical background to the particular process and examples of its isoconversional treatment. The physical processes treated in Chap. 3 are the phase transitions in one and two component systems. The one component phase transitions include vaporization and sublimation, glass transition and aging, crystallization and melting of polymers, and morphological solid-solid transitions. The two component phase transitions are the transitions in solutions. They include mixing and demixing, gelation and gel melting, and helix-coil transitions. Chapter 4 deals with the chemical processes most commonly treated by isoconversional methods. These include the processes of polymerization and crosslinking, thermal and thermo-oxidative degradation of polymers, and thermal decomposition of solids. Finally, Chap. 5 is a brief epilogue that collects a few thoughts of mine on the present and future status of isoconversional kinetics.

In conclusion, I would like to acknowledge the luxury of release time I enjoyed while writing this book during the summer and fall semesters of 2014. I thank the National Science Foundation (grant CHE 1052828) and the Department of

Chemistry for supporting my summer pay and the College of Arts and Sciences and the University of Alabama at Birmingham for granting me a semester of sabbatical leave. I would also like to thank the Thermal Analysis Division of Mettler-Toledo, Inc. for their exemplary commitment to isoconversional kinetics. They have implemented many of the computational tools developed by me as a part of their thermal analysis software known as "model-free kinetics" and have done a great job of popularizing isoconversional kinetics. I am very grateful to them for generously supporting my research for two decades.

Sergey Vyazovkin
Birmingham, AL 2014

Contents

About the Author

Prof. Sergey Vyazovkin received his Ph.D. from the Byelorussian State University in 1989. He then joined the Institute for Physical Chemistry (Minsk) where he worked until 1993. Since 1993, he had held visiting positions at the Technical University of Vienna, the University of Toledo, and the University of Nice Sophia-Antipolis. Before joining the University of Alabama at Birmingham, he worked in the University of Utah as a research faculty and the deputy director of the Center for Thermal Analysis. His research interests are concerned with the application of thermal analysis methods to thermally stimulated processes in a wide variety of condensed phase systems. He is a winner of the Mettler-Toledo Award in thermal analysis and of the James J. Christensen Award in calorimetry. Prof. Vyazovkin is editor of Thermochimica Acta and a member of the editorial board of Macromolecular Rapid Communications and Macromolecular Chemistry and Physics. He is a member of the American Chemical Society Analytical Division, the North American Thermal Analysis Society, and the International Confederation for Thermal Analysis and Calorimetry.

Department of Chemistry, University of Alabama at Birmingham, Birmingham, AL 35294, USA

Chapter 1
Some Basics En Route to Isoconversional Methodology

1.1 From Condensed-Phase Kinetics to Isoconversional Principle

> *Following, then, the order of nature, let us begin with the principles which come first.*
>
> Aristotle, Poetics.

This book deals with kinetics of thermally stimulated processes. Kinetics studies the rates of processes in order to accomplish two major objectives. The first is to parameterize the process rate as a function of state variables so that it can be predicted for any combination of these variables. The second is to obtain insights into the process mechanisms. Thermally stimulated processes are the processes that can be initiated by changes in temperature or, in other words, by heating or cooling. More specifically, we are concerned with the thermally stimulated processes that take place in the condensed-phase systems, i.e., liquids and solids.

A change in temperature directly affects all types of molecular motion in the system causing physical and chemical processes inside it. The energy of the molecular motion increases with increasing temperature. When the energy of the molecular motion approaches the energy of intermolecular interactions, the cohesive forces can no longer hold the molecules in the condensed phase so that the latter transforms into the gas phase. As a result, a liquid vaporizes and a solid sublimates. These are examples of a physical process, i.e., a process that does not break the bonds within the molecules. On the other hand, physical processes can also be stimulated by a decrease in temperature. As the energy of the molecular motion drops, the state of the system becomes increasingly determined by the intermolecular interactions that may cause the formation of various structures. Examples of such physical processes are crystallization of a melt or gelation of a solution.

However, when the temperature is raised sufficiently high, the energy of the molecular motion begins approaching the energy of chemical bonds so that the latter break and cause the system to undergo chemical transformations. Thermal decom-

S. Vyazovkin, *Isoconversional Kinetics of Thermally Stimulated Processes,*
DOI 10.1007/978-3-319-14175-6_1

position of a solid substance and thermal polymerization of a liquid monomer are examples of a chemical process.

A change in temperature not only stimulates a variety of physical and chemical processes but also affects their kinetics. There are many experimental techniques that can be used for measuring the kinetics of thermally stimulated processes as a function of temperature. Although the applications of the kinetic methodology discussed in this book are not limited to any particular experimental techniques, all kinetic results collected here have been obtained by either differential scanning calorimetry (DSC) or thermogravimetric analysis (TGA). Other applications include mass spectrometry [1, 2], infrared spectroscopy [3, 4], dilatometry [5], rheometry [6], thermomechanical, dynamic mechanical analysis [3, 7], and acoustic measurements [8].

DSC and TGA are the most common techniques falling under the umbrella of thermal analysis. Detailed information on the techniques and their applications is available elsewhere [9–11]. Briefly, TGA measures changes in the sample mass that makes it suitable for monitoring the kinetics of mass loss in such processes as vaporization, sublimation, decomposition, or of mass gain in oxidation. DSC measures the heat flow either from or to the sample. Since practically any process generates detectable heat flow, DSC has an extremely broad application range. However, it is most commonly employed to measure the kinetics of processes that occur without any mass change such as crystallization, melting, gelation, and polymerization. Either technique, TGA or DSC, is capable of conducting measurements under precisely controlled temperature conditions that can be isothermal or nonisothermal. The latter typically means heating or cooling at a constant rate of temperature change.

The rate of many thermally stimulated processes can be parameterized in terms of T and α as follows:

$$\frac{\mathrm{d}\alpha}{\mathrm{d}t} = k(T) f(\alpha), \tag{1.1}$$

where t is the time, T is the temperature, α is the extent of conversion, $f(\alpha)$ is the reaction model, and $k(T)$ is the rate constant. The latter is almost universally represented by the Arrhenius equation:

$$k(T) = A \exp\left(\frac{-E}{RT}\right), \tag{1.2}$$

where A is the preexponential factor, E is the activation energy, and R is the gas constant. Equation 1.1 is quite different from the basic rate equation found in textbooks dealing with homogeneous reactions in gases and solutions [12]:

$$-\frac{\mathrm{d}C}{\mathrm{d}t} = k(T) C^n, \tag{1.3}$$

where C is the concentration and n is the reaction order. For a reaction to be homogeneous, the reactants should be miscible at the molecular level and be present in the form of single phase. Then, the reaction would occur throughout the whole reaction volume and its rate would be proportional to the amount of reactants in this volume or, in other words, to their concentrations. For instance, in a gas-phase reaction:

$$H_{2(g)} + I_{2(g)} \rightarrow 2HI_{(g)},$$

the two gases are mixed in a reaction vessel and the reaction zone is the whole volume of the vessel. Increasing the amounts of gases in the reaction vessel increases the number molecules in the reaction zone and, thus, the reaction rate.

However, this does not hold if the reactants cannot be mixed at the molecular level and thus have to be present as individual phases. Such reactions can occur only at the interface of the reactant phases. The reactions of this type are called heterogeneous. For example, in a reaction:

$$2Cu_{(s)} + S_{(s)} \rightarrow Cu_2S_{(s)},$$

two solid reactants are brought into a contact so that the reaction zone is limited to the interfacial contact area. If the copper and sulfur reactants are prepared in the form of cylinders (Fig. 1.1) with the circular bases of equal size and made to react by bringing the bases of the solid cylinders into a contact, the reaction rate will be proportional to the area of the circular bases. Nevertheless, it will be independent of the total amount of copper and sulfur outside the interfacial reaction zone, i.e., independent of the cylinder heights. For this reason, the total amounts of the reactants that can be expressed as the concentration do not carry much meaning for heterogeneous kinetics.

Note that the processes that include a condensed phase generally tend to demonstrate heterogeneous kinetics. Reactions between solids, or solids and liquids,

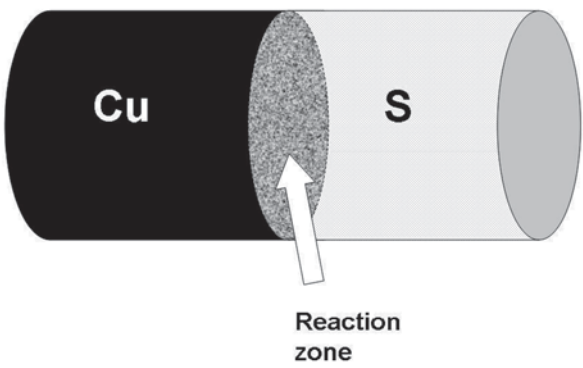

Fig. 1.1 Schematic representation of a reaction between two solids, *Cu*(s) and *S*(s)

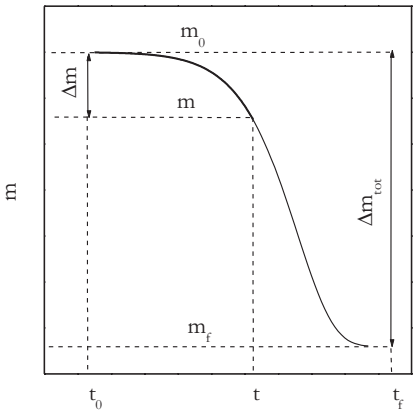

Fig. 1.2 Evaluation of conversion from TGA curve

or two immiscible liquids, decomposition of solids to gases, reaction of gases with solids and liquids, dissolution of solids, evaporation of liquids, sublimation, and melting of solids are all examples of processes whose kinetics is heterogeneous. Considering that for the heterogeneous kinetics the only concentration that matters is the concentration of the reactants in the interfacial reaction zone and that this concentration is not readily measurable, it is only practical to switch from the concentration to the extent of the reactant conversion (α). This parameter simply reflects the reaction progress from the initial state, i.e., before the reaction starts ($\alpha=0$) to the final state, i.e., when the reaction is complete ($\alpha=1$).

The conversion is readily determined as a fractional change of any physical property associated with the reaction progress. When the process progress is monitored as a change in mass by TGA, α is determined as a ratio of the current mass change, Δm, to the total mass change, Δm_{tot} occurred throughout the process:

$$\alpha = \frac{m_0 - m}{m_0 - m_f} = \frac{\Delta m}{\Delta m_{\text{tot}}}, \tag{1.4}$$

where m_0 and m_{f}, respectively, are the initial and final masses (Fig. 1.2). In its turn, when the progress is measured as a change in heat by DSC, α is evaluated as a ratio of the current heat change, ΔH, to the total heat released or absorbed, ΔH_{tot} in the process:

$$\alpha = \frac{\int_{t_0}^{t} (\mathrm{d}H/\mathrm{d}t)\mathrm{d}t}{\int_{t_0}^{t_{\text{f}}} (\mathrm{d}H/\mathrm{d}t)\mathrm{d}t} = \frac{\Delta H}{\Delta H_{\text{tot}}}, \tag{1.5}$$

where $\mathrm{d}H/\mathrm{d}t$ is the heat flow measured by DSC (Fig. 1.3).

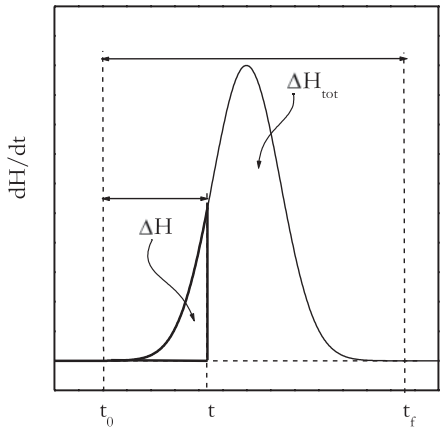

Fig. 1.3 Evaluation of conversion from DSC curve

Similarly, if the concentration of a reactant is available, it can easily be converted to the conversion. For example, if the value of C varies throughout the reaction from the initial value C_0 to zero, the conversion is:

$$\alpha = \frac{C_0 - C}{C_0}. \tag{1.6}$$

Isolating C from Eq. 1.6 and substituting the resulting expression into Eq. 1.3 leads to:

$$\frac{\mathrm{d}\alpha}{\mathrm{d}t} = k'(T)(1-\alpha)^n, \tag{1.7}$$

where $k'(T) = C_0^{n-1}k(T)$. Equation 1.7 is the basic equation of homogeneous kinetics. Comparing it against Eq. 1.1 suggests that homogeneous kinetics can be described by a simple reaction model:

$$f(\alpha) = (1-\alpha)^n. \tag{1.8}$$

that is called a reaction-order model.

Fitting the rate to the reaction models may provide some clues about the reaction mechanism. Fitting homogeneous kinetics data to a reaction-order model (Eq. 1.8) and determining that n equals 1 or 2 suggests that the reaction is, respectively, monomolecular or bimolecular. In heterogeneous kinetics, the situation is not nearly as simple. There are dozens of heterogeneous reaction models that have been derived under various mechanistic assumptions [9, 13]. Such multitude of the models arises from the need to describe the multitude of ways by which the spatially localized reaction zone propagates throughout the reactants. The mathematical equations and names of some models are collected in Table 1.1. Figure 1.4 displays the model dependencies of $f(\alpha)$ on α.

Table 1.1 Some kinetic models used in the heterogeneous kinetics

	Reaction model	Code	$f(\alpha)$	$g(\alpha)$
1	Power law	P4	$4\alpha^{3/4}$	$\alpha^{1/4}$
2	Power law	P3	$3\alpha^{2/3}$	$\alpha^{1/3}$
3	Power law	P2	$2\alpha^{1/2}$	$\alpha^{1/2}$
4	Power law	P2/3	$2/3\alpha^{-1/2}$	$\alpha^{3/2}$
5	One-dimensional diffusion	D1	$½\alpha^{-1}$	α^{2}
6	Mampel (first order)	F1	$1-\alpha$	$-\ln(1-\alpha)$
7	Avrami–Erofeev	A4	$4(1-\alpha)[-\ln(1-\alpha)]^{3/4}$	$[-\ln(1-\alpha)]^{1/4}$
8	Avrami–Erofeev	A3	$3(1-\alpha)[-\ln(1-\alpha)]^{2/3}$	$[-\ln(1-\alpha)]^{1/3}$
9	Avrami–Erofeev	A2	$2(1-\alpha)[-\ln(1-\alpha)]^{1/2}$	$[-\ln(1-\alpha)]^{1/2}$
10	Three-dimensional diffusion	D3	$3/2(1-\alpha)^{2/3}[1-(1-\alpha)^{1/3}]^{-1}$	$[1-(1-\alpha)^{1/3}]^{2}$
11	Contracting sphere	R3	$3(1-\alpha)^{2/3}$	$1-(1-\alpha)^{1/3}$
12	Contracting cylinder	R2	$2(1-\alpha)^{1/2}$	$1-(1-\alpha)^{1/2}$
13	Two-dimensional diffusion	D2	$[-\ln(1-\alpha)]^{-1}$	$(1-\alpha)\ln(1-\alpha)+\alpha$

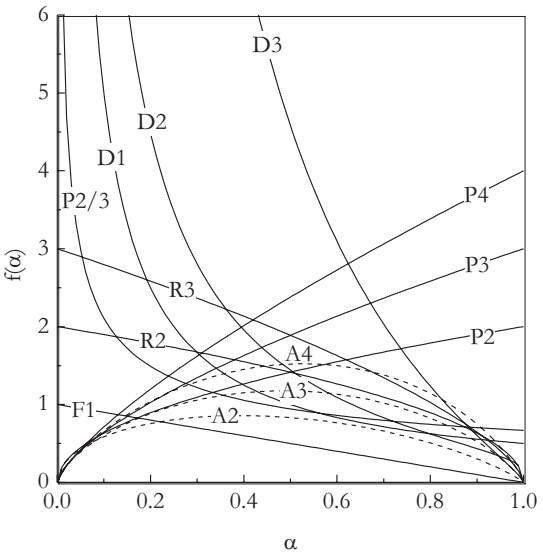

Fig. 1.4 The $f(\alpha)$ on α dependencies for the reaction models from Table 1.1

Since under the isothermal conditions (i.e., $T=\text{const}$) $k(T)$ is constant, the rate is directly proportional to $f(\alpha)$:

$$\frac{d\alpha}{dt} = Const \cdot f(\alpha). \tag{1.9}$$

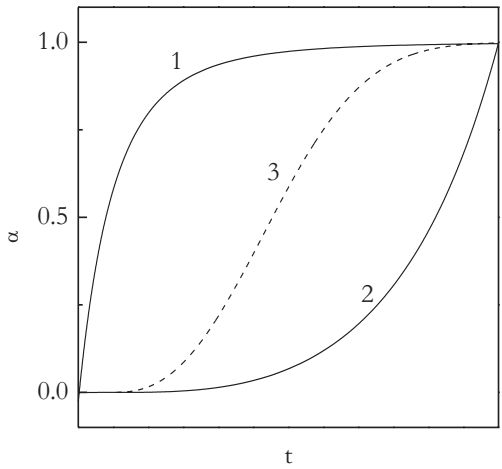

Fig. 1.5 Three major types of integral kinetic curves obtained under isothermal conditions: *1* decelerating; *2* accelerating; *3* autocatalytic (sigmoid)

Then from the $f(\alpha)$ dependencies presented in Fig. 1.4, we can identify three major types of heterogeneous kinetics: decelerating, accelerating, and autocatalytic. For the decelerating kinetics, the rate is continuously decreasing as the process progresses from $\alpha = 0$ to 1. This type of behavior is represented by the diffusion models and the models of contracting geometry. This is also the typical behavior for the homogeneous kinetics that obey the reaction-order model (Eq. 1.8). For the accelerating kinetics, the rate is constantly increasing throughout the process progress. The power law models provide an example of such behavior. The autocatalytic models describe processes whose rate passes through a maximum. The Avrami–Erofeev models of nucleation and growth are typical representatives of such kinetic behavior.

The three types of heterogeneous kinetics are also easy to recognize from the integral kinetic curves, α versus t, obtained under isothermal conditions (Fig. 1.5). The decelerating kinetic curves are almost linear in the initial portion but start to bend at larger extents of conversion and ultimately reach a plateau as α approaches 1. The accelerating and autocatalytic kinetic curves demonstrate little change at the lowest extents of conversion, sometimes featuring a distinct plateau. The latter is also called an induction period. Past this period, the curves starts to bend at a continuously increasing angle. In the accelerating curves, this trend persists until completion, i.e., $\alpha = 1$. In the autocatalytic curves, acceleration switches to deceleration at some intermediate extent of conversion. This gives rise to the characteristic sigmoid shape of the curves. The respective reaction models and kinetics are sometimes referred to as sigmoid.

Speaking of indentifying particular reaction models (Fig. 1.4) rather than the types of kinetics (Fig. 1.5), a quick review of Fig. 1.4 immediately reveals that many of the models do not show a significant difference especially in certain ranges of α. Considering that all models largely oversimplify the reality, experimental data tend not to follow the models accurately. It is frequently found that experimental data fall between two model dependencies, or coincide with one model at smaller

conversions but with another at larger ones, or do not follow any model within a certain range conversions. This creates a serious problem of identifying the reaction models by means of the model-fitting procedure.

The problem of identifying the reaction models becomes practically insurmountable when model fitting is performed on experimental data obtained in a nonisothermal run at a single heating rate, β. Note that under isothermal conditions the conversion dependence of the reaction rate (i.e., an experimental dependence of $f(\alpha)$ on α) is easy to isolate because the rate is directly proportional to $f(\alpha)$ (see Eq. 1.9). However, under nonisothermal conditions when the temperature changes linearly with the time:

$$\beta = \frac{\mathrm{d}T}{\mathrm{d}t}, \tag{1.10}$$

both α and T change simultaneously that thwarts clean separation of $f(\alpha)$ and $k(T)$ in Eq. 1.1. That is, when Eq. 1.1 is fitted to nonisothermal data, any inaccuracy in selecting the reaction model becomes compensated by the respective inaccuracy in the rate constant. As a result of this compensation, there always is more than one set of $k(T)$ and $f(\alpha)$ that can fit the experimental data equally well from the statistical point of view [14]. The resulting different rate constants give rise to widely differing pairs of the Arrhenius parameters, E and A, which, however, are strongly correlated via the so-called compensation effect [15]:

$$\ln A_j = aE_j + b, \tag{1.11}$$

where the subscript j denotes a particular reaction model $f_j(\alpha)$ that is used in the model-fitting procedure. A set of $f_j(\alpha)$, E_j, and A_j is frequently called a kinetic triplet. Experimental examples of the problem have been considered by Vyazovkin and Wight [14]. Instructive simulated examples are found in the papers by Criado et al. [16, 17], who have demonstrated that three different kinetic triplets can give rise to exactly the same kinetic curve α versus T (Fig. 1.6). Note that the respective Arrhenius parameters are strongly correlated via the compensation effect (Fig. 1.7).

Although the deficiency of single-heating-rate kinetic analyses had been emphasized repeatedly, their general inability to produce reliable kinetic triplets was officially recognized by the community only in the discussions [18–21] of the results of the 2000 Kinetic Project sponsored by the International Confederation of Thermal Analysis and Calorimetry (ICTAC). One of the most important conclusions of that project was that the single-heating-rate kinetic analyses should be avoided. As an alternative, one should use kinetic analyses based on the simultaneous use of multiple heating rates or, more, generally, multiple temperature programs. According to the 2011 recommendations [22] of the ICTAC Kinetics Committee, such kinetic analyses should be performed by using either model-fitting or isoconversional (model-free) kinetic methodologies. The use of the model-fitting methodology is outside this book's scope. The book focuses entirely on the applications of the isoconversional kinetic methodology or, simply, isoconversional kinetics.

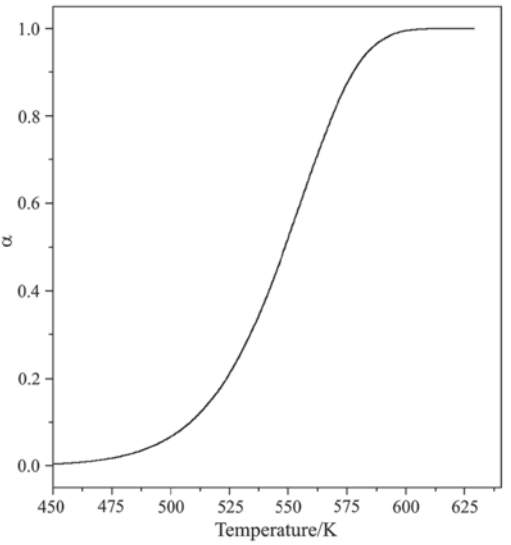

Fig. 1.6 The same kinetic curve can be represented by three different triplets (F1: $E=172.3$ kJ mol^{-1}, $A=2.30\times10^{13}$ s^{-1}; $A2$: $E=118.1$ kJ mol^{-1}, $A=1.24\times10^{8}$ s^{-1}; $A3$: E = 100.0 kJ mol^{-1}, $A=1.66\times10^{6}$ s^{-1}; heating rate is 1°C min^{-1}). (Reproduced from Criado et al. [17] with permission of Springer)

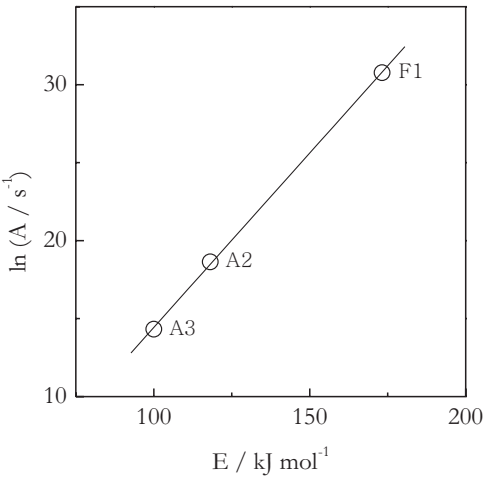

Fig. 1.7 Arrhenius parameters related to the kinetic curve in Fig. 1.6 obey the compensation effect: $\ln A=aE+b$

The isoconversional kinetics takes its origin in the isoconversional principle that allows one to eliminate the reaction model from kinetic computations. The principle states that the process rate at constant extent of conversion is only a function of temperature. This is easy to derive from Eq. 1.1 by taking the logarithmic derivative of the rate at $\alpha=$const:

$$\left[\frac{\partial \ln(\mathrm{d}\alpha/\mathrm{d}t)}{\partial T^{-1}}\right]_{\alpha}=\left[\frac{\partial \ln k(T)}{\partial T^{-1}}\right]_{\alpha}+\left[\frac{\partial \ln f(\alpha)}{\partial T^{-1}}\right]_{\alpha}, \tag{1.12}$$

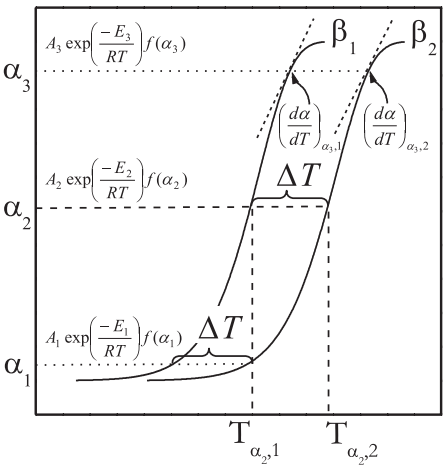

Fig. 1.8 Isoconversional method uses an individual rate equation for each extent conversion and a narrow temperature interval ΔT, related to this conversion. The use of different heating rates, β_1 and β_2, allows for determining different rates $\left(\frac{d\alpha}{dt} = \beta\frac{d\alpha}{dT}\right)$ at the same conversion. (Reproduced from Vyazovkin and Sbirrazzuoli [23] with permission of Wiley)

where the subscript α indicates isoconversional values, i.e., the values related to a given extent of conversion. The second addend on the right-hand side of Eq. 1.12 is zero because at α=const, $f(\alpha)$ is constant. The first addend readily derives from Eq. 1.2 so that Eq. 1.12 reduces to:

$$\left[\frac{\partial \ln(d\alpha / dt)}{\partial T^{-1}}\right]_{\alpha} = -\frac{E_{\alpha}}{R}. \tag{1.13}$$

It follows from Eq. 1.13 that the temperature dependence of the isoconversional rate can be utilized to determine the isoconversional values of the activation energy, E_α without identifying or assuming any form of the reaction model. That is why isoconversional methods are frequently termed as "model-free" methods. While catchy, this term is not to be taken literally. It should be kept in mind that although the methods do not have to identify explicitly the model, they still assume implicitly that there is some $f(\alpha)$ that defines the conversion dependence of the process rate.

The temperature dependence of the isoconversional rate is obtained experimentally by performing a series of runs at different temperature programs. It usually takes four to five runs at different heating rates or at different temperatures to determine such dependence. Figure 1.8 [23] illustrates the idea of determining the isoconversional rate from two nonisothermal runs conducted at the heating rates β_1 and β_2. The conversion versus temperature plots can be estimated by scaling TGA data in accord with Eq. 1.4 (Fig. 1.2). By selecting a certain conversion α, one then finds the temperature related to it at each heating rate, i.e., $T_{\alpha,1}$ and $T_{\alpha,2}$. The conversions need to be selected in a wide α range, e.g., 0.05–0.95 with a step not larger than 0.05. Since it is unlikely that the experimental α versus T curves would contain points exactly at selected values of α one has to use interpolation to find the values of T_α. Then the slope (numerical derivative) of the α versus T curve at T_α would give the values of $\left(\frac{d\alpha}{dT}\right)_{\alpha}$ that can be converted to the isoconversional rate as follows:

$$\left(\frac{\mathrm{d}\alpha}{\mathrm{d}t}\right)_{\alpha} = \left(\frac{\mathrm{d}\alpha}{\mathrm{d}T}\right)_{\alpha} \beta. \tag{1.14}$$

Equation 1.14 is derived by substitution of the derivatives in accord with Eq. 1.9. The isoconversional rates are also obtainable from DSC data that would have to be converted to α versus T curves (Eq. 1.5, Fig. 1.3) to estimate the values of T_{α}. The isoconversional rate is then estimated from the experimentally measured flow rate at T_{α} as follows:

$$\left(\frac{\mathrm{d}\alpha}{\mathrm{d}t}\right)_{\alpha} = \frac{1}{\Delta H_{\mathrm{tot}}}\left(\frac{\mathrm{d}H}{\mathrm{d}t}\right)_{T_{\alpha}}. \tag{1.15}$$

Once the temperature dependence of the isoconversional rate is determined from a series of temperature programs, e.g., several heating rates or several temperatures, it can be parameterized through a combination of Eqs. 1.1 and 1.2 as:

$$\ln\left(\frac{\mathrm{d}\alpha}{\mathrm{d}t}\right)_{\alpha,i} = \ln[A_{\alpha} f(\alpha)] - \frac{E_{\alpha}}{RT_{\alpha,i}}, \tag{1.16}$$

where the subscript i represents the number of the temperature program. This equation is the base of the differential isoconversional method by Friedman [24]. A plot on the left-hand side of Eq. 1.16 against the reciprocal temperature gives a straight line whose slope yields the isoconversional value of the effective activation energy, E_{α}, without any assumptions about the process model. The two other parameters of the kinetic triplet (preexponent and reaction model) are encrypted in the intercept but they can be evaluated by using several simple techniques discussed in Chap. 2.

Repeating the calculations (Eq. 1.16) for every value of α results in evaluating a dependence of the effective activation energy on the extent of conversion. Obtaining such dependence is the major outcome of the application of the Friedman method as well as of any other isoconversional method. An overview of the methods is provided in Chap. 2. For now, we need to point out the effective nature of the activation energy estimated. The term "effective" as well as "overall," or "global," or "apparent" is used to emphasize that the activation energy estimated from experimental kinetic data does not necessarily have a simple meaning signified by Eq. 1.1. This equation is an equation of a single-step process that means that all the reactants become converted to the products by overcoming the same energy barrier, E. As discussed later, single-step pathways in condensed-phase and heterogeneous kinetics are rather an exception than a rule. The application of the single-step equation to a process whose rate may be determined by more than one step results in estimating an activation energy that may be linked to more than one energy barrier. For this reason, experimentally determined activation energy generally provides information on an averaged or effective energy barrier that is the barrier that corresponds to the actual temperature dependence of the experimentally measured process rate. It

should be noted that experimental estimates of the preexponential factor and reaction model are also generally effective in their nature.

This book discusses amply how the E_α versus α dependencies can be estimated and employed for obtaining mechanistic insights, making kinetic predictions, and estimating the two other members of the kinetic triplet. All these actions comprise the body of isoconversional kinetic analysis. The first thing one learns from this analysis is whether the effective activation energy varies with conversion. If E_α does not demonstrate any significant variation with α, the process can be described by a single effective activation energy. This does not necessarily mean that the process in question is a single-step process. More likely, it is a multistep process that has one step whose rate determines the overall process rate. It may also be that the steps that dominate the overall kinetics have insignificantly different activation energies.

When E_α is found to vary significantly with α, the process is likely to involve two or more steps having differing activation energies. Under this circumstance, a single-step rate equation (Eq. 1.1) cannot be applied to describe the process kinetics in the whole range of experimental conversions and temperatures. Nevertheless, the occurrence of a multistep process should not be taken as immediate invalidation of the isoconversional principle, notwithstanding the latter holds strictly for a single-step process. The principle still works as a fair approximation because isoconversional methods describe the process kinetics by using multiple single-step kinetic equations, each of which represents only a single extent of conversion and a narrow temperature range (ΔT) associated with it (Fig. 1.8).

Multistep model fitting is sometimes suggested as a better alternative to isoconversional kinetic analysis. In the ideal case when the number of steps and interrelationship between them (i.e., the mechanism) are known, the multistep model fitting would certainly secure the best possible solution. In reality, most of the time one has to deal with the processes whose mechanism is unknown. In this situation, the number of steps and the mechanism that comprises them have to be guessed and tested by statistical criteria of the fits. It is not uncommon when multistep model fitting cannot differentiate statistically between alternative mechanisms, e.g., parallel and consecutive reactions [18, 20]. For any particular mechanism, the number of steps is usually determined by increasing it consecutively until the introduction of a new step does not result in statistically significant improvement of the fit.

Even if statistical analysis allows one to select a particular mechanism and the number of steps with fair certainty, it does not mean that the resulting multistep model is an accurate representation of the actual process. It should always be kept in mind that statistics evaluates the models only by the quality of the data fit but not by the physical sense of applying the models to the data. The best fist can be easily accomplished by an equation devoid of any physical meaning [25]. This is not to say that multistep model fitting is inferior to isoconversional kinetic analysis. Rather, each approach has its limitations and inaccuracies. An isoconversional method approximates multistep kinetics by a sequence of independent single-step equations, none of which is an accurate representation of the actual multistep kinetics. Multistep fitting approximates multistep kinetics by an interrelated combination of single-step equations, in which the number and interrelationship of the steps do

not represent accurately the actual multistep kinetics. In either case, the result of analysis is a set of kinetic triplets that are effective because the actual kinetics gets averaged through the use of approximate models. At any rate, when dealing with condensed-phase and heterogeneous kinetics one needs to understand the meaning of effective kinetic parameters. Applied to isoconversional methods, this means to understand the concept of variable activation energy.

1.2 Understanding Variable Activation Energy

> *Then I wanted to know the meaning of the fourth beast, which was different from all the others and most terrifying.*
>
> Daniel 7:19

Variable activation energy (i.e., the activation energy that varies with temperature and/or conversion) would be much easier to appreciate, if it were not for that eye-catching graph found in undergraduate general or physical chemistry texts in sections dealing with kinetics or, more specifically, with the activated-complex theory. An example of such graph is shown in Fig. 1.9 borrowed from a classical paper by Eyring [26]. This graph perfectly captures the essence of a reaction act, in which reactants must overcome some energy barrier in order to turn into products. The graph is so self-explanatory and the idea appears so straightforward that the constancy

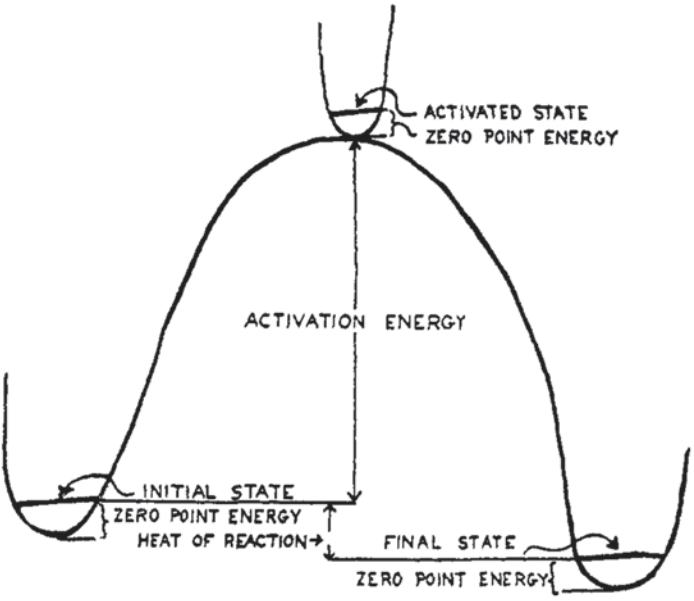

Fig. 1.9 Energy barrier in the theory of the activated complex. (Reproduced from Eyring [26] with permission ACS)

of the energy barrier as well as of the activation energy representing this barrier does not raise much of a doubt. Nonetheless, the situation presented in this graph is grossly oversimplified. It represents a reaction between two reactant molecules that get converted to two product molecules. That is, there is no reaction medium, in which the energies of the molecules, engaged in the reaction act, would be affected by intermolecular interactions with surrounding inactive molecules. Such simplification may be appropriate only for gas-phase reactions and thus is of little relevance to condensed-phase and heterogeneous kinetics. Nevertheless, it is worthy a note that even in the gas-phase reactions the energy barrier height is known [27] to demonstrate a variation with temperature due to temperature dependence of the heat capacity of activation and tunneling effects.

When it comes to condensed-phase kinetics, the processes take place in the liquid or solid medium. In this situation, the energy barrier becomes dependent on the properties of the medium. The size of the barrier may thus change as the properties of the medium change with either temperature or reaction progress. Let us first illustrate [28] a variation with conversion by considering a single-step reaction $A \rightarrow B$ such as isomerization. In general, the energetic state of the reactant A is affected by the molecules that surround it. At the early stage of the reaction, when α is close to 0, the reactant is surrounded by other molecules of A. As the reaction nears completion (i.e., α is close to 1) the reactant will be predominantly surrounded by the product molecules B. If intermolecular forces between A and A are stronger than the forces between A and B, the molar enthalpy of A will be lower in initial ($\alpha=0$) than in final ($\alpha=1$) stages of the reaction (Fig. 1.10). By similar argument, in the final stages ($\alpha=1$) when the product B is surrounded by the molecules B, its molar enthalpy is lower than in the initial stages of reaction ($\alpha=0$). Obviously, as this reaction progresses from $\alpha=0$ to $\alpha=1$, its exothermicity should increase and its energy barrier should decrease. In other words, the observed activation energy should progressively decrease as a function of conversion, α.

A variation of the energy barrier with temperature follows directly from the activated-complex theory developed for reactions of ions or polar molecules in solutions [29]. In accord with this theory, the rate constant of reaction between two ions is given as

$$\ln k = \ln k_0 - \frac{z_A z_B e^2}{\varepsilon d_{AB} k_B T}, \tag{1.17}$$

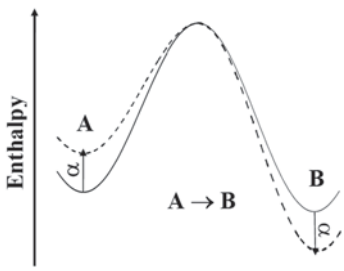

Fig. 1.10 Illustration of how intermolecular interactions may affect the height of the energy barrier throughout the reaction progress

where e is the electronic charge, z_A and z_B the numbers of charges on the ion, ε is the dielectric constant of the medium, d_{AB} is the distance between the centers of the ions in the activated state, and k_B is the Boltzmann constant. The energy barrier in Eq. 1.17 includes the dielectric constant, whose temperature dependence causes a variation in the activation energy [29]. In addition, we should note that an elementary step of any chemical reaction is the process of electron transfer. Per the Marcus theory [30, 31], the rate constant of this process is

$$k = A\exp\left(\frac{-\Delta G^*}{k_B T}\right), \tag{1.18}$$

where among several components the free energy of activation, ΔG^* involves the solvent reorganization energy, which can vary significantly with temperature [32].

It should be stressed that the aforementioned examples explain variations in the energy barrier for a single-step processes, which is the reaction act itself. The rate of the reaction act is determined by the probability of the reacting molecules to jump over the energy barrier. What is missing from this picture is the rate, at which molecules arrive at the reacting situation or, to put it differently, the rate of molecular mobility or diffusion. If in gases the rate of diffusion is much faster than the rate of the reaction act and thus can be neglected, it is not the case of the condensed media, in which the cohesive forces exert significant resistance to molecular motion.

For example, in liquids the rate of diffusion is inversely proportional to viscosity. The activated-complex theory does not account directly for the effect of viscosity on the reaction rate. However, the effect is treated adequately by the Kramers' theory [33], which introduces viscosity of the medium as a crucial kinetic factor. According to this theory, in the case of large viscosity the rate constant take on the following form:

$$k = k_{\text{ac}}\kappa(\eta), \tag{1.19}$$

where k_{ac} is the activated-complex theory rate constant, $\kappa(\eta)$ is a term that accounts for the effect of the generalized viscosity on the reaction rate. Extensive testing of the effect demonstrates [34] that k on η dependencies are strongly nonlinear and, in certain cases, may even be bell-shaped. Considering that viscosity is temperature dependent, the effective activation energy estimated from the temperature dependence of the rate constant (Eq. 1.5) should also be temperature dependent.

Although the activated-complex theory does not account for the diffusion effect of a viscous medium on the reaction rate, the effect can be accounted for by using the so-called addition of kinetic resistances [35]. The idea was originally explored by several workers, including Rabinowitch [36], who proposed that the characteristic time of a process can be defined as the sum of the characteristic time of the reaction act and the characteristic time for reactants to diffuse toward each other. In the simple case of a first-order reaction, the characteristic times can be replaced with the reciprocal rate constants

$$k_{\mathrm{ef}}^{-1} = k^{-1} + k_{\mathrm{D}}^{-1}, \tag{1.20}$$

where k_{ef}, k, and k_{D}, respectively, are the effective, reaction, and diffusion rate constants. Assuming that k and k_d obey the Arrhenius temperature dependence, we can derive the effective activation energy of the overall process as follows

$$E_{\mathrm{ef}} = -R\left(\frac{\mathrm{d}\ln k_{\mathrm{ef}}}{\mathrm{d}T^{-1}}\right) = \frac{E_{\mathrm{D}}k + Ek_{\mathrm{D}}}{k + k_{\mathrm{D}}}, \tag{1.21}$$

where E and E_{D} are the activation energies of the reaction and diffusion. In Eq. 1.21, E_{D} can be reasonably well approximated by the activation energy of viscous flow [37]. Because both k and k_{D} vary with temperature, E_{ef} should generally vary with temperature taking the values between E and E_{D}. Figure 1.11 displays the respective temperature dependence of E_{ef} estimated under assumption that E_{D} is typically smaller than E. Equation 1.21 also suggests that E_{ef} can be constant in two special cases. First, when diffusion is much faster than the reaction ($k_{\mathrm{D}} >> k$) the process is said to occur in the reaction regime, and the value of $E_{\mathrm{ef}} = E$. Second, when the process occurs in the diffusion regime ($k >> k_{\mathrm{D}}$) then $E_{\mathrm{ef}} = E_{\mathrm{D}}$. The effect of diffusion is equally important for reactions of solids such as decomposition or oxidation when escape of a gaseous product or delivery of gaseous reactant can be controlled by diffusion through a solid product formed on the surface of a solid reagent [38].

All in all, we should recognize that strong intermolecular interactions encountered in condensed-phase media generally affect a single reaction step to such extent that its kinetics depends on the reaction medium properties and the energy barrier varies as these properties change with conversion and/or temperature. Furthermore, a single reaction step can be complicated by additional steps such as diffusion. Then the kinetics of the overall process that involves a reaction and diffusion step becomes driven by two energy barriers. The temperature dependence of such pro-

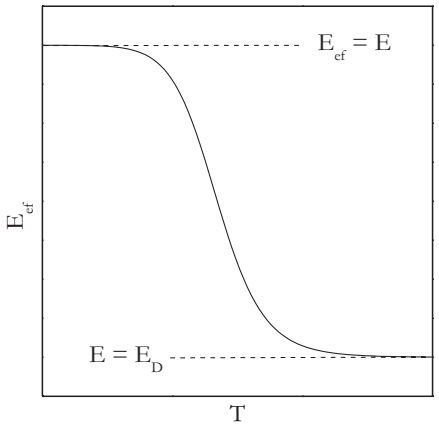

Fig. 1.11 Temperature variation of the effective activation energy of a process, whose overall rate is determined by the rate of both diffusion and reaction (Eq. 1.20)

cess gives rise to the effective activation energy, whose value is a temperature- and/or conversion-dependent function of the activation energies of the individual steps. This holds true for any multistep process regardless of whether it involves diffusion or not. For example, if a reaction involves two competing steps, its rate is described by the following equation

$$\frac{\mathrm{d}\alpha}{\mathrm{d}t} = k_1(T) f_1(T) + k_2(T) f_2(T). \tag{1.22}$$

The effective activation energy of such reaction can be determined by taking the logarithmic derivative of the reaction rate at a constant extent of conversion (cf., Eq. 1.13):

$$E_\alpha = -R\left[\frac{\partial \ln(\mathrm{d}\alpha / \mathrm{d}t)}{\partial T^{-1}}\right]_\alpha = \frac{E_1 k_1(T) f_1(\alpha) + E_2 k_2(T) f_2(\alpha)}{k_1(T) f_1(\alpha) + k_2(T) f_2(\alpha)}. \tag{1.23}$$

This equation clearly suggests that the effective activation energy depends on both temperature and extent of conversion. An example of the dependence is displayed in Fig. 1.12. The dependence has been simulated [39] by using the activation energies and reaction models experimentally established for the two competing steps in the thermal decomposition of nickel formate. It should also be noted that the occurrence of multiple steps is the most common reason why the activation energy experimentally determined for a condensed-phase reaction happens to be variable.

Although examples of variable activation energy are plentiful, we finish by mentioning the one that has a special significance. It is the inversion of sucrose. As widely accepted [40], the birth of chemical kinetics is marked by the work of Wilhelmy, who in 1850 measured the rate of this reaction. It seems symptomatic that this initial reaction later became known [41] as having variable activation energy.

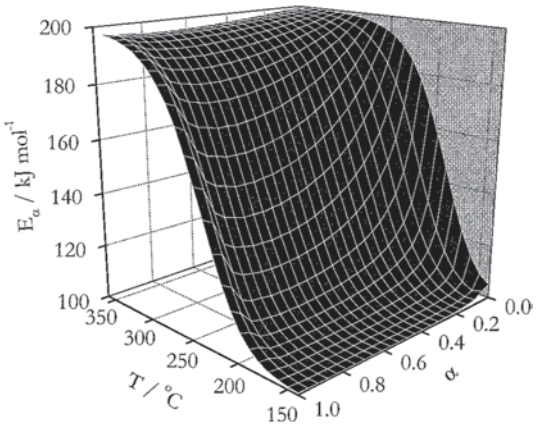

Fig. 1.12 Process that involves two parallel reactions having the following kinetic triplets: $f_1(\alpha)=(1-\alpha)^{2/3}$, $E_1=200$ kJ mol^{-1}, $A_1=10^{16}$ min^{-1} and $f_2(\alpha)=\alpha(1-\alpha)$ and $E_2=100$ kJ mol^{-1}, $A_2=10^7$ min^{-1}. (Reproduced from Vyazovkin [39] with permission of Taylor & Francis)

The effect is illustrated in Fig. 1.13. It appears that oftentimes revealing the variability is a matter of time as well as of having the proper tools. Undoubtedly, the isoconversional method is one of such tools.

A frequently asked question is what is a meaning of variable activation energy? Some people believe that the variability of the effective activation energy deprives it of a physical meaning. To be fair, one should first state what the expected physical meaning is. Oftentimes, the expected meaning is the height of a single and constant energy barrier. However, as we showed earlier, this is not a very realistic expectation, and this is the meaning that variable activation energy can only deliver when it is found to be invariable, which is a possible experimental outcome. In our opinion, variable activation energy is physically meaningful as long as it can be explained in terms of the activation energies for individual steps of the overall process (cf., Eq. 1.21 or 1.23).

To reinforce the point, we can draw an analogy with another widely used effective physical property: the atomic masses of elements. From theory we know that an atom contains a certain number of protons and neutrons whose total mass constitutes the mass of an atom. Since to a high degree of accuracy the mass of either proton or neutron is 1 Da, the atomic masses of elements should be practically integer numbers. However, the actual atomic masses that we find in a periodic table rarely agree with this theoretical expectation because they are effective masses averaged over the natural abundances of isotopes encountered on Earth. Although these effective masses cannot be interpreted within a concept of a single atom, they are by no means physically meaningless parameters. Rather, they are the masses that matter practically.

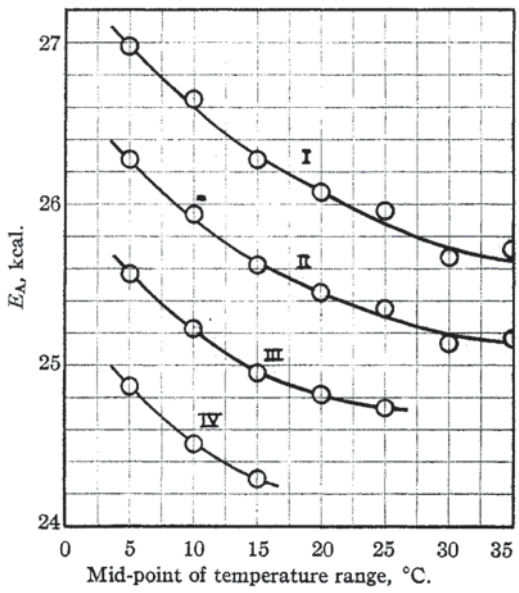

Fig. 1.13 Effect of temperature on the activation energy of sucrose inversion, not catalyzed (*I*) and catalyzed by hydrochloric acid of different concentrations (*II* 1M, *III* 2M, *IV* 3M). (Reproduced from Leininger and Kilpatrick [41] with permission of ACS)

1.3 Obtaining Computation-Worthy Data

...and many a good experiment, born of good sense, and destined to succeed, fails, only because it is offensively sudden.
Ralph Waldo Emerson, The Conduct of Life

Before investing the time and effort in performing kinetic computations, one should invest both in obtaining computation-worthy experimental data. Neither conditions of kinetic runs should be selected arbitrarily nor should the sample shape and size be chosen randomly. The actual measurements should be preceded by exploratory runs, whose purpose is to reveal the effects of the sample and conditions on the kinetic data as well as repeatability of the measurements. The idea is to arrange the sample and conditions so that small changes in them have little or no effect on the kinetic data. Since it is rarely possible to obtain kinetic data that are entirely independent of the conditions and sample, one has to make sure that throughout the whole series of measurements the conditions and sample are well defined and controlled and that their effects on the kinetics are known. Only in this case one can obtain computation-worthy data, i.e., the data that are adequate to the actual kinetics of a process under study.

Although the aforementioned general approach to obtaining computation-worthy data may seem simple, concrete ways of accomplishing this goal depend on the type of a process studied. For practical advice on how to collect adequate kinetic data for a variety of processes, one is recommended to get acquainted with the recommendations [42] of the ICTAC Kinetics Committee. Here, we discuss briefly some basic rules that must be kept in mind when designing kinetic experiments.

There are two constituents of kinetics measurements that control the adequacy of kinetic data to the process kinetics: sample and instrument. This is obvious from the procedure of data production schematically shown in Fig. 1.14. Because a process is necessarily confined to the sample, the sample parameters unavoidably affect the process conditions. At the same time, the instrument controls a set of conditions the sample is exposed to. The adequacy of kinetic data is accomplished only when both sample and instrument defined conditions are controlled properly. The instrument-defined conditions include the temperature, the rate of temperature change (i.e., the

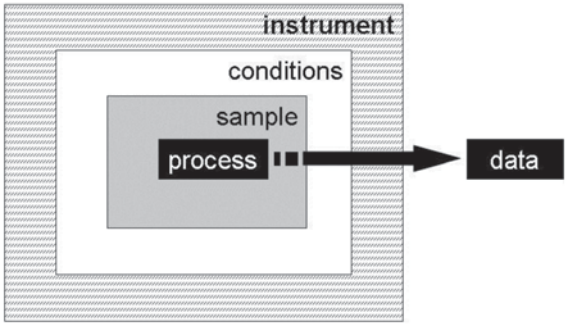

Fig. 1.14 The process of data production. The sample, conditions, and instrument unavoidably affect the data and may distort their adequacy to the process. (Reproduced from Vyazovkin et al. [42] with permission of Elsevier)

heating or cooling rate), the gas atmosphere and its flow rate, and the pressure. The sample-defined conditions include the sample form and size as well as a sample holder (pan or crucible).

To understand better the role of all these conditions on the kinetics, we need to start by reviewing the basic kinetic equation. Most commonly it is written and used in the form of Eq. 1.1 that ignores a pressure-dependent term, $h(P)$. A more accurate form of the basic kinetic equation is:

$$\frac{\mathrm{d}\alpha}{\mathrm{d}t} = k(T) f(\alpha) h(P). \tag{1.24}$$

Experimentally measured rate is adequate to the actual process kinetics only when the process variables (α, T, and P) are controlled accurately and precisely. Ignoring $h(P)$ in Eq. 1.24 is equivalent to assuming that it remains constant during the run. This is a reasonable assumption for a process that does not involve gaseous reactants and/or products, e.g., crystallization. Otherwise, the process may be dependent on the partial pressure of the gaseous reactant and/or product. If a process involves a gaseous reactant as in the case of oxidation of solids or liquids, the constancy of $h(P)$ is accomplished by securing a large excess of the gaseous reactant supplied at a sufficiently high flow rate. If a process produces a gaseous product that may be reactive toward the reactant or the product as in the case of autocatalytic and reversible reactions, the constancy of $h(P)$ is accomplished by effectively removing gaseous products with a sufficiently high flow rate of a purge gas. The actual constancy of $h(P)$ should be tested by conducting a few runs at significantly different flow rates of either reactive or purge gas. If the assumption $h(P) = \text{const}$ holds, the kinetic curves of α or $\mathrm{d}\alpha/\mathrm{d}t$ versus time should not demonstrate any systematic shifts with increasing the flow rate.

The proper instrumental control of α means that the signals used to calculate α, i.e., the heat flow in DSC or the mass in TGA are measured accurately. The accuracy is secured via calibration. The heat calibration of DSC is performed by measuring the heats of melting of reference substances (ice, indium, zinc, aluminum, etc.). The TGA balance is usually capable of self-calibration. However, this calibration is insufficient because it is done at an ambient temperature and, thus, disregards the temperature dependence of the upward buoyant (Archimedes) force, which is proportional to the density of the gas surrounding the sample. When the temperature increases, the gas density decreases diminishing the buoyant force so that the sample mass appears increasingly heavier (Fig. 1.15). The resulting systematic error is eliminated by performing a blank TG run on an empty sample pan and then subtracting the resulting blank TG curve from the TG curve measured by having placed a sample in the same pan (Fig. 1.15).

The proper control of the sample temperature is accomplished by controlling both instrument and sample. The sample temperature is determined by the rate of heat transfer from the instrument-controlled furnace into the sample. Because of the limited thermal diffusivity of the sample, its temperature lags behind that of the

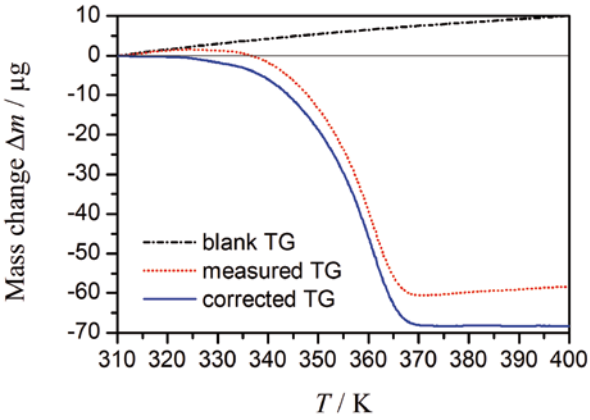

Fig. 1.15 TGA curves for an empty pan (blank TG) and 555 μg sample of calcium oxalate monohydrate placed in this pan (measured TG). Corrected TG is obtained by subtracting blank TG from measured TG. *TGA* thermogravimetric analysis. (Reproduced from Vyazovkin et al. [42] with permission of Elsevier)

furnace. The temperature lag is accounted for by temperature calibration. Temperature calibration of DSC is normally done by measuring the melting temperatures of reference substances, e.g., metals. The same approach is used for temperature calibration of TGA instruments capable of measuring the differential thermal analysis (DTA) or DSC signal. Alternatively, one can heat ferromagnetic materials (e.g., alumel, nickel, cobalt, etc.) in a sample pan while placing a magnet under or above the furnace [43]. The temperature of the mass jump that occurs during the ferromagnetic to paramagnetic transition is then identified with the Curie temperature of the material. Another option is to use a dropping weight (platinum coil) connected to the balance beam by a fusible link, which is a thin wire made of melting point metal standard [44].

Temperature calibration is done in a certain temperature range and under certain heat transfer conditions: heating rate, gas atmosphere, pan material, and sample substance. These are the range and conditions for which the calibration holds most accurately. Thus, it should be performed in the temperature range and under the conditions that are as close as possible to those of the actual kinetic runs. In particular, this means that when nonisothermal runs are carried out at several heating rates, the calibration should be conducted in the whole range of the heating rates used. Using the same pans and gas atmosphere for both calibration and measurement are easy conditions to satisfy. It is rarely possible to calibrate the instrument by using substances whose thermal diffusivity is similar to that of the actual sample. Typical calibration standards are metals whose thermal diffusivity is significantly larger than that for most of inorganic and, especially, organic and polymeric samples. This means that the actual sample may still experience some temperature lag unaccounted by calibration.

Another important reason why the sample temperature deviates from the furnace temperature is the sample self-heating/cooling due to the thermal effect of the process. Due to its limited thermal diffusivity, the sample cannot exchange the process heat with the surroundings instantaneously. As a result, a temperature gradient arises within the sample. This temperature deviation cannot be accounted for

via calibration, but it can be reduced by adjusting the sample size and its form. To secure a quick and uniform distribution of heat and, thus, to minimize the temperature deviation of the sample temperature, the sample should form a thin (not thicker than a few 100 microns) uniform layer on the pan bottom. The heat exchange with the surroundings is also accelerated by employing pans made from materials of high thermal diffusivity. Note that the latter decreases about 200 times in the row: Al, Pt, Al_2O_3, steel, quartz, and glass.

To decrease further the temperature gradients due to the thermal effect of the process, one needs to decrease the total amount of heat produced by the process and the rate of its production. The total amount of heat is decreased by keeping the sample mass as small as possible. Considering the sensitivity of modern DSC and TGA instruments, one normally needs no more than a few mg of a sample. The rate of heat production is reduced by keeping the process rate slower. Slower rate is accomplished by using lower temperatures in isothermal runs and slower heating (or cooling) rates in nonisothermal runs. The values of temperatures and heating rates should be selected so that a process of interest is studied in a reasonably wide temperature range, preferably not narrower than 20–40 °C. Wide temperature ranges are easy to cover in a series of nonisothermal runs, in which the fastest heating rate is about ten times greater than the slowest. Typically, the heating rates are selected to be within the range 1–20 °C min^{-1}. The initial and final temperature of the run should be selected, respectively, ~50 °C below the temperature at which the process starts and ~50 °C above the temperature at which it ends. This would secure accurate determination of the baseline signals.

Covering a wide range of temperatures in isothermal runs presents a certain challenge. The maximum temperature is limited due to the presence of the heat-up period, during which the sample reaches the preset isothermal temperature. The sample unavoidably transforms during this period so that when the temperature sets in, the α value is already larger than zero. The maximum isothermal temperature should be selected so that the total process time is much longer (e.g., 100 times) than the heat-up time. Once the maximum temperature is identified, other temperatures can be selected by a simple approximate rule: Decreasing the temperature by 10 °C decreases the process rate by two to three times. That is, if at the maximum temperature a process takes 1 h to complete, at 20 °C lower temperature its completion would take about 4–9 h. Since the process becomes so much slower, the minimum temperature is limited by acceptable length of experiment and detection limit of the instrument.

Whatever the range of the temperatures or heating rates is chosen, one needs to conduct the runs at four to five different temperatures or heating rates. At the very least, one has to conduct runs at three temperature programs. It should however be noted that this would yield the Arrhenius or a similar linear kinetic plot that has only three points on it. From the statistical standpoint, such a plot can be accepted as linear with 95 % confidence only when its respective correlation coefficient, r is greater than 0.997 ($r^2 = 0.994$), which is frequently not the case. At four and five points, the respective critical values of r are more reasonable: 0.950 and 0.878. Another argument in favor of more than three runs is that increasing the number of points makes it easier to detect possible nonlinearity of the Arrhenius type of plots.

This is important as one of the ways to reveal the temperature dependence of the activation energy.

Last but not least, when selecting the temperature range for kinetic experiments one should be mindful of possible phase transitions (e.g., melting or solid–solid transformations of the solid reactant) that a reactant may undergo within that range. For example, the respective rates and Arrhenius parameters for solid- and for liquid-state decomposition can differ substantially [45], although they may also remain practically unchanged [46]. Significant changes in the reactivity may also be encountered due to the solid–solid phase transitions. This phenomenon is known as the Hedvall effect [47, 48]. Therefore, one needs to exercise great care when combining kinetic data collected in the temperature ranges below and above the phase transition temperature. To detect the presence of possible phase transitions, one has to carry out a DSC run because they are undetectable by TGA.

The aforementioned techniques allow one to minimize deviations of the sample (process) temperature from the reference (furnace) temperature. Nevertheless, some smaller deviations would continue to be present as long as a process is accompanied by a thermal effect. It is good practice to compare the sample temperature against the reference one. Both values are usually made available by modern DSC and TGA instrumentation. The smaller the difference between the two temperatures the better but it should not exceed 1–2 °C, if the kinetic calculations are to be conducted by means of the isoconversional methods that rely on the reference temperature. When the difference is larger, one should consider reducing the sample mass and/or decreasing the heating rates of nonisothermal runs or the temperatures of isothermal ones. Larger temperature deviations can be tolerated [42, 49] when using the isoconversional methods that permit directly using the sample temperature. A detailed discussion of such methods is provided in Chap. 2.

References

1. Vyazovkin S, Goryachko V, Bogdanova V, Guslev V (1993) Thermolysis kinetics of polypropylene on rapid heating. Thermochim Acta 215:325–328
2. Bonnet E, White RL (1998) Species-specific isoconversion effective activation energies derived by thermogravimetry-mass spectrometry. Thermochim Acta 311:81–86
3. Ramis X, Salla JM, Mas C, Mantecón A, Serra A (2004) Kinetic study by FTIR, TMA, and DSC of the curing of a mixture of DGEBA resin and γ-butyrolactone catalyzed by ytterbium triflate. J Appl Polym Sci 92:381–393
4. White DR, White RL (2008) Isoconversion effective activation energy profiles by variable temperature diffuse reflection infrared spectroscopy. Appl Spectr 62:116–120
5. Badrinarayanan P, Zheng W, Simon SL (2008) Isoconversion analysis of the glass transition. Thermochim Acta 468:87–93
6. Madbouly SA, Otaigbe JU (2006) Kinetic analysis of fractal gel formation in waterborne polyurethane dispersions undergoing high deformation flows. Macromolecules 39:4144–4151
7. Ramis X, Cadenato A, Morancho JM, Salla JM (2003) Curing of a thermosetting powder coating by means of DMTA, TMA and DSC. Polymer 44:2067–2079
8. van den Beukel A (1986) Analysis of chemical short range ordering in amorphous $Fe_{40}Ni_{40}B_{20}$. J Non-Cryst Solids 83:134–140

9. Brown ME (2001) Introduction to thermal analysis, 2nd edn. Kluwer, Dordrecht
10. Wunderlich B (2005) Thermal analysis of polymeric materials. Springer, Berlin
11. Menczel JD, Prime RB (eds) (2009) Thermal analysis of polymers: fundamentals and applications. Wiley, Hoboken
12. Atkins P, de Paula J (2010) Physical chemistry, 9th edn. W.H. Freeman, New York
13. Khawam A, Flanagan DR (2006) Solid-state kinetic models: basics and mathematical fundamentals. J Phys Chem B 110:17315–17328
14. Vyazovkin S, Wight CA (1999) Model-free and model-fitting approaches to kinetic analysis of isothermal and nonisothermal data. Thermochim Acta 340/341:53–68
15. Vyazovkin S, Linert W (1995) False isokinetic relationships found in the nonisothermal decomposition of solids. Chem Phys 193:109–118
16. Criado JM, Ortega A, Gotor F (1990) Correlation between the shape of controlled-rate thermal analysis curves and the kinetics of solid-state reactions. Thermochim Acta 157:171–179
17. Criado JM, Perez-Maqueda LA (2005) Sample controlled thermal analysis and kinetics. J Therm Anal Calorim 80:27–33
18. Brown ME, Maciejewski M, Vyazovkin S, Nomen R, Sempere J, Burnham A, Opfermann J, Strey R, Anderson HL, Kemmler A, Keuleers R, Janssens J, Desseyn HO, Li CR, Tang TB, Roduit B, Malek J, Mitsuhashi T (2000) Computational aspects of kinetic analysis. Part A: the ICTAC kinetics project-data, methods and results. Thermochim Acta 355:125–143
19. Maciejewski M (2000) Computational aspects of kinetic analysis. Part B: the ICTAC kinetics project—the decomposition kinetics of calcium carbonate revisited, or some tips on survival in the kinetic minefield. Thermochim Acta 355:145–154
20. Vyazovkin S (2000) Computational aspects of kinetic analysis. Part C: the ICTAC kinetics project—the light at the end of the tunnel? Thermochim Acta 355:155–163
21. Burnham AK (2000) Computational aspects of kinetic analysis. Part D: the ICTAC kinetics project—multi-thermal–history model-fitting methods and their relation to isoconversional methods. Thermochim Acta 355:165–170
22. Vyazovkin S, Burnham A K, Criado JM, Pérez-Maqueda LA, Popescu C, Sbirrazzuoli N (2011) ICTAC kinetics committee recommendations for performing kinetic computations on thermal analysis data. Thermochim Acta 520:1–19
23. Vyazovkin SV, Sbirrazzuoli N (2006) Isoconversional kinetic analysis of thermally stimulated processes in polymers. Macromol Rapid Commun 27:1515–1532
24. Friedman HL (1964) Kinetics of thermal degradation of char-forming plastics from thermogravimetry. Application to a phenolic plastic. J Polym Sci Part C 6:183–195
25. Vyazovkin S, Wight CA (1998) Isothermal and non-isothermal kinetics of thermally stimulated reactions of solids. Int Rev Phys Chem 17:407–433
26. Eyring H (1935) The activated complex and the absolute rate of chemical reactions. Chem Rev 17:65–77
27. Hulett JR (1964) Deviations from the Arrhenius equation. Quart Rev 18:227–242
28. Vyazovkin S, Wight CA (1997) Kinetics in solids. Annu Rev Phys Chem 48:125–149
29. Glasstone S, Laidler KJ, Eyring H (1941) The theory of rate processes. McGraw-Hill, New York
30. Marcus RA (1964) Chemical and electrochemical electron transfer theory. Annu Rev Phys Chem 15:155–196
31. Marcus R A (1993) Electron transfer reactions in chemistry. Theory and experiment. Rev Mod Phys 65:599–610
32. Vath P, Zimmt MB, Matyushov DV, Voth GA (1999) A failure of continuum theory: temperature dependence of the solvent reorganization energy in highly polar solvents. J Phys Chem B 103:9130–9140
33. Kramers HA (1940) Brownian motion in a field of force and the diffusion model of chemical reactions. Physica 7:284–304
34. Schroeder J, Troe J (1993) Solvent effects in the dynamics of dissociation, recombination, and isomerization reactions. In: Fleming GR, Hänggi P (eds) Activated barrier crossing. World Scientific, Singapore, pp 206–240

35. Frank-Kamenetskii DA (1969) Diffusion and heat transfer in chemical kinetics, 2nd edn. Plenum Press, New York
36. Rabinowitch E (1937) Collision, co-ordination, diffusion and reaction velocity in condensed systems. Trans Faraday Soc 33:1225–1233
37. Vyazovkin S, Sbirrazzuoli N (2000) Effect of viscosity on the kinetics of initial cure stages. Macromol Chem Phys 201:199–203
38. Vyazovkin SV (1993) An approach to the solution of the inverse kinetic problems in the case of complex reactions. IV. Chemical reaction complicated by diffusion. Thermochim Acta 223:201–206
39. Vyazovkin S (2000) Kinetic concepts of thermally stimulated reactions in solids: a view from a historical perspective. Int Rev Phys Chem 19:45–60
40. Laidler KJ (1987) Chemical kinetics, 3rd edn. Harper Collins, New York
41. Leininger PM, Kilpatrick M (1938) The inversion of sucrose. J Am Chem Soc 60:2891–2899
42. Vyazovkin S, Chrissafis K, Di Lorenzo ML, Koga N, Pijolat M, Roduit B, Sbirrazzuoli N, Suñol JJ (2014) ICTAC kinetics committee recommendations for collecting experimental thermal analysis data for kinetic computations. Thermochim Acta 590:1–23
43. Gallagher PK, Blaine R, Charsley EL, Koga N, Ozao R, Sato H, Sauerbrunn S, Schultze D, Yoshida H (2003) Magnetic temperature standards for TG. J Therm Anal Calorim 72:1109–1116
44. McGhie AR, Chiu J, Fair PG, Blaine RL (1983) Thermogravimetric apparatus temperature calibration using melting point standards. Thermochim Acta 67:241–250
45. Bawn CEH (1955) Decomposition of organic solids. In: Garner WE (ed) Chemistry of the solid state. Butterworth, London, pp 254–267
46. Vyazovkin S, Clawson JS, Wight CA (2001) Thermal dissociation kinetics of solid and liquid ammonium nitrate. Chem Mater 13:960–966
47. Hedvall JA (1934) Changes in crystal structure and their influence on the reactivity and catalytic effect of solids. Chem Rev 15:139–168
48. Gallagher PK, Sanders JP (2003) Ceramics, glass, and electronic materials. In: Brown ME, Gallagher PK (eds) The handbook of thermal analysis & calorimetry, vol 2. Applications to inorganic and miscellaneous materials. Elsevier, Amsterdam, pp 191–260
49. Vyazovkin S (1997) Evaluation of the activation energy of thermally stimulated solid-state reactions under an arbitrary variation of the temperature. J Comput Chem 18:393–402

Chapter 2
Isoconversional Methodology

2.1 Evolution of Isoconversional Methods

You must have accurate and honest weights and measures.
Deuteronomy 25:15

2.1.1 Early Methods

The birth of isoconversional methods dates back to the 1925 work by Kujirai and Akahira [1]. In their work, they applied thermogravimetric analysis (TGA) data to follow the decomposition kinetics of some insulating materials under isothermal conditions. The mass loss data were fitted to an empirical equation

$$\log t = \frac{Q}{T} - F(w), \tag{2.1}$$

where w is the mass loss in percentage of the initial value, t is the time to reach the extent of decomposition w at different temperatures, and Q is what they called "material constant" that determines the temperature dependence of the decomposition rate. The Q values were estimated as a slope of $\log t$ versus T^{-1} straight line.

It is not difficult to translate the meaning of Q and $F(w)$ to modern kinetic language. Our basic kinetic equation can be written as:

$$\frac{\mathrm{d}\alpha}{\mathrm{d}t} = A\exp\left(\frac{-E}{RT}\right) f(\alpha). \tag{2.2}$$

Its integration for isothermal conditions yields:

$$g(\alpha) \equiv \int_0^{\alpha} \frac{\mathrm{d}\alpha}{f(\alpha)} = A\exp\left(\frac{-E}{RT}\right) t, \tag{2.3}$$

S. Vyazovkin, *Isoconversional Kinetics of Thermally Stimulated Processes,*
DOI 10.1007/978-3-319-14175-6_2

where $g(\alpha)$ is the integral form of the reaction model. Solving Eq. 2.3 for t and taking the decimal logarithm gives:

$$\log t = \frac{E}{2.303RT} - \log\left[\frac{g(\alpha)}{A}\right]. \tag{2.4}$$

For any constant value of α, the second term in Eq. 2.4 is constant and E can be determined from the slope of log t versus T^{-1} without indentifying the form of the reaction model. As long as the total mass loss in percentage is independent of temperature, a constant value of w is equivalent to a constant value of α. Then a comparison of Eq. 2.1 against Eq. 2.4 suggests that $Q = E/2.303R$ and $F(w) = \log[g(\alpha)/A]$.

By using the method proposed by Kujirai and Akahira and their data, we can evaluate the activation energy as a function of mass loss, w. The resulting dependencies are shown in Fig. 2.1 [2]. It is worthy of note that the first ever isoconversional kinetic study reveals significant variations in the effective activation energy.

The work of Kujirai and Akahira did not seem to have much impact, so the method proposed by them was rediscovered by Dakin [3] in 1948. It appears to be of significance that in both papers the idea to bypass models in kinetic calculations came to mind of the workers who dealt with decomposition of complex materials, i.e., the materials that are nearly impossible to represent adequately by models. Nevertheless, isoconversional methods do not seem to have played any major role in isothermal kinetics, although sporadic examples of their use are found in monographic literature [4–7]. Isothermal kinetics appears to have always remained overwhelmingly focused on the model-fitting approach [8–10]. A rise of isoconversional methods to prominence is associated entirely with nonisothermal kinetics.

Since the early 1950s, commercially available thermal analysis instrumentation has been widely used to study thermal behavior of condensed-phase materials under nonisothermal conditions. This catalyzed intensive development of computational

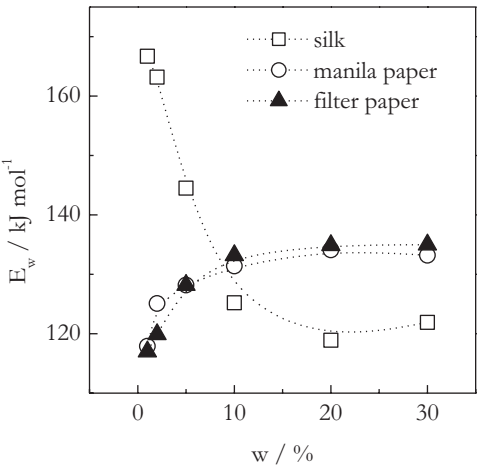

Fig. 2.1 The activation energies derived from data reported by Kujirai and Akahira [1]. (Reproduced from Vyazovkin [2] with permission of Taylor and Francis)

methods for evaluating nonisothermal kinetics. A comprehensive overview of the early methods is found in several books [11, 12]. The first isoconversional methods proposed for treatment of nonisothermal kinetics appeared nearly simultaneously in the 1960s. These were the differential method of Friedman [13] and the integral methods of Ozawa [14] as well as of Flynn and Wall [15, 16].

A simple rearrangement of Eq. 2.2 allows one to arrive at the equation of the Friedman method:

$$\ln\left(\frac{\mathrm{d}\alpha}{\mathrm{d}t}\right)_{\alpha,i} = \ln[f(\alpha)\,A_\alpha] - \frac{E_\alpha}{RT_{\alpha,i}}, \tag{2.5}$$

where the index i identifies an individual heating rate and $T_{\alpha,i}$ is the temperature at which the extent of conversion α is reached under ith heating rate. Then for any given α, the value of E_α is estimated from the slope of a plot of $\ln(\mathrm{d}\alpha/\mathrm{d}t)_{\alpha,i}$ against $1/T_{\alpha,i}$. A great advantage of Eq. 2.5 is that it is applicable to not only linear heating program but also any temperature program at all. In particular, one can apply this equation to the actual sample temperature that may deviate from the preset nonisothermal or isothermal programs because the thermal effect of a process induces sample self-heating or self-cooling (see Sect. 1.3). The method is best applied to the data of differential type such as heat flow in differential scanning calorimetry (DSC). The application of the method to experimental data of the integral type such as mass loss data in TGA reveals an important disadvantage caused by the need of using numerical differentiation for estimating $\mathrm{d}\alpha/\mathrm{d}t$. The procedure dramatically amplifies the noise present in experimental data. For this reason, numerical differentiation has to be combined with smoothing. The latter must be performed with great care because it is known to introduce a systematic error (shift) in the smoothed data that would ultimately appear as a systematic error in the values of kinetic parameters.

The integral data are best treated by integral isoconversional methods that are derived from the integral form of Eq. 2.2:

$$g(\alpha) = A\int_0^t \exp\left(\frac{-E}{RT}\right)\mathrm{d}t. \tag{2.6}$$

If the temperature is raised at a constant rate:

$$T = T_0 + \beta t, \tag{2.7}$$

where β is the heating rate; integration over time can be replaced with integration over temperature:

$$g(\alpha) = \frac{A}{\beta}\int_{T_0}^{T} \exp\left(\frac{-E}{RT}\right)dT \equiv \frac{A}{\beta}I(E,T), \tag{2.8}$$

where T_0 is the initial temperature at $t=0$ when the heating starts. The temperature integral, $I(E, T)$, has no analytical solution. It is solved either by replacing with one of numerous approximation functions [17] or by numerical integration. The traditional integral methods rely on the approximating functions, $S(T)$, that represent the integral value estimated within the integration limits from 0 to T, i.e.,

$$S(T) \approx \int_0^T \exp\left(\frac{-E}{RT}\right) dT. \tag{2.9}$$

Then, $I(E, T)$ in Eq. 2.8 should be equal to the difference in the values of the approximating functions estimated for the respectively different upper limits of integration, T and T_0:

$$I(E,T) \approx S(T) - S(T_0). \tag{2.10}$$

The traditional integral methods are derived by neglecting $S(T_0)$, i.e., the integral from 0 to T_0. This is equivalent to the assumption that the process rate between 0 and T_0 is negligible. It is a reasonable assumption unless a process in question has low activation energy and becomes detectable at temperature close to the initial temperature. In such cases, neglecting the integral from 0 to T_0 may introduce some error to the estimated value of E. The issue has been studied by Starink [18], and some of the results of that study are shown in Fig. 2.2. It is seen that as long as a process becomes detectable more than 50 °C above the initial temperature, the error in the estimated activation energy is likely to be negligible.

The Ozawa and Flynn and Wall methods were the first among a series of the traditional integral isoconversional methods. They both replace the temperature integral with a rather crude approximating function by Doyle [19]. The methods are represented by the same equation:

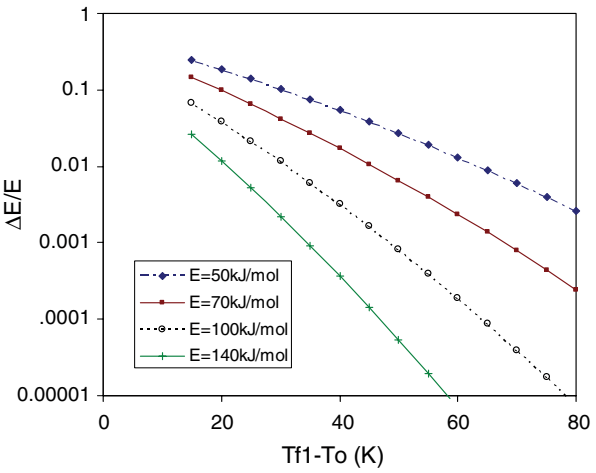

Fig. 2.2 The relative error in the activation energy as a function of the activation energy and the distance between the initial temperature (T_0) and temperature of a given conversion (T_{f1}) at the slowest heating rate β_1. (Reproduced from Starink [18] with permission of Springer)

$$\ln(\beta_i) = \text{Const} - 1.052\left(\frac{E_\alpha}{RT_{\alpha,i}}\right), \tag{2.11}$$

where E_α is estimated as a slope of the linear plot $\ln(\beta_i)$ against $1/T_{\alpha,i}$. Repeating the procedure for a set of different α's gives rise to a dependence of E_α on α. Note that the integral methods can be also applied to the differential type of data that would have to be integrated numerically. Unlike numerical differentiation, integration does not amplify experimental noise that makes integral methods well suitable of either type of data.

It does not appear accidental that all three methods (i.e., Friedman, Ozawa, and Flynn and Wall) were proposed by workers who studied decomposition of complex polymeric materials, i.e., the processes for which finding an adequate kinetic model is more than challenging. It should be noted that the first applications of the methods immediately brought to light the issue of variable activation energy. Friedman [13] observed a variation in E_α (Fig. 2.3) for decomposition of cured phenolic resin. Ozawa [14] found that E_α varied for decomposition of both Nylon 6 and CaC_2O_4 (Fig. 2.4). By using simulated data for competing and independent parallel reactions, Flynn [16] linked a variation in E_α to the activation energies of the individual steps. This link has been explored systematically by Elder [20–23] and Dowdy [24, 25] for competing or independent reactions and by Vyazovkin for reactions complicated by diffusion [26], as well as for consecutive [27] and reversible reactions [28]. The studies have concluded that analysis of the E_α can be used for obtaining some

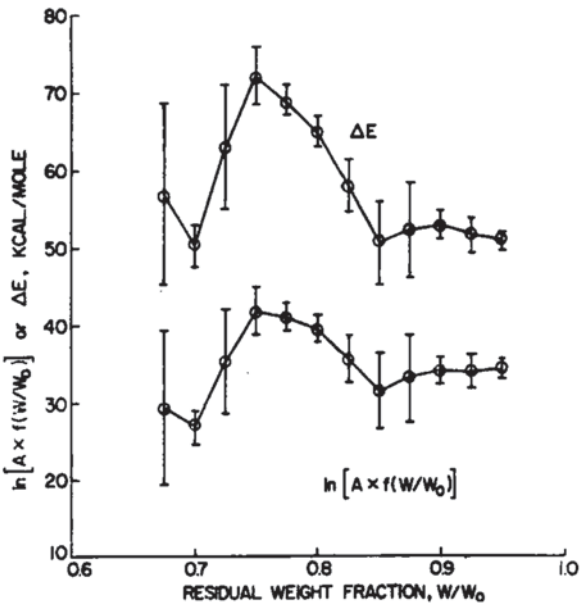

Fig. 2.3 The activation energies determined by Friedman for the thermal degradation of phenolic plastic. (Reproduced from Friedman [13] with permission of Wiley)

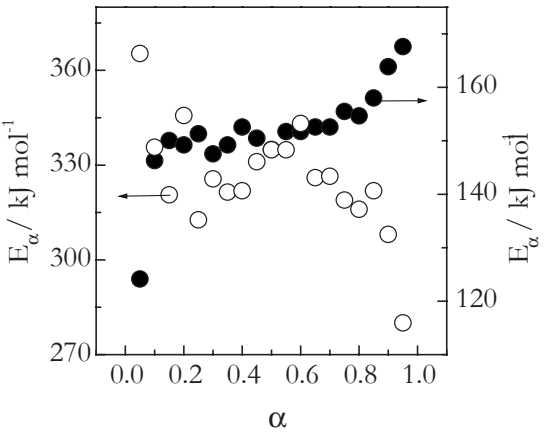

Fig. 2.4 The activation energies reported by Ozawa [14] for the thermal decomposition of calcium oxalate (*open circles*) and Nylon 6 (*solid circles*)

clues about the reaction mechanisms as well as estimates of the activation energies of the individual steps [29].

As mentioned earlier, Eq. 2.11 is based on a very crude approximation of the temperature integral and, thus, should not be used without performing an iterative correction as described elsewhere [30, 31]. Alternatively, one can use isoconversional methods based on a more accurate approximation to the temperature integral. Starink [32] has demonstrated that many of these approximations give rise to linear equations of the general form:

$$\ln\left(\frac{\beta_i}{T_{\alpha,i}^{B}}\right) = \text{Const} - C\left(\frac{E_\alpha}{RT_{\alpha,i}}\right), \tag{2.12}$$

where B and C are the parameters determined by the type of the temperature integral approximation. For example, Doyle's approximation gives rise to $B=0$ and $C=1.052$ that turns Eq. 2.12 into Eq. 2.11 used by the methods of Ozawa and Flynn and Wall. A more accurate approximation by Murray and White gives rise to $B=2$ and $C=1$ and leads to another popular equation that is frequently called the Kissinger–Akahira–Sunose equation [33]:

$$\ln\left(\frac{\beta_i}{T_{\alpha,i}^{2}}\right) = \text{Const} - \frac{E_\alpha}{RT_{\alpha,i}}. \tag{2.13}$$

Relative to Eq. 2.11, Eq. 2.13 offers a significant improvement in the accuracy of the E_α values. According to Starink [32], even more accurate estimates of E_α can be accomplished when setting $B=1.92$ and $C=1.0008$ so that Eq. 2.12 takes the following form:

$$\ln\left(\frac{\beta_i}{T_{\alpha,i}^{1.92}}\right) = \text{Const} - 1.0008\left(\frac{E_\alpha}{RT_{\alpha,i}}\right). \tag{2.14}$$

2.1.2 Modern Methods

Any further increase in the accuracy can be reached by means of isoconversional methods that compute the temperature integral as a part of evaluating E_α. These methods can be referred to as flexible integral methods. By way of contrast, the traditional integral methods can be referred to as rigid integral methods. This is because in the latter integration was carried out as a part of deriving the final equation and thus cannot be modified. Several flexible isoconversional methods have been developed by Vyazovkin [34–36]. The methods employ the same numerical algorithm [34] that was developed under the basic isoconversional assumption that for any given α, $g(\alpha)$ remains unchanged when changing the temperature program, e.g., the heating rate. Then, for n different heating rates, one can use the basic integral rate Eq. 2.8 to write the following equality:

$$g(\alpha)=\frac{A_\alpha}{\beta_1}I(E_\alpha,T_{\alpha,1})=\frac{A_\alpha}{\beta_2}I(E_\alpha,T_{\alpha,2})=\ldots=\frac{A_\alpha}{\beta_n}I(E_\alpha,T_{\alpha,n}). \tag{2.15}$$

When the equality holds strictly, Eq. 2.15 is equivalent to

$$\sum_{i=1}^{n}\sum_{j\neq i}^{n}\frac{I(E_\alpha,T_{\alpha,i})\beta_j}{I(E_\alpha,T_{\alpha,j})\beta_i}=n(n-1). \tag{2.16}$$

Since the values of T_α are unavoidably measured with some error, the strict equality cannot be reached and the difference between left- and right-hand sides of Eq. 2.16 has to be minimized. The difference converges to a minimum when the left-hand side reaches a minimum. That is, E_α is found as the value that secures a minimum of the following function:

$$\Phi(E_\alpha)=\sum_{i=1}^{n}\sum_{j\neq i}^{n}\frac{I(E_\alpha,T_{\alpha,i})\beta_j}{I(E_\alpha,T_{\alpha,j})\beta_i}. \tag{2.17}$$

The temperature integral in this equation is solved numerically or, for faster results, can be replaced with one of the highly accurate approximating functions [17] in accord with Eq. 2.10, i.e., without setting $S(T_0)$ to 0. The minimization procedure is repeated for each value of α to obtain a dependence of E_α on α.

A comparison of the relative errors in the activation energies estimated by Eqs. 2.17 and 2.13 (the method of Kissinger–Akahira–Sunose) indicates (Fig. 2.5) that the former is virtually error-free. On the other hand, the errors associated with the latter are practically negligible except when $x=E/RT$ is very small, i.e., when a process occurs at high temperature and has unusually small activation energy. However, the major advantage of the proposed flexible method is that the user has total control over the process of integration and thus can modify it. In order to appreciate the value of such approach, one needs to realize that when using the traditional (i.e.,

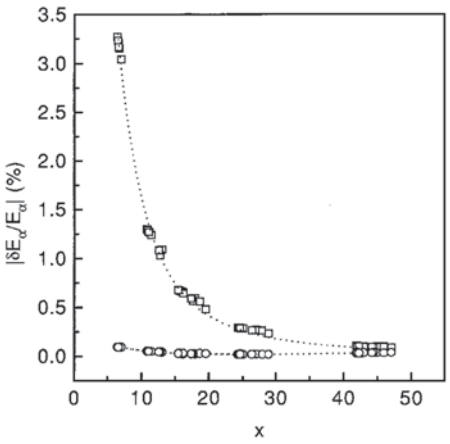

Fig. 2.5 Relative error in the activation energy as a function of $x = E/RT$; nonlinear method, Eq. 2.16 (*circles*), linear Kissinger–Akahira–Sunose equation, Eq. 2.13 (*squares*). (Reproduced from Vyazovkin and Dollimore [34] with permission of ACS)

rigid) integral methods, the resulting activation energies are estimated in accord with a set of built-in assumptions. While maybe not obvious, these assumptions cannot be changed because they are a part of the final equation used for estimating the activation energy.

There are four built-in assumptions that affect the estimates of the activation energy determined with the rigid integral methods. The first one is using 0 instead of T_0 for the lower integration limit in $I(E, T)$ has already been mentioned. Since in a flexible method (e.g., Eq. 2.17) both integration limits are controlled by the user, one can perform integration from the actual value of T_0.

The second assumption is that the process occurs on heating making the traditional methods inapplicable to the processes that take place on cooling, such as crystallization. The heating-only assumption arises from the fact that $I(E, T)$ is approximated as $S(T)$ and not as the difference shown in Eq. 2.10. As cooling starts from the upper temperature T_0 and T continuously decreases, the extent of conversion should increase in proportion to the increasing area $S(T_0)-S(T)$ (Fig. 2.6). In the traditional integral methods, this area is approximated as $S(T)$ and thus it would decrease with deceasing T. This is equivalent to a continuous decrease in the extent of conversion that obviously does not make sense. However, the area $S(T_0)-S(T)$ can be determined correctly when using the flexible integral methods that make them suitable for treating a process that takes place on cooling.

The third built-in assumption is that the process temperature at any moment of time is determined entirely by the value of β (Eq. 2.7). In reality, the temperature estimated by Eq. 2.7 is the so-called reference temperature or simply the furnace temperature. The process temperature, though, is the sample temperature that can deviate from that of the reference due to either self-heating or self-cooling caused by the thermal effect of the process. Unless the deviations are negligible, one has to use the actual sample temperature in kinetic computations. The sample temperature can be used directly in the differential method such as that by Friedman (Eq. 2.5). However, it cannot be used in the integral methods whose equations include a single constant value of β. The fact that such value is included in the equation of an

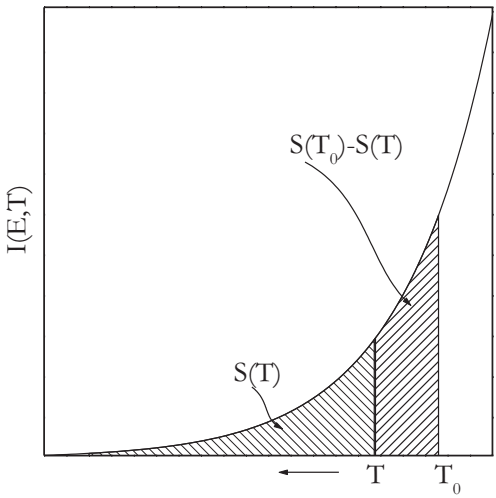

Fig. 2.6 For a process that takes place on cooling from T_0 to T, the flexible methods estimate E_α from the area $S(T_0)-S(T)$ that corresponds to the actually accomplished extent of conversion. The rigid methods estimate E_α from $S(T)$ that represents the conversion, which is yet to be accomplished

integral method means that respective integration is performed assuming that the process temperature is equal to the furnace temperature. This issue can be resolved in a flexible integral method by replacing integration over temperature with integration over time. A specific method has been proposed by Vyazovkin [35]. In this method, the aforementioned algorithmic solution (Eqs. 2.15, 2.16 and 2.17) is adjusted to integration over time. The E_α value is then determined by minimizing the following function [35]:

$$\Phi(E_\alpha) = \sum_{i=1}^{n} \sum_{j \neq i}^{n} \frac{J[E_\alpha, T_i(t_\alpha)]}{J[E_\alpha, T_j(t_\alpha)]}, \tag{2.18}$$

where $J[E_\alpha, T(t_\alpha)]$ is defined as:

$$J[E_\alpha, T(t_\alpha)] = \int_0^{t_\alpha} \exp\left[\frac{-E_\alpha}{RT(t)}\right] dt \tag{2.19}$$

and $T_i(t)$ is a set of arbitrary temperature programs. The integral is solved numerically and minimization is repeated for each value of α to obtain a dependence of E_α on α. Equation 2.19 affords substitution of the actual sample temperatures for $T(t)$. The use of the actual sample temperature in Eq. 2.19 makes the method applicable to any preset program (i.e., isothermal as well as nonisothermal, be it linear or not) even if it is distorted by the thermal effect of the process.

The fourth built-in assumption is that at any α, the value of E_α is estimated as being constant in the whole range from 0 to α. This again arises from the fact that the traditional rigid integral methods estimate the temperature integral in the form of Eq. 2.9, i.e., from 0 to T. As a result of such integration, the estimated E_α values are strictly accurate only when E_α does not vary with α. Otherwise, the E_α estimates

contain a systematic error whose size increases with increasing range of E_α variability. The error can be eliminated by using a flexible integral method. All it takes is to perform either time or temperature integration by segments that correspond to small intervals of conversion, $\Delta\alpha$. Vyazovkin has proposed a method [36] that effectively eliminates this error by performing integration over small time segments. The method is based on Eq. 2.18, whereas Eq. 2.19 is modified as follows:

$$J[E_\alpha, T(t_\alpha)] = \int_{t_{\alpha-\Delta\alpha}}^{t_\alpha} \exp\left[\frac{-E_\alpha}{RT(t)}\right] \mathrm{d}t. \tag{2.20}$$

When integration is carried out over small segments, the E_α value is assumed to be constant only within a small interval of $\Delta\alpha$ that is typically taken to be 0.01–0.02. The efficiency of integration by segments can be demonstrated by comparing the resulting E_α versus α dependence with that estimated by the Friedman method (Eq. 2.5). Because the latter is a differential method, it does not introduce the aforementioned integration error into the E_α values. The application of the integral method with integration by segments and the differential Friedman method to the same set of simulated data demonstrates [36] that the resulting E_α versus α dependencies are virtually identical.

As already mentioned, in the integral methods, the systematic error introduced by non-constancy of E_α is proportional to the magnitude of E_α variation. In the case of significant variation of E_α with α, the relative error in E_α can be as large as 20–30 %. A process that is well known [2] to demonstrate significant variability of E_α is the thermal dehydration of calcium oxalate monohydrate. The E_α dependencies obtained by respectively neglecting and accounting for variability of E_α are displayed in Fig. 2.7 which also shows the size of the error introduced when the variability is neglected. It is generally recommended [37] that one should account for variability

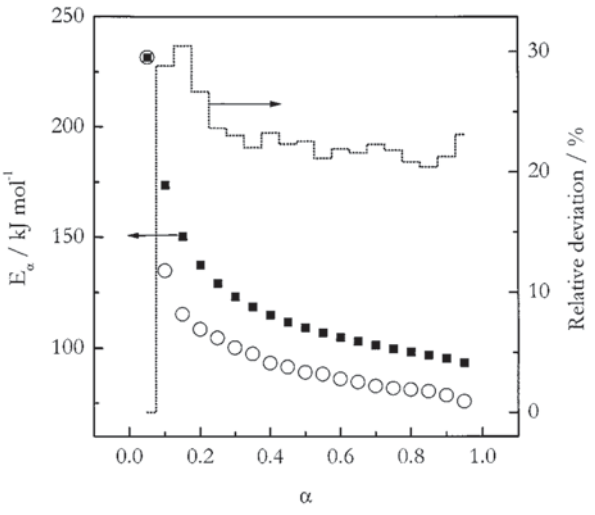

Fig. 2.7 E_α dependencies estimated for thermal dehydration of $CaC_2O_4 \cdot H_2O$ by isoconversional method (Eq. 2.18). *Squares* represent the E_α values obtained when using regular integration (Eq. 2.19). *Circles* represent the E_α values estimated via integration by segments (Eq. 2.20). The *dotted line* shows the size of the relative error in E_α caused by integration that does not account for variability of E_α. (Reproduced from Vyazovkin [36] with permission of Wiley)

in E_α when the difference between the maximum and minimum values of E_α is more than 20–30 % of the average E_α value. In the case of calcium oxalate monohydrate, this difference is close to 100 % of the average value.

Needless to say that performing integration over small temperature segments in accord with Eq. 2.21:

$$I(E_\alpha, T_\alpha) = \int_{T_{a-\Delta\alpha}}^{T_a} \exp\left(\frac{-E_\alpha}{RT}\right) \mathrm{d}T \tag{2.21}$$

would also eliminate the error associated with the variability of E_α in the isoconversional method based on Eq. 2.17. Consistency of the resulting E_α dependence with the dependence produced by the Friedman method has been demonstrated by Budrugeac [38], who also proposed a new nonlinear differential isoconversional method that makes use of a numerical algorithm similar to that represented by Eqs. 2.15 and 2.16.

In addition to the methods proposed by Vyazovkin, there are several other flexible integral isoconversional methods [39–46]. Among them, a method proposed by Popescu [39] deserves a special attention because it combines the flexibility with computational simplicity. The method makes use of the so-called mean value theorem to approximate the temperature integral. The theorem states that a definite integral of a continuous function $f(x)$ on the closed interval [*a, b*] can be presented as:

$$\int_a^b f(x)dx = (b-a)f(c), \tag{2.22}$$

where $f(c)$ is the mean value of $f(x)$ over the interval [*a,b*]. The equality is exact because the mean value is defined as:

$$f(c) = \frac{1}{(b-a)} \int_a^b f(x)dx. \tag{2.23}$$

The theorem does not say where the point *c* is located, it only proves that it is located within the interval [*a, b*]. The application of the theorem to the temperature integral defined on the temperature interval $[T_m, T_n]$ allows one to arrive at the following equation [39]:

$$\int_{T_m}^{T_n} \exp\left(\frac{-E}{RT}\right) dT = (T_n - T_m) \exp\left(\frac{-E}{RT_\xi}\right). \tag{2.24}$$

The equation is exact only when the value of T_ξ is such that the respective value of the exponential function equals the mean value of the function in the interval $[T_m, T_n]$. Unfortunately, there is no simple practical way to determine such tempera-

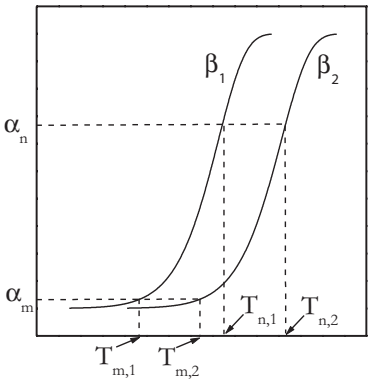

Fig. 2.8 Illustration to the Popescu method (Eq. 2.26)

ture. For practical purposes, it can be approximated as the mean value of the interval $[T_m, T_n]$, i.e., $T_\xi = (T_m + T_n)/2$. This approximation is accurate only for integration of a linear function. For any other function, the accuracy of this approximation would depend on the size of the interval $[T_m, T_n]$ so that the smaller the interval, the better the accuracy. Subject to Eq. 2.24, one can write Eq. 2.8 for two arbitrary conversions α_m and α_n, as follows:

$$g(\alpha_n) - g(\alpha_m) = \frac{A}{\beta}(T_n - T_m)\exp\left(\frac{-E}{RT_\xi}\right), \tag{2.25}$$

where T_m and T_n are the temperatures that correspond, respectively, to the conversions α_m and α_n on the α versus T curve at a given heating rate β (Fig. 2.8). Assuming that the form of the reaction model does not change with the heating rate, the left-hand side of Eq. 2.25 is constant for a set of different heating rates, β_i. Then Eq. 2.25 can be rearranged to:

$$\ln\frac{\beta_i}{T_{n,i} - T_{m,i}} = \text{Const} - \frac{E}{RT_{\xi,i}} \tag{2.26}$$

The activation energy can be determined from the slope of a linear plot of the left-hand side of Eq. 2.26 against $1/T_{\xi,i}$.

Although in the original publication [39] by Popescu, the intervals $\Delta\alpha = \alpha_m - \alpha_n$ used are relatively wide (0.3–0.8), the relative errors in the estimated E values remain within the tenths of percent. However, the primary advantage of the method is in the flexibility to choose the integration limits by selecting any desired values of $\alpha_m - \alpha_n$. In particular, by making the $\Delta\alpha$ intervals smaller (e.g., 0.01–0.02), one can practically eliminate the integration error that arises from the variability of E_α with α. This opportunity has been explored efficiently by Ortega [42], who applied the mean-value theorem to derive isoconversional equations for the conditions when

temperature increases linearly, stays constant, or changes nonlinearly. Figure 2.9 demonstrates the efficiency of the method as applied to a simulated process under conditions of linear heating. It is seen that approximating the temperature integral via the mean value theorem while keeping $\Delta\alpha$ as small as 0.02 allows one to evaluate the correct E_α dependence. The accuracy of this method appears to be comparable to that of the methods proposed by Vyazovkin (Eqs. 2.18 and 2.20) and by Friedman (Eq. 2.5). Not surprisingly, the methods of Ozawa and Flynn and Wall (Eq. 2.11) as well as of Kissinger, Akahira, and Sunose (Eq. 2.13) cannot retrieve the correct E_α dependence because the integration used in these methods is not capable of accounting for variability of E_α.

Note that the equation derived by Ortega for linear heating conditions is similar to Eq. 2.26 obtained by Popescu, the only difference being that T_ζ is taken as T_α, i.e., the upper limit of integration. The use of a single rather than averaged value of temperature as T_ζ can be a source of an unnecessary error as mentioned by Han et al., [47] who proposed to evaluate T_ζ as the mean of five temperatures from the interval $T_{\alpha-\Delta\alpha} - T_\alpha$. This simple modification has been shown [47] to improve the accuracy of the method in the case of noisy simulated and actual experimental data.

All flexible integral isoconversional methods should in principle be applicable to treat processes that take place on cooling. This expands the application area of the methods to such processes as crystallization [48, 49], gelation [50], as well as some other phase transitions [51] that can be initiated by decreasing temperature. If a flexible method is based on integration with respect to temperature (e.g., Eq. 2.21 or 2.24), then under conditions of cooling, both temperature integral and heating rate

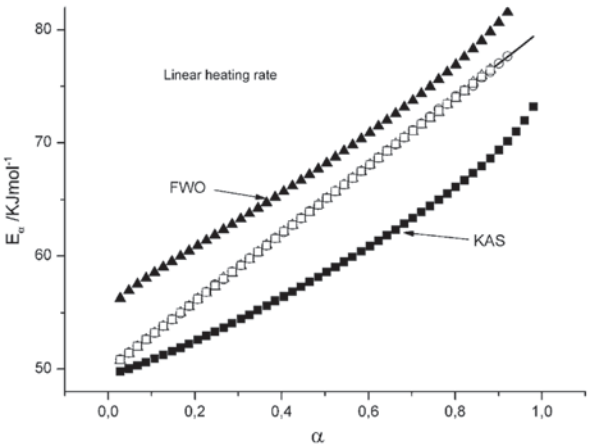

Fig. 2.9 The process was simulated to have E_α to vary linearly with α. *Solid line* represents the simulated E_α versus α dependence. *Open circles, triangles,* and *squares* represent the E_α values estimated according to the methods proposed, respectively, by Ortega, Vyazovkin, and Friedman. All three methods yield the E_α values that coincide with the simulated ones. FWO and KAS represent the values estimated by the method of Flynn and Wall and Ozawa and by the method of Kissinger, Akahira, and Sunose. (Reproduced from Ortega [42] with permission of Elsevier)

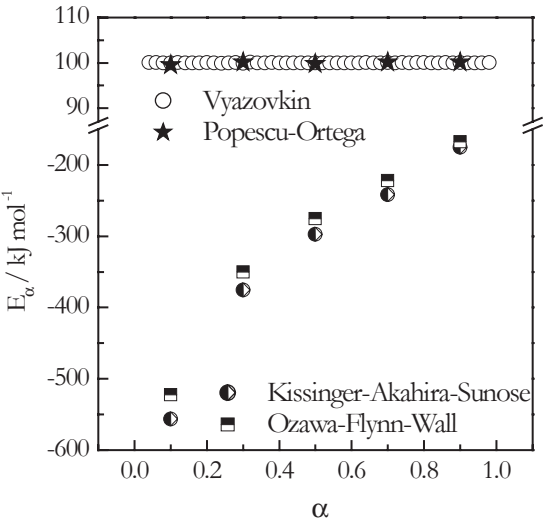

Fig. 2.10 The E_α values estimated by flexible (Vyazovkin, and Popescu and Ortega) and rigid (Ozawa and Flynn and Wall, and Kissinger and Akahira and Sunose) integral isoconversional methods. The size of the $\Delta\alpha$ interval was taken to be 0.02 in both Vyazovkin and Popescu–Ortega methods

become negative so that $g(\alpha)$ remains positive as it should (see Eq. 2.8). If integration is done with respect to time, the integral (Eq. 2.6) remains positive regardless of the direction in which temperature changes.

The appropriateness of the flexible integral methods for the processes occurring on cooling can be illustrated by applying two flexible integral methods to simulated data [52]. The data represent a process taking place on cooling with an activation energy 100 kJ mol^{-1}. The methods selected are that proposed by Vyazovkin (Eqs. 2.18 and 2.20) and that proposed by Popescu and Ortega (Eq. 2.26). As seen from Fig. 2.10, both methods successfully retrieve the correct value of E from the cooling data. To reinforce the earlier made point that the rigid integral methods are not suitable for treating cooling data, we have applied the methods of Ozawa and Flynn and Wall as well as of Kissinger, Akahira, and Sunose to the same data set. These methods obviously produce erroneous values of the activation energy (Fig. 2.10). The failure is the direct consequence of the aforementioned (Fig. 2.6 and related discussion) inability of the rigid integral methods to properly evaluate the temperature integral on cooling.

As seen from the above brief overview, over a couple of past decades, isoconversional methods have developed into quite sophisticated computational tools capable of exploring thermally stimulated kinetics under a wide variety of temperature conditions. They have now become the most popular methods for kinetic analysis of the thermally stimulated processes. Per Scopus database, there are over two thousand papers that report the use of isoconversional methods over the last 4 years (2011–2014). However, the popularity of the methods started to grow quickly less than a decade ago. Apparently, the process was accelerated by the results of the 2000 Kinetic Project sponsored by the International Confederation for Thermal Analysis and Calorimetry (ICTAC) that once more highlighted critical deficiency of the single-heating-rate methods and vigorously emphasized [53–56] the necessity of abandoning them in favor of the methods based on multiple temperature programs.

It should be noted that single-heating-rate methods had dominated the field for decades, which was not very surprising. Given a choice, not many people would pick an isoconversional method that requires multiple runs in favor of a method that promises to produce the same information from just a single run. As a matter of fact, the need to perform more than a single run was considered [11] as a major disadvantage of isoconversional methods. The other point of critique typically was that isoconversional methods did not offer direct ways of determining the other two components of the kinetic triplet, i.e., the reaction model and preexponential factor. Computational techniques for estimating these two components are discussed in the next section.

2.2 Estimating Reaction Models and Preexponential Factors

Tao creates the One.
The One creates the Two.
The Two creates the Three.
The Three creates all things.

Lao Tzu, Tao Te Ching: 42

2.2.1 Prelude

The ability of isoconversional methods to estimate the activation energy without estimating the reaction model has long been considered as one of their advantages. However, it is sometimes believed that the methods are not capable of estimating the reaction model as well as the preexponential factor. This is complete fallacy. As a matter of fact, the seminal paper [13] by Friedman describes not only the isoconversional method of estimating the activation energy but also a way of determining the preexponential factor and the reaction order model. Since then, some more sophisticated and accurate methods for estimating the preexponential factor and reaction model have been developed. Two very popular methods are discussed in this section.

Before we get to discussion of these methods, we need to forewarn one against some rather unsound approach to the problem that unfortunately is not quite uncommon. In it, the reaction model and preexponential factor are estimated by matching the activation energy estimated by an isoconversional method with the activation energy determined by some method that uses model fitting of single-heating-rate data. For example, one can fit $\mathrm{d}\alpha/\mathrm{d}t$ versus T data obtained at one heating rate to Eq. 2.27

$$\ln\left(\frac{1}{f_j(\alpha)}\frac{\mathrm{d}\alpha}{\mathrm{d}t}\right) = \ln A_j - \frac{E_j}{RT}. \tag{2.27}$$

The equation is readily obtained by rearranging Eq. 2.2. The kinetic triplet is estimated by substituting some reaction model $f_j(\alpha)$ in the left-hand side of Eq. 2.27 and fitting its dependence on the reciprocal temperature to a straight line. The intercept and slope of the line would, respectively, yield $\ln A_j$ and $-E_j/R$. Such model-fitting results in obtaining as many kinetic triplets as the number of the reaction models one chooses to substitute in Eq. 2.27. Then, out of the multitude of obtained triplets, one picks a triplet whose E_j value matches best the activation energy value obtained by an isoconversional method. Such approach is unsound because of several methodological flaws. First, the E_j value frequently does not match the isoconversional activation energy with sufficient accuracy. Second, it is also not uncommon when more than one reaction model yields E_j values that match the isoconversional value within its confidence limits. Third, for the same reaction model, the E_j and A_j values commonly change with the heating rate. These factors introduce considerable inaccuracy in evaluation of the reaction models and preexponential factors.

On the other hand, the two methods discussed further afford accurate evaluation of the reaction model and preexponential factor subject to one important condition. The condition is that the process under study can be adequately represented by the single-step Eq. 2.2. This is readily verifiable by means of an isoconversional method. The condition is satisfied when the E_α values do not demonstrate a systematic dependence on α within a reasonably wide range of α, e.g., 0.1–0.9. It is practically acceptable when the difference between the maximum and minimum values of E_α is less than 10% of the average E_α value. In the case of larger variability, the process cannot be considered as a single-step one. Any attempts to describe a multistep process by a single-reaction model and a value of the preexponential factor would give rise to inaccurate estimates of both.

2.2.2 The Use of the Compensation Effect

The first method we are going to discuss here allows one to employ the compensation effect for evaluation of the preexponential factor and the reaction model [29]. The method was originally proposed [57] for a single-step process. Later it was demonstrated [58] to work for estimating the preexponential factors of multistep processes. The method has been perfected by Sbirrazzuoli [59]. The compensation effect was already discussed briefly in Chap. 1 (Eq. 1.11). More detailed information is furnished elsewhere [60].

For the purpose of the present discussion, it would suffice to mention that the Arrhenius parameters $\ln A_j$ and E_j estimated by a single-heating-rate method (e.g., Eq. 2.27) are strongly correlated in the form of a linear relationship known as the compensation effect:

$$\ln A_j = aE_j + b, \tag{2.28}$$

where a and b are the parameters of the compensation effect. The original work [57] by Vyazovkin and Lesnikovich has demonstrated two important properties of the compensation effect that are relevant to accurate evaluation of the preexponential factor. First, even if the correct model is not included in the list of models used to determine the $\ln A_j$ and E_j values and if none of these values matches the correct values $\ln A_0$ and E_0, the latter still lie on the compensation line determined by Eq. 2.28. This means that if the correct value of the activation energy is known, one can estimate the correct value of the preexponential factor by substituting E_0 into Eq. 2.28. Second, although the parameters of the compensation effect depend on the heating rate, the latter does not affect the value of the preexponential factor estimated by substituting E_0 into Eq. 2.28 obtained at different heating rates. The property arises from the fact [61] that the compensation lines related to different heating rates intersect at the points $\ln A_0$ and E_0 (Fig. 2.11). As a result, substitution of the correct value of the activation energy into the compensation line equation yields the same value of the preexponential factor regardless of the heating rate [57].

Overall, the method of estimating the preexponential factor boils down to the following four steps. First, an isoconversional method is applied to determine the activation energy, E_α, as a function of conversion. Second, a single-heating-rate method is employed to determine several $\ln A_j$ and E_j pairs. Third, the $\ln A_j$ and E_j values are fitted to Eq. 2.28. Fourth, the E_α values are substituted into Eq. 2.28 to yield the respective value of the preexponential factor:

$$\ln A_\alpha = aE_\alpha + b. \tag{2.29}$$

If E_α is independent of α, as one would expect for a single-step process, the resulting $\ln A_\alpha$ is also invariable. Substitution of variable E_α value obviously yields $\ln A_\alpha$ value that depends on α, which would be the case of a multistep process. As shown earlier [58], a dependence of $\ln A_\alpha$ on α can be used to estimate the preexponential factors of a multistep process. This has been recently reconfirmed by Sbirrazzuoli

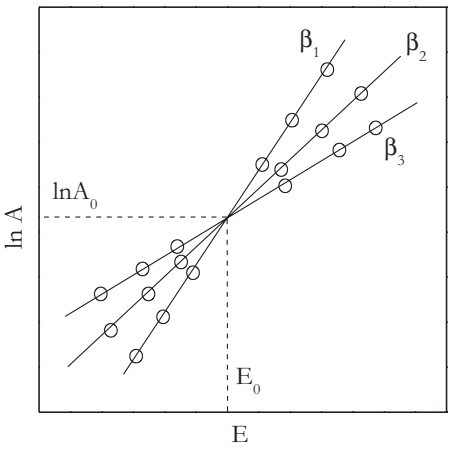

Fig. 2.11 Compensation lines $\ln A_j = aE_j + b$ at three different heating rates $\beta_1 < \beta_2 < \beta_3$. The lines intersect at the correct values of the activation energy and preexponential factor. *Circles* represent the actual values of $\ln A_j$ and E_j estimated by a single-heating-rate method (e.g., Eq. 2.27) while using different reaction models

[59], who also demonstrated that highly accurate values of the preexponential factor can be obtained when one evaluates the parameters of the compensation effect from only four pairs of A_j and E_i estimated by the single-heating-rate method of Tang et al. [62] when using the reaction models of Mampel (F1) and Avrami–Erofeev (A2, A3, A4).

Once both E_α and A_α have been evaluated, it becomes possible to reconstruct numerically the reaction model in either integral or differential form [63]. The integral reaction model is reconstructed as follows:

$$g(\alpha) = \frac{A_\alpha}{\beta} \int_0^{T_\alpha} \exp\left(\frac{-E_\alpha}{RT}\right) \mathrm{d}T. \tag{2.30}$$

Inserting in Eq. 2.30 the values of E_α, A_α, and T_α for each value of α yields numerical values of $g(\alpha)$ that can be matched to the theoretical g(α) models (Fig. 2.12). In Eq. 2.30, T_α is the experimentally measured temperature of reaching a certain α at a given heating rate, β. However, the resulting values of $g(\alpha)$ should not demonstrate any significant difference when using the T_α values related to different heating rates. Note that the independence of the g(α) dependences on β should be expected when E_α (and thus A_α) are independent of α, i.e., for a single-step process. As a matter of fact, accurate values of $g(\alpha)$ can generally be evaluated when the process is a single-step one, because only in this case, the process can be described by a single-reaction model. When a process demonstrates significant variability of E_α, its accurate description would require in general more than one kinetic triplet and in particular more than one reaction model. Nevertheless, analysis of the single $g(\alpha)$ evaluated for a multistep process in some cases may provide useful insights [59].

Similar procedure and principles are applied when restoring the differential reaction model. The respective equation is obtained by rearranging Eq. 2.2 as follows:

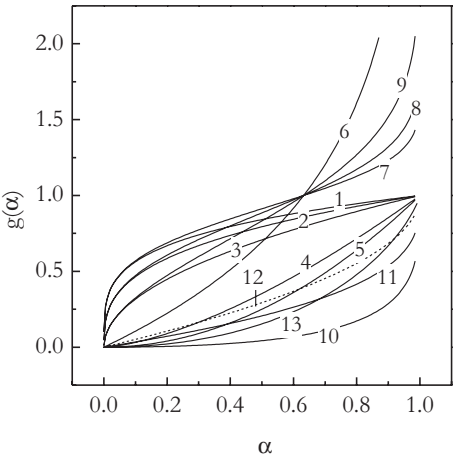

Fig. 2.12 Theoretical $g(\alpha)$ dependencies. The numbers correspond to the model numbers from Table 1.1

$$f(\alpha) = \beta \left(\frac{\mathrm{d}\alpha}{\mathrm{d}T} \right)_a \left[A_\alpha \exp\left(\frac{-E_\alpha}{RT_\alpha} \right) \right]^{-1}, \tag{2.31}$$

where E_α is estimated by an isoconversional method, A_α is evaluated via the compensation effect, and T_α and $(\mathrm{d}\alpha/\mathrm{d}T)_\alpha$ are experimental values measured at the heating rate β. Substitution of the values into Eq. 2.31 yields numerical values of $f(\alpha)$, which can further be matched to the theoretical $f(\alpha)$ models (Fig. 1.4).

Figures 2.13 and 2.14 exemplify the application of the aforementioned method in the case of thermal dehydration of nedocromil sodium trihydrate that occurs in two well-separated steps [64]. For both steps, the E_α values estimated by an isoconversional method do not demonstrate practically any dependence of α (Fig. 2.13). The compensation effect (Eq. 2.29) has been used to estimate the A_α values, which were substituted in Eq. 2.30 to evaluate the reaction model, $g(\alpha)$ in numerical form (points in Fig. 2.14). Comparison of the $g(\alpha)$ values against the theoretical reaction models suggests that the first step of dehydration follows the zero-order reaction model, $g(\alpha)=\alpha$ (R1).

However, for the second dehydration step, the $g(\alpha)$ values fall between two diffusion models D2 and D3 (Table 1.1). This is not very unusual considering the

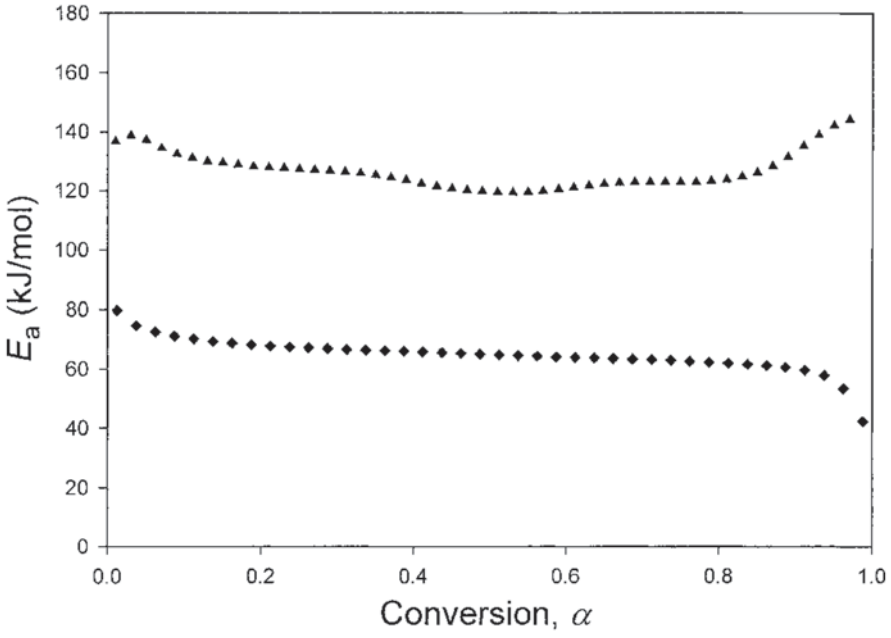

Fig. 2.13 E_α values estimated by an isoconversional method for first (*diamonds*) and second (*triangles*) steps of dehydration of nedocromil sodium trihydrate. (Reproduced from Zhu et al. [64] with permission of Wiley)

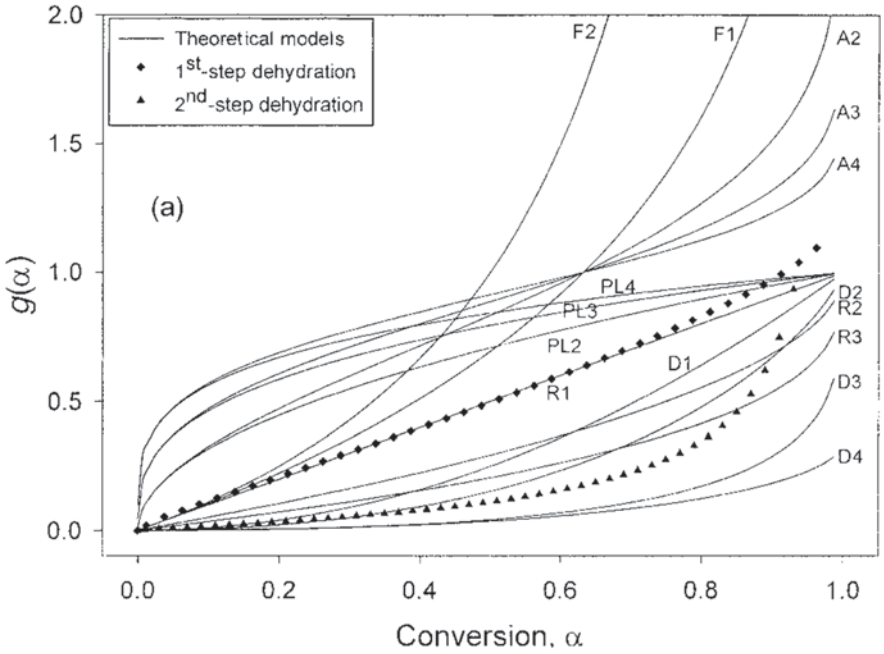

Fig. 2.14 The $g(\alpha)$ values estimated for the first (*diamonds*) and second (*triangles*) steps of dehydration of nedocromil sodium trihydrate. The solid lines represent the theoretical models. (Reproduced from Zhu et al. [64] with permission of Wiley)

following two problems. First, the selection of the models is always subjective and incomplete so that the proper model may simply be missing from the list. Second, the theoretical models were developed for largely idealized processes that oftentimes do not represent accurately the reality. For this reason, the theoretical reaction model is frequently used in the form with adjustable parameters, most popular being the so-called truncated Sestak–Berggren (SB) model [37]:

$$f(\alpha) = \alpha^m (1-\alpha)^n. \tag{2.32}$$

Although this equation is frequently referred to simply as the SB model, the latter has one term more [65] than Eq. 2.32. On the other hand, Eq. 2.32 has been used in the heterogeneous kinetics years before [66, 67] the influential work [65] by Sestak and Berggren. A great advantage of Eq. 2.32 is that depending on the values of n and m it can imitate the three major types of kinetic curves, i.e., decelerating, accelerating, and sigmoid ones. Furthermore, Perez-Maqueda et al. have shown [68] that Eq. 2.32 can accurately match a number of theoretical models. The parameters n and m are easy to estimate by fitting the right-hand side of Eq. 2.32 to the numerical $f(\alpha)$ values determined by Eq. 2.31. Unfortunately, the model does not exist in the integral form because the integral

$$g(\alpha) = \int_0^{\alpha} \frac{d\alpha}{\alpha^m (1-\alpha)^n} \tag{2.33}$$

does not have an analytical solution. However, the values of n and m can still be determined by fitting the right-hand side of Eq. 2.33 to the numerical values of $g(\alpha)$ estimated by Eq. 2.30.

2.2.3 The Use of the y(α) or z(α) Master Plots

The use of the $y(\alpha)$ or $z(\alpha)$ master plots is another popular method of estimating the reaction models and preexponential factors. The method is contingent on E_α being practically invariable with respect to α. Therefore, as the first step in using this method, one needs to apply an isoconversional method for estimating E_α as a function of α and making sure that there is no significant variation. Then E_α can be replaced with the mean value, E_0. The $y(\alpha)$ function [69] has the following form:

$$y(\alpha) = \left(\frac{\mathrm{d}\alpha}{\mathrm{d}t}\right)_\alpha \exp\left(\frac{E_0}{RT_\alpha}\right) = Af(\alpha). \tag{2.34}$$

Equation 2.34 is derived by rearranging Eq. 2.2. The values of $y(\alpha)$ are calculated by using the experimental dependence of $(\mathrm{d}\alpha/\mathrm{d}t)_\alpha$ on T_α and multiplying it by the exponential term containing the E_0 value estimated by an isoconversional method. The resulting numerical values of $y(\alpha)$ are then plotted against α and matched with the theoretical $y(\alpha)$ master plots. The best match identifies a suitable model. Each heating rate gives rise to one experimental dependence of $\mathrm{d}\alpha/\mathrm{d}t_\alpha$ on T_α and, those, to one $y(\alpha)$ plot. However, the resulting $y(\alpha)$ plots should not demonstrate any significant variation with β producing a single $y(\alpha)$ plot.

The fact that A is constant in 2.34 suggests that the shape of the $y(\alpha)$ master plot is defined exclusively by the shape of the $f(\alpha)$ functions (Fig. 1.4) that represent the differential form of the reaction model. Since the preexponential factor is yet to be estimated, the experimental and theoretical $y(\alpha)$ plots are matched in a normalized form that sets their range of variation from 0 to 1. Examples of some normalized theoretical $y(\alpha)$ plots derived from the $f(\alpha)$ models (Table 1.1) are depicted in Fig. 2.15. The shape of the experimental $y(\alpha)$ plot provides the first clue about the type of the reaction model. A convex decreasing dependence of $y(\alpha)$ on α is an indication of the contracting geometry models (coded R in Table 1.1). A concave decreasing plot is indicative of the diffusion models (code D). A dependence with a maximum is representative of either the Avrami–Erofeev (code A) or truncated SB models. The position of the maximum, α_m, depends on the model (Table 2.1) that can help with identifying a particular one.

Table 2.1 Values of α_m and α_p corresponding, respectively, to the maximum of the $y(\alpha)$ and $z(\alpha)$ functions for different kinetic models [37]

Kinetic model	α_m	α_p
R2	0	0.750
R3	0	0.704
F1	0	0.632
A2	0.393	0.632
A3	0.283	0.632
SB[a]	$m/(n+m)$	?[b]
D2	0	0.834
D3	0	0.704

[a] SB stands for the truncated Sestak–Berggren equation (Eq. 2.32)
[b] There is no general analytical solution for α_p

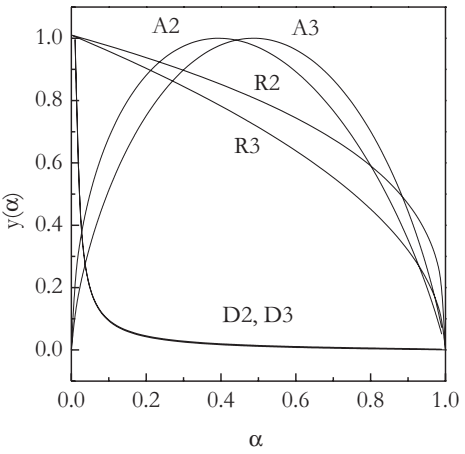

Fig. 2.15 Some $y(\alpha)$ plots built by normalizing the $f(\alpha)$ functions of the respective reaction models (Table 1.1)

The $z(\alpha)$ master plots are derived by combining the differential and integral forms of the reaction models. The temperature integral in Eq. 2.8 can be replaced with one of the multiple approximations [17], $\pi(x)$, as follows:

$$g(\alpha) = \frac{AE}{\beta R}\exp(-x)\left[\frac{\pi(x)}{x}\right], \tag{2.35}$$

where $x = E/RT$. Combining Eqs. 2.35 and 2.2 and performing some rearrangements allow one to arrive at the $z(\alpha)$ function as follows:

$$z(\alpha) = f(\alpha)g(\alpha) = \left(\frac{\mathrm{d}\alpha}{\mathrm{d}t}\right)_\alpha T_\alpha^2\left[\frac{\pi(x)}{\beta T_\alpha}\right]. \tag{2.36}$$

The last term in the brackets of Eq. 2.36 can be neglected [70] as it does not practically affect the shape of the $z(\alpha)$ plot. Therefore, the $z(\alpha)$ values can be calculated

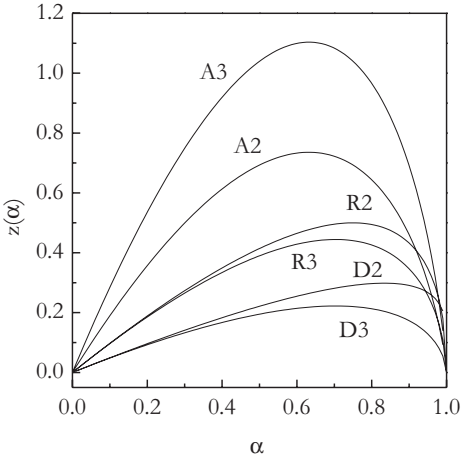

Fig. 2.16 Some $z(\alpha)$ plots build as the product of $g(\alpha)$ and $f(\alpha)$ in accord with Eq. 2.36

by multiplying the experimental values of $\left(\mathrm{d}\alpha/\mathrm{d}t\right)_\alpha$ by T_α^2. The resulting experimental $z(\alpha)$ values are plotted against α and matched with the theoretical $z(\alpha)$ master plots. The best match indicates an appropriate reaction model. As mentioned before, each heating rate produces one $\left(\mathrm{d}\alpha/\mathrm{d}t\right)_\alpha$ versus T_α dependence and thus one experimental $z(\alpha)$ plot. However, all these plots should be nearly identical.

The theoretical $z(\alpha)$ plots are obtained by plotting the product $f(\alpha)g(\alpha)$ against α for different reaction models. Figure 2.16 shows the theoretical $z(\alpha)$ master plots for some of the models from Table 1.1. It is seen that all $z(\alpha)$ plots pass through a maximum. Depending on the model, the $z(\alpha)$ plots reach their maxima at specific values of conversion, α_p, that are found from the condition [69]

$$g(\alpha)f'(\alpha) = -1. \tag{2.37}$$

The values of α_p have been estimated [71] for a number of reaction models (Table 2.1). Comparing the maximum of the experimental $z(\alpha)$ plot against the theoretical value (Table 2.1) provides the first clue about the type of the reaction model that might be applicable to the data.

Figures 2.17 and 2.18 provide an example of using the $y(\alpha)$ and $z(\alpha)$ plots to identify the reaction model for the thermal decomposition of nickel nitrate in air [72]. The use of the isoconversional methods demonstrates (Fig. 2.17) that the value of E_α does not practically vary with α. The experimental $y(\alpha)$ and $z(\alpha)$ plots are nearly identical and independent of the heating rate (Fig. 2.18). The presence of the maximum on the $y(\alpha)$ plots suggests that an appropriate model should be either one of the Avrami–Erofeev or the truncated SB models. The experimental values of α_m and α_p were determined [72] to be smaller than those expected for the Avrami–Erofeev model (Table 2.1). For this reason, further analysis was based on the truncated SB model, for which the parameters m and n were estimated via model fitting.

Analysis of the $y(\alpha)$ and $z(\alpha)$ plots results in identification of the reaction model. The preexponential factor is estimated by the following equation [69]:

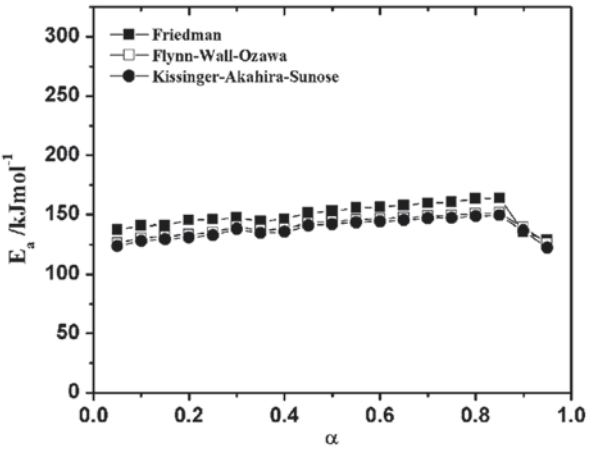

Fig. 2.17 Activation energy determined by three different isoconversional methods for the thermal decomposition of nickel nitrate in air. (Reproduced from Jancovic et al. [72] with permission of Elsevier)

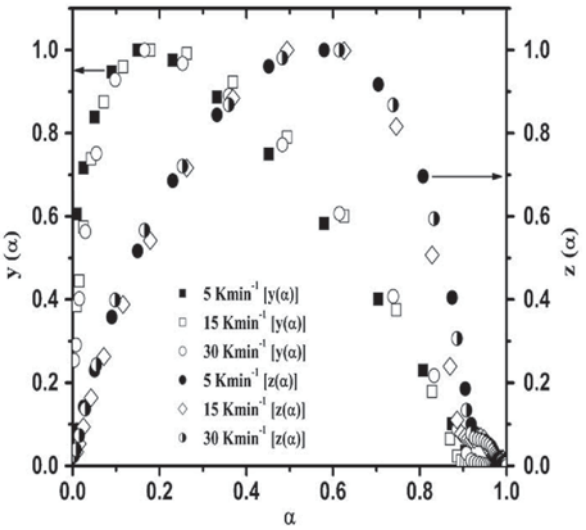

Fig. 2.18 The $y(\alpha)$ and $z(\alpha)$ plots for the thermal decomposition of nickel nitrate in air. (Reproduced from Jancovic et al. [72] with permission of Elsevier)

$$A = \frac{-\beta E_0}{RT_{\max}^2 \quad f'(\alpha_{\max})} \exp\left(\frac{E_0}{RT_{\max}}\right). \tag{2.38}$$

In Eq. 2.38, the subscript max denotes the values related to the maximum of the differential kinetic curve obtained at a given heating rate. That is, $T_{\max}$ represents the peak temperature and $\alpha_{\max}$ the extent of conversion at this temperature.

2.3 Kinetic Predictions

But it had been one thing to foresee it mentally, and it was another to behold it actually.

Henry James, The Portrait of a Lady

2.3.1 Why Predictions?

Kinetic predictions constitute the most important practical aspect of kinetic analysis. The essence of the latter is parameterization of the experimentally measured process rate as a function of such variables as the temperature, extent of conversion, and, sometimes, pressure. Parameterization means evaluating parameters of the equations (i.e., models) that represent a response of the process rate to a change in the aforementioned variables. Most commonly, one needs to parameterize the rate in terms of the temperature and conversion. This type of parameterization is accomplished by evaluating the kinetic triplet. Knowledge of a single kinetic triplet should be sufficient to predict the kinetics of a single-step process. Prediction of multistep kinetics would then require estimating multiple kinetic triplets, which is accomplished through model-fitting computations. However, isoconversional methods can be used to make adequate kinetic predictions for single- and multistep processes without estimating either preexponential factor or reaction model.

When it comes to kinetic predictions, one is typically interested in extrapolating some experimental kinetic measurements outside the actual temperature range, within which they were taken. The need in the extrapolations arises from practical difficulties of measuring the kinetics in the temperature range of interest. The actual measurements can be prohibitively difficult because the process is either too slow or too fast to measure by regular methods. Excessive costs as well as time limitations are among other practical factors that make one to choose predictions over actual measurements. A typical practical situation would be when one needs to select the most efficient stabilizer for a material that degrades slowly, e.g., on the scale of several years, at an ambient temperature. Measuring kinetics for several samples on such timescale would be unacceptably long and may require very expensive and sensitive equipment. A practicable alternative is to measure the kinetics at 40–50 °C above ambient temperature. This would accelerate the process and shorten its timescale from years to hours. Then, the higher-temperature kinetic data can be parameterized with respect to temperature and conversion, and the resulting parameters can be used to predict the kinetics at ambient temperature. The procedure is based naturally on the assumption that the kinetics would not change over the temperature range of extrapolation. In other words, it has to be assumed that the kinetic parameters estimated from higher temperature data should remain unchanged at ambient temperature. The same assumption allows one to make predictions from lower to higher temperature which is just as important. For instance, thermal stability of polymeric materials at

combustion temperatures can be predicted from experimental kinetic measurements conducted at significantly lower temperatures of thermal degradation.

Most commonly predicted parameter is the so-called lifetime. By its meaning, this is the time beyond which the material loses its properties to such degree that it cannot serve efficiently its intended purpose. For example, when exposed to heat, plastic polymeric material may lose plasticizer together with it its plasticity. The methods of thermal analysis such as TGA and DSC are among the most common experimental techniques employed for estimating the lifetime of materials exposed to heat. As long as decay in the property of interest can be linked to a change in the mass or heat, the lifetime of a material can be estimated by the thermal analysis methods. TGA, for instance, can be readily used to measure the kinetics of plasticizer loss while exposing polymeric material to heating. Suppose that the critical decay of plasticity is reached when the material has lost 20 wt.% of plasticizer. Then, in kinetic terms, the initial state, when no plasticizer is lost, corresponds to the extent of conversion, $\alpha=0$. On continuous heating, the material would gradually lose 100 wt.% of plasticizer, reaching the final state ($\alpha=1$). The critical state of the material would be reached at $\alpha=0.2$, i.e., at 20 wt.% loss of plasticizer. Then, the lifetime of the material can be estimated as the time to reach $\alpha=0.2$, i.e., $t_{0.2}$. Let us consider several methods of estimating (predicting) the time to reach a given extent of conversion, t_α.

2.3.2 Model Based Versus Model Free

For a single-step process taking place at constant temperature, T_0, the time to reach any given value of α is readily determined by rearranging Eq. 2.3:

$$t_\alpha = \frac{g(\alpha)}{A\exp\left(\frac{-E}{RT_0}\right)}. \tag{2.39}$$

Equation 2.39 affords prediction of the lifetime of material exposed to isothermal heating at the temperature T_0. To employ this equation, one needs to evaluate the whole kinetic triplet for the process responsible for the decay in the property of interest. For example, in the aforementioned case of the polymeric material losing its plasticity, this process is the mass loss of the plasticizer. The triplet can be evaluated from isothermal as well as nonisothermal experiments. However, one should be warned specifically against using single-heating-rate methods. These methods produce notoriously unreliable kinetic triplets that give rise to meaningless kinetic predictions [73].

Equation 2.39 provides a foundation for two American Society for Testing and Materials (ASTM) methods developed for evaluating the thermal stability from TGA (E1641 [74]) and DSC (E698 [75]) data. The predictive equation utilized by E1641 is:

$$t_\alpha = \frac{-\ln(1-\alpha)}{A\exp\left(\dfrac{-E}{RT_0}\right)}, \tag{2.40}$$

where the value of E is estimated by the Flynn and Wall method (Eq. 2.11). Comparison of Eqs. 2.40 and 2.39 suggests that $g(\alpha) = -\ln(1-\alpha)$, which means that Eq. 2.40 is based on the assumption that the process obeys first-order kinetics (Table 1.1). This assumption is also used to estimate the preexponential factor in Eq. 2.41:

$$A = \frac{-\bar{\beta} R}{E_r}\ln(1-\alpha)10^a, \tag{2.41}$$

where $\bar{\beta}$ is the mean of the experimental heating rates used to determine E by the Flynn and Wall method (Eq. 2.11). The E_r value is the corrected value of the activation energy. It is determined by dividing the experimental value of E by the correction factor that compensates for the inaccuracy of Dolyle's approximation of the temperature integral. The ASTM document [74] lists the values of both the correction factor and the parameter a in Eq. 2.41.

The predictive equation utilized by E698 is the same as the one used by E1641 (Eq. 2.40). The value of E is recommended to be estimated either by the method of Kissinger [76, 77] or by the methods of Ozawa and Flynn and Wall (Eq. 2.11). In the latter case, the ASTM document [75] recommends replacing T_α in Eq. 2.11 with the peak temperature, T_p. Just as E1641, the E698 method makes the assumption of the first-order kinetics in its predictive equation and in the equation for estimating the preexponential factor:

$$A = \frac{\beta E}{RT_p^2}\exp\left(\frac{E}{RT_p}\right). \tag{2.42}$$

The major shortcoming of both ASTM methods is that the lifetime is predicted by assuming the first-order kinetics as well as the constancy of the activation energy. If any of these assumptions does not hold, the prediction would be in error. Figure 2.19 demonstrates a considerable deviation of the ASTM prediction from the experimental data on the thermal degradation of poly(ethylene 2,6-naphthalate) (PEN), the process that demonstrates a significant variation of E_α with α [78]. More examples of similar problems with the ASTM predictions are found elsewhere [73, 79]. Therefore, before using the ASTM methods, one should be advised to check whether E_α does not vary significantly with α and whether the reaction model is that of first order.

The shortcomings of the ASTM methods are circumvented by employing the model-free predictions. The latter utilize the dependence of E_α on α evaluated by an

isoconversional method. Originally, the model-free predictive equation was derived [29, 80] in the following form:

$$t_\alpha = \frac{\int_0^{T_\alpha} \exp\left(\frac{-E_\alpha}{RT}\right) \mathrm{d}T}{\beta \exp\left(\frac{-E_\alpha}{RT_0}\right)}. \tag{2.43}$$

This equation is derived by equating the right-hand sides of Eqs. 2.3 and 2.8 and cancelling the A values. This action is justified by the aforementioned assumption that the kinetic triplet does not change over the temperature range of extrapolation. There is an important methodological difference between Eqs. 2.43 and 2.39. The latter does not directly use any experimentally measured kinetic curves to make the predictions. The kinetic curves are replaced with the kinetic triplet. On the other hand, Eq. 2.43 makes use of the kinetic curve α versus T measured at certain heating rate β. In other words, Eq. 2.43 is a way of converting actually measured nonisothermal kinetic data into isothermal data expected at a given temperature T_0. Since several heating rates are used to evaluate the E_α dependence, any of the respective α versus T curves can be used for making predictions by Eq. 2.43. In theory, there should be no significant difference between the lifetimes predicted when using the α versus T curves obtained at different β. This is because the numerator of Eq. 2.43 divided over β is $g(\alpha)$, whose value is constant at α=const for all heating rates involved. In practice, the lifetime predicted from different heating rates can demonstrate some variability that is reduced by replacing the respective t_α values with the mean or median value.

Since Eq. 2.43 performs integration from 0 to T_α, assuming that E_α remains constant from 0 to α, it cannot properly account for variability of the activation energy with the extent of conversion. As mentioned earlier, this can lead to significant systematic errors in the case of a strong variation of E_α with α. For this reason, the original Eq. 2.43 was later [81] modified to account for such variations. The latter are accounted properly when performing integration by small segments (see Eq. 2.21). Then, if the interval from 0 to α is split in k segments, Eq. 2.43 can be used to predict time for each individual segment:

$$t_{\alpha,i} = \frac{\int_{T_{\alpha,i-1}}^{T_{\alpha,i}} \exp\left(\frac{-E_{\alpha,i}}{RT}\right) \mathrm{d}T}{\beta \exp\left(\frac{-E_{\alpha,i}}{RT_0}\right)}. \tag{2.44}$$

Then, the total time to reach α will be the sum of the times for all k segments:

$$t_\alpha = \sum_{i=1}^{k} t_{\alpha,i} = \frac{1}{\beta} \sum_{i=1}^{k} \frac{I(E_{\alpha,i}, T_{\alpha,i})}{\exp\left(\frac{-E_{\alpha,i}}{RT_0}\right)}. \tag{2.45}$$

The resulting Eq. 2.45 allows one to use nonisothermal constant heating-rate experiments to predict the isothermal lifetimes while properly accounting for variation of E_α with α. Similarly, the isothermal lifetimes can be predicted from data obtained under arbitrary temperature programs, $T(t)$. The respective equation is as follows:

$$t_\alpha = \sum_{i=1}^{k} t_{\alpha,i} = \sum_{i=1}^{k} \frac{J[E_{\alpha,i}, T[(t_{\alpha,i})]]}{\exp\left(\frac{-E_{\alpha,i}}{RT_0}\right)}, \tag{2.46}$$

where $t_{\alpha,i}$ is calculated as [81]

$$t_{\alpha,i} = \frac{\int_{t^*_{\alpha,i-1}}^{t^*_{\alpha,i}} \exp\left[\frac{-E_{\alpha,i}}{RT(t)}\right] dt}{\exp\left(\frac{-E_{\alpha,i}}{RT_0}\right)}. \tag{2.47}$$

In Eq. 2.47, t_α^* is the experimentally estimated time to reach a given value of α under the temperature program, $T(t) = T^*(t)$. This is one of the several temperature programs employed for evaluating the E_α dependence.

The predictions made by Eqs. 2.43, 2.45, and 2.46 can be called "model-free predictions," because they get rid of the reaction model $g(\alpha)$ in the numerator of Eq. 2.39. The most important feature of the model-free predictions is that each value of t_α is predicted by using the corresponding value of E_α. In other words, the model-free predictive equations allow for using the actual E_α dependence. This expands the application area of these equations to both single-step (E_α does not depend on α) and multistep (E_α depends on α) processes. The model-free predictions provide two obvious advantages over the ASTM methods. First, they are not limited to the first-order kinetics or any other reaction model. Second, they do not require E_α to be invariable with α. For this reason, they generally give rise to more reliable kinetic predictions than the ASTM methods. This fact is exemplified in Fig. 2.19 and elsewhere [73, 79].

Although most commonly one makes predictions of the lifetime at a given constant temperature, T_0, by using a set of nonisothermal measurements, the kinetic predictions can be made from kinetic data measured at temperature programs $T^*(t)$ to any temperature program of interest, $T_0(t)$. Using the same assumption as in deriving Eq. 2.43, one can arrive at a model-free equation:

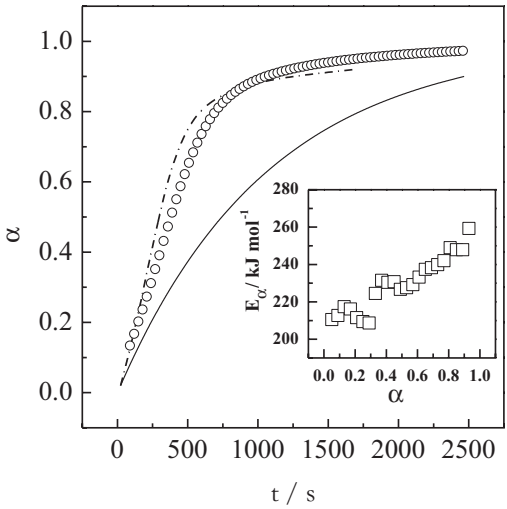

Fig. 2.19 ASTM E1641 (*solid line*) and model-free (*dash–dot line*) predictions of the thermal degradation of PEN in nitrogen at 420 °C compared to the actually measured data (*circles,* the initial portion is not shown to avoid overcrowding). Inset shows the E_α dependence evaluated by an isoconversional method from nonisothermal TGA data. (Reproduced from Prime et al. [78] with permission of Wiley.) *ASTM* American Society for Testing and Materials, *PEN* poly(ethylene 2,6-naphthalate)

$$J[E_\alpha, T_0(t_\alpha)] = J[E_\alpha, T^*(t_\alpha^*)]. \tag{2.48}$$

In Eq. 2.48, the right-hand side represents the integral (Eq. 2.21) over a particular experimental temperature program, $T^*(t)$. Then the lifetime t_α at any desired temperature program $T_0(t)$ is estimated as a numerical solution of Eq. 2.48.

2.3.3 Understanding Precision and Accuracy of Predictions

It is important to keep in mind that any kinetic prediction has its inherent limits in terms of precision and accuracy. Unavoidable noise in experimental measurements (i.e., T, α, $d\alpha/dt$) leads to random errors in estimating the kinetic triplet. These random errors further propagate into the error of the lifetime value. For example, the relative error in the lifetime predicted by Eq. 2.43 is estimated [82] approximately to be

$$\left|\frac{\Delta t_\alpha}{t_\alpha}\right| \approx \left|\Delta E_\alpha \left(\frac{1}{RT_0} - \frac{1}{RT_\alpha} - \frac{1}{E_\alpha}\right)\right|. \tag{2.49}$$

This equation suggests that as the temperature of prediction, T_0, moves further away from the experimental temperature, T_α, the relative error in the lifetime increases

and should at certain point exceed 1, i.e., 100 %. This means that the absolute error Δt_α would exceed the t_α value itself that deems the prediction meaningless. For example, if $E_\alpha = 200 \pm 10$ kJ mol^{-1} and $T_\alpha = 400$ K, the 100 % error is reached when predicting to $T_0 = 297$ K. Although the error in the lifetime depends on the parameters of Eq. 2.49, the obtained estimate gives a fair idea about how far the prediction temperature can be stretched beyond the actual experimental region. Typically, it is rather difficult to make reasonably precise predictions at temperatures that deviate from the experimental temperature region by more than several tens of degrees.

The limited accuracy of kinetic predictions is even bigger problem than the limited precision. This is because the accuracy cannot be evaluated without performing actual measurements under the conditions to which the prediction is made. Since kinetic predictions cannot be carried out without first making some kinetic assumption, the resulting predictions are always as accurate as the underlying assumption made to carry them out. As already mentioned, the underlying assumption of kinetic predictions is that the rate equations and respective kinetic triplets evaluated within an experimental range of temperatures would remain the same outside this range. Extensive experience suggests that most of the time such assumption is fairly accurate at least when the temperature range of the predictions does not extend more than several tens of degrees beyond the experimental range. However, this should not be taken as a rule because sometimes even very small temperature can cause a failure of the underlying assumption. An example of such situation is when the temperature regions of experiment and prediction are separated by a phase transition. As discussed in Sect. 1.3, the kinetic triplets may change significantly due to melting [83] or solid–solid phase transitions [84, 85]. In particular, one should be extremely cautious when trying to predict the thermal stability of a solid material from higher temperature data obtained above the melting temperature of the solid material.

Another implicit assumption that may affect the accuracy of kinetic predictions is that a process proceeds to completion, i.e., α changes from 0 to 1, regardless of the heating rate and/or temperature. This is not always the case. A well-known example is the reaction of epoxy curing. At higher temperatures and/or faster heating rates, the reaction proceeds to completion (i.e., $\alpha = 1$), yielding a fully cured epoxy material that is characterized by the limiting glass transition temperature. If curing is performed isothermally below the limiting glass transition temperature, the reaction system vitrifies effectively, stopping the process. The resulting material reaches some ultimate extent of cure that is smaller than 1 (i.e., $\alpha < 1$). The use of progressively lower curing temperatures results in progressively smaller ultimate extents of cure. Then, the use of complete cure data for predicting the curing below the limiting glass transition temperature would result in inaccurate predictions, with the ultimate extent of cure equal to 1 as shown in Fig. 2.20 [86]. Elimination of the inaccuracy requires introduction of a diffusion correction factor that accounts for vitrification [86].

Yet another source of inaccuracy in kinetic predictions is linked to the inaccuracy of determining $\alpha = 0$. This is easy to understand upon recognizing that Eq. 2.39 takes its origin from Eq. 2.6, in which the lower limit of integration is 0. This means that Eq. 2.39 assumes that the process starts when t and α are zero. However, for all practical purposes, the process starts when it becomes detectable experimentally.

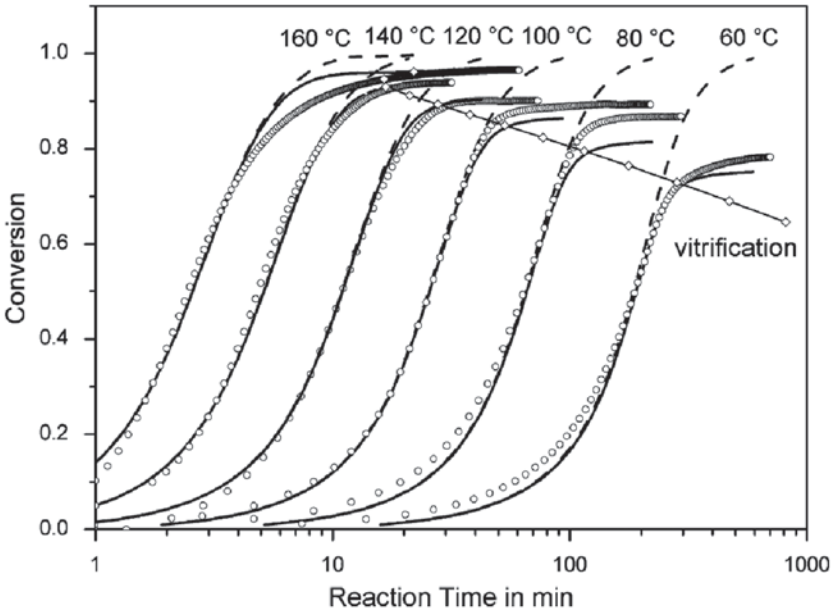

Fig. 2.20 Model-free predictions (*dash lines*) of epoxy-amine curing reaction at a series of temperatures from 60 to 160 C. *Dots* represent the actually measured data. *Solid lines* are predictions corrected for vitrification. (Reproduced from Schawe [86] with permission of Elsevier)

This happens when α reaches the detection limit, α_0. This obviously occurs at a non-zero value of the time, t_0. Therefore, accepting the α_0 and t_0 values as being negligibly different from zero introduces some systematic error into Eq. 2.39. As a result, the lifetimes predicted by Eq. 2.39 are underestimated by the actual value of t_0:

$$t_0 = \frac{g(\alpha_0)}{k(T)}. \tag{2.50}$$

Equation 2.50 indicates that the error depends on the type of $g(\alpha)$. As seen from Fig. 2.12, in the vicinity of $\alpha_0 \approx 0$, the value of $g(\alpha_0)$ is vanishingly small for some models (e.g., diffusion and contracting geometry type) but relatively large for others (e.g., Avrami–Eroffev and power law models). This means that the assumption that α_0 and t_0 being zero would introduce negligible errors for the first type of the models but may result in significant error for the second kind of the models. Recall that the models of the first type belong to the class of decelerating models (see Sect. 1.1, Fig. 1.5). They represent processes whose rate under isothermal conditions is the fastest at $\alpha = 0$. For this reason, the process tends to become detectable at negligibly small values of t_0.

The second type of models is from the class of either accelerating or sigmoid models. Under isothermal conditions, the respective processes have the slowest rate at $\alpha = 0$ (Fig. 1.5). More importantly, these models represent the processes that tend to have an induction period. In this case, the process may become detectable when

t_0 is much larger than zero. Therefore, when an isothermal experiment identifies a process as belonging to this type, one should be mindful of making predictions especially to lower temperatures. This is because, as per Eq. 2.50, the systematic error increases exponentially with decreasing temperature.

References

1. Kujirai T, Akahira T (1925) Effect of temperature on the deterioration of fibrous insulating materials. Sci Papers Inst Phys Chem Res Tokyo 2:223–252
2. Vyazovkin S (2000) Kinetic concepts of thermally stimulated reactions in solids: a view from a historical perspective. Int Rev Phys Chem 19:45–60
3. Dakin TW (1948) Electrical insulation deterioration treated as chemical rate phenomenon. AIEE Trans 67:113–122
4. Emanuel NM, Knorre DG (1973) Chemical kinetics (homogenous reactions). Wiley, New York
5. Barret P (1973) Heterogeneous kinetics. Gauthier-Villars, Paris (in French)
6. Rozovskii AYa (1974) Kinetics of topochemical reactions. Chemistry. Khimiya, Moscow (in Russian)
7. Tret'yakov YuD (1978) Solid-state reactions. Chemistry. Khimiya, Moscow (in Russian)
8. Garner WE (ed) (1955) Chemistry of the solid state. Butterworth, London
9. Young DA (1966) Decomposition of solids. Pergamon, Oxford
10. Schmalzried H (1995) Chemical kinetics of solids. Wiley, Weinheim
11. Brown ME, Dollimore D, Galwey AK (1980) Reactions in the solid state. Elsevier, Amsterdam
12. Wendlandt WWm (1986) Thermal analysis, 3rd edn. Wiley, New York
13. Friedman HL (1964) Kinetics of thermal degradation of char-forming plastics from thermogravimetry. Application to a phenolic plastic. J Polym Sci Part C 6:183–195
14. Ozawa T (1965) A new method of analyzing thermogravimetric data. Bull Chem Soc Japan 38:1881–1886
15. Flynn JH, Wall LA (1966) A quick, direct method for the determination of activation energy from thermogravimetric data. J Polym Sci B Polym Lett 4:323–328
16. Flynn JH, Wall LA (1966) General treatment of the thermogravimetry of polymers. J Res Nat Bur Standards Part A 70:487–523
17. Flynn JH (1997) The 'Temperature Integral'—its use and abuse. Thermochim Acta 300:83–92
18. Starink MJ (2007) Activation energy determination for linear heating experiments: deviations due to neglecting the low temperature end of the temperature integral. 42:483–489
19. Doyle CD (1962) Estimating isothermal life from thermogravimetric data. J Appl Polym Sci 6:639–642
20. Elder JP (1984) Multiple reaction scheme modeling. I. Independent and competitive first order reactions. J Therm Anal 29:1327–1342
21. Elder JP (1988) Multiple reaction scheme modeling. II. Parameter selection and re-examination of mutually independent first order reactions. J Therm Anal 34:1467–148
22. Elder JP (1989) Multiple reaction scheme modeling. III. Mutually independent nth order reactions. J Therm Anal 35:1965–1984
23. Elder JP (1990) Multiple reaction scheme modeling. IV. Mutually independent random nucleation reactions. J Therm Anal 36:1077–1112
24. Dowdy DR (1987) Meaningful activation energies for complex systems. I. The application of the Ozawa-Flynn-Wall method to multiple reactions. J Therm Anal 32:137–147
25. Dowdy DR (1987) Meaningful activation energies for complex systems. II. Evaluation of the Friedman method when applied to multiple reactions, and comparison with the Ozawa-Flynn-Wall method. J Therm Anal 32:1177–1187

26. Vyazovkin SV (1993) An approach to the solution of the inverse kinetic problems in the case of complex reactions. IV. Chemical reaction complicated by diffusion. Thermochim Acta 223:201–206
27. Vyazovkin SV (1994) Conversion dependence of activation energy for model DSC curves of consecutive reactions. Thermochim Acta 236:1–13
28. Vyazovkin S, Linert W (1995) Kinetic analysis of reversible thermal decomposition of solids. Int J Chem Kinet 27:73–84
29. Vyazovkin S (1996) A unified approach to kinetic processing of nonisothermal data. Int J Chem Kinet 28:95–101
30. Flynn JH (1983) The isoconversional method for determination of energy of activation at constant heating rates. J Therm Anal 27:95–102
31. Sbirrazzuoli N, Girault Y, Elégant L (1997) Simulations for evaluation of kinetic methods in differential scanning calorimetry. Part 3—peak maximum evolution methods and isoconversional methods. Thermochim Acta 293:25–37
32. Starink MJ (2003) The determination of activation energy from linear heating rate experiments: a comparison of the accuracy of isoconversion methods, Thermochim Acta 404:163–176
33. Akahira T, Sunose T (1971) Method of determining activation deterioration constant of electrical insulating materials. Res Report Chiba Inst Technol (Sci Technol) 16:22–31
34. Vyazovkin S, Dollimore D (1996) Linear and nonlinear procedures in isoconversional computations of the activation energy of thermally induced reactions in solids. J Chem Inf Comp Sci 36:42–45
35. Vyazovkin S (1997) Evaluation of the activation energy of thermally stimulated solid-state reactions under an arbitrary variation of the temperature. J Comput Chem 18:393–402
36. Vyazovkin S (2001) Modification of the integral isoconversional method to account for variation in the activation energy. J Comput Chem 22:178–183
37. Vyazovkin S, Burnham A K, Criado JM, Pérez-Maqueda LA, Popescu C, Sbirrazzuoli N (2011) ICTAC Kinetics committee recommendations for performing kinetic computations on thermal analysis data. Thermochim Acta 520:1–19
38. Budrugeac P (2002) Differential non-linear isoconversional procedure for evaluating the activation energy of non-isothermal reactions. J Therm Anal Calorim 68:131–139
39. Popescu C (1996) Integral method to analyze the kinetics of heterogeneous reactions under non-isothermal conditions. A variant on the Ozawa-Flynn-Wall method. Thermochim Acta 285:309–323
40. Simon P, Thomas PS, Okuliar J, Ray AS (2003) An incremental integral isoconversional method. Determination of activation parameters. J Therm Anal Calorim 72:867–874
41. Tang W, Chen D (2005) An integral method to determine variation in activation energy with extent of conversion. Thermochim Acta 433:72–76
42. Ortega A (2008) A simple and precise linear integral method for isoconversional data. Thermochim Acta 474:81–86
43. Cai J, Chen S (2009) New iterative linear integral isoconversional method for the determination of the activation energy varying with the conversion degree. J Comput Chem 30:1986–1991
44. Budrugeac P (2010) An iterative model-free method to determine the activation energy of non-isothermal heterogeneous processes. Thermochim Acta 511:8–16
45. Budrugeac P (2011) An iterative model-free method to determine the activation energy of heterogeneous processes under arbitrary temperature programs. Thermochim Acta 523:84–89
46. Han Y, Chen H, Li N (2011) New incremental isoconversional method for kinetic analysis of solid thermal decomposition. J Therm Anal Calorim 104:679–683
47. Han Y, Li T, Saito K (2013) A modified Ortega method to evaluate the activation energies of solid state reactions. J Therm Anal Calorim 112:683–687
48. Vyazovkin S, Sbirrazzuoli N (2002) Isoconversional analysis of nonisothermal crystallization of a polymer melkt. Macromol Rapid Commun 23:766–770

49. Vyazovkin S, Sbirrazzuoli N (2004) Isoconversional approach to evaluating the Hoffman-Lauritzen parameters (U^* and K_g) from the overall rates of nonisothermal crystallization. Macromol Rapid Commun 25:733–738
50. Chen K, Vyazovkin S (2009) Temperature dependence of sol-gel conversion kinetics in gelatin-water system. Macromol Biosci 9:383–392
51. Farasat R, Yancey B, Vyazovkin S (2013) High temperature solid-solid transition in ammonium chloride confined to nanopores. J Phys Chem C 117:13713–13721
52. Vyazovkin S (2002) Is the Kissinger equation applicable to the processes that occur on cooling? Macromol Rapid Commun 23:771–775
53. Brown ME, Maciejewski M, Vyazovkin S, Nomen R, Sempere J, Burnham A, Opfermann J, Strey R, Anderson HL, Kemmler A, Keuleers R, Janssens J, Desseyn HO, Li CR, Tang TB, Roduit B, Malek J, Mitsuhashi T (2000) Computational aspects of kinetic analysis. Part A: the ICTAC kinetics project-data, methods and results. Thermochim Acta 355:125–143
54. Maciejewski M (2000) Computational aspects of kinetic analysis. Part B: the ICTAC kinetics project—the decomposition kinetics of calcium carbonate revisited, or some tips on survival in the kinetic minefield. Thermochim Acta 355:145–154
55. Vyazovkin S (2000) Computational aspects of kinetic analysis. Part C: the ICTAC kinetics project—the light at the end of the tunnel? Thermochim Acta 355:155–163
56. Burnham AK (2000) Computational aspects of kinetic analysis. Part D: the ICTAC kinetics project—multi-thermal–history model-fitting methods and their relation to isoconversional methods. Thermochim Acta 355:165–170
57. Vyazovkin SV, Lesnikovich AI (1988) Estimation of the pre-exponential factor in the isoconversional calculation of the effective kinetic parameters. Thermochim Acta 128:297–300
58. Vyazovkin S, Linert W (1995) False isokinetic relationships found in the nonisothermal decomposition of solids. Chem Phys 193:109–118
59. Sbirrazzuoli N (2013) Determination of pre-exponential factors and of the mathematical functions $f(\alpha)$ or $G(\alpha)$ that describe the reaction mechanism in a model-free way. Thermochim Acta 564:59–69
60. Vyazovkin S, Linert W (1995) Thermally induced reactions of solids: isokinetic relationships of nonisothermal systems. Int Rev Phys Chem 14:355–369
61. Lesnikovich AI, Levchik SV (1983) A method of finding invariant values of kinetic parameters. J Therm Anal 27:89–93
62. Tang W, Liu Y, Zhang H, Wang C (2003) New approximate formula for Arrhenius temperature integral. Thermochim Acta 408:39–43
63. Vyazovkin SV (1992) Alternative description of process kinetics. Thermochim Acta 211:181–187
64. Zhou D, Schmitt EA, Zhang GGZ, Law D, Wight CA, Vyazovkin S, Grant DJW (2003) Model-free treatment of the dehydration kinetics of nedocromil sodium trihydrate. J Pharm Sci 92:1367–1376
65. Sestak J, Berggren G (1971) Study of the kinetics of the mechanism of solid-state reactions at increased temperature. Thermochim Acta 3:1–12
66. Akulov NS (1940) Basic of chemical dynamics. Mocow Sate University, Moscow. (in Russian)
67. Young DA (1966) Decompositions of solids. Pergamon, Oxford
68. Perez-Maqueda LA, Criado JM, Sanchez-Jimenez PE (2006) Combined kinetic analysis of solid-state reactions: a powerful tool for the simultaneous determination of kinetic parameters and the kinetic model without previous assumptions on the reaction mechanism. J Phys Chem A 110:12456–12462
69. Malek J (1992) The kinetic-analysis of nonisothermal data. Thermochim Acta 200:257–269
70. Malek J (1995) The applicability of Johnson-Mehl-Avrami model in the thermal analysis of the crystallization kinetics of glasses. Thermochim Acta 267:61–73
71. Criado JM, Malek J, Ortega A (1989) Applicability of the master plots in kinetic-analysis of non-isothermal data. Thermochim Acta 147:377–385

72. Jankovic B, Mentus S, Jelic D (2009) A kinetic study of non-isothermal decomposition process of anhydrous nickel nitrate under air atmosphere. Physica B 404:2263–2269
73. Vyazovkin S, Wight CA (1999) Model-free and model-fitting approaches to kinetic analysis of isothermal and nonisothermal data. Thermochim Acta 340–341:53–68
74. ASTM E1641-07 (2007) Standard test method for decomposition kinetics by thermogravimetry, Annual book of ASTM standards, vol 14.02, ASTM International, West Conshohocken
75. ASTM E698-05 (2005) Standard test method for Arrhenius kinetic constants for thermally unstable materials, Annual book of ASTM standards, vol 14.02, ASTM International, West Conshohocken
76. Kissinger HE (1956) Variation of peak temperature with heating rate in differential thermal analysis. J Res Natl Bur Stand 57:217–221
77. Kissinger HE (1957) Reaction kinetics in differential thermal analysis. Anal Chem 29:1702–1706
78. Prime RB, Bair HE, Vyazovkin S, Gallagher PK, Riga A (2009) Thermogravimetric analysis. In: Menczel JD, Prime RB (eds) Thermal analysis of polymers, fundamentals and applications. Wiley, New York, pp 241–317
79. Vyazovkin S, Sbirrazzuoli N (1996) Mechanism and kinetics of epoxy-amine cure studied by differential scanning calorimetry. Macromolecules 29:1867–1873
80. Vyazovkin SV, Lesnikovich AI (1988) Transformation of “degree of conversion against temperature” into “degree of conversion against time” kinetic data. Russ J Phys Chem 62:1535–1537
81. Vyazovkin S, Dranca I, Fan X, Advincula R (2004) Kinetics of thermal and thermo-oxidative degradation of polystyrene clay nanocomposite. Macromol Rapid Commun 25:498–503
82. Vyazovkin S, Linert W (1994) Reliability of conversion—time dependencies as predicted from thermal analysis data. Anal Chim Acta 295:101–107
83. Bawn CEH (1955) Decomposition of organic solids. In: Garner WE (ed) Chemistry of the solid state. Butterworth, London, pp 254–267
84. Hedvall JA (1934) Changes in crystal structure and their influence on the reactivity and catalytic effect of solids. Chem Rev 15:139–168
85. Gallagher PK, Sanders JP (2003) Ceramics, glass, and electronic materials. In: Brown ME, Gallagher PK (eds) The handbook of thermal analysis & calorimetry. Applications to inorganic and miscellaneous materials, vol 2. Elsevier, Amsterdam, pp 191–260
86. Schawe JEK (2002) A description of chemical and diffusion control in isothermal kinetics of cure kinetics. Thermochim Acta 388:299–312

Chapter 3
Physical Processes

3.1 Phases and Transitions Between Them

Every transition is a crisis…
Johann Wolfgang von Goethe, Wilhelm Meister's Apprenticeship

A phase is a macroscopic amount of substance which possesses uniform chemical composition and physical properties and is confined by a boundary surface. Single-component substance can exist in four major states of matter: gas, liquid, crystal, and glass [1]. The conversion from one state to another is called a phase transition. At constant pressure, a phase transition is caused by changes in temperature. An increase in temperature intensifies molecular motion that destabilizes molecular structure of a given phase so that at a certain temperature it rearranges to the structure of another more energetically favorable phase, i.e., a phase that has lower molar Gibbs energy, G (Fig. 3.1). Normally this would be a more loosely packed (more mobile) phase. The transition happens at the temperature when two phases have the same Gibbs energy, i.e., $\Delta G = 0$. It means that at this temperature the phases can coexist in equilibrium.

When heated, a typical crystal would melt first. This happens at the temperature of melting, T_m, past which a tightly packed crystalline lattice rearranges to a loosely packed liquid phase. Further heating to the temperature of boiling, T_b, causes liquid to vaporize. At this temperature, the vapor pressure of the liquid rises to the atmospheric pressure, and the liquid structure unpacks to practically unbound molecules of the gas phase. Crystalline compounds can transform directly into the gas phase without melting, provided that the liquid phase does not exist at a given pressure. This is the sublimation transition and it occurs at the temperature, T_s. At this temperature, the vapor pressure of the crystal becomes equal to the atmospheric pressure. There are a very few crystalline compounds that can coexist in equilibrium with its vapor phase at ambient pressure. The best-known example is carbon dioxide (dry ice) for which T_s at 1 atm is −78.5 °C [2].

It should be stressed that the transition temperatures T_m, T_b, and T_s denote equilibria between the bulk phases. In other words, on crossing the transition

S. Vyazovkin, *Isoconversional Kinetics of Thermally Stimulated Processes,*
DOI 10.1007/978-3-319-14175-6_3

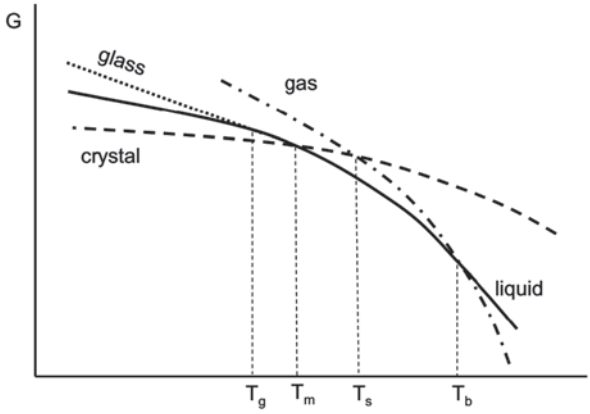

Fig. 3.1 Temperature dependence on the Gibbs free energy for solid, liquid, gas, and glass phases at constant pressure

temperature, the whole bulk of one phase would convert entirely to another phase. However, the processes of vaporization and sublimation occur to some extent well below their respective transition temperatures. This is an entirely surface phenomenon. Because the surface molecules are bound to fewer neighbors than the molecules in the bulk, they have higher mobility and through fluctuation can gain enough energy to leave the surface. As long as the condensed substance is enclosed in a container whose volume is not much larger than the volume of the substance, the process would continue until the vapor phase saturates, i.e., its pressure reaches an equilibrium value at a given temperature. Otherwise, it will continue until the condensed phase is gone. Similarly, the higher mobility of the surface layer in the crystal melts at a temperature lower than T_m, while the bulk of the crystal remains solid indefinitely.

From the equilibrium standpoint, the reverse transitions are supposed to happen at the same temperature as the forward ones, i.e., condensation of vapor to crystal at T_s, condensation of vapor to liquid at T_b, and crystallization of liquid at T_m. In reality, all these processes occur at markedly lower temperatures because of a significant energy barrier to nucleation, i.e., the energy of creating the surface of a nucleus of the new condensed phase [3, 4]. The barrier can only be overcome when ΔG (Fig. 3.1) is negative enough to outweigh the surface energy of the new phase, i.e., when the fluid phase is supercooled below the equilibrium transition temperature, at which ΔG is zero.

An important property of supercooled or metastable liquids [3] is their ability to form the glass phase. While thermodynamic drive toward crystallization increases with decreasing temperature, the molecular mobility becomes increasingly slower. At certain temperature, T_g (Fig. 3.1), the molecular mobility becomes so slow that the supercooled liquid cannot maintain the equilibrium liquid structure at a given rate of cooling. At this point, the supercooled liquid turns into a glass, and the respective temperature is taken as the glass transition temperature. The glass is a non-equilibrium phase and, thus, its Gibbs energy is larger than that of the supercooled liquid. Therefore, the glass is bound to relax continuously toward the supercooled liquid. Unlike the equilibrium phases, the glass cannot coexist in equilibrium with any other phases, and for that reason, the glass transition temperature can never be

defined with the same certainty as the transition temperatures between the equilibrium phases.

Another important difference between the glass transition and other transitions presented in Fig. 3.1 is that at T_g the G versus T curve for glass merges smoothly with the curve for liquid, whereas the G versus T curves for other transitions demonstrate a change in the slope at the transition temperature. Mathematically, a change in the slope is equivalent to discontinuity of the first derivative of G with respect to T, which, in turn, means discontinuity in the entropy, S, and enthalpy, H:

$$S = -\left(\frac{\partial G}{\partial T}\right)_P \tag{3.1}$$

$$H = \left[\frac{\partial (G/T)}{\partial (1/T)}\right]_P. \tag{3.2}$$

Per Ehrenfest's classification [5], the phase transitions that show discontinuity in the first derivative of the Gibbs energy are defined as transitions of first order. The glass transition does not show discontinuity in the first but in the second derivative of G with respect to T, which means discontinuity in the heat capacity:

$$C_P = -T\left(\frac{\partial^2 G}{\partial T^2}\right)_P = \left(\frac{\partial H}{\partial T}\right)_P. \tag{3.3}$$

Discontinuity in the second derivative classifies a phase transition as being of second order. Although the glass transition reveals this feature of a second-order transition, it is not the classical second-order transition that occurs between two phases coexisting in equilibrium with each other.

The aforementioned difference between the glass and first-order transitions has direct implication for experimental measurements of these processes by differential scanning calorimetry (DSC). The instrument measures the heat flow that has two principal contributions:

$$\Phi \equiv \frac{\mathrm{d}H}{\mathrm{d}t} = C_P\left(\frac{\mathrm{d}T}{\mathrm{d}t}\right) + \Delta H\left(\frac{\mathrm{d}\alpha}{\mathrm{d}t}\right). \tag{3.4}$$

The first term in the right-hand side represents a contribution from the sensible heat flow. This is the heat produced by substance of finite heat capacity in response to changing temperature. The second term is a contribution from the latent heat flow. This heat arises from a change in the enthalpy, ΔH, due to a phase transition or chemical reaction. Per Eq. 3.2, first-order transitions are accompanied by the latent heat. In DSC, they manifest themselves as peaks because as seen from Eq. 3.4, the heat is released in proportion to the processes rate ($\mathrm{d}\alpha/\mathrm{d}t$), which under the conditions of continuous heating (or cooling) always starts from and finishes at zero, passing some nonzero value in between. On the other hand, the glass transition is

not accompanied by the latent heat, i.e., $\Delta H = 0$ in Eq. 3.4. Then, the heat flow signal is produced by the first term in Eq. 3.4. According to Eq. 3.3, the glass transition is accompanied by a change in the heat capacity. At T_g, its value changes from C_P of the glass to C_P of the liquid, if the transition is measured on heating, or other way around when it is measured on cooling. As a result, the glass transition manifests itself as a step change between two nearly linear segments of the heat flow.

As follows from the above discussion, the solid state of matter can exist either as the crystal or as the glass phase. The issue, however, can be further complicated by the existence of more than one crystal phase for the same solid compound. This phenomenon known as polymorphism [1] is widely encountered in inorganic [6, 7] and organic [8] compounds as well as in elements, for which it is referred to as allotropy. The polymorphic solid–solid transitions can be of first and second order. They are typically easy to measure by DSC.

Different liquid phases can be encountered in a single-component liquid. The examples of the liquid–liquid transitions in isotropic liquids are quite rare [9–12]. Much more common are the transitions in liquid crystals, whose liquid state can exist in disordered (isotropic) as well as in ordered (smectic, nematic, cholesteric) phases [4]. The liquid crystalline phases are also called mesophases to emphasize their intermediate character between the solid and liquid phases. For liquids involving more than one component (i.e., mixtures or solutions), a common liquid–liquid phase transition is mixing and demixing (phase separation). The transition can be caused by heating or cooling of a solution and results in its separation in the solvent-rich and solute-rich phases. A very special case of a phase transition in a solution is gelation [4, 13]. It results in conversion of a liquid solution into a gel, which is a network of cross-linked solute molecules that entrap a solvent. A gel is a soft solid or a liquid that has lost its ability to flow. Most of the aforementioned transitions in liquids are of first order and normally appear in DSC as well-defined peaks, although some transitions [14] in liquid crystals can be of second order.

The following sections of this chapter provide a discussion about the kinetics of most of the aforementioned transitions.

3.2 Vaporization and Sublimation

All existing things soon change, and they will either be reduced to vapor, if indeed all substance is one, or they will be dispersed
Marcus Aurelius, Meditations

3.2.1 Background

Vaporization and sublimation are phase transitions in which the respective liquid and solid compounds transform to the gas phase. Both processes are promoted by heating that intensifies molecular motion and thus initiates breakage of the intermolecular (cohesive) bonds that hold a compound in the condensed state. Depending

on the strength of the inter- and intramolecular bonds, vaporization and/or sublimation may or may not be accompanied by decomposition. For example, a typical covalent compound such as a hydrocarbon is held in the condensed phase by weak van der Waals forces. It would undergo vaporization or sublimation at temperatures that are too low to break the strong covalent bonds and cause decomposition of the compound. However, decomposition may readily occur in ionic compounds that are held in the condensed phase by strong ionic forces. Decomposition can complicate significantly the kinetics of vaporization or sublimation that by itself is relatively simple.

In 1913, Langmuir [15, 16] proposed an equation that describes the rate of vaporization in vacuum:

$$-\frac{\mathrm{d}m}{\mathrm{d}t} = \gamma\ P\sqrt{\frac{M}{2\pi RT}}, \tag{3.5}$$

where $\mathrm{d}m/\mathrm{d}t$ is the rate of mass loss per unit of the surface area, M is molecular mass of the gaseous compound, P is the vapor pressure of the compound, R is the gas constant, T is the temperature, and γ is the accommodation coefficient. The latter was taken to be close to unity for reasonable molecular masses, e.g., it is 0.98 for carbon dioxide [16]. The equation was derived from the Knudsen equation [17] for the effusion rate through an orifice that lies in the foundation of the Knudsen method for determining molar mass or/and the vapor pressure from the mass loss rate data [18].

We can isolate the temperature-dependent parameters in Eq. 3.5 and write it in a more convenient form using the extent of conversion:

$$\frac{\mathrm{d}\alpha}{\mathrm{d}t} = \mathrm{Const}PT^{-0.5}, \tag{3.6}$$

where Const collects all temperature-independent parameters. The vapor pressure in Eq. 3.6 depends on temperature in accord with the Clausius–Clapeyron equation:[18]

$$\ln P = C - \frac{\Delta H}{RT}, \tag{3.7}$$

where C is a constant and ΔH is the enthalpy of vaporization or sublimation. Then with regard to Eq. 3.7, Eq. 3.6 can be used to derive the activation energy of the process as follows:

$$E = -R\left[\frac{\mathrm{d}\ln(\mathrm{d}\alpha/\mathrm{d}t)}{\mathrm{d}T^{-1}}\right] = \Delta H - \frac{1}{2}RT. \tag{3.8}$$

The second term in Eq. 3.8 does not exceed a few kilojoules in any reasonable temperature range and thus can be neglected. Therefore, Eq. 3.8 suggests that if one

fits the temperature dependence of the rate of vaporization or sublimation to the Arrhenius equation, the resulting activation energy should provide a fair estimate for the enthalpy of the process.

As fairly noticed by Price and Hawkins [19], the accommodation coefficient in Eq. 3.5 should not be assumed to be unity when the mass loss measurement is conducted in a flow of a purge gas at ambient pressure as typically is the case of regular thermogravimetric analysis (TGA) runs. The actual measurements on methylparaben by Chatterjee et al. [20] have produced an estimate of $\gamma = 5.8 \times 10^{-5}$ that is too low to be meaningful. Some rational insights into the problem have been provided by Pieterse and Focke [21], who suggested that in order to be applicable to the conditions other than vacuum, the Langmuir equation needs to account for diffusion of the vapor in surrounding gas. The equation derived by Pieterse and Focke is as follows:

$$-\frac{\mathrm{d}m}{\mathrm{d}t} = PD\frac{M}{zRT}, \tag{3.9}$$

where D is the diffusion coefficient of the vapor compound in the surrounding gas, and z is the height of the pan occupied by the gas. Comparing Eq. 3.9 with Eq. 3.5 suggests that the value of the coefficient γ is:

$$\gamma = \frac{D}{z}\sqrt{\frac{2\pi M}{RT}}. \tag{3.10}$$

Equation 3.10 affords explaining the excessively small values of γ. The order of magnitude of γ is determined primarily by the value of D whose typical order of magnitude is about $10^{-4} - 10^{-5}$ m^2s^{-1}. Substitution of the actual values *D, z, T,* and M for vaporization of methylparaben yields $\gamma = 4.8 \times 10^{-5}$ which is quite close to the value experimentally found by Chatterjee et al. [20].

Following the same logic as above, we can use Eq. 3.9 to derive the activation energy of vaporization or sublimation. The resulting expression is as follows:

$$E = -R\left[\frac{\mathrm{d}\ln(\mathrm{d}\alpha/\mathrm{d}t)}{\mathrm{d}T^{-1}}\right] = \Delta H + E_\mathrm{D} - RT, \tag{3.11}$$

where E_D is the activation energy of diffusion. For diffusion of gases in gases, the typical values of E_D are quite small. Figure 3.2 demonstrates the Arrhenius plots for the temperature dependence of the diffusion coefficient of several gases in helium [22]. It is seen that the plots have nearly the same slopes. The E_D values estimated from these slopes fall in the range 5–6 kJ mol^{-1}. Considering that the RT term in Eq. 3.11 has similar magnitude but its sign is opposite to E_D, we can expect these two terms to cancel each other at least partially. Therefore, we can conclude again that the activation energy of vaporization or sublimation should generally provide a reasonable estimate of the process enthalpy.

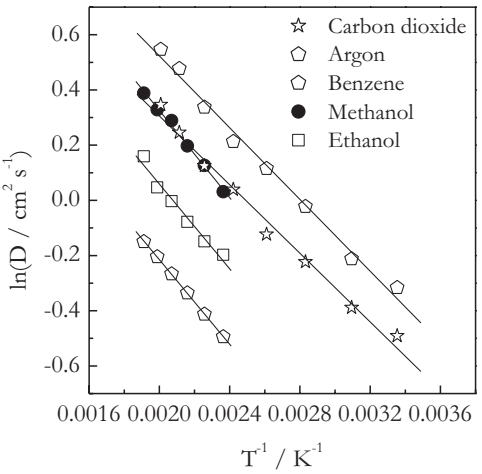

Fig. 3.2 Arrhenius plots for the temperature dependence of the diffusion coefficient of various gases in helium. (Data taken from Seager et al. [22])

3.2.2 Isoconversional Treatment

When it comes to applying an isoconversional method to treat the kinetics of vaporization or sublimation, one should notice that neither Eq. 3.5 nor Eq. 3.9 includes the value of the mass lost (m) in their respective right-hand sides. It means that if one replaces the mass with the conversion, these equations would not include in their right-hand sides any reaction model either. Although it may sound confusing, in fact these equations do include one very specific reaction model, $f(\alpha)=1$. This is called the zero-order reaction model. This model represents a process whose rate remains constant throughout the whole range of conversions from 0 to 1. However, the rate of vaporization or sublimation is proportional to the free surface area (i.e., the surface area that is in contact with surrounding gas or vacuum) of the condensed substance. Then the rate of these processes would be independent of conversion only in a specific case when the free surface area does not change with the process progress. This is a reasonable assumption when, for example, vaporization rate is measured for a liquid that fills one of cylindrical pans (Fig. 3.3a) usually used in thermal analysis studies. In this case, the free surface area of the liquid would be determined by the circular cross-sectional area of the pan until the interface reaches the pan bottom and the liquid breaks into several droplets. Nevertheless, when the condensed substance is present in the form of individual droplets or crystals (Fig. 3.3b), the free surface area as well as the process rate would be decreasing with increasing the conversion. In this situation, the rate equation for vaporization or sublimation would have to include explicitly some $f(\alpha)$ of the decelerating type such as the model of contracting sphere or cylinder.

Note that the introduction of some explicit $f(\alpha)$ in the right-hand side of Eqs. 3.5 or 3.9 would not affect the values of the isoconversional activation energy estimated as:

$$E_\alpha = -R\left[\frac{\partial \ln(\mathrm{d}\alpha/\mathrm{d}t)}{\partial T^{-1}}\right]_\alpha . \tag{3.12}$$

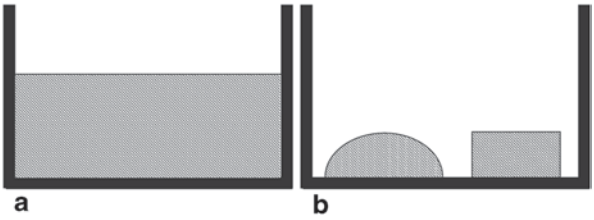

Fig. 3.3 Schematic representation of vaporization or sublimation of different form samples placed in cylindrical pan. **a** Sample in the form of continuous volume of a liquid or solid substance. **b** Sample in the form of individual droplets (*left*) or crystals (*right*)

This is because the logarithmic derivative of $f(\alpha)$ is zero at a constant value of α (Eq. 1.12). Therefore, Eqs. 3.8 and 3.11 would remain true under the isoconversional conditions. That is, for the process of vaporization or sublimation, one should generally expect the isoconversional values of E_α to be practically independent α and close to the value of the process enthalpy. Some systematic dependencies as well as deviations may occur naturally because the enthalpy depends on temperature in accord with the Kirchhoff's law:[18]

$$\Delta H^0(T_2) = \Delta H^0(T_1) + \int_{T_1}^{T_2} \Delta C_P \mathrm{d}T, \tag{3.13}$$

where ΔH^0 is the standard enthalpy change at the temperatures T_1 and T_2, and ΔC_P is the heat capacity change due to a transition from the condensed to gaseous state.

However, the issue of using proper reaction models arises when isoconversional analysis is applied to determine the preexponential factor and reaction model. An instructive example of isoconversional analysis of vaporization of 2,2′-bipyridyl is given by Vecchio et al. [23] (Figs. 3.4 and 3.5). As seen in Fig. 3.4, the E_α values do not practically depend on α. The respective average activation energy is 61±2 kJ mol^{-1}. The value agrees very well with the independently measured enthalpy of vaporization, 59±2 kJ mol^{-1} [23]. The reaction model of vaporization

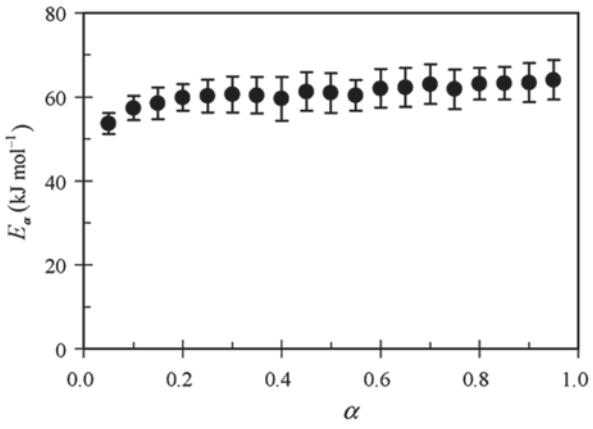

Fig. 3.4 E_α dependence for vaporization of 2,2′-bipyridyl. (Reproduced from Vecchio et al. [23] with permission of Elsevier)

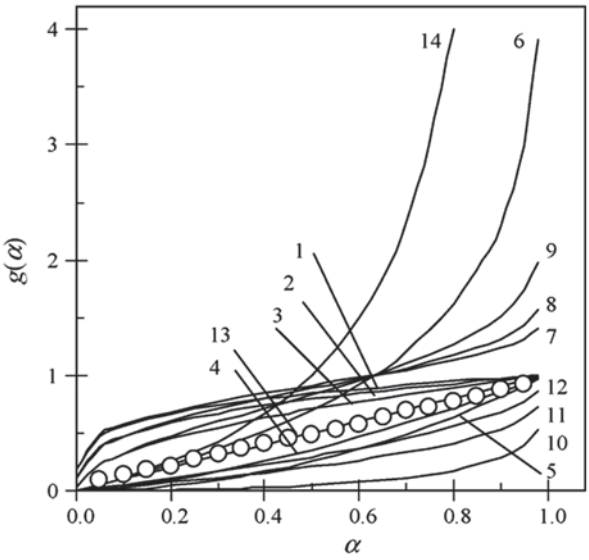

Fig. 3.5 Determination of the reaction model for vaporization of 2,2′-bipyridyl. (Reproduced from Vecchio et al. [23] with permission of Elsevier)

has been determined by using the technique described in Sect. 2.2.2. According to Fig. 3.5, the best-fitting model of this process is N13, which is $g(\alpha)=\alpha$ (i.e., $f(\alpha)=1$) or zero order [23]. This is obviously consistent with the basic assumption of Eqs. 3.5 and 3.9. However, as already mentioned, this is not always the case. For example, both vaporization and, especially, sublimation of ammonium nitrate demonstrate clear deviation from the zero order to decelerating type of kinetics [24].

The rate of diffusion of the condensed substance vapor in the surrounding gas is a very important factor when measurements are conducted under the conditions of regular thermal analysis experiments. The surrounding gas is a purge gas, such as nitrogen, that is delivered to the sample at an ambient pressure and a certain flow rate. If the forming vapor diffuses too slowly, the surrounding gas may become saturated with it. The local vapor pressure may start approaching its equilibrium values that would promote the reverse reaction of condensation. That is why the rate of vaporization or sublimation should be measured at sufficiently fast flow rates that would secure efficient removal of the forming vapor and suppress its condensation.

The effect of the purge gas flow rate on vaporization of methyl salicylate has been demonstrated by Cheng et al. [25]. It has been found that a systematic increase in the flow rate of nitrogen resulted in a small but systematic shift of TGA mass loss curves to lower temperature. This effect is typical to find in reversible processes [26]. The isoconversional activation energies of vaporization also have demonstrated a systematic shift as illustrated in Fig. 3.6. It is seen as an increase in the flow rate causes a systematic decrease in the activation energy of vaporization, bringing its value closer to the reference value of the vaporization enthalpy (52 kJ mol^{-1}).

The rate equations 3.5 and 3.9 rely on the mass loss that makes TGA a method of choice for measuring the kinetics of vaporization and sublimation. However, DSC

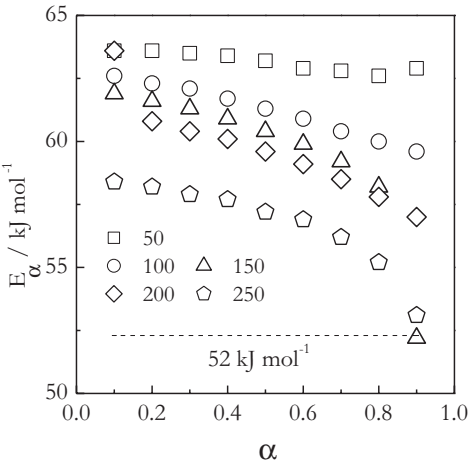

Fig. 3.6 Effect of the nitrogen gas flow rate on the activation energy of vaporization of methyl salicylate. Numbers by symbols represent the flow rate in mL min^{-1}. (Data taken from Cheng et al. [25])

can be used in such studies as well. Figure 3.7 shows a dependence of the effective activation energy estimated from DSC data on vaporization of water [27]. The isoconversional values of E_α are practically independent of α in a rather wide range. The average E_α value in the range $\alpha = 0.4–0.6$ is 43.80 ± 0.03 kJ mol^{-1}. The value is somewhat larger than the reference value [2] of the enthalpy of vaporization of water, 40.7 kJ mol^{-1}. It should be noted that this reference value corresponds to the enthalpy of vaporization at 100 °C, i.e., the boiling temperature, which is a common way of reporting the enthalpies of vaporization. However, under the conditions of DSC runs (open pan, flow of nitrogen), water is completely vaporized by 60 °C.

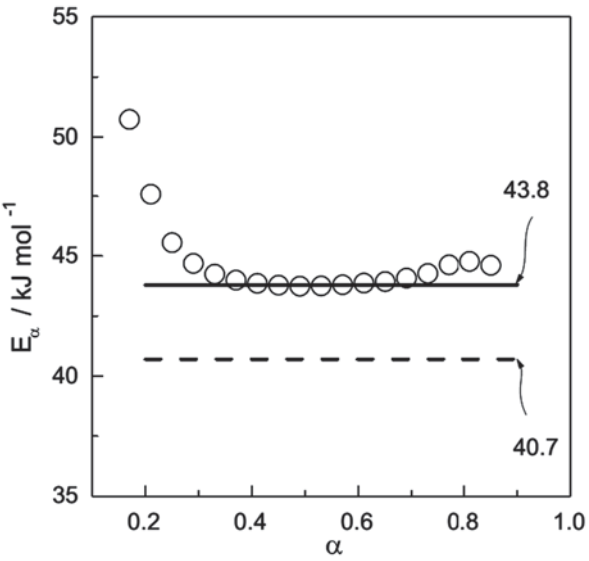

Fig. 3.7 Isoconversional values of the activation energy for vaporization of water. *Solid line* represents the average of the E_α values in the range of $\alpha = 0.4–0.6$. *Dash line* denotes the enthalpy of water vaporization at 100 °C. (Reproduced from Prado and Vyazovkin [27] with permission of Elsevier)

About 50 % of water becomes vaporized around 40 °C. The vaporization enthalpy of water at this temperature can be estimated from Kirchhoff's law (Eq. 3.13) by using the values of the heat capacity for liquid and gaseous water, which are [2] 75.29 and 33.58 J $mol^{-1}K^{-1}$, respectively. Neglecting the temperature dependence of the heat capacity, the vaporization enthalpy at 40 °C is estimated to be:

$$\Delta H^0(40^\circ\mathrm{C}) = \Delta H^0(100^\circ\mathrm{C}) + \Delta C_P(T_2 - T_1)$$

which is 43.2 kJ mol^{-1}. This value is almost identical to the average E_α value (Fig. 3.7).

Overall, the examples considered suggest that the activation energy estimated from the rates of vaporization of liquids is similar to the enthalpy of vaporization. There are many more examples in the literature that confirm this correlation. However, in the case of sublimation of solids, the correlation is not nearly as consistent. The direct application of the Langmuir equation to the mass loss data provides about equal number of examples when the correlation is good as when it is poor [28]. It is not very surprising considering that the mechanism of sublimation [29] is more complex than that of vaporization. If vaporization of a liquid involves essentially one step, in which a molecule breaks the surface tension, sublimation of a solid involves multiple steps. First, a molecule breaks away from a site where it is bound to a fewer neighbors such as a kink or ledge site. Then, it diffuses along the surface and finally desorbs from it. Schematically, it can be seen as a mechanism of three consecutive steps:

$$A_{\text{solid}} \xrightarrow{\text{breaking away}} A_{\text{surface}} \xrightarrow{\text{diffusion}} A_{\text{adsorbed}} \xrightarrow{\text{desorption}} A_{\text{vapor}}.$$

Any of these three steps can be rate limiting during sublimation. As a result, the activation energy estimated from the sublimation rate data can be the one for any of these steps. To complicate matters further, the surface molecule may undergo a chemical reaction of dissociation or association, which also can become a rate-limiting step of sublimation. However, the enthalpy of sublimation is invariably determined by the difference in the enthalpies for A_{vapor} and A_{solid}.

3.3 Glass Transition

> *Only there's no equilibrium in the world. It's just an error of some kilogram and a half over the universe as a whole, but it's really a surprising thing*
>
> Daniil Kharms, On Equilibrium

3.3.1 Background

Typically, the glass phase is formed in supercooled liquids that are cooled so fast that they do not have sufficient time to crystallize. Ultimately, any liquid can be

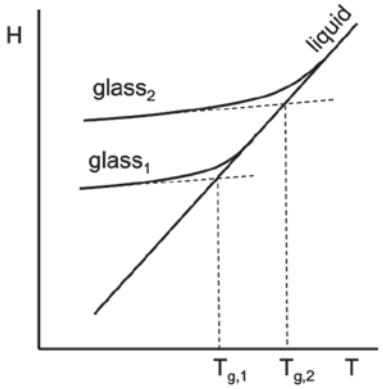

Fig. 3.8 Enthalpy versus temperature diagram for the formation of two glass phases: $glass_1$ and $glass_2$. The $glass_2$ phase is formed at faster cooling rates than $glass_1$ and thus has a larger glass transition temperature that is determined as intersection of the glass and liquid tangent lines

converted to glass subject to sufficiently fast rate of cooling. For slow crystallizing liquids such as the melts of some polymers, the glass can be formed on cooling at tens of degrees per minute. Fast crystallizing liquids such as water may have to be cooled at millions degrees per second to form the glass phase. Anyway, the key reason of the glass formation is the limited rate of the molecular mobility that slows down progressively as liquid is cooled. At certain point, the mobility becomes insufficient to maintain the equilibrium liquid structure so that a supercooled liquid becomes a glass. The respective temperature is called the glass transition temperature, T_g. Since the glass is a nonequilibrium phase, its T_g designates the transition between the supercooled liquid and a specific glassy structure that depends particularly on the cooling rate and generally on the overall thermal history. Figure 3.8 demonstrates a change in the temperature dependencies of the enthalpy for liquid and two glasses formed at different cooling rate. Obviously, the faster liquid is cooled, the sooner it falls out of equilibrium and forms the glass phase. Therefore, faster cooling produces the glass of a more nonequilibrium structure that has larger glass transition temperature.

On reheating, the glass does not follow the same enthalpic trace as on cooling (Fig. 3.9). The respective enthalpy values are lower because the glass is relaxing continuously toward the supercooled liquid state. Another important feature of the glass transition observed on heating is the "enthalpy overshoot." Upon reaching the equilibrium liquid line, the glass does not immediately convert to the liquid but continues to follow the glass line for some time. The reason is that at this point the molecular mobility of the glass is too slow to assume immediately the liquid structure. Therefore, it continues to maintain the glassy structure until the point when temperature accelerates the molecular mobility to such extent that the glass can quickly restore the liquid structure. For the glass formed at a certain cooling rate, the use of faster heating rates results in increasing the magnitude of the enthalpy overshoot. The heating and cooling traces are brought closer to each other when the heating and cooling rates are equal.

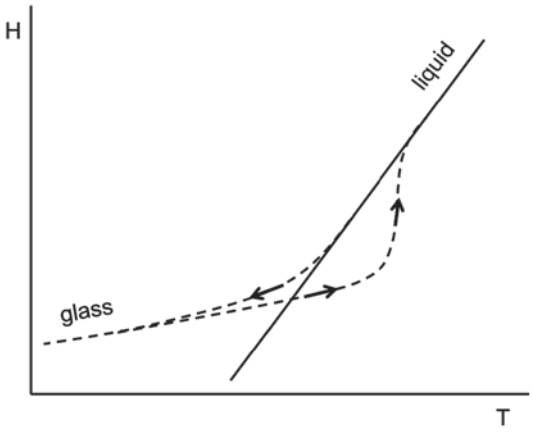

Fig. 3.9 When glass is reheated, its enthalpy crosses (overshoots) the liquid line and returns to it at higher temperature

The enthalpy plot (Fig. 3.9) is helpful in understanding the DSC (heat flow) traces measured on heating and cooling. According to Eq. 3.4, the heat flow related to the glass transition originates from a change in the heat capacity between the values for the liquid and glass phase. By virtue of Eq. 3.3, the heat capacity would change as the first derivative of the plots presented in Fig. 3.9. On cooling, DSC shows some small stepwise change in the heat flow. On the other hand, on heating, the DSC signal is complicated by a peculiar feature associated with enthalpy overshoot, which manifests itself as a relatively small endothermic peak at the end of the glass transition step. Figure 3.10 displays an example of this feature observed in the glass transition of polystyrene (PS) and PS–clay nanocomposite [30].

The nonequilibrium structure of the glass phase reveals itself in the relaxation kinetics. When the glass freezes dynamically, it conserves a heterogeneous structure

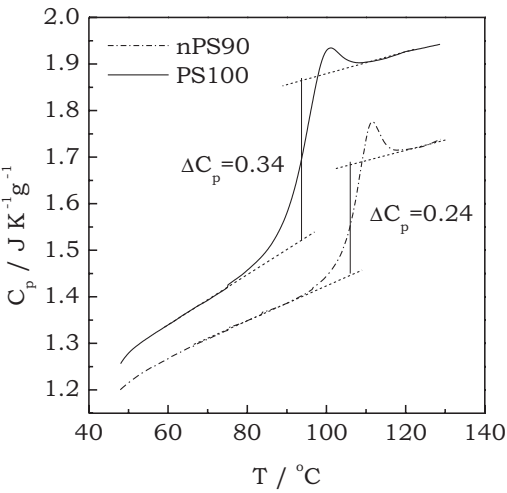

Fig. 3.10 Heat capacity change during the glass transition in polystyrene (PS100) and polystyrene–clay nanocomposite (nPS90) on heating at 10 °C min^{-1}. (Reproduced from Vyazovkin and Dranca [30] with permission of ACS)

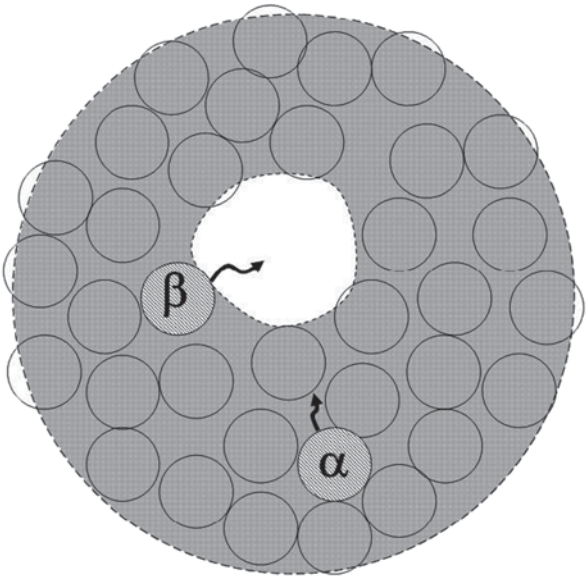

Fig. 3.11 Schematic representation of molecular mobility in the glass phase. The letters α and β represent molecules respectively involved in cooperative and noncooperative motion. The *open area* is a mobility island

that contains significant density fluctuations (Fig. 3.11). The lower density areas form the mobility islands [31] inside the glass. As a result, the molecules of the glass phase find themselves in a variety of the spatial situations of different crowdedness. Those, stuck in highly congested situations, can only move cooperatively, i.e., together with moving the closest neighbors. The respective motion is termed the α-process (relaxation). This is a slow process characterized by high activation energy whose value is typically on the order of hundreds of kilojoules per mole. On the other hand, the molecules located in the vicinity of the mobility islands can move rather freely, i.e., in a noncooperative manner. The respective motion is referred to as the β-process (relaxation) or Johari–Goldstein process. This process is fast and its activation energy amounts to several tens of kilojoules per mole.

When glass relaxes toward the equilibrium supercooled liquid structure, the overall process would occur generally via both cooperative and noncooperative motion. However, one particular mechanism may dominate depending on temperature or the stage of relaxation. Since cooperative and noncooperative processes can occur in parallel with each other, at any given temperature, the kinetics of relaxation is dominated by the fastest process, i.e., a process having the smallest relaxation time, τ. Cooperative and noncooperative processes have distinctly different temperature dependencies of the relaxation time. Noncooperative processes, such as β-relaxation, obey the Arrhenius equation:

$$\tau = C \exp\left(\frac{E}{RT}\right), \tag{3.14}$$

where C is the temperature-independent preexponential factor, E is the activation energy, and R is the gas constant. It follows from Eq. 3.14 that

$$E = R\left(\frac{\mathrm{d}\ln\tau}{\mathrm{d}T^{-1}}\right). \tag{3.15}$$

This means that for a noncooperative process, the plot of $\ln\tau$ versus T^{-1} should be a straight line whose slope is E/R.

The temperature dependence of a cooperative process, such α-relaxation, follows the Vogel–Tammann–Fulcher (VTF) equation:

$$\tau = B\exp\left(\frac{A}{T - T_0}\right), \tag{3.16}$$

where B is the temperature-independent preexponential factor, A is a constant, and T_0 is a reference temperature, typically well below T_g. By using the same principle as in Eq. 3.15, we can derive the activation energy from Eq. 3.16:

$$E = R\left[\frac{AT^2}{\left(T - T_0\right)^2}\right]. \tag{3.17}$$

Equation 3.17 suggests that the activation energy and, thus, the slope of the plot of $\ln\tau$ versus T^{-1} increase with decreasing temperature. A similar result is obtained [32] from the Williams–Landel–Ferry (WLF) equation:

$$E = 2.303R\left[\frac{C_1C_2T^2}{(C_2 + T - T_g)^2}\right], \tag{3.18}$$

where $C_1 = 17.44$ and $C_2 = 51.6$ are universal constants. Both VTF and WLF equations are applied commonly to describe the temperature dependence of viscosity of supercooled liquids. Although the equations can be used interchangeably, the WLF equation is most frequently applied to polymers, whereas the VTF equation to low molecular weight species.

The non-Arrhenius type of the temperature dependence (i.e., the VTF or WLF dependence) breaks down in the vicinity of T_g, below which the dependence takes the Arrhenius form (Fig. 3.12a). This is empirically found in a variety of liquids [3]. An explanation of this phenomenon is provided by the theoretical results of Di Marzio and Yang [33]. The change in the type of the temperature dependence around T_g has important implications for estimating experimental activation energies (Fig. 3.12b). That is, above T_g, the transition from the glass to liquid phase should demonstrate large values of the activation energy that decrease with temperature. However, when glass relaxes to supercooled liquid below T_g, one should

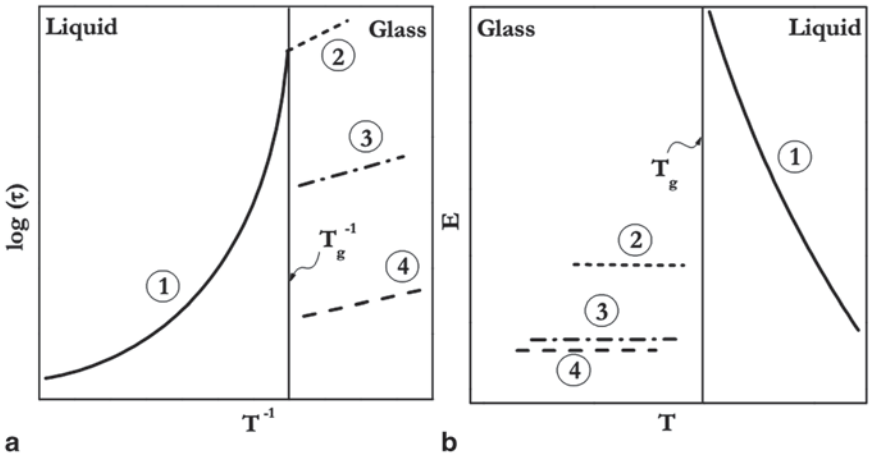

Fig. 3.12 Schematic representation of the temperature dependencies of the relaxation time (**a**) and the respective activation energies (**b**). **a** Curve 1 represents a typical VTF dependence of the α-relaxation. Straight lines 2–4 represent various processes occurring in the glassy state: 2 nonequilibrium mode of the α-relaxation; 3 α' process; 4 β-process. **b** Sub-T_g processes 2–4 have significantly lower activation energy than the α-process (1). VTF Vogel–Tammann–Fulcher. (Reproduced from Vyazovkin and Dranca [35] with permission of Elsevier)

expect the activation energy values to be markedly smaller and decreasing with decreasing temperature down to the values characteristic of the β-process.

It should be noted that beyond the β-relaxation, there are some processes that occur below T_g and similarly demonstrate the temperature dependencies of the Arrhenius type and the activation energies that are smaller than those for cooperative α-process occurring above T_g [34]. One of them is the nonequilibrium mode of the α-relaxation that manifests itself as a break point in the respective VTF dependence that occurs at T_g and gives rise to a smaller slope and, thus, lower activation energy (Fig. 3.12) [35]. The latter is either somewhat larger [36, 37] or comparable [37] to that of the β-process. Another is the so-called α'-relaxation process that is observed in metallic [38] as well as polymeric glasses [39]. It is reported [38] to be associated with the "frozen-in relaxation sites" and has small activation energies (Fig. 3.12), which makes it very similar to the regular β-relaxation. However, both nonequilibrium α-process and α'-process are detected at higher temperatures than the regular β-process.

3.3.2 Isoconversional Treatment

In order to apply an isoconversional method to the DSC data on the glass transition, one needs first to determine the extent of conversion. This can be done in a way similar to calculating the normalized heat capacity [40].

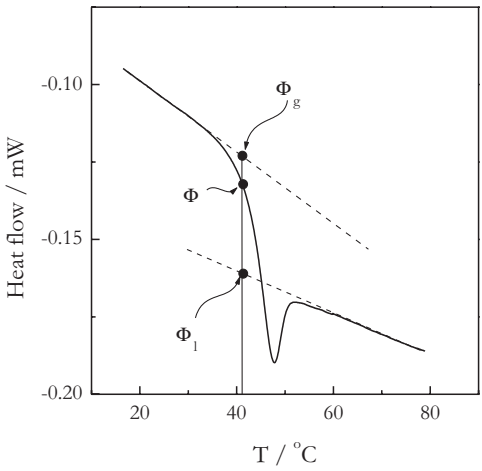

Fig. 3.13 The glass transition in amorphous indomethacin measured at 5 °C min^{-1}. Φ represents the heat flow value at a given temperature, T. Φ_l and Φ_g represent the extrapolated heat flow baselines for the liquid and glass at the same temperature T. These are the values to be substituted in Eq. 3.20 to determine α at this T

$$C_P^N = \frac{(C_P - C_{Pg})\big|_T}{(C_{Pl} - C_{Pg})\big|_T}, \tag{3.19}$$

where C_P is the current heat capacity, and C_{Pg} and C_{Pl} are the glassy and liquid heat capacity, respectively. The normalized heat capacity runs from 0 to 1, i.e., in the same way as the extent of conversion. Equation 3.19 is equally applicable to the heat flow data so that the extent of conversion is determined as follows:

$$\alpha = \frac{(\Phi - \Phi_g)\big|_T}{(\Phi_l - \Phi_g)\big|_T}, \tag{3.20}$$

where Φ is the heat flow at a given temperature T, and Φ_l and Φ_g are the heat flow values for the liquid and glass extrapolated to the same temperature T (Fig. 3.13). In practical terms, one starts by estimating the straight baseline for the glass phase and subtracting it from the whole DSC signal. Then at each given T, α is calculated as the ratio of the resulting heat flow to the heat flow obtained from extrapolation of the straight baseline for the liquid phase to this temperature.

The application of the aforementioned procedure results in α versus T curves similar to those obtained for the glass transition in amorphous drug indomethacin (IM) [41] (Fig. 3.14). The enthalpy overshoot (the endothermic peak at the end of the glass transition step) observed on heating (see Fig. 3.13), gives rise to the α-values in excess of unity. This feature does not appear when the glass transition is measured on cooling. When the glass transition kinetics is measurement on heating, each heating run has to be preceded by cooling performed from temperature significantly above T_g to significantly below T_g at the rate of cooling whose absolute value

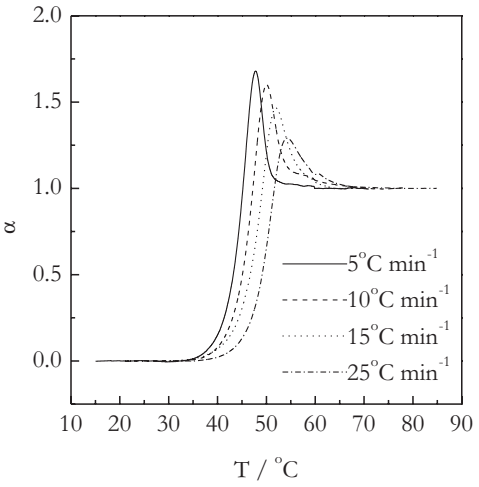

Fig. 3.14 Conversion against temperature curves for the glass transition of amorphous indomethacin at four heating rates

is equal to the rate of the following heating [42, 43]. A suitable temperature range of measurements is typically from T_g+40 to T_g-40.

For measurements performed on heating (Fig. 3.14), the isoconversional calculations need to use only the ascending part of the α versus T curves up to $\alpha=1$. The resulting dependence of the activation energy of conversion is shown in Fig. 3.15. The observed decreasing shape of the E_α versus α dependence is typical for the glass transition and has been observed in variety of other systems, including many polymers [44]. The decrease in E is easy to understand in terms of the cooperative molecular mobility discussed earlier (Fig. 3.12). The glassy phase is characterized by a small amount of free volume that permits only local noncooperatve motion (e.g., the β-process) that dominates well below T_g. As temperature rises approach-

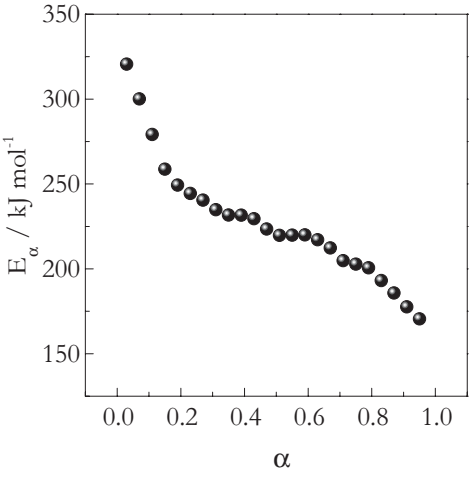

Fig. 3.15 Conversion dependence of the activation energy evaluated from the data shown in Fig. 3.14. (Adapted from Vyazovkin and Dranca [41] with permission of ACS)

ing the glass transition region, the molecular motion intensifies, and the free volume increases, initiating the α-process. The latter involves considerable cooperativity between the molecules and, thus, a large energy barrier as reflected in the large value of E at the initial stages of the transition (Figs. 3.12b and 3.15). As temperature continues to rise, the free volume continues to increase. The molecular packing becomes increasingly looser, allowing the molecules to move less dependently, i.e., in a less cooperative fashion. This relieves the energetic constrains, and the activation energy decreases.

A decrease in E is consistent with the predictions of the VTF and WLF equations (Eqs. 3.17 and 3.18). A similar trend is predicted by the Adam–Gibbs equation[45]

$$\tau = A \exp\left(\frac{z^* \Delta\mu}{k_B T} \right), \tag{3.21}$$

where k_B is the Boltzmann constant, $\Delta\mu$ is the activation energy per particle, and z^* is the number of particles that cooperatively rearrange. In Eq. 3.21, z^* is inversely proportional to the configurational entropy that increases with T so that both z^* and the effective activation energy (i.e., $z^*\Delta\mu$) decrease with T.

Note that even before the first applications [30, 46] of isoconversional methods to the glass transition kinetics, the trend for the activation energy to decrease with increasing temperature was observed in other studies [47–49]. In them, the activation energy was determined from the shift in the value of T_g with the heating rate in accord with the equation proposed by Moynihan et al.: [42, 43]

$$E = -R \frac{\mathrm{d}\ln|\beta|}{\mathrm{d}T_g^{-1}}, \tag{3.22}$$

where β can be the rate of heating or cooling. However, the value of T_g can be defined in the order of its increase as the onset temperature, the temperature of the midpoint step in the heat flow, and the endset temperature. For the glass transition of sorbitol, Angell et al. [47] have found that Eq. 3.22 gives rise to a significantly larger E when T_g is determined as the onset temperature than when T_g is estimated as the temperature of the heat capacity peak. A similar effect was reported by Lacey et al. [48] for PS oligomer and side-chain polysiloxane and by Hancock et al. [49] for some pharmaceutical glasses, including poly(vinylpyrrolidone) (PVP), IM, and several sugars. The observed temperature dependence of the activation energy suggests that the plot of $\ln\beta$ versus T_g^{-1} should be nonlinear. The nonlinearity can be quite obvious when T_g is measured in a wide range of the heating rates as illustrated in Fig. 3.16 for the glass transition in PS [30]. From this plot, we can see again that the activation energy of the glass transition decreases with increasing temperature.

Our numerous applications of the isoconversional method to the glass transition in a variety of systems indicate that the obtained activation energies are in reasonable agreement with the activation energies obtained by other techniques, such as

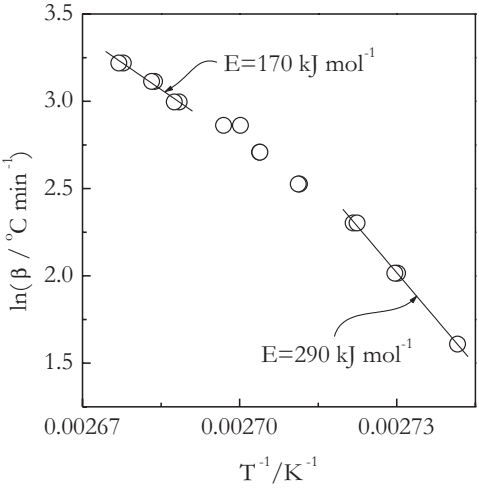

Fig. 3.16 Plot of lnβ versus T_g^{-1} measured for the glass transition in polystyrene at nine heating rates from 5 to 25 °C min^{-1}. T_g was measured twice at each heating rate and determined as the temperature at midpoint of the glass transition step. The E values of 290 and 170 kJ mol^{-1} are found respectively from the three slowest and the three fastest heating rates. (Adapted from Vyazovkin and Dranca [30] with permission of ACS)

dielectric and mechanical spectroscopy, for the α-relaxation [44, 46]. Of course, one should not expect precise agreement between the absolute values. This is not only because different techniques measure different physical properties but also because the activation energy of the α-relaxation depends on temperature and the temperature regions employed by different techniques rarely coincide. In particular, it has been reported [50] that the E values derived from DSC data obtained on cooling are markedly larger than those derived from the heating data. However, what is essential is that a variation in E is detected by different techniques, including DSC, as long as DSC data are analyzed by an isoconversional method.

Although an isoconversional method consistently produces a decreasing E versus α dependence for the transition from the glass to liquid phase, the absolute values of E and the degree of its variability with temperature change dramatically between the glassy substances. Note that an E versus α dependence (e.g., Fig. 3.15) can be converted to an E versus T dependence by replacing the values of α with the mean value of the temperatures related to this α at different heating rates (see Fig. 3.14). Figure 3.17 presents a set of the E versus T dependencies evaluated by applying an isoconversional method to the glass transition in a series of substances: poly(vinyl chloride) (PVC), poly(*n*-butyl methacrylate) (PBMA), PVP, poly(ethylene 2,6-naphthalate) (PEN), PS, poly(ethylene terephthalate) (PET), and boron oxide (B_2O_3) [44, 46]. The differences in the activation energy variability are really staggering. At one extreme, we have PVC and PET, in which the glass transition occurs in a very narrow temperature range and accompanied by a drastic change in the activation energy. At another extreme we see PBMA and B_2O_3 whose glass transition stretches over a wide temperature range with little change in the activation energy.

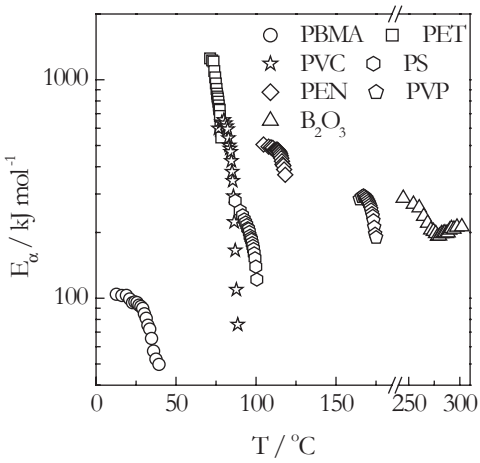

Fig. 3.17 Temperature dependencies of the activation energy for the glass transition in various substances. *PBMA* poly(*n*-butyl methacrylate), *PET* poly(ethylene terephthalate), *PVC* polyvinyl chloride, *PS* polystyrene, *PEN* poly(ethylene 2,6-naphthalate), *PVP* poly(vinylpyrrolidone). (Adapted from Vyazovkin et al. [44, 46] with permission of Wiley)

In order to characterize the variability in E numerically, we have introduced [44] a variability parameter defined as

$$\Delta_E = \frac{E_{0.25} - E_{0.75}}{T_{0.25} - T_{0.75}}, \tag{3.23}$$

where $E_{0.25}$ and $E_{0.75}$ are the E_α values at $\alpha = 0.25$ and 0.75, respectively, and $T_{0.25}$ and $T_{0.75}$ are the values of T_α for the respective values of α. The dependencies presented in Fig. 3.17 yield the Δ_E values collected in Table 3.1. In terms of the logτ versus T^{-1} plots, larger variability of E means larger curvature of the plot (Fig. 3.12). Ultimately, when the plot is linear (i.e., of the Arrhenius type), E becomes independent of T, and Δ_E turns into zero. That is, the variability parameter should correlate with the departure of the logτ versus T^{-1} plot from the Arrhenius behavior, or, in other words, with the dynamic fragility.

The concept of fragility was introduced by Angell [51] to characterize the differences in the temperature dependencies of viscosity or relaxation time of glass-forming liquids. According to this concept, the strong liquids are those that demonstrate close to linear or Arrhenius type of logτ versus T^{-1} (Fig. 3.18). The fragile liquids, on the contrary, demonstrate nonlinear plots of the VTF or WLF type. Typically, the strong liquids are inorganic glass formers, whereas polymers belong to the most fragile liquids. Deviation from the Arrhenius behavior is estimated as the fragility parameter, m. By assuming the VTF type of the temperature dependence (Eq. 3.16), the parameter is defined as:[52]

$$m = \frac{A / T_g}{\ln 10 \cdot (1 - T_0 / T_g)^2}. \tag{3.24}$$

Table 3.1 Estimated (Eq. 3.23) values of the variability parameter and literature values of the fragility parameter

Substance	Δ_E (kJ mol^{-1} K^{-1})	m
B_2O_3	−0.6	32 [53]
PBMA	−2.3	48 [55]
PEN[a]	−10.0	99 [57], 66[58]
PVP[b]	−11.1	102
PS	−11.5	139 [53], 77[54]
PVC	−73.0	191 [53], 160 [54]
PET	−110.6	156 [56]

PBMA poly(n-butyl methacrylate), *PEN* poly(ethylene 2,6-naphthalate), *PVP* poly(vinylpyrrolidone), *PS* polystyrene, *PVC* polyvinyl chloride, *PET* poly(ethylene terephthalate)

[a] The m values have been estimated from the VTF parameters reported in the respective papers

[b] For PVP, the m value has been predicted from Δ_E by the correlation shown in Fig. 3.19

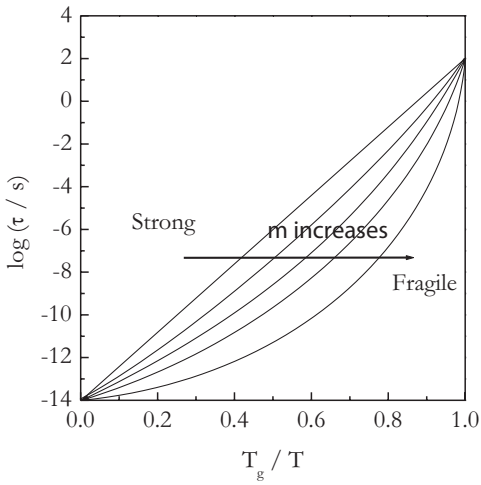

Fig. 3.18 Temperature dependencies of the relaxation time in the strong and fragile liquids

For all the compounds presented in Table 3.1, except PVP, the values of m are found in the literature [53–58]. As seen from Table 3.1, the Δ_E and m parameters are correlated. The correlation is nonlinear, but can be reduced to a linear form by replacing Δ_E with $\log(-\Delta_E)$ (Fig. 3.19). The dataset from Table 3.1 demonstrates strong correlation ($r = 0.9665$) of the following form:

$$\log(-\Delta_E) = -0.438 + 0.0145m. \tag{3.25}$$

Surmising that the correlation (3.25) holds for a wide class of glasses, one can use it to estimate the fragility parameter from Δ_E. For example, based on Eq. 3.25, the m value for PVP should be around 102.

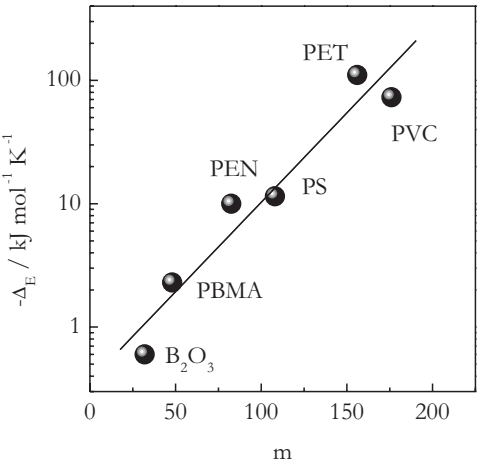

Fig. 3.19 Correlation of the parameters of variability ($-\Delta_E$) and fragility (m). The m values are from Table 3.1 (if there is more than one literature value, the mean value is used). *PET* poly(ethylene terephthalate), *PVC* polyvinyl chloride, *PS* polystyrene, *PEN* poly(ethylene 2,6-naphthalate), *PBMA* poly(*n*-butyl methacrylate). (Adapted from Vyazovkin et al. [44] with permission of Wiley)

3.4 Glass Aging

The glass is falling hour by hour, the glass will fall for ever
Louis MacNeice, Bagpipe Music

3.4.1 Background

When liquid is well above its T_g, its relaxation time is significantly shorter than the timescale of regular measurements, which typically last from minutes to hours. On such timescale, any fluctuations of the molecular structure of liquid are relaxed, i.e., liquid is at equilibrium. When temperature drops below T_g, the relaxation time of liquid exceeds the experimental timescale, and the structural fluctuations do not have enough time to relax. Instead, they become frozen kinetically as the nonequilibrium glass phase (Fig. 3.20). This phase is driven thermodynamically to relax its structure toward that of the equilibrium supercooled liquid. The relaxation can occur on heating (i.e., when temperature raises continuously) of a glass through the glass transition temperature. In this case, the process is referred to as the glass transition (Sect. 3.3).

However, this relaxation also occurs on annealing (i.e., when temperature is held constant) below the glass transition temperature. This process is called physical aging [59]. Physical aging is accompanied by a change in mechanical, dielectric, magnetic, and optical properties of a glass. Thermodynamically, the process is characterized by a decrease in three thermodynamic parameters: the enthalpy, entropy, and volume (Fig. 3.20). That is, physical aging is an exothermic process, during which the glass becomes more ordered structurally and its volume shrinks.

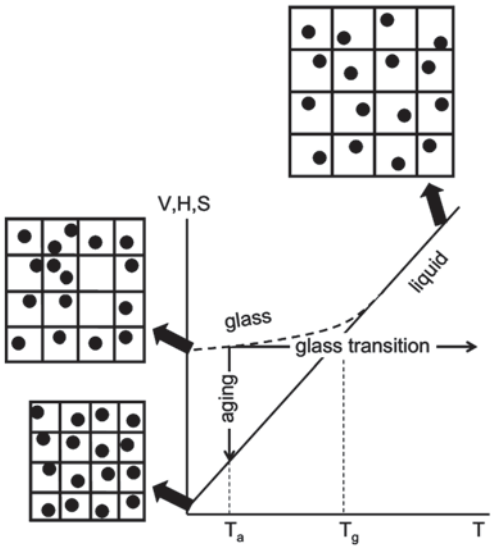

Fig. 3.20 Relaxation of the nonequilibrium glassy structure can occur under rising temperature conditions as the glass transition or at constant temperature as aging

The kinetics of physical aging is of great practical importance because it determines for how long a glassy material can remain useful at temperature of operation. The stability of a glass increases with increasing the difference between the temperatures of the glass transition and operation. For example, regular household glassware made of silicate glass is used about 500 °C below its glass transition temperature. This makes it stable for all designed practical purposes.

However, even in the case of silicate glasses used far below T_g, the signs of aging are detectable on the scale of decades [60–62]. An intriguing example [60, 62] includes data on aging of glass thermometers used by the renowned physicist James Prescott Joule. Joule regularly calibrated his thermometers and noticed that what he called the zero point was increasing systematically, shifting totally by 0.91 F over 23 years. The effect is explicable [60, 62] by the glass shrinkage due to physical aging.

The kinetics of physical aging is usually followed by measuring either volume of enthalpy of a glassy sample. The heat flow released during physical aging is too small to follow the process by regular DSC instruments in real time. The measurements are thus conducted discretely, i.e., in steps. The idea is that the enthalpy lost on aging can be recovered when heating an aged glassy sample through the glass transition temperature. As seen from Fig. 3.21, the sample held at aging temperature T_a will continue to lose its enthalpy until the glass reaches equilibrium, i.e., turns into supercooled liquid. As discussed earlier (Fig. 3.9), reheating of unaged glass results in the enthalpy overshoot. When glass ages, it assumes a denser and more ordered structure that results in a decrease of the molecular mobility and an increase of the relaxation time. For this reason, when aged glass crosses the equilibrium liquid line, it takes longer to restore the liquid structure than for unaged glass.

Thus, the more glass aged (points B and C in Fig. 3.21), the more it overshoots the liquid line. The inflection point on the enthalpy recovery line corresponds to the temperature, T_p, of the DSC peak that appears at the end of the glass transition step

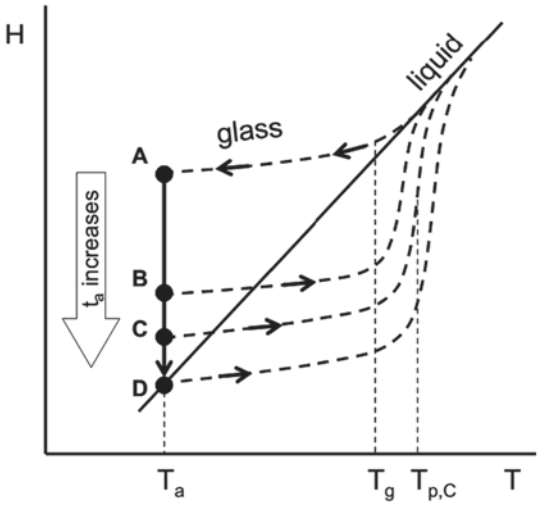

Fig. 3.21 As glass ages, its enthalpy lowers and its mobility slows down so that on reheating the enthalpy overshoot becomes larger and shifts to higher temperature. T_p denotes the position of the overshoot peak

measured on heating. The size of the peak is proportional to the enthalpy lost on aging. The effect is illustrated in Fig. 3.22 [63]. Both peak temperature and recovered enthalpy increase with aging time, t_a, until they reach ultimate values, which correspond to completely relaxed glass (point D in Fig. 3.21). The magnitude of the ultimate values depends on chosen T_a.

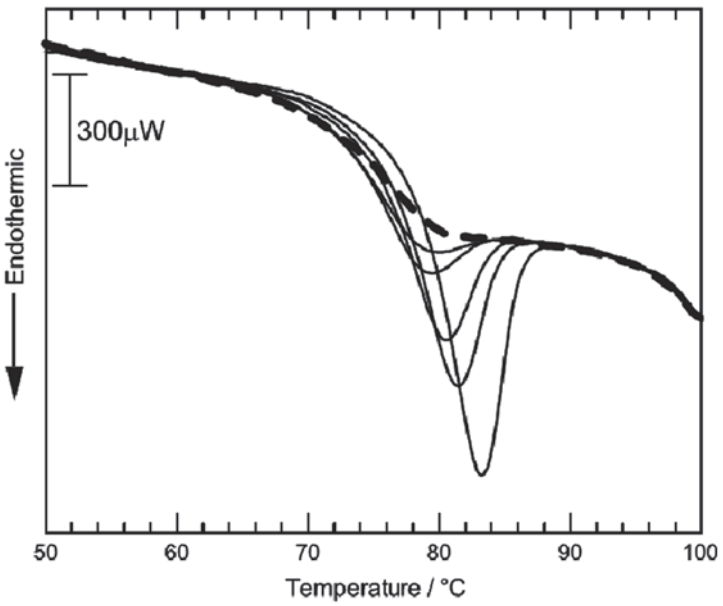

Fig. 3.22 DSC curves of poly(cyanobiphenyl ethylacrylate) heated at 5 °C min–1 after aging at 64 °C for 34, 64, 305, 725, and 3963 min (*solid lines* in order of increasing the peak size). The *dash line* represents the curve for unaged sample. (Reproduced from Tanaka and Yamamoto [63] with permission of Elsevier)

3.4.2 Isoconversional Treatment

The recovered enthalpy of aging, ΔH_a, can be estimated as the difference in the integrals of the DSC curves for aged and unaged samples [64]. The measurements are performed on the same sample, which is first relaxed for a few minutes at a temperature well above T_g, then cooled quickly at a controlled rate to a temperature well below T_g, and then heated back to the initial temperature at a given heating rate. This would produce a DSC trace for unaged glass. To obtain the trace for aged glass, the sample is exposed to the same temperature protocol, except that the cooling segment is interrupted by the aging segment, which maintains temperature T_a for a period t_a. After that the cooling segment continues, followed by the heating segment. The difference in the integrals of the respective DSC traces would yield ΔH_a related to a given aging time t_a. Another point on the kinetic curve ΔH_a versus t_a is produced by maintaining the whole cooling–heating protocol but changing the length of the aging segment. An example of ΔH_a versus t_a is shown in Fig. 3.23 for aging of maltitol (Mt) glass [65].

The aging temperatures are usually taken within 10 °C below the glass transition temperatures. It may take months to reach equilibrium at 10 °C below T_g and about a day at 5 °C below T_g. Equilibrium is easy to detect when converting the time to the logarithmic scale (Fig. 3.23). On this scale, aging progresses almost linearly with time. On approaching equilibrium, the line breaks and turns horizontal. For example, it takes Mt glass about 20 h to reach equilibrium at 6 °C below its T_g (Fig. 3.23). The time to equilibrium in seconds, t_∞, can be estimated by using an equation proposed by Struik: [59]

$$t_\infty \approx 100 \exp[0.77(T_g - T_a)]. \tag{3.26}$$

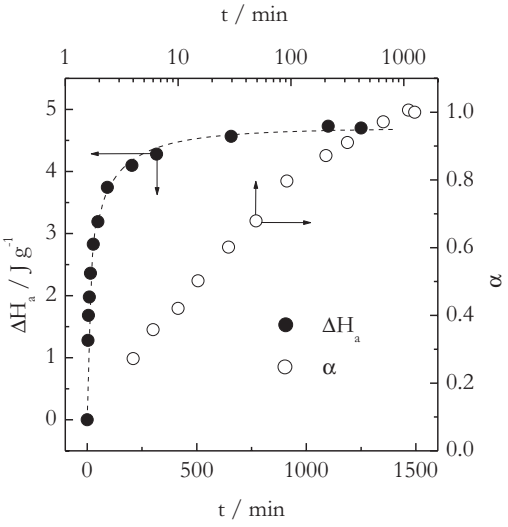

Fig. 3.23 Progress of maltitol aging at 40 °C. *Solid circles* represent recovered enthalpy of aging, *open circles* conversion. (Partially adapted from Chen and Vyazovkin [65] with permission of ACS)

The equation is not very accurate [66] because it was derived assuming that the temperature dependence of the relaxation time obeys the WLF equation [32]. However, below T_g, the relaxation processes tend to follow [33, 67] the Arrhenius equation that predicts much weaker temperature dependence. In addition, the rate of aging can differ substantially for different materials. For instance, the aging data [68] for polycarbonate and PS suggest that at similar $T_g - T$, the former reaches equilibrium almost ten times faster than the latter. Nonetheless, Eq. 3.26 can provide a reasonable estimate for the magnitude of the aging time, i.e., hours, days, and months.

To perform the isoconversional calculations, experimentally measured curves of the recovered enthalpy versus aging time need to be converted to the curves of the conversion versus time. For any given aging time, the extent of aging, i.e., the extent of conversion from the glass to supercooled liquid phase, is determined as:

$$\alpha = \frac{\Delta H_a(t)}{\Delta H_\infty}, \tag{3.27}$$

where $\Delta H(t)$ is the enthalpy measured at the aging time, t, and ΔH_∞ in the equilibrium (plateau) value. Since aging runs are conducted isothermally, the activation energy can be evaluated straightforwardly by Eq. 3.28

$$E_\alpha = R\frac{\mathrm{d}\ln t_\alpha}{\mathrm{d}T^{-1}}, \tag{3.28}$$

i.e., as the slope of a plot of the natural logarithm of the time, t_a, to reach a given extent of aging, α, against the reciprocal aging temperature. By repeating this procedure for a series of the conversions, one obtains a dependence of E_α on α.

The use of Eq. 3.28 requires determining the time to reach a given extent of conversion at different aging temperatures. Unfortunately, it is impossible to measure reliably small extents of conversion. The aging rate is the fastest in the initial moments so that the smallest values of conversion are experimentally detected after only a few minutes of aging. For instance, 4-min aging of Mt resulted in α being about 0.27 (Fig. 3.23). The values of t_α can be found by interpolating the discrete experimental dependence of α versus t by the Kohlrausch–Williams–Watts (KWW) equation [3, 4]

$$\alpha = 1 - \exp\left[-\left(\frac{t}{\tau_{ef}}\right)^\gamma\right]. \tag{3.29}$$

The equation has two fit parameters: τ_{ef}, which is the effective relaxation time, and γ, which is the stretch exponent. The KWW equation is generally found to describe accurately the relaxation kinetics of glasses, although it is commonly found that [69] the parameter γ varies systematically with temperature. Once the values of τ_{ef} and γ are estimated, Eq. 3.29 can be used to find t_α for any α.

The isoconversional plots of $\ln t_\alpha$ versus T^{-1} for aging of Mt glass are seen in Fig. 3.24. The most remarkable feature of these plots is that their slopes increase

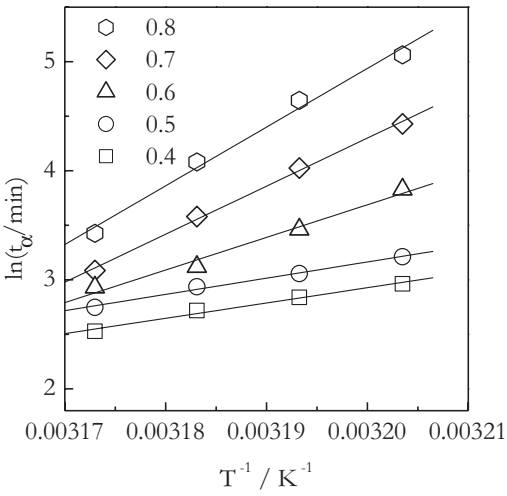

Fig. 3.24 Isoconversional plots obtained from the enthalpy recovery data for maltitol aged at temperatures 39, 40, 41, and 42 °C. (Reproduced from Chen and Vyazovkin [65] with permission of ACS)

markedly with increasing conversion. This means that the activation energy of aging increases throughout the aging process. A dependence of the isoconversional values of E_α on α is shown in Fig. 3.25. The data suggest that the later stages of aging demonstrate the activation energies whose values are similar to the activation energy of the glass transition process in Mt, i.e., 413±20 kJ mol^{-1}[70]. However, the most important is that the activation energy of the early stages of aging is several times smaller.

The kinetics of physical aging can also be followed by the heat capacity relaxation. Physical aging is known [71, 72] to be accompanied by a decrease in the excess heat capacity, C_P. The effect is measured by temperature-modulated (TM) DSC under quasi-isothermal conditions that are accomplished by overlaying a constant

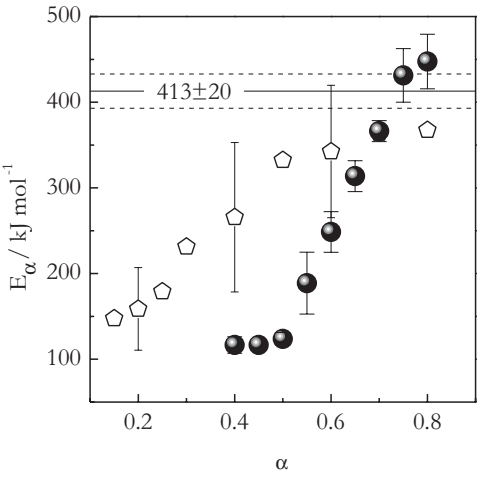

Fig. 3.25 Variation of the activation energy of aging of maltitol with the extent of conversion from glass to supercooled liquid. *Pentagons* and *spheres* represent respectively the values derived from the heat capacity and enthalpy relaxation data. (Reproduced from Chen and Vyazovkin [65] with permission of ACS)

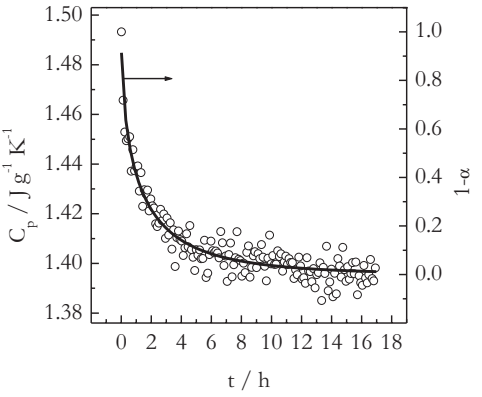

Fig. 3.26 Decrease in the excess heat capacity of maltitol at 39 °C. *Solid line* represents the KWW fit (Eq. 3.29). KWW Kohlrausch–Williams–Watts. (Adapted from Chen and Vyazovkin [70] with permission of Elsevier)

temperature with small amplitude temperature perturbations. The effect has been attributed [71] to the heat capacity contributions from faster modes of molecular motion that include the noncooperative β or Johari–Goldstein process and faster portions of the cooperative α-process. An advantage of the heat capacity relaxation measurements is that the measurements are conducted continuously and take less time than the discrete and laborious enthalpy relaxation measurements.

The loss of the excess heat capacity for Mt glass is presented in Fig. 3.26. The C_P versus t data are converted to the α versus t curves as follows:

$$\alpha = \frac{C_{P,\mathrm{i}} - C_P(t)}{C_{P,\mathrm{i}} - C_{P,\mathrm{f}}}, \tag{3.30}$$

where $C_{P,\,\mathrm{i}}$, $C_{P,\,\mathrm{f}}$, and $C_P(t)$ are respectively the initial (nonaged), final (plateau), and current values of the heat capacity. The resulting α versus t curves obtained at several aging temperatures can be treated by an isoconversional method in the same fashion as the enthalpy relaxation curves. The E_α versus α dependence evaluated from the heat capacity relaxation data is quite similar to that determined from the enthalpy relaxation measurements (Fig. 3.25). In both cases, the E_α values for the early stages of aging are about three times smaller than the activation energy for the glass transition.

Isoconversional analysis of the aging kinetics indicates that the early stages of the process are dominated by a faster process having smaller activation energy and the later stages by a slower process of larger activation energy. Because at conversions close to unity, the E_α value approaches the activation energy of the glass transition, it is logical to conclude that the slower process of larger activation energy is the cooperative α-relaxation. Then the faster process of lower activation energy is likely to be associated with relaxations of low cooperativity. As discussed earlier (Fig. 3.12), these may include the nonequilibrium mode of α-, α'-, and β-relaxations. They have progressively smaller activation energies, each of which being smaller than the typical values found for the α-relaxation. Mt is known [73] to demonstrate the nonequilibrium α-mode. Although the activation energy has not been reported

for this process, the slope of the respective Arrhenius plot is significantly larger than that for the β-relaxation. For the latter, the activation energies have been reported to be 62 [73], 57 [74], and 71 [35] kJ mol^{-1}. On the other hand, extending the aging temperatures of Mt below 30 °C brings the activation energies of the initial stages of aging down to 60–80 kJ mol^{-1}[65].

All in all, it appears that the activation energy of the early stages of aging is much closer to the activation energy of the β- than α-relaxation. Also, the values get even closer when aging is performed at lower temperatures. This is in agreement with the results of Nemilov [60, 61] and Nemilov and Johari [62] for silicate glasses, of Cangialosi et al. [75] for polycarbonate, and of Hu and Yue [76] for hyperquenched GeO_2 that demonstrate that at temperatures markedly below T_g, the overall aging kinetics is controlled by processes whose activation energy is approaching the values characteristic of the β-relaxation process.

Considering the spatial heterogeneity of glass (Fig. 3.11), the initial stages of aging should occur predominantly via collapse (densification) of low-density mobility islands. This process would be driven by faster relaxation processes of lower cooperativity and lower activation energy. As aging glass becomes denser and more homogenous, the molecular mobility becomes more cooperative that causes the energy barrier to increase continuously toward the value characteristic of cooperative α-relaxation. This simple phenomenological picture explains well an increase in the effective activation energy revealed by an isoconversional analysis. In conclusion, we should note that the observed increase in the effective activation energy is not unique to physical aging of Mt. The effect has been reported [77, 78] for metallic glasses, although was not correlated with the α- or β-relaxation processes in the respective glasses.

3.4.3 Activation Energies of β-Relaxation from DSC

As discussed in the previous section, the activation energy of the early stages of aging approaches the activation energy of the β-relaxation, E_β, when the aging temperature is decreased significantly below T_g. In that regard, it is of interest to consider an original method proposed by Bershtein and Egorov [79] for estimating E_β from the pre-glass transition annealing peaks. The peaks of this kind were originally reported by Illers [80], who observed that reheating of PVC annealed significantly below T_g gives rise to small and broad endothermic DSC peak that may occur well before the glass transition step. Similar observation was made later by Chen [81, 82] for several metallic glasses and by Bershtein et al. [83, 84] for several polymers. Chen interpreted the effect as the partial enthalpy relaxation (during annealing) and recovery (during reheating) that occurs at the expense of the faster part of a broad relaxation spectrum of the glassy state. However, Bershtein et al. [83, 84] linked the effect to the β-relaxation process that is typically detected by mechanical [85] and dielectric [86] spectroscopy.

Chen as well as Bershtein et al. proposed that a shift in the annealing peak temperature, T_p, with the heating rate, β, can be used to determine the activation energy of the underlying process as follows:

$$E = -R\frac{\mathrm{d}\ln\beta}{\mathrm{d}T_p^{-1}}. \tag{3.31}$$

The E values estimated from the annealing peaks were found [81–84] being several times smaller than the respective activation energies for the glass transition (i.e., α-relaxation) event. The ratio of the respective activation energies was consistent with that reported [85, 86] for the β- and α-relaxations in polymers.

The annealing peaks observed below T_g result from the same reason as the regular aging peaks at the end of the glass transition step (Fig. 3.22). It is nothing else but endothermic recovery of the enthalpy lost on aging. The only difference is that when a glass is aged well below T_g (typically around $0.8T_g$), the recovery takes place before the glass transition step begins. However, as aging temperature is increased, the position of the annealing peak shifts to higher temperature so that it can appear at the beginning of the glass transition step, or in its middle, or ultimately at its end as regular aging peak (Fig. 3.27).

As long as the recovery occurs below the beginning of the glass transition step, the molecular mobility in the respective temperature region is likely to be dominated by the local noncooperative process, including the β-relaxation (Fig. 3.12). It thus seems reasonable to expect that a fair estimate of the E_β value can be obtained by analyzing the annealing peak data. We have tested this method of estimating E_β on a variety of polymeric (PS and its nanocomposite [30], PVP [87], poly(methyl methacrylate) (PMMA) [35], PET [35]), and small molecule organic (ursodeoxycholic acid [87], IM [41], glucose (Gl) [35], Mt [35]) glasses. For most of these glasses, the E_β values are known from traditional studies based on dielectric or me-

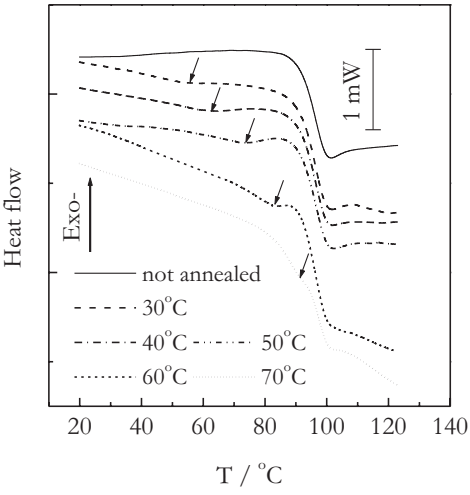

Fig. 3.27 DSC curves obtained on heating of polystyrene at 10 °C min^{-1} without annealing and after annealing for 30 min at different temperatures. *Arrows* point at the location of annealing peaks. (Adapted from Vyazovkin and Dranca [30] with permission of ACS)

chanical spectroscopy and, thus, can be directly compared with the values derived from the annealing peaks. An additional test is possible by comparing the activation energies estimated from the annealing peaks against the empirical correlation:

$$E_\beta = (24 \pm 3) R T_g \tag{3.32}$$

reported by Kudlik et al. [88]. This correlation holds very well for a great number of the E_β values for both polymers and small-molecule glasses [89].

The annealing peaks are produced by annealing a glass at about $0.8T_g$. The peaks are especially easy to produce in rapidly cooled glasses, which can be obtained by fast cooling directly in DSC or by quenching separately in liquid nitrogen. Faster cooling freezes a glass further from equilibrium that secures faster initial rate of aging. For rapidly cooled glasses, it usually takes about half an hour of aging to produce a well-detectable annealing peak. Once the aging period is finished, the glass needs to be cooled quickly well below the aging temperature to stop aging and immediately after that reheated at a relatively fast heating rate.

In DSC, the annealing peak manifests itself as a very broad and shallow endotherm, which starts to evolve above the annealing temperature (Fig. 3.27). The peaks are readily detected when comparing DSC traces for annealed and not annealed samples. The peaks obtained at any given annealing temperature would shift to higher temperature with increasing the heating rate. This permits estimating the activation energy from the slope of the plot $\ln\beta$ versus T_p^{-1} (Eq. 3.31). A series of such plots corresponding to different annealing temperatures is seen in Fig. 3.28.

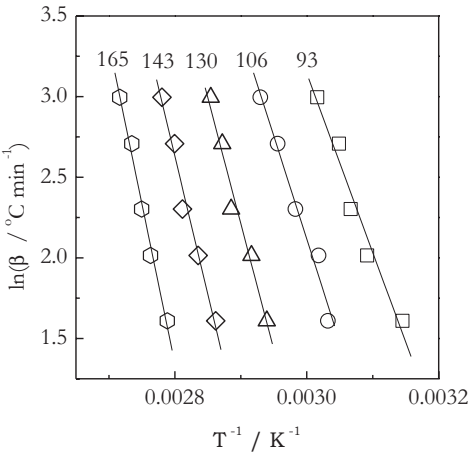

Fig. 3.28 Evaluating activation energies (Eq. 3.31) from the annealing peaks for polystyrene aged at different temperatures: 30 °C (*squares*), 40 °C (*circles*), 50 °C (*triangles*), 60 °C (*diamonds*), and 70 °C (*hexagons*). Numbers by the lines are the activation energies in kJ mol^{-1}. (Adapted from Vyazovkin and Dranca [30] with permission of ACS)

The slope of the plots as well as the activation energy decreases systematically with decreasing the annealing temperature.

For reasons explained earlier, the use of the lowest feasible annealing temperature yields better estimates for the activation energy of the β-relaxation. Following this principle, we have found [35] that considering their respective confidence intervals, all E_β values estimated from the annealing peaks are consistent with the correlation (Eq. 3.32). Furthermore, the obtained estimates of E_β appear to compare quite well against the literature values (Fig. 3.29). Our estimates typically involve ~10–20% of uncertainty. It is seen that most of the estimates deviate by less than 20% from the literature values, especially if one disregards a few extreme literature values, which may be outliers.

It is obvious that the activation energies derived from the annealing peaks correlate fairly well with the activation energies of the β-relaxation. Nevertheless, the respective assignment must be made with care. Note that annealing is conducted around $0.8T_g$, i.e., in the temperature region where one typically finds the absorption peaks due to the β-relaxation when using traditional methods of dielectric and mechanical spectroscopy [90]. However, the recovery process gives rise to the annealing peaks, whose peak temperatures are found about 20–30 °C above the annealing temperature. In this temperature range, the β-relaxation is not necessarily dominant so that the activation energy estimated from the annealing peaks may have a sizeable contribution from higher temperature and higher activation energy relaxation processes (see Fig. 3.12).

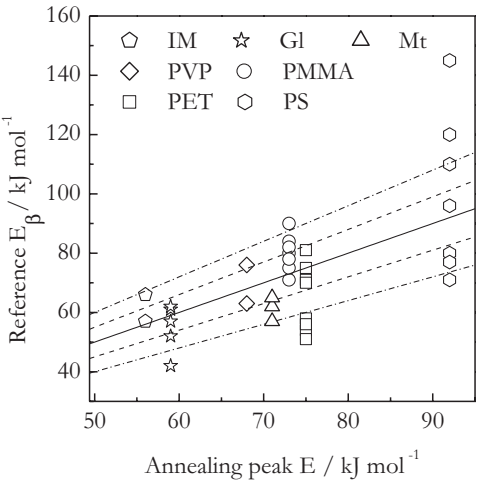

Fig. 3.29 Correlation of the E_β estimates from the annealing peaks with the literature values. *Solid line* represents exact equality; *dash* and *dash-dot lines* represent 10 and 20% deviations, respectively. *IM* indomethacin, *GI* glucose, *Mt* maltitol, *PVP* poly(vinylpyrrolidone), *PMMA* poly(methyl methacrylate), *PET* poly(ethylene terephthalate), *PS* polystyrene. (Reproduced from Vyazovkin and Dranca [35] with permission of Elsevier)

3.5 Nucleation

...matter cannot long do without the shaping, constructive force, and the force cannot do without the constructible material

J. C. Friedrich von Schiller, Letters upon the Æsthetic Education of Man

This section provides some basic introduction into the kinetics of nucleation because nucleation is the most common mechanism of the phase transition. The nucleation mechanism rests on a simple assumption that the formation of a new phase starts from the formation of a very small embryo of this phase. This mechanism is applicable to a variety of phase transitions, including the transitions discussed further in this chapter. Most common example is crystallization of melts on cooling. From the thermodynamic standpoint (Fig. 3.1), the melt should crystallize spontaneously as soon as temperature drops below the equilibrium melting temperature, T_m, because then the Gibbs free energy of the crystal is lower than that of the liquid phase (i.e., melt). The difference in the respective Gibbs energies is a negative value called the volume Gibbs energy, ΔG_V. In reality, crystallization occurs only when the melt reaches significant supercooling. Crystallization is delayed because the creation of the crystalline phase nucleus faces a free energy barrier associated with the surface free energy, ΔG_S. This value is the difference in the Gibbs energy of the surface and the bulk of the nucleus. The Gibbs energy of the surface is always larger by the value of the surface energy (surface tension), σ. That is why the value of ΔG_S is positive. The total free energy of nucleation is:

$$\Delta G = \Delta G_S + \Delta G_V. \tag{3.33}$$

It is clear from Eq. 3.33 that the spontaneous formation of a new phase nucleus can start only at temperature when ΔG_V is negative enough to outweigh ΔG_S.

If one assumes that the nucleus has a spherical shape of the radius, r, then the terms ΔG_S and ΔG_V can be determined respectively as the surface area of the sphere times the surface energy σ, and as the volume of the sphere times the volume energy per unit volume, ΔG_V:

$$\Delta G = 4\pi r^2 \sigma + \frac{4}{3}\pi r^3 \Delta G_V. \tag{3.34}$$

Figure 3.30 displays a dependence of ΔG_S and ΔG_V on the nucleus radius. The sum of these two terms (i.e., ΔG) passes through a maximum that represents the free energy barrier to nucleation, ΔG^*. The nucleus radius, r^*, that corresponds to ΔG^* is the critical size of a stable nucleus. A nucleus of a larger size would grow spontaneously forming a new phase. The size of the critical nucleus is found from the condition of ΔG maximum, i.e., by setting to zero the first derivative of ΔG with respect to r. This yields Eq. 3.35:

$$r^* = \frac{-2\sigma}{\Delta G_V}. \tag{3.35}$$

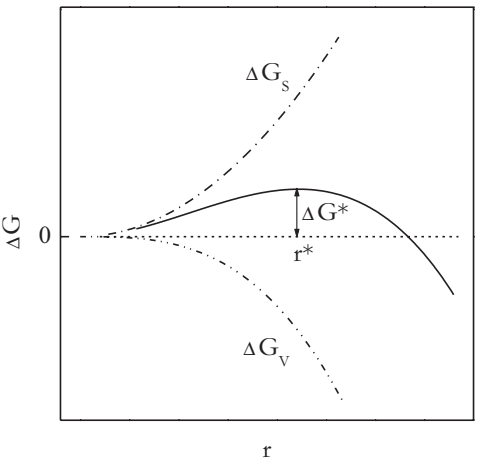

Fig. 3.30 Free energy of nucleation as a function of nucleus radius. (Adapted from Vyazovkin [91] with permission of Elsevier)

Inserting this value into Eq. 3.34 allows one to determine the height of free energy barrier as:

$$\Delta G^* = \frac{16\pi\sigma^3}{3(\Delta G_V)^2}. \tag{3.36}$$

The ΔG^* can be linked to supercooling through the temperature dependence of ΔG_V:

$$\Delta G_V = \Delta H_V - T\Delta S_V. \tag{3.37}$$

Assuming that ΔH_V and ΔS_V do not depend much on temperature, ΔS_V in Eq. 3.37 can be replaced with its value at equilibrium (i.e., when $T = T_m$ and $\Delta G_V = 0$):

$$\Delta G_V = \Delta H_V - T\frac{\Delta H_V}{T_m} = \frac{-\Delta H_f \Delta T}{T_m}, \tag{3.38}$$

where $\Delta T = T_m - T$ is the supercooling and $\Delta H_f = -\Delta H_V$ is the enthalpy of fusion per unit volume. Substitution of Eq. 3.38 into Eq. 3.36 gives:

$$\Delta G^* = \frac{16\pi\sigma^3 T_m^2}{3(\Delta H_f)^2(\Delta T)^2}, \tag{3.39}$$

where ΔH is the heat of fusion per unit volume. Similarly, substitution of Eq. 3.38 into 3.35 reveals a dependence of the critical nucleus size on supercooling:

$$r^* = \frac{2\sigma T_m}{\Delta H_f \Delta T}. \tag{3.40}$$

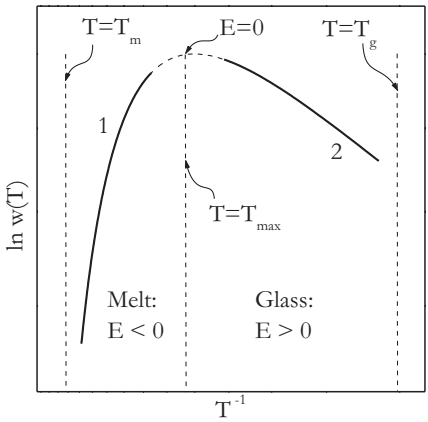

Fig. 3.31 Arrhenius plot for nucleation in temperature range T_g–T_m (1 melt nucleation, 2 glass nucleation). (Adapted from Vyazovkin [91] with permission of Elsevier)

The nucleation rate constant is commonly expressed in the Arrhenius form:

$$w(T) = w_0 \exp\left(\frac{-\Delta G^*}{RT}\right), \tag{3.41}$$

where w_0 is the preexponential factor. However, the temperature dependence of the nucleation constant is more complex than that of the regular rate constant (Eq. 1.2) because ΔG^* depends strongly on ΔT, whose magnitude changes with temperature. This causes the Arrhenius plots of $\ln w(T)$ versus T^{-1} to be nonlinear (Fig. 3.31) [91]. Also, as supercooling decreases with decreasing temperature, both critical nucleus size (Eq. 3.40) and energy barrier (Eq. 3.39) decrease so that the nucleation rate constant increases. Therefore, it demonstrates a negative (or anti-Arrhenian) temperature dependence. Figure 3.31 shows an Arrhenius plot for the nucleation rate. The plot has a positive slope that corresponds to the negative temperature dependence. When the melt crystallization data are fitted to the Arrhenius equation, the fit yields a negative value of the effective activation energy. Also, the slope varies strongly with the temperature, reaching infinity at $T = T_m$ (Eq. 3.39).

Just below the melting point, the nucleation rate quickly increases with decreasing temperature (Fig. 3.32). However, the nucleation rate does not increase indefinitely. It passes through a distinct maximum at a certain temperature, T_{max}. Below this temperature, the nucleation rate starts to decrease with decreasing temperature. This happens because the molecular mobility decreases with temperature. The melt becomes increasingly more viscous, creating an energy barrier, E_D, to diffusion of molecules across the phase boundary. Introduction of the respective energy term into Eq. 3.41 gives rise to the Turnbull and Fisher equation [92]:

$$w(T) = w_0 \exp\left(\frac{-\Delta G^*}{RT}\right)\exp\left(\frac{-E_D}{RT}\right), \tag{3.42}$$

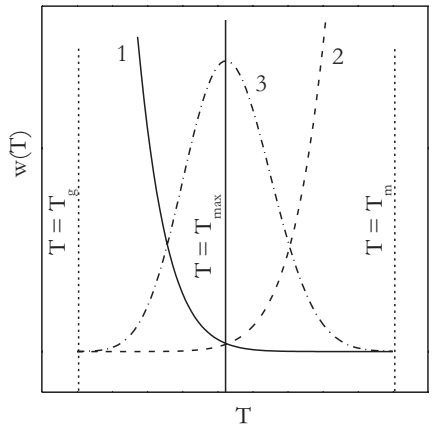

Fig. 3.32 Temperature dependence of nucleation rate (1 $\exp(-\Delta G^*/RT)$, 2 $\exp(-E_D/RT)$, 3 product of 1 and 2). (Adapted from Vyazovkin [91] with permission of Elsevier)

where E_D is the activation energy of the diffusion process. Unlike the ΔG^* term, the E_D term represents a typical Arrhenius temperature dependence (Fig. 3.32). The product of these two terms (Eq. 3.42) yields a temperature dependence that demonstrates a maximum in the nucleation rate. Below T_{max}, the process becomes controlled by diffusion that results in a dramatic decrease of the nucleation rate.

If for a particular compound the maximum nucleation rate is not very large, the respective melt can be readily turned into the glass phase on cooling. Glasses can crystallize on heating. Once the temperature rises above the glass transition temperature, the glass relaxes turning into the metastable supercooled liquid. As temperature continues to rise, the molecular mobility increases, promoting nucleation and crystallization of the supercooled liquid. The glass crystallization on heating is frequently called "cold crystallization." Cold crystallization normally occurs below T_{max}. In this temperature range, the nucleation rate increases with increasing temperature because the rate is limited by diffusion. The corresponding Arrhenius plot (Fig. 3.31) has the regular negative slope that represents a positive (or Arrhenian) temperature dependence. Fitting glass crystallization data to the Arrhenius equation yields a positive value of the effective activation energy. Note that the slope of the Arrhenius plot decreases with increasing temperature.

To better understand the temperature dependence of the effective activation energy for the process of nucleation in the melt and glass crystallization, we can use Eq. 3.42 to derive a theoretical expression for E versus T. The effective activation energy is generally defined as the logarithmic derivative of the rate constant with respect to the reciprocal temperature:

$$E = -R\frac{\mathrm{d}\ln w(T)}{\mathrm{d}T^{-1}}. \tag{3.43}$$

Assuming that the temperature dependence of ΔG^* is determined only by ΔT (see Eq. 3.39), Eq. 3.42 can be rewritten as:

$$w(T) = w_0 \exp\left[\frac{-A}{RT(\Delta T)^2}\right] \exp\left(\frac{-E_D}{RT}\right), \tag{3.44}$$

where A is constant that includes all the parameters from the right-hand side of Eq. 3.39 but ΔT. With regard to Eq. 3.43, the effective activation energy is:

$$E = E_D - A\left[\frac{2T}{(\Delta T)^3} - \frac{1}{(\Delta T)^2}\right]. \tag{3.45}$$

The temperature dependence of E that results from Eq. 3.45 is shown in Fig. 3.33. The equation suggests that when crystallization occurs on cooling from the melt at small supercoolings, E should demonstrate large negative values ($E \to -\infty$, when $\Delta T \to 0$). On the other hand, when crystallization occurs on heating from the glass phase, E should demonstrate positive value whose magnitude for early stages of crystallization should be comparable to the E_D value. When one decreases the temperature of the melt crystallization or increases the temperature of the glass crystallization, the effective activation energy respectively increases or decreases toward zero.

The above analysis can be extended to predict the dependencies of the isoconversional activation energies on conversion. Expressing the rate of the nucleation-driven crystallization by the basic rate equation

$$\frac{d\alpha}{dt} = w(T) f(\alpha), \tag{3.46}$$

the isoconversional activation energy can be estimated as usual (see Eq. 1.13):

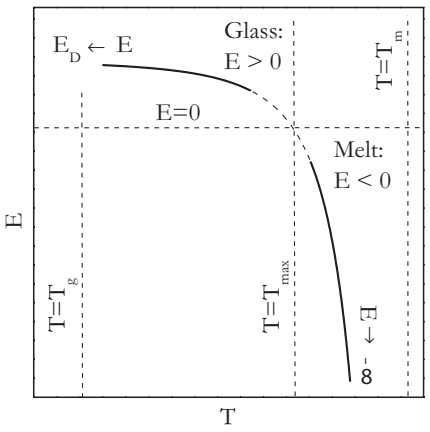

Fig. 3.33 Theoretical dependencies of the activation energy for the melt and glass crystallization predicted by Eq. 3.45

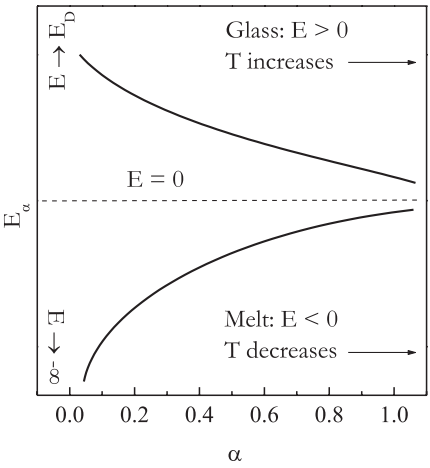

Fig. 3.34 Theoretically predicted dependencies of E_α on α for melt and glass crystallization. (Adapted from Vyazovkin [91] with permission of Elsevier)

$$E_\alpha = -R\left[\frac{\partial \ln(\mathrm{d}\alpha/\mathrm{d}t)}{\partial T^{-1}}\right]_\alpha . \tag{3.47}$$

By virtue of the isoconversional principle (Eq. 1.12), the right-hand side of Eq. 3.47 is equal to that of Eq. 3.45. It means that E_α has the same form as E in Eq. 3.45. Since an increase in α is equivalent to a decrease in T for the melt crystallization and to increase in T for the glass crystallization, the E_α versus α dependencies take the forms displayed in Fig. 3.34. Having the opposite signs, the E_α values for the melt and glass crystallization tend toward zero as crystallization progresses from $\alpha = 0$ to 1.

To conclude this section, two short comments need to be made about limitations of the above derivations. First, the derivations have been performed for a spherical, i.e., three-dimensional type of nucleus. Changing the assumption about the nucleus shape to a two-dimensional type, such as a disk, would introduce important changes into some of the equations [93]. For instance, ΔG^* would be inversely proportional to ΔG_V, not to $(\Delta G_V)^2$ as in the case of the three-dimensional type of nucleus (Eq. 3.36). Consecutively, $(\Delta T)^2$ in Eq. 3.44 would change to ΔT. Second, the derivations have been made under the assumption of homogeneous nucleation, i.e., when a nucleus is formed inside the melt phase. However, the nuclei can form on the substrate (e.g., solid impurity, container wall, etc.), i.e., heterogeneously. The free energy barrier of heterogeneous nucleation is substantially smaller than that of homogeneous nucleation. For example, when a spherical nucleus is formed homogeneously, the free energy barrier of its formation is proportional to the surface free energy of the entire surface of the sphere. However, when the nucleus is formed at the substrate, it assumes the shape of a spherical cup, which at the same radius has a smaller surface area than the whole sphere. As a result, the free energy barrier to heterogeneous nucleation, G^*_{het}, is always smaller than that for the homogeneous one, by some geometrical factor, $f(\Theta) < 1$:

$$\Delta G^*_{het} = \Delta G^* f(\Theta). \tag{3.48}$$

The magnitude of $f(\Theta)$ is determined by the contact angle, Θ, between the substrate and forming phase. For a spherical nucleus on a flat substrate, the geometrical factor is defined by the following equation: [3, 4, 93].

$$f(\Theta) = \frac{(2+\sin\Theta)(1-\cos\Theta)^2}{4}. \tag{3.49}$$

A detailed discussion of the geometrical factors for different type of nuclei and substrates is provided by Mandelkern [93].

3.6 Crystallization of Polymers

the crystal has only one manifestation of life, crystallisation, which afterwards has its fully adequate and exhaustive expression in the rigid form, the corpse of that momentary life.
Arthur Schopenhauer, The World as Will and Idea

3.6.1 Background

As any first-order transition, crystallization is accompanied by a significant enthalpy change that makes DSC a method of choice for measuring the overall rates of polymer crystallization [93, 94]. The overall kinetics of isothermal conversion from the amorphous (liquid or solid) to crystalline phase is commonly described in terms of the equation:

$$\alpha = 1 - \exp\left[-k(T)t^{\mathrm{m}}\right] \tag{3.50}$$

which is frequently called the Avrami equation [95–97]. In Eq. 3.50, t is the time, α is the extent of conversion from the amorphous to crystalline phase, m is the Avrami exponent that is associated with the crystallization mechanism, and $k(T)$ is the overall (macroscopic) rate constant. The latter is usually replaced with $k'(T) = [k(T)]^{1/\mathrm{m}}$ to keep the product in the brackets dimensionless. There are several techniques that allow Eq. 3.50 to be applied to nonisothermal conditions [93, 94].

It should be stressed that the rate constant in Eq. 3.50 does not have the Arrhenius temperature dependence. As long as the temperature range is sufficiently wide, the Arrhenius plots reveal substantial nonlinearity as seen in Fig. 3.35 that presents the $k'(T)$ values reported [98] for the melt and glass crystallization of poly(trimethylene terephthalate). It is easy to recognize that the presented plot is similar to the one (Fig. 3.31) derived theoretically from the Turnbull and Fisher equation (3.42). Needless to say that the use of such plots for estimating the activation energy would yield the value that varies with temperature in accord with Eq. 3.45 (Fig. 3.33).

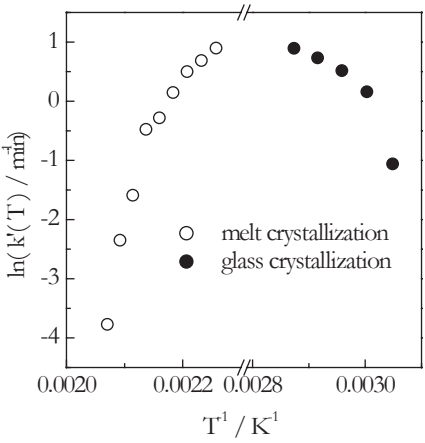

Fig. 3.35 Arrhenius plot for crystallization of poly(trimethylene terephthalate) from melt and crystalline phases. (The Avrami rate constants are taken from Hong et al. [98])

Speaking of estimating the activation energies for polymer crystallization, a special comment needs to be made about the widespread application of the Kissinger method [99, 100] to the melt crystallization data, i.e., data obtained on cooling. The method allows for a quick and simple evaluation of the activation energy by the following equation:

$$E = -R\frac{\mathrm{d}\ln(\beta / T_\mathrm{p}^2)}{\mathrm{d}T_\mathrm{p}^{-1}}, \tag{3.51}$$

where β is the heating rate, and T_p is the temperature of DSC (or differential thermal analysis, DTA) peak. Unfortunately, the application is so common that it is claimed sometimes that the method was developed for crystallization and that β in its equation is the cooling rate. None of that is true. As a matter of fact, neither of the two papers [99, 100] that introduce the method even contains the words "cooling" or "crystallization." Furthermore, it has been demonstrated [101] that the use of cooling rates in Eq. 3.51 is a mathematically invalid operation that results in evaluation of erroneous values of the activation energy. As far as the application of the method to the glass crystallization data (i.e., data obtained on heating), the limitation is that the method produces a single value of the activation energy for the whole temperature range whereas the value is likely to be temperature dependent.

Although the Avrami equation generally fits the polymer crystallization data quite well, one should remember that the model was developed having in mind crystallization of metals. Therefore, it does not account for any specifics of crystallization of long, flexible, and entangled polymer chains. For example, in Eq. 3.50, α is supposed to represent the absolute extent of crystallinity that changes from 0 (entirely amorphous phase) to 1 (fully crystalline phase). The metals readily attain fully crystalline state. However, crystallization of polymers results in the extents of crystallinity that are significantly smaller than 1, which is a direct consequence of the polymer chain dynamics. Thus, the application of the Avrami equation to poly-

mers requires an empirical adjustment, when the actual maximum extent of crystallinity is taken as $\alpha = 1$. In addition to the rate constant, the Avrami analysis yields the Avrami exponent, which according to the theory can take some specific values from ½ to 4. Note that even in this case, the values of m do not allow for singular mechanistic interpretation [93, 94]. It is also not uncommon when the m values vary markedly with temperature. All in all, the Avrami analysis is rather "a convenient representation of experimental data" [102] than a way of obtaining physical insights in the polymer crystallization kinetics.

A widely accepted kinetic theory of polymer crystallization was developed by Hoffman and Lauritzen [103, 104]. The theory makes use of the Turnbull–Fisher model (Eq. 3.42) and adjusts it to the chain folding mechanism that drives crystallization of polymers. The basic equation of the theory describes the temperature dependence of the growth rate of polymer spherulites as follows:

$$\Lambda = \Lambda_0 \exp\left(\frac{-U^*}{R(T - T_\infty)}\right)\exp\left(\frac{-K_g}{T\Delta T f}\right), \tag{3.52}$$

where Λ_0 is the preexponential factor, U^* is the activation energy of the segmental jump, $\Delta T = T_m - T$ is the supercooling, $f = 2T/(T_m + T)$ is the correction factor, and T_∞ is a hypothetical temperature where motion associated with viscous flow ceases that is usually taken 30 K below the glass transition temperature, T_g. The kinetic parameter K_g has the following form:

$$K_g = \frac{nb\sigma\sigma_e T_m}{\Delta h_f k_B}, \tag{3.53}$$

where b is the surface nucleus thickness, σ is the lateral surface free energy, σ_e is the fold surface free energy, T_m is the equilibrium melting temperature, Δh_f is the heat of fusion per unit volume of crystal, k_B is the Boltzmann constant, and n takes the value 4 for crystallization regime I and III, and 2 for regime II. The dependence of the growth rate on temperature passes through a maximum (Fig. 3.36) in similar fashion as the rate of nucleation (Fig. 3.32).

The parameter U^* is typically assumed to have the universal value 6.3 kJ mol^{-1} (i.e., 1.5 kcal mol^{-1}) [103]. This assumption in combination with little algebra affords Eq. 3.52 to be transformed to Eq. 3.54:

$$\ln\Lambda + \frac{U^*}{R(T - T_\infty)} = \ln\Lambda_0 - \frac{K_g}{T\Delta T f}. \tag{3.54}$$

Then K_g can be determined from the linear plot of the left-hand side of Eq. 3.54 against $(T\Delta T f)^{-1}$. The equation is known [103] to describe adequately the growth kinetics in a range of supercoolings as wide as 40–100 °C. This means that at least potentially both melt and glass crystallization kinetics can be described by a single set of the constant parameters U^* and K_g.

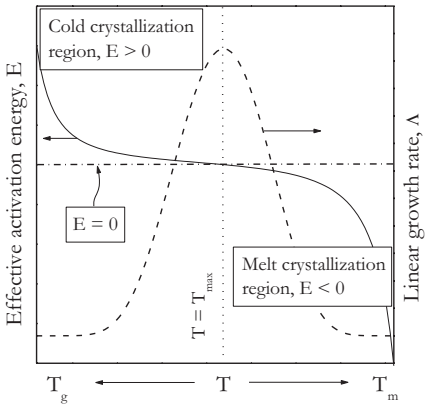

Fig. 3.36 Schematic presentation of the temperature dependencies for the growth rate (*dash line*) from Eq. 3.52 and the effective activation energy (*solid line*) from Eq. 3.60. (Adapted from Vyazovkin and Dranca [108] with permission of Wiley)

Equations 3.54 and 3.52 rely on the spherulite growth rate that is measured directly by using microscopy. This rate cannot be measured by DSC. The technique measures the heat flow of crystallization that is proportional to the overall growth rate. On the other hand, the heat flow is linked to the growth rate as follows: [105]

$$\Phi = \Delta h S \Lambda, \tag{3.55}$$

where Δh is the volumetric heat of crystallization and S is the total area of the growth surface. The problem here is the unknown value of S. Toda et al. [105] have demonstrated that it can be eliminated when determining the logarithmic derivative of the heat flow:

$$\frac{\mathrm{d}\ln\Phi}{\mathrm{d}T} = \frac{\mathrm{d}\ln\Lambda}{\mathrm{d}T}. \tag{3.56}$$

Equation 3.56 is remarkable because it establishes the equivalence of the temperature coefficients of the heat flow and the growth rate. Toda et al. [105, 106] have confirmed this equivalence experimentally for several polymers by applying TM DSC and microscopy to measure respectively the left- and right-hand sides of Eq. 3.56.

Equation 3.56 can easily be transformed into Eq. 3.57:

$$-R\frac{\mathrm{d}\ln\Phi}{\mathrm{d}T^{-1}} = -R\frac{\mathrm{d}\ln\Lambda}{\mathrm{d}T^{-1}}. \tag{3.57}$$

In DSC, the overall crystallization rate is determined as the ratio of the heat flow to the total heat of crystallization, ΔH, i.e.,

$$\frac{\mathrm{d}\alpha}{\mathrm{d}t} = \frac{\Phi}{\Delta H}. \tag{3.58}$$

Then, if in Eq. 3.57, the derivate of Φ is taken at a constant extent of conversion, it would yield an isoconversional value of the activation energy:

$$E_\alpha = -R\frac{\mathrm{d}\ln\Lambda}{\mathrm{d}T^{-1}}. \tag{3.59}$$

Substituting Λ from Eq. 3.52 into Eq. 3.59 and taking its respective derivative allows us to derive [107] a practically important equation:

$$E_\alpha = U^*\frac{T^2}{(T-T_\infty)^2} + K_\mathrm{g}R\frac{T_\mathrm{m}^2 - T^2 - T_\mathrm{m}T}{(T_\mathrm{m}-T)^2T}. \tag{3.60}$$

In this equation, the left-hand side represents an experimental temperature dependence of the effective activation energy derived by an isoconversional method. The right-hand side, however, is a theoretical dependence whose parameters U^* and K_g can be determined by fitting this dependence to the experimental one. Therefore, isoconversional analysis of the overall rate of DSC data can be used to extract the parameters of the Hoffman–Lauritzen theory that otherwise would have to be evaluated from the microscopy data on linear growth of the spherulites.

Analysis of the right-hand side of Eq. 3.60 suggests that the second term is negative in the temperature range between $\sim 0.618T_\mathrm{m}$ and T_m. The absolute value of this term quickly increases as temperature approaches T_m. This means that the effective activation energy of the melt crystallization should have very large negative values at small supercoolings as well as at low extents of conversions when the measurements are done on continuous cooling. As temperature of the melt crystallization decreases further away from T_m, the effective activation energy should increase toward zero. The first term, on the other hand, is always positive. Its value increases as temperature approaches T_∞. Therefore, as the temperature of the glass crystallization increases, the effective activation energy should decrease toward zero. The overall temperature dependence of the effective activation energy is shown in Fig. 3.36 [108].

3.6.2 Isoconversional Treatment

The first step in isoconversional analysis of the polymer crystallization data is identifying an appropriate isoconversional method. The major point of concern is the treatment of the melt crystallization data, i.e., the data obtained on cooling. It has been emphasized in Sect. 2.1.2 (Figs. 2.6, 2.10) that the rigid integral methods should not be used for treating the data obtained on cooling. Adequate isoconversional methods include the flexible integral methods or the differential method of Friedman.

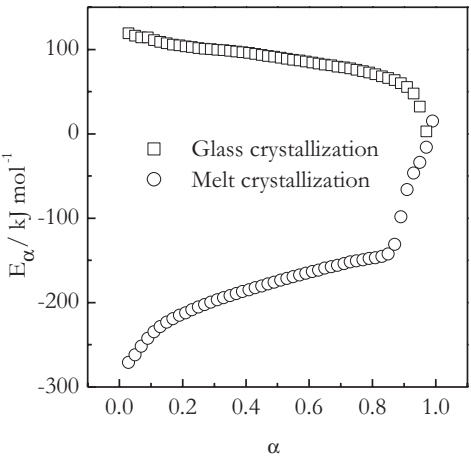

Fig. 3.37 Isoconversional values of the effective activation energy for glass and melt crystallization of poly(ethylene terephthalate). (Adapted from Vyazovkin et al. [107, 108] with permission of Wiley)

Once an appropriate method is selected, it can be applied to a set of DSC curves collected at several heating or cooling rates. As a result, one obtains a dependence of the effective activation energy on the extent of conversion from the amorphous to crystalline state. Example of such dependencies for crystallization of PET is shown in Fig. 3.37. In agreement with the earlier discussion (Fig. 3.36), the activation energies for the melt crystallization are negative and for the glass crystallization positive. It is also seen that in both cases the E values tend to zero as crystallization progresses from $\alpha=0$ to 1. Again, this is consistent with the temperature-dependent trends for E presented in Fig. 3.36. Recall that an increase in α represents an increase in temperature for the glass crystallization and a decrease in temperature for the melt crystallization.

In order to be able to parameterize the obtained isoconversional activation energies in terms of the Hoffman–Lauritzen theory, one needs to switch from a dependence of E_α versus α to a dependence of E_α versus T. Since any given value α is reached at different temperatures, depending on the heating (or cooling) rate (Fig. 1.8), the respective set of temperatures is replaced with a single mean value. Then, by replacing each value of α with the mean temperature related to it (Fig. 3.38), one obtains a dependence of E_α versus T.

The E_α versus T dependence for the melt crystallization of PET is shown in Fig. 3.39. As follows from Fig. 3.36, the E_α values are expected to be negative at temperatures below T_{max} that is experimentally found for PET in the region 170–190 °C [109]. A remarkable feature of the dependence is a break point at ~475 K (i.e., ~202 °C) that signals a change in the crystallization mechanism. For isothermal PET crystallization, Lu and Hay [110] and Rahman and Nandi [111] have reported a change in the crystallization mechanism revealed as a break point in the Hoffman–Lauritzen plot (Eq. 3.54) at the respective temperatures 217 and 236 °C. Also, Okamoto et al. [112] have observed a change in the crystallization regime at 202 °C.

Because of the change in the crystallization mechanism, the higher temperature ($T>475$ K) and lower temperature ($T<475$ K) portions of the E_α versus T dependence should be analyzed separately. It means that Eq. 3.60 should be fitted individ-

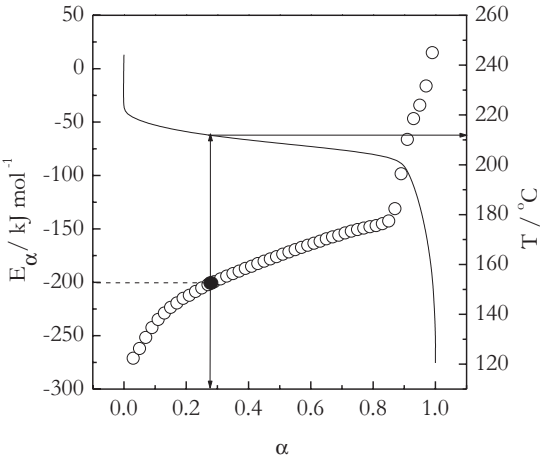

Fig. 3.38 Converting dependence of E_α versus α (*circles*) to dependence of E_α versus T. *Solid line* represents a dependence of α on the mean temperature. $E_\alpha = -200$ kJ mol^{-1} corresponds to $\alpha = 0.28$, which, in turn, corresponds to the mean temperature 212 °C. (Adapted from Vyazovkin and Sbirrazzuoli [107] with permission of Wiley)

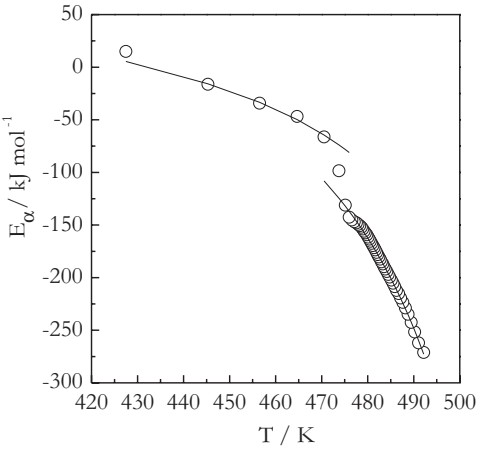

Fig. 3.39 Dependence of the effective activation energy on the mean temperature. *Solid lines* represent fits of Eq. 3.60. (Adapted from Vyazovkin and Sbirrazzuoli [107] with permission of Wiley)

ually to the two portions of the experimental E_α versus T dependence. The computation requires the values of T_g and T_m which are 342 and 553 K, respectively [113].

The fits result in the K_g and U^* values shown in Table 3.2 that also collects the values reported in the literature [110, 111, 114–118] for isothermal crystallization of PET. There is obviously a considerable spread in the literature values. However, the values obtained from fitting Eq. 3.60 to the experimental E_α versus T dependence appear to be reasonably consistent with the reported values, although seem to be on the low side. At least partially, this is because Eq. 3.60 treats both K_g and U^* as variables whereas most of the calculations in Table 3.2 have been done by setting U^* in Eq. 3.54 to the constant value 6.3 kJ mol^{-1} and fitting K_g. Although 6.3 kJ mol^{-1} is used widely as "the universal value," Hoffman et al. [103] have found that for a set of polymers studied, the best-fit values of U^* vary between 4 and 17 kJ mol^{-1}. In addition, they have noted that increasing the value of U^* results in evaluating a

Table 3.2 Hoffman–Lauritzen parameters for crystallization of PET

$K_g \times 10^{-5}$ (K^2)		U^* (kJ mol^{-1})	Ref.
Regime I/III	Regime II		
5.0	2.5	6.3	[110]
8.7	6.1	6.3	[111]
12.80[a]		12.75	[114]
	2.8	6.3	[115]
	3.0	6.3	[116]
3.7[b]		6.3	[117]
	2.3	6.3	[118]
3.2	1.9	4.3/2.3	Equation 3.60

[a] *Identified as* regime III
[b] *Regime is not identified*

larger value of K_g. Therefore, fitting both K_g and U^* seems like a better approach that should result in more reliable estimates of these values.

The use of Eq. 3.60 yields the K_g values 3.2 and 1.9×10^5 K^2 for respectively higher and lower temperature portions of E_α versus T dependence. It is noteworthy that the higher temperature portion gives the K_g value that is 1.7 times larger than the value related to the lower temperature portion. The ratio is very close to the theoretical ratio 2 that represents a change in the crystallization mechanism from regime I to regime II [103]. This is an important clue regarding the mechanism of crystallization.

It was mentioned earlier that the Hoffman–Lauritzen equation holds for supercoolings as large as 100 °C that makes it potentially possible to fit both melt and glass crystallization kinetics with one set of the K_g and U^* parameters. Figure 3.40 presents the E_α versus T dependencies for crystallization of PET glass and melt. The

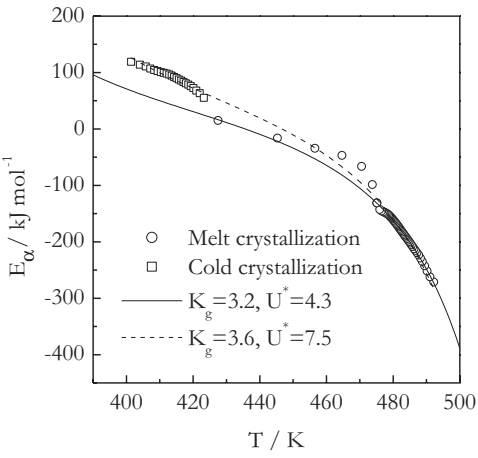

Fig. 3.40 Experimental E_α versus T data for melt (*circles*) and glass (*squares*) crystallization of PET. *Solid line* represents a fit for the melt data. *Dashed line* has been obtained by fitting combined (*melt and glass*) crystallization data. (Reproduced from Vyazovkin and Dranca [108] with permission of Wiley)

E_α versus T dependence for the glass crystallization is obtained from the E_α versus α data (Fig. 3.37) in the same manner as explained earlier for the melt crystallization data. It is seen that the higher temperature portion of the E_α versus T data for the melt crystallization appears to follow the same trend as the E_α versus T data for the glass crystallization.

Fitting Eq. 3.60 to the combined dataset yields the following parameters: $K_g = 3.6 \times 10^5$ K^2 and $U^* = 7.5$ kJ mol^{-1}. Both values have increased relative to their counterparts values obtained from the melt data (Table 3.2). The value of K_g has increased by a little over 10%. Its ratio to the regime II $K_g = 1.9 \times 10^5$ K^2 has become even closer to 2. The U^* value has increased significantly by over 70%. Note that the obtained value of U^* has moved much closer to the universal value 6.3 kJ mol^{-1}. It seems logical to expect that adding the cold crystallization data may improve the accuracy of the U^* value. The cold crystallization kinetics is limited primarily by diffusion so that cold crystallization data contain mostly information about this process and, thus, should afford its better description in the form of a more accurate value of U^*. More importantly, this and other examples [108, 119, 120] clearly demonstrate that both melt and glass crystallization kinetics can be fitted successfully with a single set of the Hoffman–Lauritzen parameters.

3.7 Melting of Polymers

the damsel took the lute, and tuned its strings, and played upon it in a manner that would melt iron

The story of Nur-Ed-Din and Enis-El-Jelis, One Thousand and One Nights

3.7.1 Background

A most common approach to the process of melting is based on thermodynamics. It suggests that melting occurs nearly instantaneously at an equilibrium temperature that remains constant throughout the crystal-to-melt conversion because the heat supplied to the crystal phase is converted to the entropy of the liquid phase. However, it has long been known that melting occurs at a finite rate, whose magnitude increases with the superheating, i.e., the difference between the actual and equilibrium temperature. This feature of the melting process is reminiscent of nucleation, whose rate is exponentially proportional to the supercooling (Sect. 3.5). The exponential dependence of the rate on the superheating has been demonstrated by Toda et al. [121] for melting of several polymers, including PET and poly(ε-caprolactone) (PCL). This prompted Toda et al. [121] to propose a model of nucleation-driven kinetics of polymer melting. The aforementioned exponential dependence has been reported in several other publications [122–126].

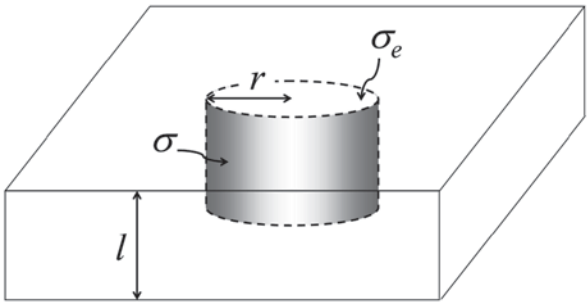

Fig. 3.41 Schematic depiction of a cylindrical nucleus of the radius r formed inside a lamellar crystal of the thickness l. σ and σ_e represent the free energy of the lateral and the fold surface, respectively

The melt nucleation model is derived as follows [127]. Similar to Eq. 3.33, the free energy barrier to the formation of a melt nucleus consists of the surface and volume components:

$$\Delta G = \Delta G_S S + \Delta G_V V, \tag{3.61}$$

where ΔG_S and ΔG_V are the free energy per unit area and unit volume, respectively, and S and V are the nucleus area and volume. The melt nucleus is assumed to have the shape of a cylinder and form inside a lamellar crystal whose thickness is l (Fig. 3.41). The assumption of the cylindrical shape is quite common for crystalline polymers because they crystallize by chain folding so that a crystalline nucleus presents itself as several chain folds of about the same height. Under this assumption, Eq. 3.61 can be written as:

$$\Delta G = 2\pi rl\sigma - 2\pi r^2\sigma_e + \pi r^2 l\Delta G_V, \tag{3.62}$$

where the first and second terms represent respectively the lateral (side) and folding (top and bottom) surface free energy of a cylinder. The second term is negative because during melting, the folding surface disappears, merging with the surrounding melt. The third term represents the volume free energy. Its value depends on temperature as follows:

$$\Delta G_V = \Delta H_f \frac{T_m^0 - T}{T_m^0}. \tag{3.63}$$

Equation 3.63 is obtained the same way as Eq. 3.38, the only difference being that for melting $\Delta H_V = \Delta H_f$. When lamellar crystal is sufficiently thin (l is very small), it can melt at temperature T_m below reaching the equilibrium melting temperature T_m^0. The temperature difference is determined by the Gibbs–Thomson equation: [128]

$$T_m^0 - T_m = \frac{2\sigma_e T_m^0}{l\Delta H_f}. \tag{3.64}$$

It follows from Eq. 3.64 that

$$2\sigma_e = l\Delta H_f \frac{T_m^0 - T_m}{T_m^0}. \tag{3.65}$$

Substitution of the right-hand sides of Eqs. 3.63 and 3.65 into Eq. 3.62 followed by some rearrangements yields:

$$\Delta G = 2\pi rl\sigma - \pi r^2 l\Delta H_f \frac{T - T_m}{T_m^0}. \tag{3.66}$$

Taking the derivative of ΔG with respect to r and setting it to zero allows one to determine the critical radius of the nucleus:

$$r^* = \frac{\sigma T_m^0}{\Delta H_f \Delta T}, \tag{3.67}$$

where $\Delta T = T - T_m$ is superheating with respect to the nonequilibrium melting temperature, T_m. Substitution of r^* into Eq. 3.66 gives rise to the magnitude of the nucleation barrier to the polymer crystal melting:

$$\Delta G^* = \frac{\pi l\sigma^2 T_m^0}{\Delta H_f \Delta T}. \tag{3.68}$$

Then ΔG^* can be substituted into Eq. 3.41 for the nucleation rate constant. Assuming that the temperature dependence of ΔG^* is determined by ΔT alone, the nucleation rate constant can be written as:

$$w(T) = w_0 \exp\left(\frac{-\Delta G^*}{RT}\right) = w_0 \exp\left(\frac{-A}{RT\Delta T}\right), \tag{3.69}$$

where A is a constant that includes all parameters from ΔG^* (Eq. 3.68) but ΔT.

According to Toda et al. [121], the overall rate of polymer melting can be described by the following equation:

$$\frac{d\alpha}{dt} = -w(T)\alpha, \tag{3.70}$$

where α is the crystalline fraction that changes from 1 to 0 as crystals melt. By replacing α with $1-\alpha$, Eq. 3.70 can be easily rewritten for the extent of conversion from crystal to melt that:

$$\frac{d\alpha}{dt} = w(T)(1-\alpha). \tag{3.71}$$

This is a well-familiar form of a first-order rate equation. Equation 3.71 can now be used to derive an equation for the isoconversional activation energy. As usual, it is done by taking the logarithmic derivative of the rate (Eq. 3.71) at a constant extent of conversion. This leads to Eq. 3.72: [129]

$$E_\alpha = -R\left[\frac{\partial \ln\left(\mathrm{d}\alpha / \mathrm{d}t\right)}{\partial T^{-1}}\right]_\alpha = A\left[\frac{1}{\Delta T} + \frac{2T}{(\Delta T)^2}\right]. \tag{3.72}$$

Note that because the derivative is taken at a constant extent of conversion, the obtained result is independent of the type of the reaction model used in Eq. 3.71.

In Eq. 3.72, E_α is the temperature-dependent activation energy estimated by an isoconversional method. The right-hand side of this equation represents a theoretical E versus T dependence determined by a single parameter A. By its meaning, A is always positive and so is the expression in the brackets. At very early stages of meting, when temperature is just above the nonequilibrium melting temperature (T_m), ΔT is close to zero so that E_α can take on extremely large values. However, the E_α values would decrease as ΔT continues to increase throughout the melting process. Overall, the nucleation model predicts that the effective activation energy of melting should exhibit a decreasing dependence on temperature. Also, fitting the theoretical E versus T dependence to the experimental one should afford estimating the parameter A and possibly the lateral surface free energy, if other parameters composing A are known.

3.7.2 Isoconversional Treatment

DSC is an efficient way of measuring the polymer melting kinetics. However, a straightforward application of an isoconversional method to polymer melting data presents a certain challenge. The problem is that the DSC melting peaks shift very little when changing the heating rate. For example, a tenfold increase in the heating rate shifts the DSC melting peak for PET by less than 3 °C (Fig. 3.42).

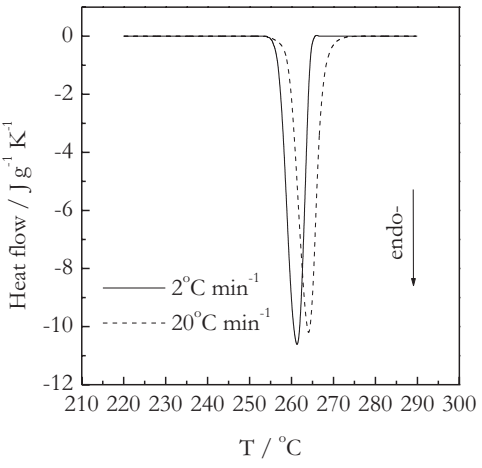

Fig. 3.42 DSC curves of PET melting at the heating rates 2 and 20 °C min^{-1}. Heat flow is normalized to the sample mass and heating rate. *PET* poly (ethylene terephthalate). (Adapted from Vyazovkin et al. [129] with permission of Wiley)

If one spreads this interval evenly between, say, five heating rates ranging from 2 to 20 °C min^{-1}, the shift in DSC peaks related to two successive heating rates would be about ~0.7 °C. For an isoconversional method to work successfully, the temperatures related to the same conversion, T_α, must increase systematically with increasing β for each value of α. This condition is hard to fulfill at the smallest and largest values of α because the shifts in T_α are so small that they become comparable to the T_α variation associated with the selection of the DSC peaks baseline.

Nonetheless, the baseline selection and adjustment does not affect practically the DSC peak temperature. This brings about the idea [129] of adapting the Kissinger method [99, 100] for estimating the experimental dependence of E versus T. The Kissinger method (Eq. 3.51) estimates the effective activation energy from the shift of the DSC peak temperature (T_p) with the heating rate. It should be noted that the method is not exactly isoconversional, i.e., the conversion related to the peak temperature may not be the same value at different heating rates [130]. Experimental data need to fulfill the isoconversional condition because this is the condition under which the theoretical E versus T dependence is derived (Eq. 3.72). The condition is easy to check by determining the conversion at T_p from the actual DSC peaks. For example, the isoconversional condition appears to be fulfilled quite satisfactorily for melting of PET and PCL because the respective conversions do not show any systematic dependence on the heating rate giving rise to the value 0.59 ± 0.02 [129] and 0.61 ± 0.03 [131]. Thus, the use of the Kissinger method for estimating the experimental E versus T dependence would be justified.

The Kissinger plots for melting of PET and PCL are presented in Fig. 3.43. It is immediately clear that the plots are nonlinear. Since at any given temperature the slope of this plot is the effective activation energy, it can be concluded that the effective activation energy of the melting process is temperature dependent. Fur-

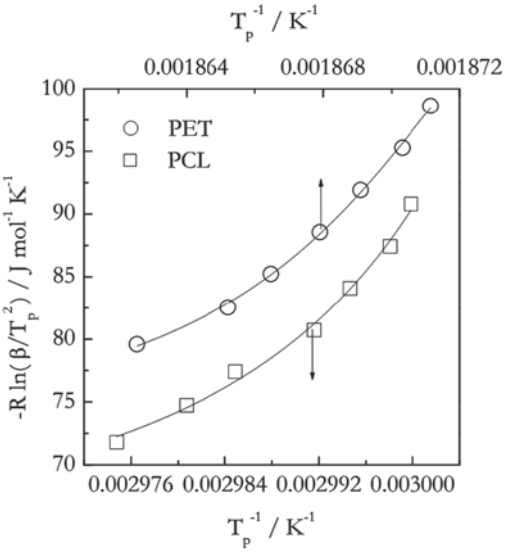

Fig. 3.43 The Kissinger plots for melting of PET and PCL. The *solid lines* represent interpolation of the experimental points. *PET* poly(ethylene terephthalate), *PCL* poly(ε-caprolactone). (Adapted from Vyazovkin et al. [129, 131] with permission of Wiley)

thermore, the effective activation energy decreases with increasing temperature as predicted by Eq. 3.72. This certainly lends support to the nucleation model because the Kissinger plot is obtained directly from the experimental data without making any assumption about nucleation.

In order to convert the Kissinger plot to the experimental E versus T dependence, one needs to differentiate the plot numerically and then replace the reciprocal temperature with temperature. To get around the problems of dealing with noisy numerical derivative of experimental data, the Kissinger plot can be replaced with some interpolating function. Differentiation of the latter would result in smooth numerical derivative.

The E versus T dependencies derived from the Kissinger plots for melting of PET and PCL are shown in Fig. 3.44. A striking feature of these dependencies is the enormous values of the effective activation energy. Lippits et al. [132] have reported similarly large values for melting of ultrahigh molecular weight polyethylene. This fact has been rationalized [132] by hypothesizing that detachment of polymer chain from the crystalline surface occurs in highly cooperative manner, i.e., by simultaneously breaking multiple bonds. However, the nucleation model suggests (Eq. 3.72) that the absolute value of E cannot be interpreted directly as the energy barrier height. Furthermore, interpretation of the large magnitude of the activation energy does not require invoking the hypothesis of cooperativity. Instead, the nucleation model provides a straightforward explanation that the E value is necessarily large because in Eq. 3.72 the ΔT is very small.

Fitting of the theoretical E versus T dependence (Eq. 3.72) to the experimental one requires estimating the nonequilibrium melting temperature because it is a part

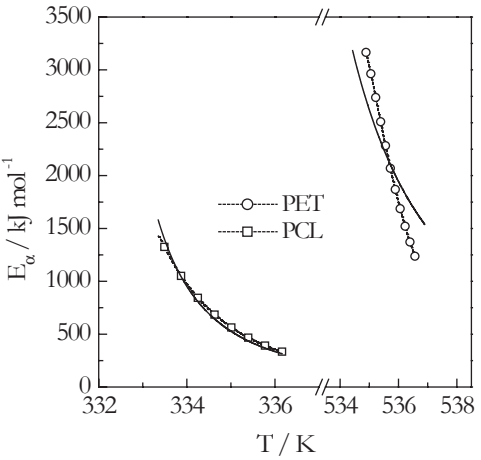

Fig. 3.44 Temperature dependence of the effective activation energy for melting of PET and PCL. Points connected by *dash line* represent the experimental dependence derived from the Kissinger plot. The *solid lines* are fits of Eq. 3.72. *PET* poly(ethylene terephthalate), *PCL* poly(ε-caprolactone). (Adapted from Vyazovkin et al. [129, 131] with permission of Wiley)

of the ΔT value. An estimate of this value is obtained from individual DSC peaks as an extrapolated onset temperature, $T_{m,\beta}$. The $T_{m,\beta}$ value depends on the heating rate, β. A heating rate-independent value is found by extrapolation of the $T_{m,\beta}$ values to $\beta = 0$, using an equation proposed by Illers: [133]

$$T_{m,\beta} = T_m + a\beta^{0.5}. \tag{3.73}$$

The intercept of the linear plot of $T_{m,\beta}$ against $\beta^{0.5}$ yields the value of T_m that can be used in fitting of Eq. 3.72 to the experimental E versus T dependence.

The fits of Eq. 3.72 to the experimental E versus T dependencies derived from the Kissinger plots for melting of PET and PCL are seen in Fig. 3.44. The fits are quite satisfactory, considering that Eq. 3.72 has only one adjustable parameter. The estimated values of the parameter A are 92 ± 4 (PET) and 11.9 ± 0.2 (PCL) kJ K mol^{-1}. The value can be used to estimate the interfacial free energy, σ. It should be noted that ΔG^* in Eq. 3.68 is in joules, whereas A is estimated (Eq. 3.72) from the values of E which are in joules per mole. With regard to this, A takes the following form:

$$A = \frac{N_A \pi l \sigma^2 T_m^0}{\Delta H_f}, \tag{3.74}$$

where N_A is the Avogadro number, 6×10^{23} mol^{-1}. Solving Eq. 3.74 for σ yields:

$$\sigma = \sqrt{\frac{A \Delta H_f}{N_A \pi l T_m^0}}. \tag{3.75}$$

For polymers, the values of T^0_m and ΔH_f are available from various literature sources, e.g., from Wunderlich [113]. For PET, $T^0_m = 553$ K and $\Delta H_f = 2.1 \times 10^8$ J m^{-3}. For PCL, according to the literature data collected by Sasaki [126], $T^0_m = 342.2$ K and $\Delta H_f = 1.9 \times 10^8$ J m^{-3}. The lamellar thickness, l, can be estimated at T_m by the Gibbs–Thomson equation (3.64) from the literature values [107, 126] of the fold surface free energy σ_e. For both polymers, l is about 15 nm [129, 131]. By inserting the above values in Eq. 3.75, one estimates the σ values to be 1.1×10^{-3} J m^{-2} (PET) and 5.1×10^{-4} J m^{-2} (PCL). Unexpectedly, both of these values are about an order of magnitude smaller than the values estimated from crystallization data: 1.2×10^{-2} J m^{-2} for PET [107] and 8.2×10^{-3} J m^{-2} for PCL [126]. A similar observation has been made in the original paper [121] by Toda et al., who found from their melting data that the Thomas–Staveley ratio [134] is about an order of magnitude smaller than is typically found from crystallization data on a variety of polymers. When applying the nucleation model to melting of PCL, Sasaki [126] has also found the σ value to be an order of magnitude smaller than that determined from crystallization data. It appears that the analysis of the polymer melting kinetics in terms of the nucleation model yields consistently the values of the lateral surface free energy which is about an order of magnitude smaller than that derived from crystallization kinetics.

The observed difference can be rationalized by considering the difference in the nature of the nucleation during crystallization and melting. If no foreign phase is present, crystallization occurs by homogenous nucleation throughout the whole melt phase. Melting, on the contrary, is a surface process [135–137]. The nuclei of the melt phase are formed at the interface, i.e., heterogeneously. The difference in the nature of homogeneous and heterogeneous nucleation entails significant energetic differences. As discussed earlier (Sect. 3.5, Eq. 3.48), the free energy barrier to heterogeneous nucleation, G^*_{het} is always smaller than that for the homogeneous one by some geometrical factor, $f(\Theta)$. For a cylindrical nucleus on a flat substrate, the geometrical factor is as follows: [93, 138]

$$f(\Theta) = \frac{(\Theta - \frac{1}{2}\sin 2\Theta)}{\pi}. \tag{3.76}$$

Note that the value of A (Eq. 3.74) corresponds to the free energy of homogenous nucleation. Thus, a small estimate of the A value unavoidably results in an unusually small value of σ (Eq. 3.75). On the other hand, if A is to be derived from the free energy of heterogeneous nucleation, the right-hand side of Eq. 3.74 would have to be multiplied by $f(\Theta)$. Then, a small value of A determined experimentally can be explained naturally by a small value of $f(\Theta)$ without invoking any changes in σ. According to Eq. 3.75, an order of magnitude decrease in σ would result from a two orders of magnitude decrease in A. This would be equivalent to $f(\Theta)$ being around 0.01. The respective contact angle estimated by Eq. 3.76 would be roughly 20°. It should be remarked that when liquid is in contact with solid of the same kind, the contact angle can be as small as a few degrees [139]. Overall, it appears that the polymer melting kinetics is consistent with the nucleation model, although it can be improved further by treating the process as heterogeneous nucleation.

3.8 Solid–Solid Transitions

The nature of the universe loves nothing so much as to change the things that are and to make new things like them. For everything that exists is in a manner the seed of that which will be

Marcus Aurelius, Meditations

3.8.1 Background

The solid–solid transitions are quite common in ionic [6, 7] and molecular [8] crystalline compounds. They represent transitions between different crystalline forms (polymorphs) of the same compound. For example, on heating above ~125 °C, ammonium nitrate crystal is known to change its crystalline structure from tetragonal to cubic lattice (Fig. 3.45) [140]. If in the cubic lattice, all three sides are perpen-

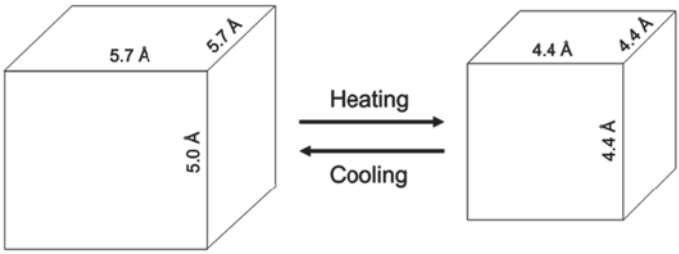

Fig. 3.45 Schematic depiction of the lattice rearrangement during the tetragonal to cubic solid–solid phase transition in ammonium nitrate. Side lengths are taken from crystallographic data [140]

dicular to each other and of the same size, in the tetragonal lattice, all sides are perpendicular but only two of them remain of equal size. Although the molecular composition of the solid compound remains unchanged during the transition, the distances between the atoms change. While may seem subtle, these changes are very important as they affect numerous physical properties of a crystalline solid.

The solid–solid phase transitions are more diverse and complex than the transitions involving the fluid media. If a liquid or gas exists in one disordered form, crystals are found in 230 space groups that represent different spatial configurations of a crystal. In terms of the rotational symmetry, crystals fall in seven different types: triclinic, monoclinic, orthorhombic, rhombohedral, tetragonal, hexagonal, and cubic [18]. This is the order in which the symmetry increases. On heating, the solid–solid transitions typically occur in the direction of increasing the symmetry.

In accord with Ehrenfest's classification, the solid–solid transitions can be designated [6–8] as being first and second order. However, the existence of second-order solid–solid transitions is a subject of significant controversy [141]. It appears that the condition for second-order transitions to proceed without changes in the enthalpy (or other first-order derivatives of the Gibbs energy) is a too stringent idealization. For example, the condition is practically satisfied by the so-called lambda transitions [6, 7] that demonstrate a discontinuity in the heat capacity (i.e., second-order derivative of the Gibbs energy) and tend to have very small enthalpy, which, however, may be not good enough to claim the value being exactly zero.

From the thermodynamic standpoint, first-order solid–solid state transitions occur at temperature, T_0, which is the intersection point of the G versus T curves for two solid phases (Fig. 3.46). The crystalline phases are commonly identified by roman numerals in order of their appearance on cooling from the melt state. That is, the highest temperature phase would be identified as phase I. As in the case of other first-order transitions (Fig. 3.1), heating across the equilibrium temperature means an abrupt increase in the slope of the G trace. Therefore, both enthalpy and entropy increase in accord with respective Eqs. 3.2 and 3.1. This means that the solid–solid phase transition is endothermic on heating and exothermic on cooling. The volume also undergoes a significant change during the transition, but it can increase as well as decrease.

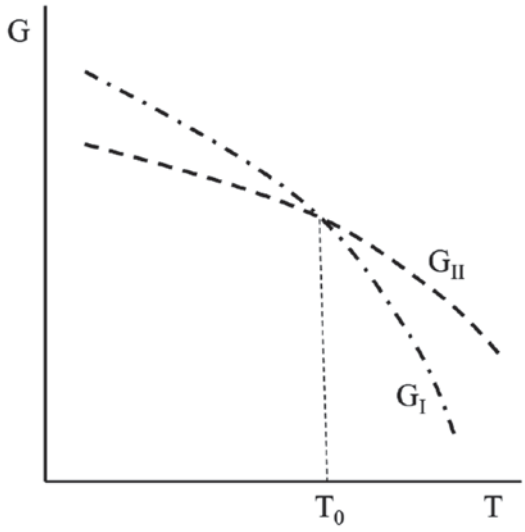

Fig. 3.46 Temperature dependence of the Gibbs energy for high temperature phase I (*dash-dot line*) and low temperature phase II (*dash line*). T_0 is the equilibrium temperature of transition between the phases

Note that the increase in entropy does not contradict to the aforementioned increase in the symmetry that also takes place on heating. The notion of the symmetry is related to the spatial arrangement of the molecules, atoms, or ions inside a crystal, whereas the entropy refers to the vibrational motion of these species around their positions in the crystalline lattice. As temperature rises, the crystalline lattice has to change to provide the medium that can accommodate increasing amplitude of the vibrations. Initially, it is accomplished by expanding and ultimately by rearranging the lattice. Apparently, a more symmetrical lattice provides the medium that affords more degrees of freedom for degenerate vibrations, therefore, putting fewer constraints on the vibrational motion.

By its meaning, the transition temperature, T_0, is the temperature at which two crystalline phases can coexist in equilibrium. It should be remarked that due to the nature of the solid–solid transitions, this temperature is difficult to pinpoint precisely. The solid–solid transitions, at least those of first order, occur by the nucleation mechanism. This means that the rate of transition is zero at T_0, but increases as temperature deviates from T_0. In other words, the transition on heating involves superheating and transition on cooling involves supercooling. As a result, there is a significant gap between the temperatures, at which the transition on heating and on cooling becomes detectable. An example of the temperature hysteresis in the solid-state transition on heating and cooling is seen in Fig. 3.47. For the transition between the phases I (cubic) and II (tetragonal) in ammonium nitrate, the gap is about 15 °C. That is, the equilibrium transition temperature in this case can be found anywhere between 113 and 128 °C.

The situation with establishing the equilibrium temperature for the solid–solid transition obviously is quite different from that for the solid–liquid transition. As discussed earlier, the transition from a crystalline solid to liquid (i.e., melt) can

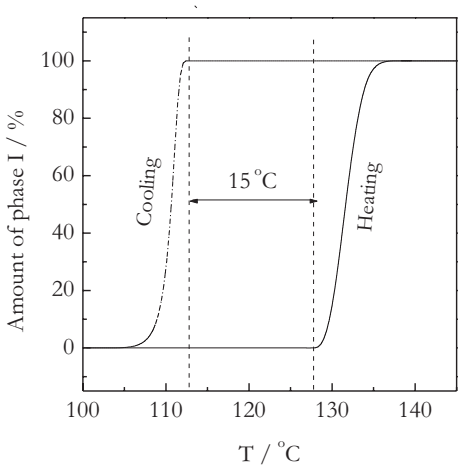

Fig. 3.47 Hysteresis in transition between phase I and II of ammonium nitrate measured on heating (*solid line*) and cooling (*dash-dot line*) at 20 °C min^{-1}

occur via nucleation (Sect. 3.7) in the same manner as the reverse transition from melt to crystal, i.e., crystallization (Sect. 3.6). However, the superheating during melting is normally negligibly small. Melting starts from the surface, and because the surface possesses higher molecular mobility, the surface layer melts before temperature reaches the bulk melting temperature. In a sense, the crystal surface is pre-nucleated so that the melt layer grows very rapidly when temperature reaches the equilibrium temperature of melting, T_m. This is the only reason why T_m provides an accurate estimate for the temperature at which a crystal can coexist in equilibrium with its melt.

The kinetics of the solid–solid transitions is generally consistent with the Turnbull–Fisher nucleation model [92]. The temperature dependence of the transition rate has a rather complex form shown in Fig. 3.48. One can obtain this dependence

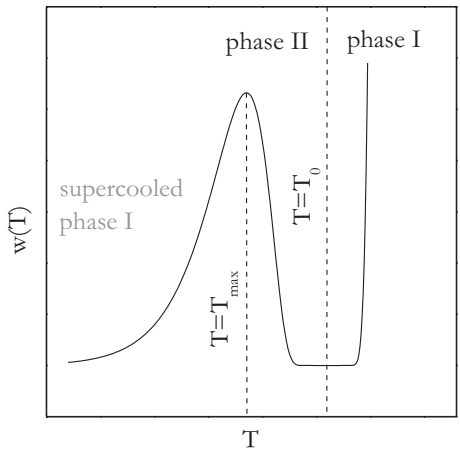

Fig. 3.48 Nucleation rate dependence derived from the Turnbull–Fisher equation (Eq. 3.44)

directly from Eq. 3.44 by varying temperature around T_0. At this temperature, the high temperature phase I is at equilibrium with the low temperature phase II. In the vicinity of T_0, the rate of the solid–solid transition is close to zero. Heating a solid above T_0 accelerates the transition from the phase II to the phase I. The temperature dependence of the rate is positive above T_0. If fitted to the Arrhenius equation, it would yield positive activation energy. When cooled below T_0, the phase I transforms to the phase II. The rate of the transition increases with decreasing temperature. Below T_0, the temperature dependence of the rate is negative. Fitting it to the Arrhenius equation would result in negative activation energy.

An interesting feature of the temperature dependence of the solid–solid transition rate is the existence of the rate maximum (Fig. 3.48) that can be found at larger supercoolings. The maximum is due to the same reason as the one observed for the rate of crystallization (Fig. 3.36). It is the deceleration of the molecular mobility (diffusion) with decreasing temperature. If the transition from the phase I to the phase II is fast, the maximum may be impossible to detect experimentally, unless one uses very fast rates of cooling. On the other hand, some of the transitions from the high- to low-temperature phase are very slow. In this circumstance, cooling of the phase I may not result in the formation of the phase II. In terms of the G versus T diagram (Fig. 3.46), the phase I continues to follow the G_I trace below T_0. When temperature drops below T_{max}, the phase I freezes kinetically in the supercooled metastable state. While metastable, the supercooled phase can exist in this state indefinitely. Recall De Beers' slogan "a diamond is forever," although at ambient temperature and pressure, diamond is a metastable crystalline form of carbon and it is bound thermodynamically to transform to graphite.

On heating, the supercooled phase I transforms to the phase II. This process normally occurs below T_{max} (Fig. 3.48). In that region, the temperature dependence of the phase transition rate is positive. When fitted to the Arrhenius equation, it would yield positive activation energy. Note that this process would be exothermic because as seen from Fig. 3.46 G_I trace has a larger slope than G_{II} so that the enthalpy for the phase I is larger than for the phase II. For a similar reason, the process would be accompanied by a decrease in entropy.

Villafuerte-Castrejon and West [142] provide a good example of the kinetics of the solid–solid phase transition between β and γ forms of Li_2ZnSiO_4 measured in all three regions (Fig. 3.49). The high-temperature γ form is at equilibrium with the low-temperature β form at around 880 °C. Heating the compound above this temperature causes the transition from the β to γ form. The rate constant, k, increases with temperature. The slope of the Arrhenius plot of log k versus T^{-1} is negative that corresponds to positive value of E. On cooling below 880 °C, the γ form converts to the β form. The rate constant increases with decreasing temperature that is consistent with the E value being negative. Finally, the γ form can be prepared in a metastable state by quick cooling below T_{max}, which is ~800 °C. Heating the metastable γ form initiates its conversion to the β form, which is the stable form below 880 °C. The respective Arrhenius plot for this transition gives rise to positive E.

Since the Turnbull–Fisher model (Eq. 3.44) is capable of correctly predicting the temperature dependence of the solid–solid transition rate, it can also be used to

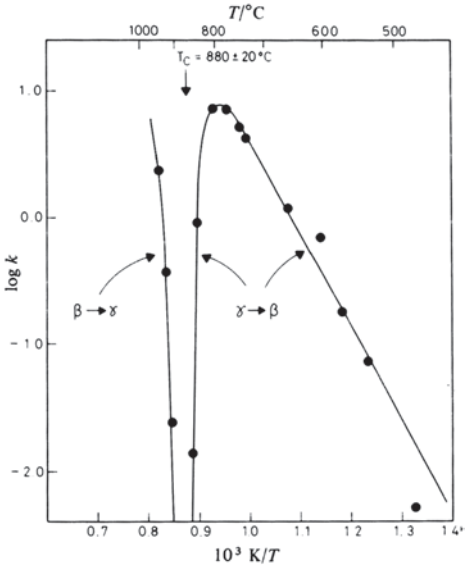

Fig. 3.49 Arrhenius plot for the kinetics of the phase transition between the β and γ forms of Li_2ZnSiO_4. T_c is the equilibrium transition temperature. (Reproduced from Villafuerte-Castrejon and West [142] with permission of RSC)

predict the temperature dependence of the effective activation energy. The equation that can be used for this purpose is Eq. 3.45. Variation of temperature around T_0 produces the E versus T dependence displayed in Fig. 3.50. It is seen that the dependence has a discontinuity at T_0. On heating above T_0, the activation energy for the transition from the phase II to I decreases from $+\infty$ down to the activation energy of diffusion E_D. On cooling below T_0, the activation energy for the transition from the phase I to II increases from $-\infty$ toward 0. If the phase I can be supercooled below T_{max}, its heating would result in the transition from the phase I to II. For this process, the activation energy would decrease from E_D toward 0.

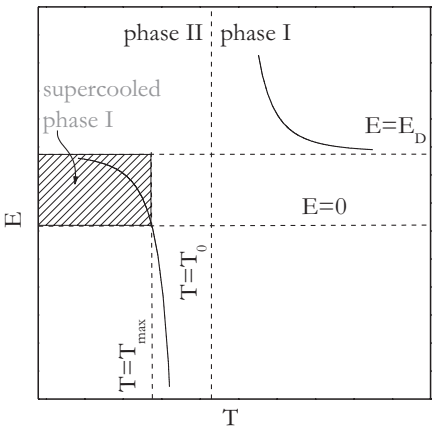

Fig. 3.50 Theoretical E versus T dependence derived from Eq. 3.45

In conclusion, we should mention that the aforementioned nucleation analysis is identical to that considered earlier for the solid–liquid (melting) and liquid–solid (crystallization) phase transitions. Since first-order transitions are accompanied by a change in volume, the molar volumes of the solid and liquid phase are generally different. Because of the mismatch of the volumes, the formation of a new phase nucleus would have to overcome an energy barrier associated with elastic strain energy. When one of the phases is liquid, the strain energy can be neglected. However, if both phases are solid, a more accurate representation of nucleation needs to account for the strain energy term as a part of the free energy barrier of the process [143].

3.8.2 Isoconversional Treatment

The kinetics of the solid–solid phase transitions is conveniently measured by DSC. Generally, one can produce a set of data at several heating rates for the transition from the low- to high-temperature phase and a set of data at several cooling rates for the reverse transition. Obtaining the high-temperature phase in the supercooled metastable state may be difficult for many substances. However, if obtained, a dataset should be generated at multiple heating rates to be able to study the kinetics of the transition from the metastable high-temperature phase into the stable low-temperature phase. The datasets are then treated by an isoconversional method. It should be emphasized that not every isoconversional method is applicable to the data obtained on cooling. The methods suitable to this task have been discussed in Sect. 2.1.2.

The application of an isoconversional method to the datasets obtained on heating and cooling results in the E_α versus α dependencies such as those shown in Fig. 3.51 for the transition between the form I (cubic) and II (tetragonal) of ammonium nitrate. The dependencies are in agreement with the E versus T dependence

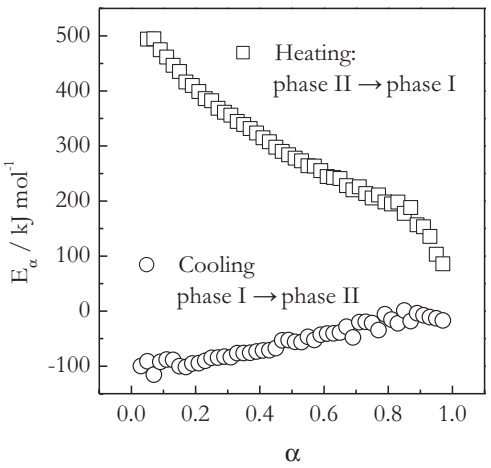

Fig. 3.51 Isoconversional activation energies estimated for the phase transition between tetragonal (*phase II*) and cubic (*phase I*) forms of ammonium nitrate

predicted by the Turnbull–Fisher model (Fig. 3.50). The transition from the form II to the form I demonstrates positive values of E_α that decrease with increasing α, which is expected because the measurements are done on heating so that α increases monotonously with increasing T. Similarly, for the transition from the form I to the form II that is measured on cooling, E_α is expected to be negative and to increase with increasing α (i.e., with decreasing T) toward 0.

The obtained E_α dependencies (Fig. 3.51) are converted to the E_α versus T dependencies by replacing each value of α with the mean temperature related to it. The resulting dependencies (Fig. 3.52) look quite similar to the theoretical ones derived from the Turnbull–Fisher model (Fig. 3.50). We can now try to fit the theoretical E_α versus T dependence (Eq. 3.45) to the experimental one. For simplicity, we assume that the E_D and A parameters of Eq. 3.45 remain the same for the forward (heating) and reverse (cooling) transition. The value of T_0 can also be used as a fit parameter. This would permit estimating the position of the equilibrium transition temperature, which, as explained earlier, is hard to measure experimentally. The resulting fit suggests that T_0 is ~396 K (~123 °C). This places the equilibrium transition temperature much closer to the onset of the transition measured on heating (128 °C) than to the one measured on cooling (113 °C; Fig. 3.47). Also, the fit yields an estimate for the activation energy of diffusion, $E_D = 63 \pm 2$ kJ mol^{-1}. This value falls in the range of the activation energies measured [144] by nuclear magnetic resonance (NMR) for translational diffusion of ammonium ion in the phases I and II of ammonium nitrate.

The solid–solid transitions are a new application area of isoconversional methods. Their full potential in this area is yet to be discovered.

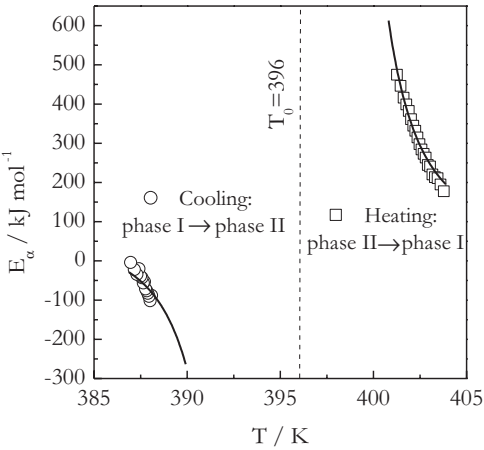

Fig. 3.52 Fitting E versus T data (*points*) to Eq. 3.45 (*solid lines*)

3.9 Mixing and Demixing

...he took the materials, of which he made a compound, mixing them all and boiling them a good while until it seemed to him they had come to perfection

Miguel de Cervantes Saavedra, Don Quixote

3.9.1 Background

So far we have discussed the phase transitions in single-component systems. If a system contains more than one component, it can exist as a single mixed phase and as several demixed phases. A transition between mixed and demixed phases is the phase transition specific to multicomponent systems. The mixed and demixed phases can coexist at equilibrium at certain temperature and pressure. A simple example is equilibrium between a solid solute and liquid solvent. If a small amount of sodium chloride (solute) is put in a large volume of water (solvent), it will disappear forming a solution, which is a single mixed phase (solution) containing sodium and chloride ions and water molecules. However, if we keep increasing the amount of sodium chloride, at some point the solution will saturate so that an excess of solid sodium chloride will coexist in equilibrium with its aqueous solution as two immiscible phases.

The transition between the mixed and demixed phases can be stimulated by changing temperature. Normally, the solubility of a solid solute increases with temperature as follows: [18]

$$\ln x = \frac{-\Delta H_{\mathrm{f}}}{RT}\left(\frac{1}{T} - \frac{1}{T_{\mathrm{m}}}\right), \tag{3.77}$$

where x, ΔH_{f}, and T_{m} are respectively the mole fraction, enthalpy of fusion, and melting temperature of the solid. This means that upon heating above certain equilibrium temperature, T_0, the two phases would merge into one. Conversely, the single-phase solution can be separated in two phases by dropping its temperature below T_0 that would force the solid solute out of solution or, in other words, would cause crystallization of the solute. Equation 3.77 gives rise to the phase diagram shown in Fig. 3.53. The solid line represents temperatures at which the solutions of different concentration can coexist at equilibrium with the solute. A solution prepared at higher temperature obviously has higher equilibrium concentration. A solution of the concentration x_1 prepared at T_1, i.e., above the respective equilibrium temperature, is a single-phase system. Dropping its temperature to T_2 would cause the solution to separate in two phases that eventually would come to equilibrium. The concentration of the solution would drop from x_1 to x_2, and the excess of the solute (i.e., $x_1 - x_2$) would fall out of solution to form the solid phase.

Something similar happens when mixing two partially miscible liquids, i.e., liquids that have limited solubility in each other. The respective phase diagram for liq-

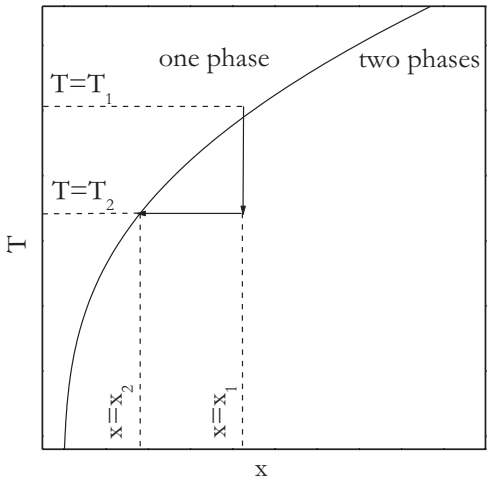

Fig. 3.53 Phase diagram for a solid–liquid system. The *solid line* represents the temperature at which solid and liquid can coexist at equilibrium

uid B dissolved in liquid A is seen in Fig. 3.54. The solid line bell curve tracks the temperatures at which a solution forms two phases of different concentration that can coexist in equilibrium. The ascending wing of the curve reflects an increase in the solubility of B as a function of temperature. The trend is similar to that seen in Fig. 3.53. The trend continues until reaching the critical temperature, T_c, above which both liquids become infinitely soluble in each other. The descending wing of the curve corresponds to the solubility of A in B. When the fraction of B becomes larger than that of A, B turns from solute to solvent. Thus, this wing represents an increase in the solubility of A as a function of temperature. If a solution of the concentration x_{B1} prepared at the temperature T_1, which is above the respective equilibrium temperature, it will exist as a single-phase system. Decreasing the solution temperature to the tem-

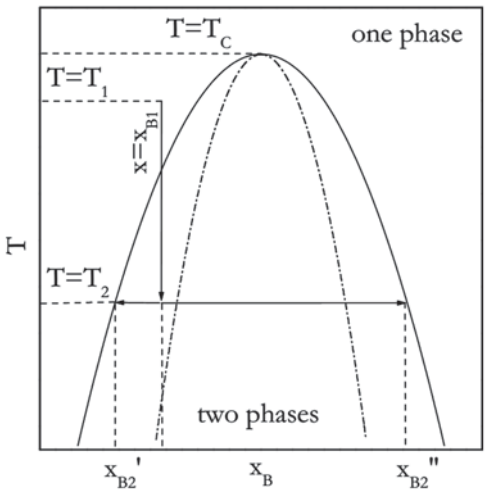

Fig. 3.54 Phase diagram for a liquid–liquid system. The *solid line* represents the temperature at which two liquid phases of different composition can coexist at equilibrium. The *dash-dot line* is the spinodal line

perature T_2 below the equilibrium temperature would make the solution to separate in two phases that over time would come to equilibrium. The two phases would be the B-poor and B-rich phases, whose respective concentrations of B are x_{B2}' and x_{B2}''.

The two considered systems (Figs. 3.53 and 3.54) are the systems that demonstrate the normal temperature dependence of the solubility, i.e., an increase with increasing temperature. In the case of the liquid–liquid mixtures, such systems are called upper critical solution temperature systems. Some systems however have the inverse temperature dependence of the solubility. Their respective phase diagrams are similar to those shown in Figs. 3.53 and 3.54 but inverted. The liquid–liquid systems of the inverse solubility are called the lower critical solution temperature systems.

The solid–liquid and liquid–liquid systems have one feature in common. When their temperature is changed from the one-phase to two-phase region, they become metastable. All metastable systems relax toward equilibrium via the process of nucleation. Nevertheless, if temperature of the liquid–liquid system is brought beyond the spinodal line (Fig. 3.54), it would become unstable. Unstable systems relax to equilibrium by another process called spinodal decomposition [3, 4]. The difference between nucleation and spinodal decomposition boils down to how concentration (density) fluctuations occur in these systems. Nucleation requires the fluctuation to be of a significant size, i.e., a nucleus must include a significant number of molecules to become stable. However, such fluctuations are very small in spatial extent because they occupy a very small fraction of the overall macroscopic volume. The fluctuation is accompanied by a large energy barrier, which decreases as temperature departs from its equilibrium value. When the energy barrier becomes negligible, the formation of a new phase becomes possible via spinodal decomposition. It is characterized by very small but multiple fluctuations of the concentration that occupy a large fraction of the macroscopic volume, i.e., they are large in spatial extent. Further discussion is limited only to nucleation because this is the mechanism that controls the new phase formation at smaller and slower departures from equilibrium.

In a solution, the driving force of the new phase formation is the supersaturation caused by a change in temperature. The supersaturation is defined as the ratio of the nonequilibrium to equilibrium concentration, x_0:

$$S = \frac{x}{x_0}. \tag{3.78}$$

If a solution of the concentration x is cooled from T_1 to T_2 (Fig. 3.53 and 3.54), i.e., from a temperature inside the one-phase region to a temperature inside the two-phase region, the supersaturation increases because the x_0 value becomes smaller. The larger the supersaturation, the faster the rate of the new phase nucleation. This is expressed by the following equation: [145]

$$w(T) = w_0 \exp\left(\frac{-16\pi\sigma^3 N_A^2 V^2}{3R^3T^3(\ln S)^2}\right)\exp\left(\frac{-E_D}{RT}\right), \tag{3.79}$$

where V is the molecular volume and N_A is the Avogadro number. The equation is arrived at from Eq. 3.35 for the critical radius of a spherical nucleus. The equation is combined with the Gibbs–Thomson relationship for size-dependent solubility to give:

$$-\Delta G_V = \frac{2\sigma}{r} = \frac{RT \ln S}{N_A V}. \tag{3.80}$$

Substitution of the right-hand side of Eq. 3.80 into Eq. 3.36 for the height of the free energy barrier yields:

$$\Delta G^* = \frac{16\pi\sigma^3}{3(\Delta G_V)^2} = \frac{16\pi\sigma^3 N_A^2 V^2}{3R^2T^2(\ln S)^2}. \tag{3.81}$$

Then Eq. 3.79 is obtained by plugging ΔG^* from Eq. 3.81 into the Turnbull–Fisher equation (3.42). Equation 3.79 can be rewritten in a simpler form

$$w(T) = w_0 \exp\left(\frac{-A}{T^3(\ln S)^2}\right)\exp\left(\frac{-E_D}{RT}\right), \tag{3.82}$$

where the constant A includes all parameters that are either independent or weakly dependent on temperature.

As derived [145], Eq. 3.79 (and, thus, 3.82) does not include directly the supercooling, i.e., $\Delta T = T_0 - T$. It can be introduced by explicitly accounting for the temperature dependence of the supersaturation. The temperature dependence of the solubility can be expressed in many forms [145]. One of them is given by Eq. 3.75 that can be rewritten as:

$$\ln x = Z + \frac{B}{T}. \tag{3.83}$$

If temperature drops from T_0 to T, the supersaturation becomes:

$$\ln S = B\left(\frac{T_0 - T}{T_0 T}\right) = \frac{-B\Delta T}{T_0 T}. \tag{3.84}$$

Then the supercooling is introduced in Eq. 3.82 by replacing ln$S$ with the right-hand side of Eq. 3.84. Now we can evaluate the temperature-dependent activation energy as usual (Eq. 3.43):

$$E = -R\frac{\mathrm{d}\ln w(T)}{\mathrm{d}T^{-1}} = E_D + \frac{AT_0^2}{B^2}\left[\frac{1}{(\Delta T)^2} - \frac{2T}{(\Delta T)^3}\right]. \tag{3.85}$$

This equation holds for a system that forms a new phase on cooling, i.e., ΔT is the supercooling. If the new phase is formed on heating, as in systems with the inverse solubility, ΔT would become the superheating, i.e., $T - T_0$. Then Eq. 3.85 would change to:

$$E = E_D + \frac{AT_0^2}{B^2}\left[\frac{1}{(\Delta T)^2} + \frac{2T}{(\Delta T)^3}\right]. \tag{3.86}$$

As mentioned earlier, Eq. 3.83 is not the only form of the temperature dependence of the solubility. A change of the form of this dependence would result in changing the final equation for the temperature-dependent activation energy. For instance, the use of an alternative form: [145]

$$\ln x = Z' + B'T \tag{3.87}$$

yields the following equation for the supersaturation:

$$\ln S = B'(T_0 - T) = B'\Delta T. \tag{3.88}$$

Replacing the supersaturation in Eq. 3.82 with the right-hand side of Eq. 3.88 followed by taking the derivative (Eq. 3.85) gives rise to the temperature-dependent activation energy of the following form:

$$E = E_D + \frac{A}{B'^2}\left[\frac{3}{(\Delta T)^2 T^2} - \frac{2}{(\Delta T)^3 T}\right]. \tag{3.89}$$

Again, ΔT in this equation is the supercooling and it holds for systems that form a new phase on cooling. For systems that form a new phase on heating, ΔT would be the superheating, and the second term in the brackets would change its sign.

Equations 3.85 and 3.86 can be used to predict the behavior of the experimental activation energy (Fig. 3.55). It is easy to demonstrate that the expression in the

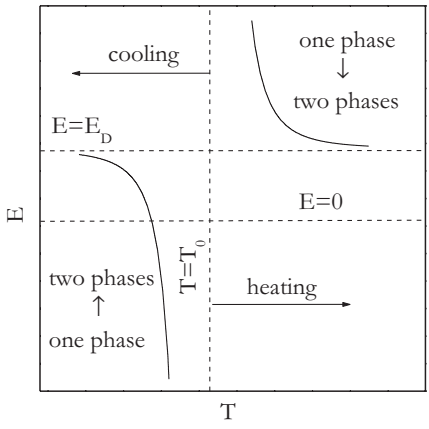

Fig. 3.55 Temperature dependence of the activation energy for the processes of the new phase formation on heating and on cooling

brackets of Eq. 3.85 tends to $-\infty$ as temperature approaches T_0 and to 0 as it departs further below T_0. It means that the effective activation energy experimentally determined on cooling should have large negative values that increase toward E_D with decreasing temperature. On the other hand, the expression in the brackets of Eq. 3.86 tends to $+\infty$ when temperature approaches T_0 and to 0 as it increases above T_0. Therefore, the activation energy estimated on heating should have large positive values at lower temperature and should decrease toward E_D as temperature rises. Similar trends can be demonstrated for Eq. 3.89.

It is noteworthy that at larger supercoolings, the system hypothetically can be brought to the state when the activation energy of the new phase formation becomes positive. In principle, this could be accomplished by cooling the system fast enough to outrun nucleation. The heating of the supercooled system then would result in the formation of a new phase, and the activation energy of this process would be positive. Something of that nature happens during the anomalous gelation discussed in Sect. 3.10.2

3.9.2 Isoconversional Treatment

The phase transitions between mixed and demixed state are usually accompanied by a significant change in the enthalpy that are detectable by DSC. As already stated, normally the solubility increases with temperature. The systems with the normal solubility absorb heat during mixing. That is, demixing in such systems is an exothermic process that takes place on cooling. The inverse solubility is not very common. It typically results from some specific interaction between solute and solvent. For example, some compounds demonstrate the inverse solubility in water because they turn into hydrated form stabilized by hydrogen bonding. The respective mixing is exothermic. While stable at lower temperature, hydrogen bonds between a solute and water break on heating and the solute molecules become dehydrated. If interaction between the dehydrated molecules is sufficiently strong, they associate with each other forming an individual phase on heating. The process is endothermic.

An example of the low critical solution temperature system is a mixture of triethylamine and water. It mixes releasing a significant amount of heat [146] and has the critical temperature of ~18 °C [147]. On heating above this temperature, the system undergoes endothermic demixing (Fig. 3.56). The application of an isoconversional method to a set of DSC curves obtained at different heating rates gives rise to the E_α dependence shown in Fig. 3.56. Since α increases monotonically with T, the decreasing shape of this dependence is consistent with that predicted by Eq. 3.86.

The actual temperature dependence of the isoconversional activation energy is obtained from the E_α versus α by replacing the values of α with the mean temperatures related to them. The resulting dependence is shown in Fig. 3.57. It is seen that the theoretical E versus T dependence established by Eq. 3.86 provides a fairly good fit to the experimental dependence. It is noteworthy that the E_D value resulted from

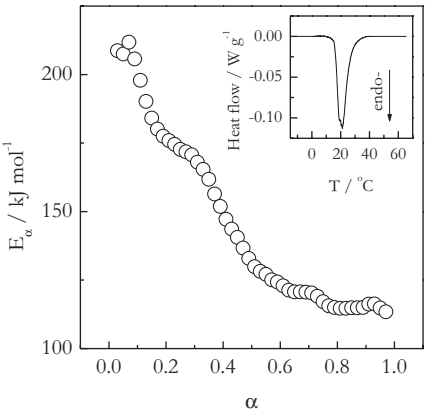

Fig. 3.56 Conversion dependence of the effective activation energy for demixing of an aqueous solution of triethylamine that takes place on heating. The inset shows a typical DSC curve of the process measured at heating rate 1 °C min^{-1}

the fit appears rather high, 117±3 kJ mol^{-1}. The activation energy of diffusion in liquids is about the same value as those of viscous flow [148]. For small spherical molecules, the latter value is about one third of the vaporization enthalpy [149], i.e., a few tens of kilojoules per mole. The obtained value is more characteristic of large molecules [148]. However, triethylamine in water exists as relatively big hydrated molecule, $(C_2H_5)_3 \cdot 2H_2O$ [150], the diffusion of which is likely to involve the breakage and restoration of hydrogen bonds that can create a significant energy barrier. Note that a solution of triethylamine in water has viscosity that is about four times larger than that of water [150]. It should also be noted that the activation energies of viscous flow in aqueous solutions of some amino acids have been reported [151] to be around a 100 kJ mol^{-1}.

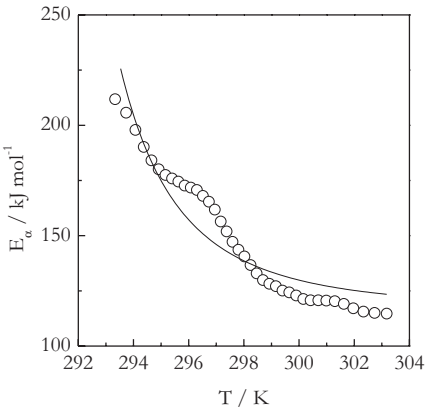

Fig. 3.57 Temperature dependence of the effective activation energy derived from E_α versus α dependence (Fig. 3.56). The *solid line* is a theoretical fit by means of Eq. 3.86

3.10 Gelation and Gel Melting

The soft overcomes the hard;
the gentle overcomes the rigid.
Everyone knows this is true,
but few can put it into practice

Lao Tzu, Tao Te Ching: 78

3.10.1 Background

Solutions may undergo a very special type of a phase transition called gelation. The latter is typically encountered in polymer solutions [13] but may occur also in sols of clays, soaps, aggregated globular proteins, etc. [152]. The initial liquid state is usually termed as sol to emphasize that a gel can form in various kinds of suspensions as well as in a true homogenous solution. The transition from sol to gel is best defined in mechanical terms. It is a transition from a flowing liquid (i.e., a sol) to a soft solid (i.e., a gel) that cannot flow. In order to be able to flow, the molecules of the solute and solvent should be able to move past each other freely. This is what happens when a polymer is dissolved in a good solvent, i.e., a solvent, in which an interaction between the solute and solvent is significantly stronger than between the solute and solute. In a poorer solvent, the solute–solvent interaction is not much stronger than the solute–solute one. Since the power of a solvent (i.e., the solubility) depends on temperature, the strength of the solute–solvent and solute–solute interactions can invert when changing temperature. As the solvent power decreases, the polymer molecules may form cross-links, losing their ability to move past each other and, thus, to flow.

A gel is a network of cross-linked solute molecules that entrap a solvent. Depending on the cross-link strength, gels can be either thermo-reversible or thermo-irreversible. Strong cross-links are formed by means of covalent bonding. In a solvent, a covalently cross-linked polymer network can swell, forming a gel, but it cannot dissolve because the solvent cannot break the covalent cross-links. In this chapter, we focus only on thermo-reversible gels. In such gels, the cross-links are formed by means of weak bonds (e.g., hydrogen or van der Waals bonds). The best known example of thermo-reversible (or physical) gelation is the thermal behavior of an aqueous solution of gelatin. Gelatin readily forms a solution in hot water. When cooled, the solution turns into a gel. Heating of the resulting gel causes its melting that gives rise to the initial solution.

Thermo-reversible gelation can been explained in terms of the phase diagrams [13, 153], which are similar to those for demixing transition in solutions (Sect. 3.9, Fig. 3.54). In the simplest case such as that of the gelatin–water system, there are only two phases: sol and gel (Fig. 3.58). The one- and two-phase regions separated by the binodal line that links the gelation temperature, T_{gel}, to the equilibrium concentrations of the polymer-rich (i.e., gel) and polymer-poor (i.e., solution) phases. The phase separation in gels is sometimes called syneresis [13, 153]. The process is quite different from demixing of two liquids that leads to the formation

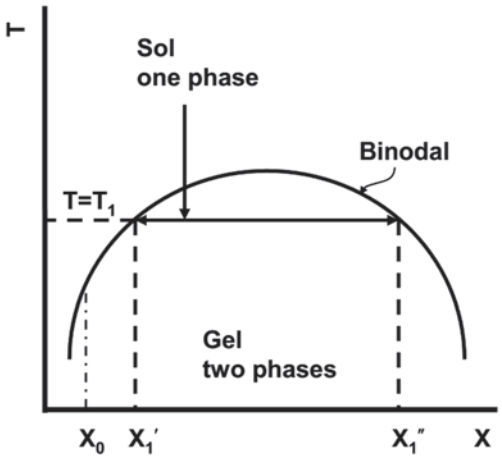

Fig. 3.58 Phase diagram for a gelling system that can exist in two states: *one-phase sol* and *two-phase gel*. Gel is not formed below the critical concentration x_0

of two homogenous macroscopic phases. In gel, the phase-separated state is microscopically heterogeneous. That is, the solvent-rich phase forms microdroplets inside the polymer-rich phase. The process of approaching equilibrium in the two-phase gels is extremely slow so that for all practical purposes such gels are fundamentally nonequilibrium systems similar to glasses. For this reason, the gel state and structure depend significantly on the thermal history of its formation. This feature of gels reveals itself vividly in the gel melting kinetics discussed in Sect. 3.10.3.

Gels cannot form when the concentration of a solution is below some critical value, x_0 (Fig. 3.58). If a solution has lower concentration, cooling it below the equilibrium temperature results in demixing of the solution without gelation.

Some gelling systems may demonstrate a more complex phase behavior (Fig. 3.59). An example is a solution of atactic PS in carbon disulfide [154]. Below

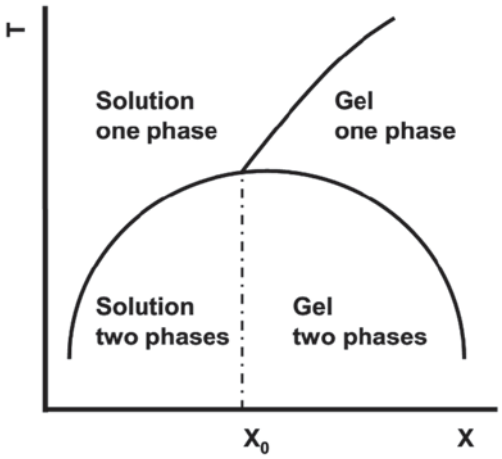

Fig. 3.59 Phase diagram for a gelling system that can form an equilibrium one-phase gel

a certain critical concentration, x_0, cooling of the one-phase solution results in the formation of a two-phase solution. However, increasing the solution concentration, while staying above the binodal line, results in the formation of a one-phase gel. This is microscopically homogeneous and equilibrium state. Cooling one-phase gel below the binodal line initiates phase separation of the gel. The clear one-phase gel turns into the turbid two-phase gel.

The described phase diagrams represent the behavior observed in solutions with the upper critical solution temperature. In these systems, the solubility increases with increasing temperature. Gelation of such solutions occurs on cooling. Gelation may also occur in solutions with lower critical temperature. Such solutions gel on heating because an increase in temperature decreases the solubility. There are a few rare examples of systems that gel on heating such as aqueous solutions of polymethacrylic acid [155] and cellulose derivatives [156, 157]. The respective phase diagrams for such systems are similar to those for regular systems (Fig. 3.58) but inverted. The gels formed on heating melt on cooling. Analogous to the process of demixing (Sect. 3.9), gelation on cooling is exothermic, whereas on heating endothermic.

The kinetics of physical gelation has been found [158] to be strikingly similar to that of polymer crystallization [93, 94]. The similarity is not surprising considering that the formation of the gel network junctions has been identified with the formation of microcrystallites in a wide variety of polymers [13, 159], including gelatin [158, 160]. For example, in gelatin gels, the microcrystallites are believed [13, 161, 162] to form via partial restoration of the triple helix structure characteristic of collagen that occurs via cooperative hydrogen bonding of gelatin coils. The rate of reversion from gelatin coil to collagen helix has long been known [163] to have the negative temperature dependence and to follow the nucleation-type kinetics, in which the nucleus is an embryo of the triple helix structure whose stability is determined by a critical length.

As in the case of crystallization, the rate of physical gelation initially increases as temperature drops further below T_{gel} but then passes through a maximum and finally drops to zero. A schematic diagram of this temperature dependence is seen in Fig. 3.60 [164]. At the high temperature end, gelation stops upon reaching equi-

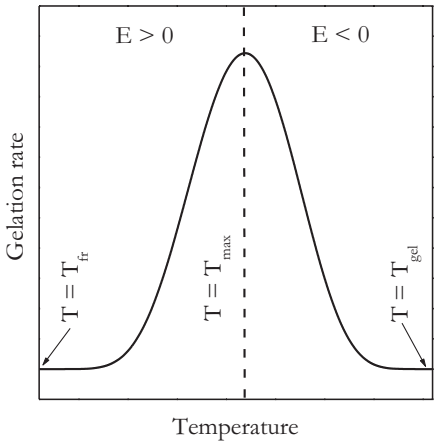

Fig. 3.60 The gelation rate passes through a maximum found between the temperatures of gelation (T_{gel}) and freezing (T_{fr}). The activation energy changes its sign when temperature traverses T_{max}. (Adapted from Guigo et al. [164] with permission of RSC)

librium at T_{gel}. At the low temperature side, it ceases on gel freezing at T_{fr}. The temperature rate dependence is obviously akin to that presented in Figs. 3.32 and 3.36 to illustrate respectively the nucleation rate in accord with the Turnbull–Fisher model and crystallization rate in accord with the Hoffman–Lauritzen model. The temperature dependence of the rate is negative above T_{max} and positive below it. Consecutively, the effective Arrhenius activation energy should be negative when estimated in the temperature range T_{max}–T_{gel} and positive when evaluated in the range T_{fr}–T_{max}. An actual example [165] of the Arrhenius plot for gelation of a gelatin solution at several temperatures is presented in Fig. 3.61. The maximum of the gelation rate is found in the range 14–19 °C. The activation energy is estimated to be −130 kJ mol^{-1} above T_{max} and 55 kJ mol^{-1} below it.

All in all, empirical evidence suggests that the kinetics of physical gelation can be parameterized in terms of some nucleation model. However, there are no nucleation models designed specifically for the process of physical gelation. In this situation, one can use the Turnbull–Fisher (Eq. 3.44) and Hoffman–Lauritzen (Eq. 3.52) models as empirical tools for exploring the kinetics of physical gelation as demonstrated in a number of publications [158, 164, 166–169].

3.10.2 Isoconversional Treatment of Gelation

Aqueous solutions of gelatin provide a well-known example of physical gelation that takes place on cooling. Gelatin is denatured (i.e., randomly coiled) form of collagen, whose native state is a triple helix made of three polypeptide chains cross-linked

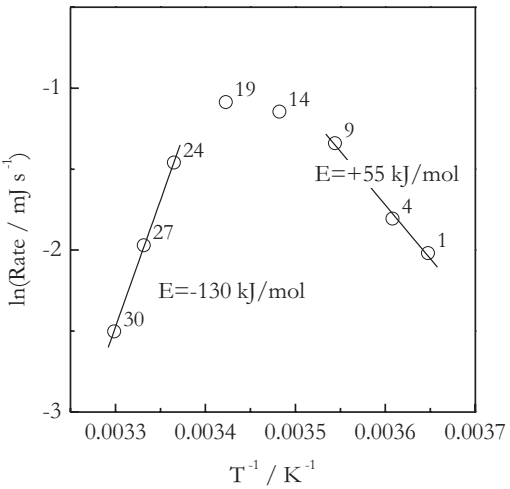

Fig. 3.61 Arrhenius plot of the initial rate of the heat release for gelation of a gelatin solution measured at eight different temperatures. The numbers by the points are the temperatures in °C. The activation energy is negative in the temperature range 24–30 °C and positive in the temperature range 1–9 °C. (Reproduced from Chen and Vyazovkin [165] with permission of Wiley)

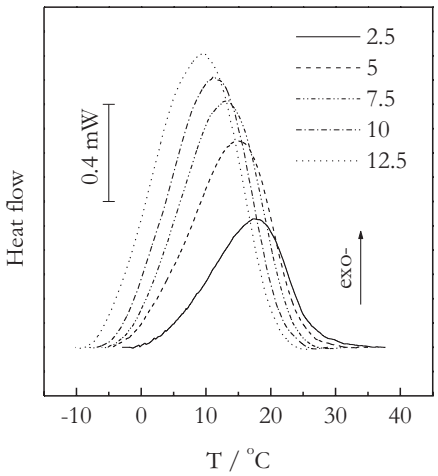

Fig. 3.62 DSC curves for gelation of 17 wt. % solution of gelatin in water. The numbers by the line types are cooling rates in °C min^{-1}. (Reproduced from Chen and Vyazovkin [165] with permission of Wiley)

by multiple hydrogen bonds. Gelatin dissolves readily in hot water. Decreasing the temperature of an aqueous gelatin solution increases the stability of the hydrogen bond cross-links that allow the polypeptide chains to restore a helical structure. This process takes place in dilute gelatin solutions [163, 170, 171]. In concentrated solutions, cross-linking becomes predominantly intermolecular, so that instead of forming separate helices, the polypeptide chains form an infinite network (i.e., a gel), in which partially restored helices serve as cross-link centers (i.e., network junctions).

The formation of hydrogen bonds during gelation of a gelatin solution produces sufficient amount of heat to follow the process by DSC (Fig. 3.62) [165]. On cooling, gelation becomes detectable below 40 °C. The gelation temperature depends on the concentration of the solution as seen from the phase diagrams (Figs. 3.58, 3.59). According to rheological measurements by Michon et al. [172], a decrease in the concentration of a gelatin solution from 20 to 1 wt. % causes a drop in T_{gel} from 33 to 26 °C. Just as in the case of crystallization, the DSC peaks shift to lower temperature with increasing the cooling rate (Fig. 3.62).

The application of an isoconversional method to DSC data on gelation of a gelatin solution is illustrated in Fig. 3.63. The obtained E_α on α dependencies demonstrate negative values of the effective activation energy. The E_α values tend to increase with the extent of the sol to gel conversion that is explicable by the departure from the equilibrium temperature (i.e., T_{gel}). In accord with either Turnbull–Fisher (Eq. 3.45) or Hoffman–Lauritzen (Eq. 3.60) equation, the effective activation energy turns to $-\infty$ at the equilibrium temperature but increases toward zero as temperature departs from the critical value. A similar type of dependencies (i.e., negative E_α increasing with α) is found for crystallization of polymer melts measured on continuous cooling, i.e., when an increase in the extent of the melt to crystal conversion reflects the departure from the melting point. An example of such behavior is seen in Fig. 3.37.

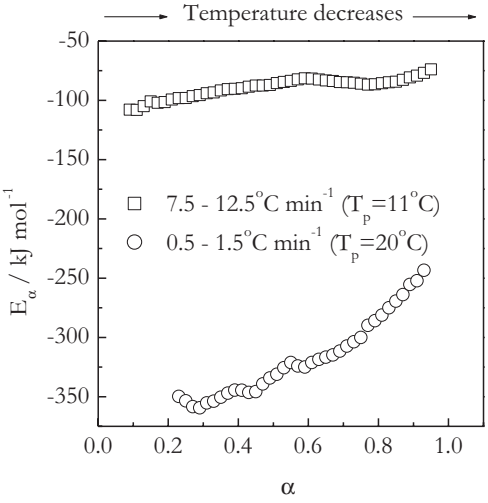

Fig. 3.63 The E_α dependencies obtained by applying an advanced isoconversional method to DSC data on gelation of 17 wt.% solution of gelatin in water. *Squares* and *circles* denote respectively different intervals of cooling rates. The intervals differ in the mean value of the DSC peak temperature, T_p, shown in parentheses. (Adapted from Chen and Vyazovkin [165] with permission of Wiley)

The effect of temperature on the E_α is even more evident when the E_α dependencies are evaluated from the data collected in different ranges of the cooling rates. As already noted with increasing the cooling rate, the DSC peaks shift to lower temperatures (Fig. 3.62). For the range of faster cooling rates (7.5, 10, and 12.5 °C min^{-1}), the average DSC peak temperature is ~11 °C so that the average value of E_α is about −90 kJ mol^{-1}. However, at slower cooling rates (0.5, 1.0, and 1.5 °C min^{-1}), the average peak temperature is markedly higher (20 °C), i.e., closer to T_{gel} so that the average E_α estimated from the slower heating rates is around −300 kJ mol^{-1} [165]. Therefore, isoconversional analysis of the continuous cooling DSC data demonstrates that under these conditions the rate of sol–gel conversion has a negative temperature coefficient, whose absolute value becomes larger when the process is measured closer to T_{gel}.

As already suggested, the kinetics of physical gelation can be reasonably well described by the Turnbull–Fisher and Hoffman–Lauritzen models. This means that one generally should be able to fit the temperature dependencies of the isoconversional activation energy to Eqs. 3.45 and/or 3.60 by substituting T_{gel} for the equilibrium temperature. For example, Eq. 3.45 derived from the Turnbull–Fisher model would take the following form:

$$E = E_D - A\left[\frac{2T}{\left(T_{gel}-T\right)^3} - \frac{1}{\left(T_{gel}-T\right)^2}\right]. \tag{3.90}$$

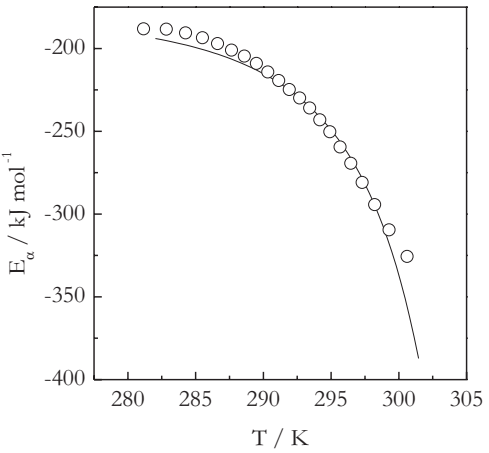

Fig. 3.64 Experimental E_α versus T dependence (*circles*) for gelation of 40 wt.% solution of gelatin in water. The *solid line* is a fit by Eq. 3.90

As seen from Fig. 3.64, this equation fits quite well the temperature dependence of the effective activation energy for gelation of 40 wt.% solution of gelatin [164]. The dependence has been derived from the E_α versus α dependence by replacing α with the average temperature corresponding to this conversion at different cooling rates. T_{gel} for this solution is ~317 K as estimated by extrapolating the gel melting data of Godard et al. [158].

Although the application of the Turnbull–Fisher and Hoffman–Lauritzen models to the process of gelation is rather empirical, it can still be used to extract meaningful information, especially for comparative purposes. One such example is the effect of the concentration on the kinetics of physical gelation of aqueous solutions of methylcellulose [169].

Aqueous solutions of methylcellulose gel on heating. The mechanism of the process has been examined in a number of studies, the results of which are briefly summarized by Kobayashi et al. [173]. Methylcellulose has the inverse solubility in water, i.e., it is soluble in cold but not in hot water. Dissolution occurs via hydration of methoxyl groups. When the solution temperature is increased, hydrogen bonds break, causing dehydration of hydrated methoxyl groups. The latter then undergo hydrophobic association forming a network, i.e., a gel.

Breakage of hydrogen bonds is accompanied by an endothermic effect that can be used to monitor gelation by using DSC. Typical DSC curves of gelation are shown in Fig. 3.65. An increase in the concentration of the methylcellulose solution causes some small shift of the process to lower temperatures. The heat of gelation per gram of methylcellulose is about −7 J g^{-1} for both 2 and 4% solutions that indicates that both samples have reached similar extent of cross-linking. For 8% solution, the heat of gelation is −5 J g^{-1}; that means, that the extent of cross-linking is about 30% smaller than in the two other samples. This is not surprising because the molecular mobility of the methylcellulose chains in the highly viscous 8% solution should be dramatically slowed down, therefore, limiting the process of cross-linking.

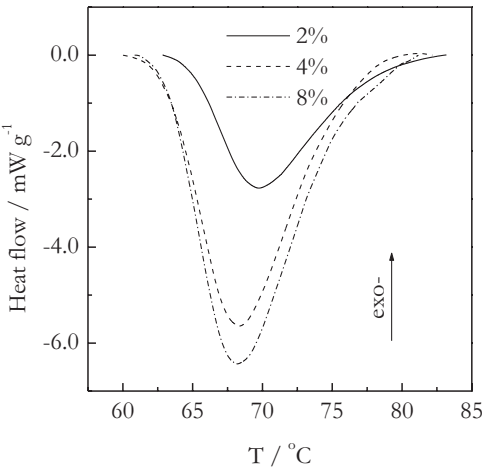

Fig. 3.65 DSC curves for heating of methylcellulose solutions of different concentration at 10 °C min^{-1}. (Reproduced from Chen et al. [169] with permission of Wiley)

The E_α versus T plots obtained from the E_α dependencies estimated by an isoconversional method are shown in Fig. 3.66. All three plots have a similar concave downward shape but shift to higher E_α values with increasing the concentration of the solutions. The initial decreasing portion of the E_α versus T dependence is consistent with that predicted by the Turnbull and Fisher model. Indeed, Eq. 3.90 suggests that just above T_{gel}, the E_α values should be large but decrease toward E_D as temperature continues to rise above T_{gel} (see Fig. 3.50 and related discussion). However, the final increasing portion cannot be rationalized within the aforementioned model.

An increase in E_α in the later stages of gelation (Fig. 3.66) is likely to be associated with changing conditions of diffusion. Cross-linking of polymer chains obstructs their mobility so that the formation of new cross-links may encounter continuously growing energy barrier to diffusion. This means that the constant activation energy

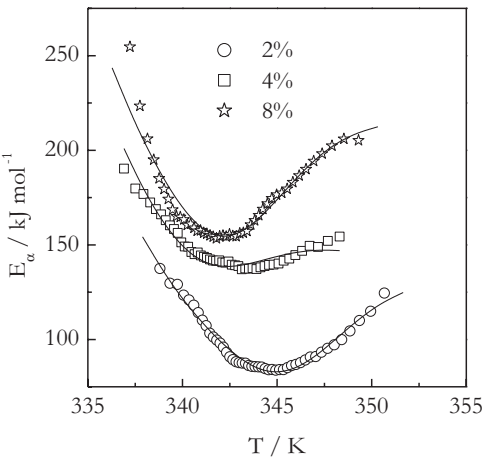

Fig. 3.66 Fits of Eq. 3.91 to experimental E_α versus T dependencies. (Reproduced from Chen et al. [169] with permission of Wiley)

in Eq. 3.90 needs to be replaced with the value that increases with increasing α. A similar approach is used to adequately describe the temperature dependence of viscosity in a system undergoing reactive polymerization [174]. A rather simple modification of Eq. 3.90:

$$E = \varepsilon\alpha^n - A\left[\frac{2T}{\left(T_{gel} - T\right)^3} - \frac{1}{\left(T_{gel} - T\right)^2}\right] \tag{3.91}$$

has proven [169] to be sufficient to account for the effect. Equation 3.91 includes three parameters. The parameter A represents a contribution of the nucleation process to the overall temperature dependence. This contribution manifests itself through a decreasing dependence of E on T. The increasing portion of the dependence corresponds to the diffusion contribution that is represented by the parameters ε and n. By its meaning, ε is the activation energy of diffusion at complete conversion, i.e., at $\alpha = 1$. The parameter n characterizes the strength of diffusion contribution: the smaller the n, the stronger the contribution, i.e., becomes operative earlier and contributes more.

Fitting Eq. 3.91 to the experimental dependencies (Fig. 3.66) requires knowledge of the T_{gel} values. They have been reported by Takahashi et al. [175] and are about 40, 38, and 36 °C for 2, 4, and 8% solutions, respectively. The resulting fits are statistically significant. The values of the adjustable parameters are given in Table 3.3. The diffusion parameters reflect an increasing contribution of diffusion to the overall temperature dependence with increasing concentration. When comparing the 2 and 8% solutions, an increase in the concentration results in larger ε (i.e., larger activation energy of diffusion at $\alpha = 1$) as well as in smaller n (i.e., larger strength of the contribution). The behavior of the 4% solution is a bit more complex. Compared to the 2% solution, it shows 10% smaller ε that would be consistent with a slightly smaller diffusional contribution. However, it also demonstrates 2.5 smaller n that suggests the overall diffusional contribution to be stronger and larger compared to the 2% solution.

On the other hand, the nucleation parameter A can be used to estimate of the free energy barrier to nucleation at any temperature as follows (see Eq. 3.44):

$$\Delta G^* = \frac{A}{\left(T_{gel} - T\right)^2}. \tag{3.92}$$

For comparison purposes, the ΔG^* values can be estimated at $T = 60$ °C, which is the threshold temperature above which gelation becomes detectable by DSC

Table 3.3 The results of fitting Eq. 3.91 to experimental E_α versus T dependencies

C (%)	A (K^2 kJ mol^{-1})	ε (kJ mol^{-1})	n	ΔG^*(60 °C; kJ mol^{-1})
2	3315.4	95.0	5	8.3
4	4879.8	85.2	2	10.1
8	6915.0	151.9	3	12.0

(Fig. 3.65). The resulting ΔG^* (Table 3.3) do not demonstrate any significant dependence on the concentration and are around 10 kJ mol^{-1}, which is comparable to the energy of a hydrogen bond [139]. Note that breaking a hydrogen bond between water and methoxyl group is likely to be a limiting step in nucleation of methylcellulose microcrystallites that serve as cross-link points in the gel. Overall, empirical application of the Turnbull–Fisher model suggests that the effect of the concentration on the kinetics of gelation of aqueous methylcellulose is due to a change in the conditions of diffusion but not the conditions of nucleation.

To conclude this section, we need to mention an interesting fact that the solutions that normally gel on cooling can be made to gel on heating [164, 176]. Anomalous gelation of this kind can be accomplished when the solution is cooled fast enough to outrun gelation. Then the solution can reach a supercooled state that can be turned into gel on heating. This situation is similar to cooling the melt fast enough to bypass crystallization so that it turns into a glass which can then crystallize on heating, i.e. undergo cold crystallization. It has been demonstrated [176] that in very diluted (~1 wt.%) solutions of gelatin, gelation can be suppressed when the solutions are cooled at 20 °C min^{-1}. However, the solutions of regular concentration that gel much faster require very fast cooling rates to bypass gelation. For example, suppressing gelation in a 40 wt.% solution of gelatin requires the solution to be cooled not slower than 500 °C s^{-1} [164]. Such fast cooling rates are accomplishable when using ultrafast DSC [177] on samples of very small (typically submicrogram) masses.

Figure 3.67 shows ultrafast DSC data obtained on heating of supercooled gelatin solution. The application of an isoconversional method to these data results in a

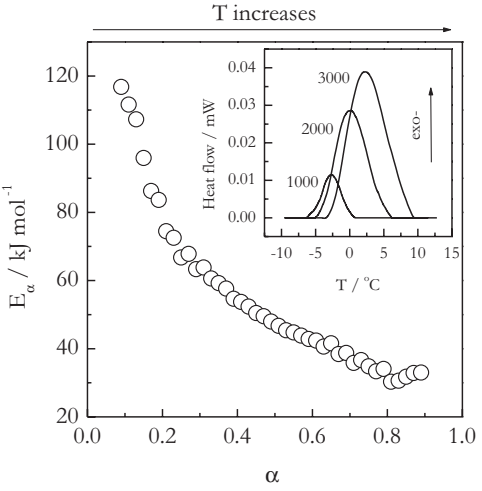

Fig. 3.67 Variation of the activation energy with conversion for gelation of 40 wt.% aqueous solution of gelatin on heating. The inset shows DSC curves obtained at the heating rates 1000, 2000, and 3000 °C s^{-1}. Prior to heating, the solution was cooled at 1000 °C s^{-1}. (Adapted from Guigo et al. [164] with permission of RSC)

decreasing dependence of effective activation energy on conversion (Fig. 3.67). It is noteworthy that the activation energies are positive and decrease toward zero as one would expect when gelation occurs below T_{max} (Fig. 3.60). Recall that it is exactly the type of dependence predicted by the Hoffman–Lauritzen model (see Fig. 3.36) for this temperature range. It is yet another example that illustrates the usefulness of the nucleation crystallization models as applied to the process of physical gelation.

3.10.3 Isoconversional Treatment of Gel Melting

As mentioned earlier, reaching equilibrium state in the two-phase gel region (Figs. 3.58 and 3.59) is generally very slow process. For example, Djabourov et al. [161] have found that 4.7 wt.% gelatin gel could not attain equilibrium at 10.5 °C for 42 days! It means that normally the two-phase gels are nonequilibrium systems, whose structure and properties depend on thermal history. This dependence manifests itself profoundly in the process of melting that can be readily studied by DSC.

The DSC peaks of gel melting can provide some quick clues about the gel network structure in terms of the total number of the network junctions points (i.e., the number of cross-links) and their size (i.e., the number of cross-links per junction). The total heat of melting is directly proportional to the number of cross-links, but it does not tell anything about the number of cross-links per junction. Indeed, the same amount of heat would be produced by melting of two gels prepared from the same amount of the same solution, if one of the gels has 100 junctions with 10 cross-links per junction and another 10 junctions with 100 cross-links per junction. However, these two gels would differ significantly in their thermal stability. The gel having more cross-links per junction has more stable junctions, breaking which would require more thermal energy. Thus, it would melt at higher temperature. Therefore, the gel meting temperature, taken from DSC as either peak or interpolated onset temperature, is representative of the size of network junctions. On the other hand, a change in thermal stability can also be expected to reveal itself in the value of the activation energy of gel melting [178].

The effect of the gel structure on the activation energy of aqueous gelatin gel melting has been explored in a kinetics study [178] that combined isoconversional method with extensive DSC measurements. Figure 3.68 demonstrates the effect of isothermal annealing time on DSC peaks of gel melting. The peaks obviously increase in size with increasing the annealing time. This is indicative of continuously increasing number of junctions. It is noteworthy that although the melting peak obtained after 2 h of annealing is about twice the size of the peak produced after 15 min, the peak temperature for these two peaks is nearly identical. That is, annealing appears to promote predominately the formation of new junctions rather than the growth of the existing ones. Since thermal stability of the gel is not affected significantly during annealing, it is reasonable to expect that the activation energies of gel melting would not be affected either.

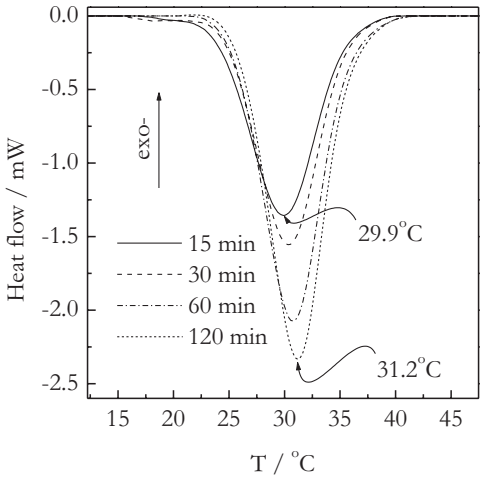

Fig. 3.68 Melting of 40 wt.% gels formed on annealing at 20 °C for periods of time from 15 to 120 min. Curved arrows mark the peak positions. Heating rate is 2.5 °C min^{-1}, sample mass 70.8 mg. (Reproduced from Dranca and Vyazovkin [178] with permission of Elsevier)

The isoconversional dependencies of the activation energy for the gelatin gel melting are seen in Fig. 3.69. As expected, the E_α dependencies evaluated for melting of the gels annealed for different periods are practically identical. For both systems, the effective activation energy decreases significantly (from ~170 to 95 kJ mol^{-1}) throughout the process of melting. Finding that E_α varies with α is typically a sign that the overall process includes multiple steps having different activation energies (see Sect. 1.2). It could be construed that the gel formed may consist of the network junctions having different stability (i.e., size) and, thus, a different energy barrier to melting. However, in such a case, the less stable junctions would disintegrate first followed by disintegration of the more stable ones so that the E_α value would rather have to increase with increasing α.

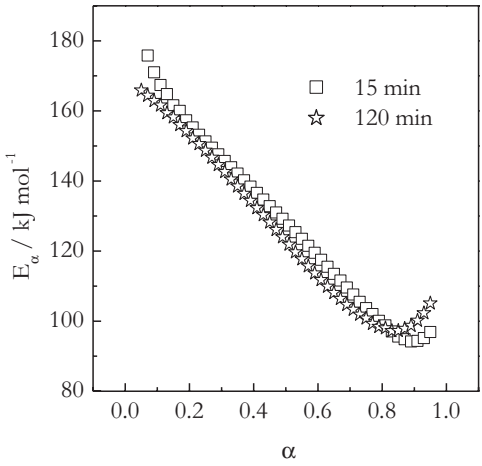

Fig. 3.69 E_α dependencies obtained for melting of 40 wt.% gels annealed at 20 °C for 15 and 120 min. (Reproduced from Dranca and Vyazovkin [178] with permission of Elsevier)

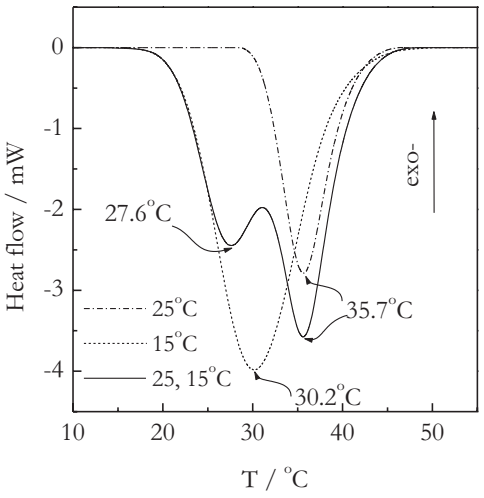

Fig. 3.70 Melting of 40 wt.% gel obtained in one- and two-step annealing at heating rate is 5 °C min^{-1}. Temperature of the annealing steps is shown by the curve types. Duration of each step is 30 min. *Curved arrows* mark the peak positions. (Adapted from Dranca and Vyazovkin [178] with permission of Elsevier)

On the other hand, the decrease observed in Fig. 3.69 is remarkably similar to that seen for the glass transition in various glasses (Sect. 3.3.2). In glasses, a large energy barrier for the initial stages of the process corresponds to strongly cooperative molecular motion under the conditions of constricted free volume. As the temperature rises, the free volume increases, relieving energetic constrains and causing the E_α values to decrease. Something similar is likely to occur in melting of gelatin gels. That is, disintegration of a typical network junction requires cooperative breaking of multiple hydrogen bonds that cross-link the polypeptide chains. Considering that typical range of hydrogen bond energies is 10–40 kJ mol^{-1} [139], the E_α values for the initial stages of melting (Fig. 3.69) can be interpreted as cooperative breaking of 5–15 bonds. After the initial large energy barrier is surmounted and multiple cross-links are broken, the polypeptide chains of the network junction gain new conformational degrees of freedom. The freed chain mobility destabilizes the network junction, therefore, lowering the energy barrier to melting.

Conversely, annealing temperature has a profound effect on thermal stability. DSC curves for melting of two gels annealed for the same period of time at two respectively different temperatures are shown in Fig. 3.70. The gel obtained at 15 °C demonstrates a larger heat of melting; that means, it has a larger number of junctions. However, the gel produced at 25 °C melts at about 5–6 °C higher temperature that suggests its network junctions contain more cross-links. The observed increase in thermal stability should entail an increase in the activation energy of gel melting. The respective E_α dependencies are presented in Fig. 3.71. Both dependencies are of the same shape as that observed in Fig. 3.69 that hints the similarity of the melting mechanisms. Nevertheless, the activation energies for melting of the gel annealed at 25 °C are consistently

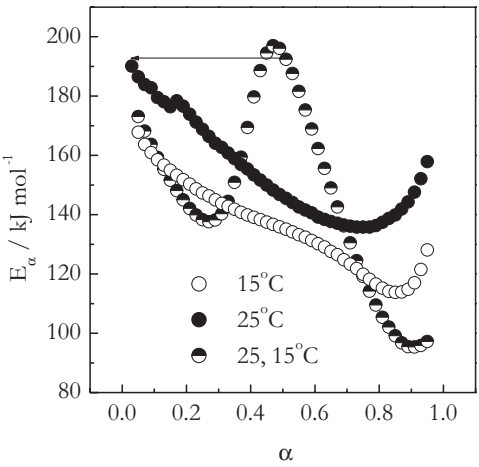

Fig. 3.71 E_α dependencies obtained for melting of 40 wt.% gels obtained in one and two 30-min annealing steps performed at temperatures shown by the point types. *Arrow* shows respectively comparable parts of two- and one-step annealing processes. (Reproduced from Dranca and Vyazovkin [178] with permission of Elsevier)

larger by 10–30 kJ mol^{-1} than those for the gel produced at 15 °C that indicates that the former gel has a few more hydrogen bonds per junction than the latter.

Another instructive experiment that illuminates the effect of the structure on gel melting involves two successive 30-min steps of annealing at 25 and 15 °C. A DSC curve for melting of the resulting gel is displayed in Fig. 3.70. The curve reveals two distinct melting peaks that apparently reflect the existence of two gel structures, which differ markedly in their thermal stabilities. The higher-temperature melting peak is found at the same temperature as the melting peak for the gel produced by single-step annealing at 25 °C. This is in agreement with the rheological measurements [179] that demonstrate that the structures formed at higher annealing temperatures are conserved during annealing at lower temperatures. In contrast, the lower temperature peak is detected at about 2–3 °C lower than the melting peak temperature for the gel produced by single-step annealing at 15 °C. That is, the gel produced on annealing at 15 °C in the two-step procedure is less thermally stable than the one formed in a single-step annealing at 15 °C. It means that the existence of the gel structures formed at 25 °C hinders the growth of the network junctions being formed at 15 °C. Apparently, the hindrance is due to the fact that in partially cross-linked gel, the conformational degrees of freedom of the polypeptide chains are largely restricted. Therefore, it is more difficult for new cross-links to form and for the network junctions to grow.

The E_α dependence determined for melting of the gel annealed consecutively at 25 and 15 °C is shown in Fig. 3.71. The dependence is easy to understand by comparison with the individual dependencies estimated for melting of the gels produced by the respective single-step annealings at 15 and 25 °C. The initial descending portion of the dependence is similar to the initial portion of the E_α dependence for melting of the gel annealed at 15 °C. For both dependencies, the E_α values at the lowest conversions are ~170 kJ mol^{-1} that suggests that the energy barriers to melting in both gels are similar. According to DSC (Fig. 3.70), melting of the gel structures formed on annealing at 15 °C contributes less to the total heat of

melting than melting of the gel structures formed on annealing at 25 °C. For this reason, a transition from melting of the lower temperature structures to melting of the higher temperature structures should occur at conversion less than 0.5. Indeed, the descending E_α dependence breaks down around $\alpha = 0.3$ and climbs sharply to $E_\alpha \approx 195$ kJ mol^{-1} at $\alpha \approx 0.5$. Since that point on the overall melting process becomes dominated by melting of the gel structures formed on annealing at 25 °C. Accordingly, the initial values of E_α for the second descending part are similar to the respective E_α values estimated for melting of the gel prepared at 25 °C. It is quite remarkable that the initial parts of both descending E_α dependencies reveal the existence of two differing energy barriers whose values agree with the values found for melting of the individual gels produced by annealing at 15 and 25 °C, respectively.

The gel structure becomes increasingly more complex when gels are prepared under the conditions of nonisothermal cooling. DSC melting data of gels prepared by continuous cooling at 1 °C min^{-1} are presented in Fig. 3.72. By comparison to isothermally prepared gels, these gels melt over a significantly wider temperature range. This indicates the existence of a wide distribution of the gel structures having differing thermal stabilities. On cooling, gelation initiates at ~40 °C, peaks at ~23.0 (40 wt.%) or 20.6 °C (20 wt.%), and finishes around 0 °C. Nonisothermal gelation can be thought of as a large number of short isothermal annealing steps conducted consecutively in the temperature range from 40 to 0 °C. Such annealing program should produce a large number of gel structures whose melting temperatures decrease with decreasing the annealing temperature in a manner similar to that shown in Fig. 3.70. The mass fractions of the structures should depend on the rate of cross-linking (Fig. 3.72). At the cooling rate 1 °C min^{-1}, the rate maxima occur around 20 ± 5 °C so that the structures formed in largest fractions should be expected to have thermal stability similar to that of the structures formed on isothermal annealing at 15, 20, and 25 °C. However, gelation continues at slower yet significant rate at temperature below 15 °C. This process should yield the gel structures whose

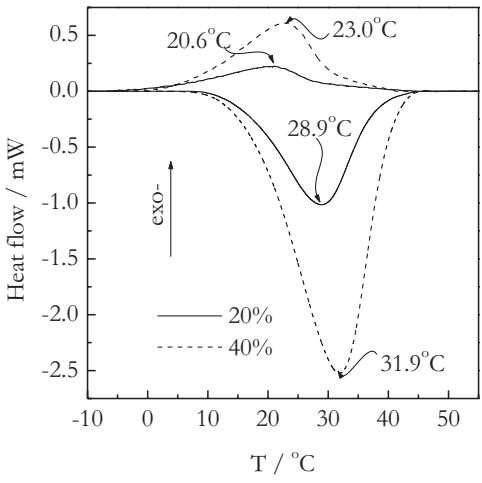

Fig. 3.72 Formation and melting of the gels obtained from 20 and 40 wt.% solutions. Exothermic gelation is measured on cooling at 1 °C min^{-1}, endothermic melting at 5 °C min^{-1}. (Reproduced from Dranca and Vyazovkin [178] with permission of Elsevier)

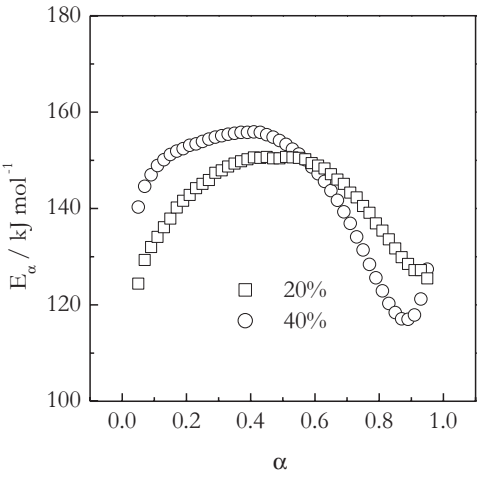

Fig. 3.73 E_α dependencies obtained for melting of 20 and 40 wt.% gels obtained on cooling of the respective solutions at 1 °C min^{-1}. (Reproduced from Dranca and Vyazovkin [178] with permission of Elsevier)

melting temperatures are lower than that of the gel prepared isothermally at 15 °C. These structures would have lower thermal stability and, thus, their melting should encounter a lower energy barrier.

The isoconversional activation energies evaluated for melting of nonisothermally prepared gels are displayed in Fig. 3.73. The resulting E_α dependencies differ noticeably from those found (Figs. 3.69 and 3.71) for melting of isothermally prepared gels. The initial part ($\alpha < 0.4$) of both dependencies is increasing. The initial E_α values are markedly smaller than the initial values estimated for melting of the isothermally prepared gels. This clearly suggests the existence of the gel structures whose disintegration encounters a lower energy barrier or, in other words, the presence of the structures, whose network junctions have fewer cross-links. While raising temperature, melting progresses by involving the structures of continuously increasing thermal stability that gives rise to the increasing E_α dependence. Note that the E_α values never rise to the values observed (Figs. 3.69 and 3.71) for the initial stages of melting of the gels prepared isothermally at 15 and 20 °C despite the aforementioned fact that the gel structures formed at 20 ± 5 °C should be present in the largest mass fraction. This is because melting of more thermally stable structures occurs in parallel with the continuing melting of less thermally stable structures so that the activation energy of the overall process is about the weight average of the activation energies of the individual parallel processes.

Once these most abundant structures become involved in melting, the E_α dependence becomes decreasing. Although there still are more thermally stable structures in the remaining gel, they are present in progressively smaller amounts so that the overall melting process is dominated by the later stages of melting of less thermally stable structures. As a result, the observed E_α dependence is similar to that estimated gels prepared by isothermal annealing at 15 and 20 °C.

In conclusion, we should mention that melting is not the only process that occurs on heating of gels. It should be remembered that as long as temperature is below the equilibrium value of T_{gel}, the solution formed by melting is capable of converting

to gel. The formation of gelation gels on heating has already been discussed [164, 176] (Sect. 3.10.2). It is also detectable during melting by using TM DSC that demonstrates [178] that about 40% of the melting heat is found in the reversing signal. That is, a substantial fraction of melted gel can form new gel structures that would have greater thermal stability than the structures melted. Perhaps, a small increase in E_α detectable at $\alpha > 0.8$ (Figs. 3.69, 3.71, and 3.73) is associated with melting of these newly formed structures of the highest thermal stability.

3.11 Helix–Coil Transition

Undoubtedly this, too, is a structure, growing and piling itself up in endless spiral lines

Victor Marie Hugo, Notre Dame de Paris

3.11.1 Background

In a solution, polymer chains normally assume the structure of a random coil. However, some polymers can assume an ordered helical structure [180]. The most notable examples of polymers forming helical structures include polypeptides, DNA, and RNA. The helical structure is stable within certain pressure and temperature limits and can be converted to the disordered coil structure by changing either of these parameters. The resulting helix–coil transition is a transition between the helical and coil phases. The transition has been commonly studied in proteins, which are composed of long-chain polypeptides.

In proteins, one recognizes the native and denatured states that respectively have the helical and coiled structure. From thermodynamic standpoint, the native and denatured states can coexist in equilibrium under certain temperature–pressure conditions as described by an elliptical phase diagram [181] shown in Fig. 3.74. At

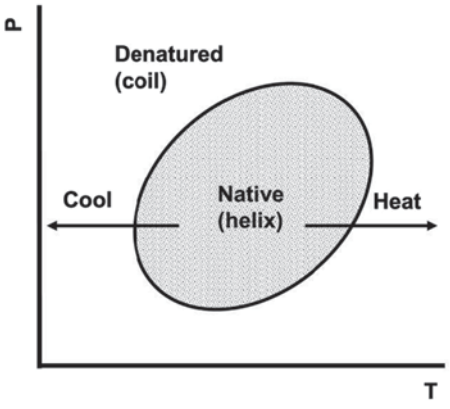

Fig. 3.74 Elliptical phase diagram of a protein. The *solid line* encompasses the area where a protein is stable in its native helical state. Outside this area a protein is stable in the denatured coiled state

a constant pressure, the helix–coil transition can be initiated by either cooling or heating. In the latter case, a protein is said to be thermally denatured. Heating of a protein causes breaking of hydrogen bonds that hold polypeptide chains in the helical conformation. As a result, the helices unfold, forming disordered coils. Since the polypeptide chains do not break but only change their conformation, the process is a phase transition somewhat similar to polymer melting. It is accompanied by significant absorption of heat that qualifies it as a first-order transition.

Unfolding of proteins is a very complex phenomenon that involves interplay of kinetic and thermodynamic factors. A largely simplified mechanism of the process was proposed by Lumry and Eyring [182].

$$\mathrm{N} \overset{K}{\Leftrightarrow} \mathrm{U} \overset{k}{\rightarrow} \mathrm{D}, \tag{3.93}$$

where N, U, and D stand respectively for the native, unfolded, and denatured states, K is the equilibrium constant of the reversible step, and k is the rate constant of the irreversible step. The model is found to be most suitable for denaturation under the conditions of high irreversibility [183]. A similar mechanism (Eq. 3.93) is used to describe the kinetics of various processes that include so-called pre-equilibria. Two most known examples are surface-catalyzed reactions that involve a reversible adsorption step (the Eley–Rideal mechanism) and enzyme-catalyzed reaction that involves a reversible formation of a bound state between the enzyme and its substrate (the Michaelis–Menten mechanism) [18]. The application of the Lumry–Eyring model to the kinetics of protein denaturation has been discussed at length in the literature [183, 184].

The rate equation for the Lumry–Eyring model is derived as follows. The rate of the formation of the denatured state is:

$$\frac{\mathrm{d}x_{\mathrm{D}}}{\mathrm{d}t} = kx_{\mathrm{U}}, \tag{3.94}$$

where x_{D} and x_{U} are respectively the mole fractions of the denatured and unfolded states. The unknown concentration of the unfolded state can be eliminated considering that the sum of all three fractions is unity, and the fraction of the native state x_{N} is related to that of the unfolded state via the equilibrium constant:

$$K = \frac{x_{\mathrm{U}}}{x_{\mathrm{N}}}. \tag{3.95}$$

Then

$$x_{\mathrm{U}} = 1 - x_{\mathrm{D}} - \frac{x_{\mathrm{U}}}{K}. \tag{3.96}$$

After some rearrangements, Eq. 3.96 converts to Eq. 3.97:

$$x_U = \frac{K}{K+1}(1 - x_D). \tag{3.97}$$

Considering that by its meaning x_D is the extent of conversion of the native to denatured state, we can replace it by customarily used α. Then substitution of Eq. 3.97 into 3.94 gives:

$$\frac{d\alpha}{dt} = \frac{kK}{K+1}(1 - \alpha). \tag{3.98}$$

Equation 3.98 can now be used to derive the effective activation energy as follows:

$$E_{ef} = -R\left[\frac{\partial \ln(d\alpha / dt)}{\partial T^{-1}}\right]_\alpha = E + \frac{\Delta H^0}{K+1}, \tag{3.99}$$

where E is the activation of the irreversible step (U → D) and ΔH^0 is the enthalpy of the reversible step (N ⇔ U). The effective activation energy obviously depends on temperature because the equilibrium constant in Eq. 3.99 is temperature dependent. The general trend of this dependence is depicted in Fig. 3.75. It suggests that in the low temperature limit, i.e., just above equilibrium, the temperature dependence of the denaturation rate should demonstrate the effective activation energy close to the sum of the activation of the irreversible step and the enthalpy of the reversible step. Note that denaturation is an endothermic process, i.e., $\Delta H^0 > 0$. However, as the process temperature shifts further from the equilibrium value, the effective activation energy should asymptotically approach the activation energy of the irreversible step.

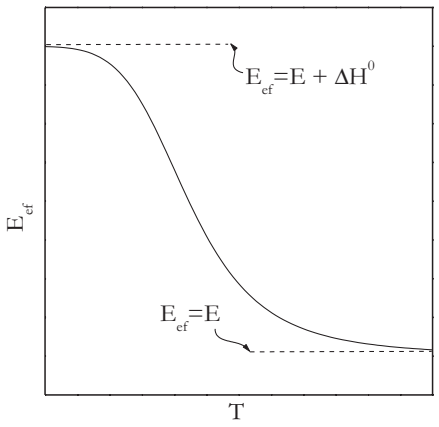

Fig. 3.75 Theoretical temperature dependence of the effective activation energy as derived from the Lumry–Eyring model (Eq. 3.99)

3.11.2 Isoconversional Treatment of Protein Denaturation

As an example of isoconversional treatment of the helix–coil transition, we consider the thermal denaturation of collagen [185]. The latter is a fibrous protein present in animal connective tissue. In its native form, collagen has a triple helical structure, whose individual strands are held together by hydrogen bonds. On heating, collagen undergoes thermal denaturation, during which the hydrogen bonds break, and the helices unfold, turning into coils. The process is accompanied by significant heat absorption that permits to monitor its kinetics by DSC.

The kinetics of the thermal denaturation of collagen and other proteins is most commonly treated as a single irreversible step N→D [186, 187], whose rate depends on temperature in accord with the Arrhenius equation. Such treatment of the collagen denaturation takes its origin in the pioneering work by Weir [188], who studied the rate of collagen shrinkage as a function of temperature. From the standpoint of the Lumry–Eyring model, the single-step treatment can be justified only in some special cases [183, 184]. For example, when denaturation occurs far from equilibrium temperature, the process can be treated as a single step describable by a constant activation energy of the irreversible step. Under other conditions, fitting the rate data to a single Arrhenius equation would yield effective activation energy whose value depends on the temperature region of measurements. The closer this region to equilibrium, the more this value would exceed the activation energy of the irreversible step and approach the sum of the activation energy of the irreversible step and the enthalpy of the reversible step.

The review papers [187, 189] report about two dozen values of the activation energy for the thermal denaturation of mammalian tissues. The range of the values is very wide (30–1300 kJ mol^{-1}). The extreme values can perhaps be explained by the strong compensation effect between the estimates of the preexponential factor and activation energy (see Sect. 2.2.2). However, a large fraction of such variation can be rationalized in terms of the temperature dependence of the effective activation energy (Eq. 3.99 and Fig. 3.75). In accord with the Lumry–Eyring model, the interval of E_{ef} variation can be as large as ΔH^0. Note that some of the literature values [190] of ΔH^0 for tissue denaturation exceed 400 kJ mol^{-1}. That is, for denaturation of exactly the same protein, the activation energy measured close to equilibrium can deviate from that measured far from equilibrium by as much as 400 kJ mol^{-1}.

Figure 3.76 displays DSC curves for the thermal denaturation of rehydrated (saturated with water) collagen. The presence of water stabilizes the denatured coiled form of collagen, which is an aqueous solution of gelatin. The process manifests itself in the form of well-defined nearly symmetrical DSC peaks. The endothermic heat of the process is around 60 J g^{-1} [191]. As expected for any kinetic process, the DSC peaks shift to higher temperature with increasing the heating rate.

The importance of the reversible step N ⇔ U in these regular DSC data is highlighted by TM DSC (Fig. 3.77). The latter demonstrates that a substantial fraction (~25 %) of the total heat flow signal arises from reversible process. This obviously lends support to the Lumry–Eyring mechanism (Eq. 3.93) and suggests that the measured kinetics is determined by both reversible and irreversible steps.

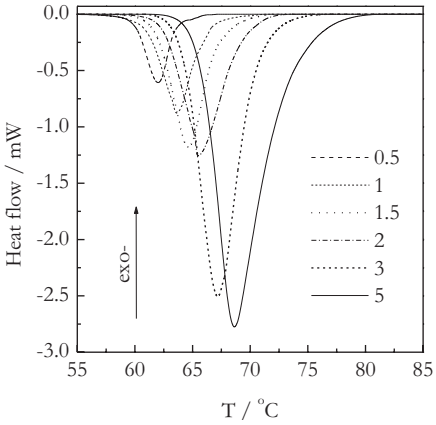

Fig. 3.76 DSC curves for the thermal denaturation of collagen in water measured at different heating rates. *Numbers by the lines* represent the heating rate in °C min^{-1}. (Reproduced from Vyazovkin et al. [185] with permission of Wiley)

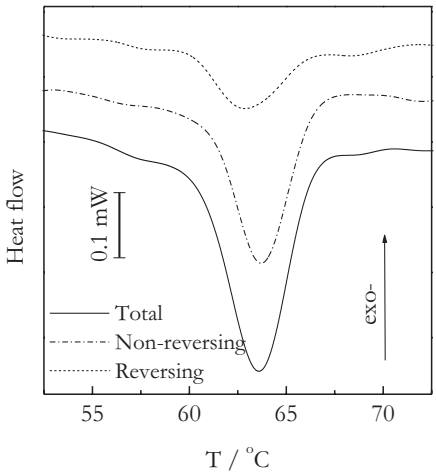

Fig. 3.77 Temperature-modulated DSC data for the thermal denaturation of collagen. The total, nonreversing, and reversing heat flow are respectively presented by *solid, dash,* and *dash-dot lines*. (Reproduced from Vyazovkin et al. [185] with permission of Wiley)

The application of an isoconversional method to the DSC data on thermal denaturation of collagen (Fig. 3.76) results in the E_α dependence seen in Fig. 3.78. Since the conversion increases with increasing temperature, the estimated dependence is consistent with the temperature dependence for the effective activation energy predicted by the Lumry–Eyring model. Undoubtedly, the model is suitable to explain the obtained isoconversional dependence of the effective activation energy. The question is whether it is suitable to extract accurate estimates of the intrinsic parameters from the E_α dependence.

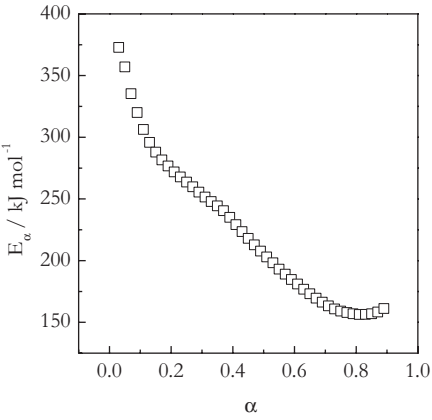

Fig. 3.78 Dependence of the effective activation energy on the extent of conversion determined by an isoconversional method. (Reproduced from Vyazovkin et al. [185] with permission of Wiley)

Clearly, E_α at $\alpha \to 1$ (Fig. 3.78) should provide an estimate for the activation energy of the irreversible step. In that region, the respective E_α values appear to approach asymptotically ~160 kJ mol^{-1}. Nevertheless, as stated earlier, most of the literature E values [187, 189] for the thermal denaturation of mammalian tissues are quite large. For example, a thermal denaturation study [192] of collagen in water in the temperature range 57–60 °C reports an activation energy 518 kJ mol^{-1}. This value is closer to the E_α at $\alpha \to 0$ (Fig. 3.78) that is associated with the lowest temperature range of the DSC data (Fig. 3.76).

E_α at $\alpha \to 0$ is approximately 370 kJ mol^{-1} that ideally should serve as an estimate for $E+\Delta H^0$. The difference between this value and 160 kJ mol^{-1}, which is an estimate for the activation energy of the irreversible step, is ~210 kJ mol^{-1}. This should give an estimate for ΔH^0. It is difficult to judge how accurate this estimate is because E_α at $\alpha \to 0$ does not demonstrate any tendency to plateau at 370 kJ mol^{-1}. Recall that the existence of the low-temperature plateau is predicted from the Lumry–Eyring model (Eq. 3.99 and Fig. 3.75). Therefore, the actual value of ΔH^0 can be larger than 210 kJ mol^{-1}. Nevertheless, this crude estimate fits fairly well within the range of the literature [190] ΔH^0 values: 190–430 kJ mol^{-1}.

The inceptive application [185] of an isoconversional method to denaturation of collagen has been followed by a series of isoconversional studies on several proteins. Several studies [193–196] have been conducted on thermal denaturation of collagen, including denaturation of dry [195] and fish [196] collagen as well as vitrified collagen gels [194]. All these studies demonstrated decreasing E_α dependencies similar to that shown in Fig. 3.78. None of these dependencies has shown a tendency to plateau at small values of α. On the other hand, decreasing E_α dependencies with a well-defined plateau at small α values has been reported [197, 198] for the thermal denaturation of the globular protein lysozyme. Also, a plateau in E_α followed by a decreasing dependence has been found [199] for thermal denaturation of keratin. On the other hand, for the thermal denaturation of bovine serum albumin, the isoconversional activation energy remains practically unchanged throughout the process [200].

References

1. Tammann G (1925) The states of aggregation. van Nostrand, New York
2. Lide DR (ed) (2002) CRC handbook of chemistry and physics, 83rd edn. CRC Press, Boca Raton
3. Debenedetti PG (1996) Metastable liquids. Concepts and principles. Princeton University Press, Princeton
4. Papon P, Leblond J, Meijer PHE (2002) The physics of phase transitions. Springer, Berlin
5. Ehrenfest P (1933) Phasenumwandlungen im ueblichen und erweiterten Sinn, classifiziert nach den entsprechenden Singularitaeten des thermodynamischen Potentiales. Proc Kon Akad Wetensch Amsterdam 36:153–157
6. Rao CNR, Rao KJ (1978) Phase transitions in solids. McGraw-Hill, New York
7. West AR (1992) Solid state chemistry and its applications. Wiley, Chichester
8. Bernstein J (2008) Polymorphism in molecular crystals. Oxford University Press, Oxford
9. Aasland S, McMillan PF (1994) Density driven liquid-liquid phase separation in the system Al_2O_3-Y_2O_3. Nature 369:633–636
10. Katayama Y, Mizutani T, Utsumi W, Shimomura O, Yamakata M, Funakoshi K (2000) A first-order liquid-liquid phase transition in phosphorus. Nature 403:170–173
11. Kurita R, Tanaka H (2004) Critical-like phenomena associated with liquid-liquid transition in a molecular liquid. Science 306:845–848
12. Kurita R, Tanaka H (2005) On the abundance and general nature of the liquid–liquid phase transition in molecular systems. J Phys Condens Matter 17:L293–L302
13. Guenet J-M (1992) Thermoreversible gelation of polymers and biopolymers. Academic, London
14. Collings PJ (2002) Liquid crystals. Nature's delicate phase of matter. Princeton University Press, Princeton
15. Langmuir I (1913) Chemical reactions at very low pressures. J Am Chem Soc 35:105–127
16. Langmuir I (1913) The vapor pressure of metallic tungsten. Phys Rev 2:329–342
17. Knudsen M (1909) Die Molekularströmung der Gase durch Offnungen und die Effusion. Ann Phys 333:999–1909
18. Atkins P, de Paula J (2010) Physical chemistry, 9th edn. W.H. Freeman, New York
19. Price DM, Hawkins M (1998) Calorimetry of two disperse dyes using thermogravimetry. Thermochim Acta 315:19–24
20. Chatterjee K, Dollimore D, Alexander K (2001) A new application for the Antoine equation in formulation development. Int J Pharm 213:31–44
21. Pieterse N, Focke WW (2003) Diffusion-controlled evaporation through a stagnant gas: estimating low vapour pressures from thermogravimetric data. Thermochim Acta 406:191–198
22. Seager SL, Geertson LR, Giddings JC (1963) Temperature dependence of gas and vapor diffusion coefficients. J Chem Eng Data 8:168–169
23. Vecchio S, Di Rocco R, Ferragina C (2008) Kinetic analysis of the oxidative decomposition in γ-zirconium and γ-titanium phosphate intercalation compounds. The case of 2,2'-bipyridyl and its copper complex formed in situ. Thermochim Acta 467:1–10
24. Vyazovkin S, Clawson JS, Wight CA (2001) Thermal dissociation kinetics of solid and liquid ammonium nitrate. Chem Mater 13:960–966
25. Cheng Y, Huang Y, Alexander K, Dollimore D (2001) A thermal analysis study of methyl salicylate. Thermochim Acta 367–368:23–28
26. Vyazovkin S, Chrissafis K, Di Lorenzo ML, Koga N, Pijolat M, Roduit B, Sbirrazzuoli N, Suñol JJ (2014) ICTAC kinetics committee recommendations for collecting experimental thermal analysis data for kinetic computations. Thermochim Acta 590:1–23
27. Prado JR, Vyazovkin S (2011) Activation energies of water vaporization from the bulk and from laponite, montmorillonite, and chitosan powders. Thermochim Acta 524:197–201
28. Ashcroft AS (1972) The measurement of enthalpies of sublimation by thermogravimetry. Thermochim Acta 2:512–514
29. Somorjai GA (1968) Mechanism of sublimation. Science 162:755–760

30. Vyazovkin S, Dranca I (2004) A DSC study of α- and β-relaxations in a PS-clay system. J Phys Chem B 108:11981–11987
31. Johari GP, Goldstein M (1970) Viscous liquids and glass transition. II. Secondary relaxation in glasses of rigid molecules. J Chem Phys 53:2372–2388
32. Williams ML, Landel RF, Ferry JD (1955) The temperature dependence of relaxation mechanisms in amorphous polymers and other glass-forming liquids. J Am Chem Soc 77:3701–3707
33. Di Marzio EA, Yang AJM (1997) Configurational entropy approach to the kinetics of glasses. J Res Natl Inst Stand Technol 102:135–157
34. Perez J, Cavaille JY (1995) Thermally stimulated creep: theoretical understanding of the compensation law. J Phys III 5:791–805
35. Vyazovkin S, Dranca I (2006) Activation energies derived from the pre-glass transition annealing peaks. Thermochim Acta 446:140–146
36. Faivre A, Niquet G, Maglione M, Fornazero J, Jal JF, David L (1999) Dynamics of sorbitol and maltitol over a wide time-temperature range. Eur Phys J B 10:277–286
37. Beiner M, Garwe F, Schroter K, Donth E (1994) Ageing effects on dynamic shear moduli at the onset of the dynamic glass transition in two poly(alkyl methacrylate)s. Polymer 35:4127–4132
38. Chen HS, Morito N (1985) Sub-Tg α′ relaxation in a PdCuSi glass; internal friction measurements. J Non-Cryst Solids 72:287–299
39. Colmenero J, Alegria A, Alberdi JM, del Val JJ, Ucar G (1987) New secondary relaxation in polymeric glasses: a possible common feature of the glassy state. Phys Rev B 35:3995–4000
40. Hodge IM (1994) Enthalpy relaxation and recovery in amorphous materials. J Non-Cryst Solids 169:211–266
41. Vyazovkin S, Dranca I (2005) Physical stability and relaxation of amorphous indomethacin. J Phys Chem B 109:18637–18644
42. Moynihan CT, Eastel AJ, Wilder J, Tucker J (1974) Dependence of the glass transition temperature of heating and cooling rate. J Phys Chem 78:2673–2677
43. Moynihan CT, Lee SK, Tatsumisago M, Minami M (1996) Estimation of activation energies for structural relaxation and viscous flow from DTA and DSC experiments. Thermochim Acta 280/281:153–162
44. Vyazovkin S, Sbirrazzuoli N, Dranca I (2006) Variation in activation energy of the glass transition for polymers of different dynamic fragility. Macromol Chem Phys 207:1126–1130
45. Adam G, Gibbs JH (1965) On the temperature dependence of cooperative relaxation properties in glass-forming liquids. J Chem Phys 43:139–146
46. Vyazovkin S, Sbirrazzuoli N, Dranca I (2004) Variation of the effective activation energy throughout the glass transition. Macromol Rapid Commun 25:1708–1713
47. Angell CA, Stell RC, Sichina W (1982) Viscosity-temperature function for sorbitol from combined viscosity and differential scanning calorimetry studies. J Phys Chem 86:1540–1542
48. Lacey D, Nestor G, Richardson MJ (1994) Structural recovery in isotropic and smectic glasses. Thermochim Acta 238:99–111
49. Hancock BC, Dalton CR, Pikal MJ, Shamblin SL (1998) A pragmatic test of a simple calorimetric method for determining the fragility of some amorphous pharmaceutical materials. Pharm Res 15:762–767
50. Badrinarayanan P, Zheng W, Simon SL (2008) Isoconversion analysis of the glass transition. Thermochim Acta 468:87–93
51. Angell CA (1991) Relaxation in liquids, polymers and plastic crystals—strong/fragile patterns and problems. J Non-Cryst Solids 131–133:13–31
52. Bohmer R, Angell CA (1993) Elastic and viscoelastic properties of amorphous selenium and identification of the phase transition between ring and chain structures. Phys Rev B 48:5857–5864
53. Bohmer R, Ngai KL, Angell CA, Plazek DJ (1993) Nonexponential relaxations in strong and fragile glass formers. J Chem Phys 99:4201–4209

54. Huang D, Colucci DM, McKenna GB (2002) Dynamic fragility in polymers: a comparison in isobaric and isochoric conditions. J Chem Phys 116:3925–3934
55. Beiner M, Huth H, Schroter K (2001) Crossover region of dynamic glass transition: general trends and individual aspects. J Non-Cryst Solids 279:126–135
56. Roland CM, Santangelo PG, Ngai KL (1999) The application of the energy landscape model to polymers. J Chem Phys 111:5593–5598
57. Nogales A, Denchev Z, Sics I, Ezquerra TA (2000) Influence of the crystalline structure in the segmental mobility of semicrystalline polymers: poly(ethylene naphthalene-2,6-dicarboxylate). Macromolecules 33:9367–9375
58. Bravard SP, Boyd RH (2003) Dielectric relaxation in amorphous poly(ethylene terephthalate) and poly(ethylene 2,6-naphthalene dicarboxylate) and their copolymers. Macromolecules 36:741–748
59. Struik LCE (1978) Physical aging in amorphous polymers and other materials. Elsevier, Amsterdam
60. Nemilov SV (2000) Physical ageing of silicate glasses at room temperature: general regularities as a basis for the theory and the possibility of a priori calculation of the ageing rate. Glass Phys Chem 26:511–530
61. Nemilov SV (2001) Physical ageing of silicate glasses at room temperature: the choice of quantitative characteristics of the process and the ranking of glasses by their tendency to ageing. Glass Phys Chem 27:214–227
62. Nemilov SV, Johari GP (2003) A mechanism for spontaneous relaxation of glass at room temperature. Philos Mag 21:3117–3132
63. Tanaka Y, Yamamoto T (2012) Enthalpy relaxation of comb-like polymer analysed by combining activation energy spectrum and TNM models. J Non-Cryst Solids 358:1687–1698
64. Petrie SEB (1972) Thermal behavior of annealed organic glasses. J Polym Sci Part A-2 10:1255–1272
65. Chen K, Vyazovkin S (2009) Isoconversional kinetics of glass aging. J Phys Chem B 113:4631–4635
66. Vyazovkin S, Dranca I (2007) Effect of physical aging on nucleation of amorphous indomethacin. J Phys Chem B 111:7283–7287
67. Donth E (2001) The glass transition: relaxation dynamics in liquids and disordered materials. Springer, Berlin
68. Rault J (2003) Ageing of glass: role of the Vogel-Fulcher-Tamman law. J Phys Condens Matter 15: S1193–S1213
69. McKenna GB, Simon SL (2002) The glass transition- its measurement and underlying physics. In: Cheng SZD (ed) Handbook of thermal analysis and calorimetry, vol 3. Elsevier, Amsterdam, pp 49–109
70. Vyazovkin S, Chen K (2007) Increase in effective activation energy during physical aging of a glass. Chem Phys Lett 448:203–207
71. Tombari E, Presto S, Salvetti G, Johari GP (2002) Spontaneous decrease in heat capacity of a glass. J Chem Phys 117:8436–8441
72. Fukao K, Sakamoto A, Kubota Y, Saruyama Y (2005) Aging phenomena in poly(methyl methacrylate) by dielectric spectroscopy and temperature modulated DSC. J Non-Cryst Solids 351:2678–2684
73. Faivre A, Niquet G, Maglione M, Fornazero J, Jal JF, David L (1999) Dynamics of sorbitol and maltitol over a wide time temperature range. Eur Phys J B 10:277–286
74. Carpentier L, Descamps M (2003) Dynamic decoupling and molecular complexity of glass-forming maltitol. J Phys Chem B 107:271–275
75. Cangialosi D, Wubbenhorst M, Schut H, van Veen A, Picken SJ (2004) Dynamics of polycarbonate far below the glass transition temperature: a positron annihilation lifetime study. Phys Rev B 69:134206-1–134206-9
76. Hu L, Yue YZ (2008) Secondary relaxation behavior in a strong glass. J Phys Chem B 112:9053

77. van den Beukel A (1986) Analysis of chemical short range ordering in amorphous Fe40Ni40B20. J Non-Cryst Solids 83:134–140
78. Koebrugge GW, Sietsma J, van den Beukel A (1992) Structural relaxation in amorphous Pd40Ni40P20. Acta Metall Mater 40:753–760
79. Bershtein VA, Egorov VM (1994) Differential scanning calorimetry of polymers: physics, chemistry, analysis, technology. Ellis Horwood Ltd, New York
80. Illers KH (1969) Einfluβ der thermischen Vorgeschichte auf die Eigenschaften von Polyvinylchlorid. Makromol Chem 127:1–33
81. Chen HS (1981) On mechanisms of structural relaxation in a Pd48Ni32P20 glass. J Non-Cryst Solids 46:289–305
82. Chen HS (1981) Kinetics of low temperature structural relaxation in two (Fe-Ni)-based metallic glasses. J Appl Phys 52:1868–1870
83. Bershtein VA, Egorov VM, Emelyanov YA, Stepanov VA (1983) The nature of β-relaxation in polymers. Polym Bull 9:98–105
84. Bershtein VA, Yegorov VM (1985) General mechanism of the β-transition in polymers. Polym Sci USSR 27:2743–2757
85. McCrum NG, Read BE, Williams G (1991) Anelastic and dielectric effects in polymeric solids. Dover, New York
86. Hedvig P (1977) Dielectric spectroscopy of polymers. Wiley, New York
87. Vyazovkin S, Dranca I (2006) Probing beta relaxation in pharmaceutically relevant glasses by using DSC. Pharm Res 23:422–428
88. Kudlik A, Benkhof S, Blochowicz T, Tschirwitz C, Rössler E (1999) The dielectric response of simple organic glass formers. J Mol Struct 479:201–218
89. Ngai KL, Capaccioli S (2004) Relation between the activation energy of the Johari-Goldstein β-relaxation and Tg of glass formers. Phys Rev E 69:031501-1–031501-5
90. Boyer RF (1976) Mechanical motions in amorphous and semi-crystalline polymers. Polymer 17:996–1008
91. Vyazovkin S (2008) Isoconversional kinetics. In: Brown ME, Gallagher PK (eds). The handbook of thermal analysis & calorimetry, vol 5: recent advances, techniques and applications. Elsevier, Amsterdam, pp 503–538
92. Turnbull D, Fisher JC (1949) Rate of nucleation in condensed systems. J Chem Phys 17:71–73
93. Mandelkern L (2004) Crystallization of polymers, vol 2. Cambridge University Press, Cambridge
94. Schultz JM (2001) Polymer crystallization. ACS & Oxford University Press, New York
95. Avrami M (1939) Kinetics of phase change. I General theory. J Chem Phys 7:1103–1112
96. Avrami M (1940) Kinetics of phase change. II Transformation time relations for random distribution of nuclei. J Chem Phys 8:212–224
97. Avrami M (1941) Granulation, phase change, and microstructure kinetics of phase change. III. J Chem Phys 9:177–184
98. Hong PD, Chung WT, Hsu CF (2002) Crystallization kinetics and morphology of poly(trimethylene terephthalate). Polymer 43:3335–3343
99. Kissinger HE (1956) Variation of peak temperature with heating rate in differential thermal analysis. J Res Natl Bur Stand 57:217–221
100. Kissinger HE (1957) Reaction kinetics in differential thermal analysis. Anal Chem 29:1702–1706
101. Vyazovkin S (2002) Is the Kissinger equation applicable to the processes that occur on cooling? Macromol Rapid Commun 23:771–775
102. Cheng SZD, Jin S (2002) Crystallization and melting of metastable crystalline polymers. In: Cheng SZD (ed) Handbook of thermal analysis and calorimetry, vol 3. Elsevier, Amsterdam, pp 167–195
103. Hoffman JD, Lauritzen JI Jr (1961) Crystallization of bulk polymers with chain folding: theory of growth of lamellar spherulites. J Res Natl Bur Stand 65A:297–336

104. Hoffman JD, Davis GT, Lauritzen JI Jr (1976) The rate of crystallization of linear polymers with chain folding In: Hannay NB (ed) Treatise on solid state chemistry, vol 3. Plenum, New York, pp 497–614
105. Toda A, Oda T, Hikosaka M, Saruyama Y (1997) A new method of analysing transformation kinetics with temperature modulated differential scanning calorimetry: application to polymer crystal growth. Polymer 38:231–233
106. Toda A, Arita T, Tomita C, Masamichi H (1999) Temperature-modulated DSC applied to the transformation kinetics of polymer crystallization. Polymer J 31:790–794
107. Vyazovkin S, Sbirrazzuoli N (2004) Isoconversional approach to evaluating the Hoffman-Lauritzen parameters (U* and Kg) from the overall rates of nonisothermal crystallization. Macromol Rapid Commun 25:733–738
108. Vyazovkin S, Dranca I (2006) Isoconversional analysis of combined melt and glass crystallization data. Macromol Chem Phys 207:20–25
109. Shultz JM, Fakirov S (1990) Solid state behavior of linear polyesters and polyamides. Prentice Hall, Engelwood Cliffs
110. Lu XF, Hay JN (2001) Isothermal crystallization kinetics and melting behaviour of poly(ethylene terephthalate). Polymer 42:9423–9431
111. Rahman MH, Nandi AK (2002) On the crystallization mechanism of poly(ethylene terepthalate) in its blends with poly(vinylidene fluoride). Polymer 43:6863–6870
112. Okamoto M, Shinoda Y, Kinami N, Okuyama T (1995) Nonisothermal crystallization of poly(ethylene terephthalate) and its blends in the injection-molding process. J Appl Polym Sci 57:1055–1061
113. Wunderlich B (2005) Thermal analysis of polymeric materials. Springer, Berlin
114. Phillips PJ, Tseng HT (1989) Influence of pressure on crystallization in poly(ethylene terephthalate). Macromolecules 22:1649–1655
115. Runt J, Miley DM, Zhang X, Gallagher KP, McFeaters K, Fishburn J (1992) Crystallization of poly(butylene terephthalate) and its blends with polyarylate. Macromolecules 25:1929–1934
116. Hwang CJ, Chen CC, Chen HL, Yang WCO (1997) Analysis of two-stage crystallization kinetics for poly(ethylene terephthalate)/ poly(ether imide) blends. Polymer 38:4097–4101
117. Chan TW, Isaev AI (1994) Quiescent polymer crystallization: modeling and measurements. Polym Eng Sci 34:461–471
118. Wu TM, Chang CC, Yu TL (2000) Crystallization of poly(ethylene terephthalate-co-isophthalate). J Polym Sci B Polym Phys 38:2515–2524
119. Bosq N, Guigo N, Zhuravlev E, Sbirrazzuoli N (2013) Nonisothermal crystallization of polytetrafluoroethylene in a wide range of cooling rates. J Phys Chem B 117:3407–3415
120. Bosq N, Guigo N, Persello J, Sbirrazzuoli N (2014) Melt and glass crystallization of PDMS and PDMS silica nanocomposites. Phys Chem Chem Phys 16:7830–7840
121. Toda A, Hikosaka M, Yamada K (2002) Superheating of the melting kinetics in polymer crystals: a possible nucleation mechanism. Polymer 43:1667–1679
122. Kovacs AJ, Gonthier A, Straupe C (1975) Isothermal growth, thickening, and melting of poly(ethylene oxide) crystals in the bulk. J Polym Sci Polym Symp 50:283–325
123. Minakov AA, Wurm A, Schick C (2007) Superheating in linear polymers studied by ultrafast nanocalorimetry. Eur Phys J E 23:43–53
124. Minakov AA, van Herwaarden AW, Wien W, Wurm A, Schick C (2007) Advanced nonadiabatic ultrafast nanocalorimetry and superheating phenomenon in linear polymers. Thermochim Acta 461:96–106
125. Toda A, Kojima I, Hikosaka M (2008) Melting kinetics of polymer crystals with an entropic barrier. Macromolecules 41:120–127
126. Sasaki T (2013) Melting of poly(ε-caprolactone) studied by step-heating calorimetry. J Therm Anal Calorim 111:717–724
127. Toda A Private communication
128. Cheng SZD (2008) Phase transitions in polymers. Elsevier, Amsterdam

129. Vyazovkin S, Yancey B, Walker K (2013) Nucleation driven kinetics of poly(ethylene terephthalate) melting. Macromol Chem Phys 214:2562–2566
130. Vyazovkin S, Burnham A K, Criado JM, Pérez-Maqueda LA, Popescu C, Sbirrazzuoli N (2011) ICTAC kinetics committee recommendations for performing kinetic computations on thermal analysis data. Thermochim Acta 520:1–19
131. Vyazovkin S, Yancey B, Walker K (2014) Polymer melting kinetics appears to be driven by heterogeneous nucleation. Macromol Chem Phys 215:205–209
132. Lippits DR, Rastogi S, Hohne GWH (2006) Melting kinetics in polymers. Phys Rev Lett 96:218303-1–218303-4
133. Illers KH (1974) Die Ermittlung des Schmelzpunktes von Kristallinen Polymeren mittels Warmeflusskalorimetrie (DSC). Eur Pol J 10:911–916
134. Thomas DG, Staveley LAK (1952) A study of the supercooling of drops of some molecular liquids. J Chem Soc 4569–4577
135. Wunderlich B (1980) Macromolecular physics, vol 3, Academic, New York
136. Maddox J (1987) Melting is merely skin-thick. Nature 330:599
137. Dash JG (1999) History of the search for continuous melting. Rev Mod Phys 71:1737–1743
138. Devoy C, Mandelkern L (1970) On the heterogeneous nucleation of long-chain molecules. J Chem Phys 52:3827–3830
139. Israelachvili J (1991) Intermolcular & surface forces, 2nd edn. Academic, Amsterdam
140. Hendricks SB, Posnjak E., Kracek FC (1932) Molecular rotation in the solid state. The variation of the crystal structure of ammonium nitrate with temperature. J Am Chem Soc 54:2766–2786
141. Mnyukh Yu (2009) Fundamentals of solid-state phase transitions, ferromagnetism and ferroelectricity, 2nd edn. Yuri Mnyukh, Farmington
142. Villafuerte-Castrejon ME, West AR (1981) Kinetics of polymorphic transitions in tetrahedral structures. Part 2. Temperature dependence of the transition $\beta \leftrightarrow \gamma$ Li2ZnSiO4. J Chem Soc Faraday Trans I 77:2297–2307
143. Balluffi RW, Allen SM, Carter WC (2005) Kinetics of materials. Wiley, Hoboken
144. Riggin MT, Knispel RR, Pintar MM (1972) Cation diffusion study in NH4NO3 by proton spin relaxation. J Chem Phys 56:2911–2918
145. Mullin JW (2002) Crystallization, 4th edn. Butterworth, Oxford
146. Campbell AN, Kartzmark EM (1969) Heats of mixing and dielectric constants of some partially miscible liquid pairs. Can J Chem 47:619–623
147. Kohler F, Rice OK (1957) Coexistence curve of the triethylamine-water system. J Chem Phys 26:1614–1618
148. Vyazovkin S, Sbirrazzuoli N (2000) Effect of viscosity on the kinetics of initial cure stages. Macromol Chem Phys 201:199–203
149. Glasstone S, Laidler K, Eyring H (1941) The theory of rate processes. McGraw-Hill, New York
150. Kartzmark EM (1967) System triethylamine-water: the equilibrium diagram and some physical properties. Can J Chem 45:1089–1091
151. Lark BS, Patyar P, Banipal TS (2007) Temperature effect on the viscosity and heat capacity behaviour of some amino acids in water and aqueous magnesium chloride solutions. J Chem Thermodyn 39:344–360
152. Flory PJ (1974) Introductory lecture. Faraday Discuss Chem Soc 57:229–241
153. de Gennes (1985) Scaling concepts in polymer physics. Cornell University Press, Ithaca
154. Tan HM, Moet A, Hiltner A, Baer E (1983) Thermoreversible gelation of atactic polystyrene solutions. Macrmolecules 16:28–34
155. Eliassaf J, Silberberg A (1962) The gelation of aqueous solutions of polymethacrylic acid. Polymer 3:555–564
156. Heymann E (1935) Studies on sol-gel transformations. I. The inverse sol-gel transformation of methylcellulose in water. Trans Faraday Soc 31:846–864
157. Doolittle AK (1946) Mechanism of solvent section. Influence of molecular size and shape on temperature dependence of solvent ability. Ind Chem Eng 38:535–540

158. Godard P, Biebuyck JJ, Daumerie M, Naveau H, Mercier JP (1978) Crystallization and melting of aqueous gelatin. J Polym Sci Polym Phys Ed 16:1817–1828
159. Domszy RC, Alamo R, Edwards CO, Mandelkern L (1986) Thermoreversible gelation and crystallization of homopolymers and copolymers. Macromolecules 19:310–325
160. Boedtker H, Doty P (1954) A study of gelatin molecules, aggregates and gels. J Phys Chem 58:968–983
161. Djabourov M, Leblond J, Papon P (1988) Gelation of aqueous gelatin solutions. I. Structural investigation. J Phys France 49:319–332
162. Guo L, Colby RH, Lusignan CP, Whitesides TH (2003) Kinetics of triple helix formation in semidilute gelatin solutions. Macromolecules 36:9999–10008
163. Flory PJ, Weaver ES (1960) Helix ↔ coil transition in dilute aqueous collagen solutions. J Am Chem Soc 82:4518–4525
164. Guigo N, Sbirrazzuoli N, Vyazovkin S (2012) Atypical gelation in gelatin solutions probed by ultra fast calorimetry. Soft Matter 8:7116–7121
165. Chen K, Vyazovkin S (2009) Temperature dependence of sol-gel conversion kinetics in gelatin-water system. Macromol Biosci 9:383–392
166. Ohkura M, Kanaya T, Kaji K (1992) Gelation rates of poly(vinyl alcohol) solution. Polymer 33:5044–5048
167. Malik S, Jana T, Nandi AK (2001) Thermoreversible gelation of regioregular poly(3-hexylthiophene) in xylene. Macromolecules 34:274–282
168. Dikshit AK, Nandi AK (2001) Gelation mechanism of thermoreversible gels of poly(vinylidene fluoride) and its blends with poly(methyl acrylate) in diethyl azelate. Langmuir 17:3607–3615
169. Chen K, Baker AN, Vyazovkin S (2009) Concentration effect on temperature dependence of gelation rate in aqueous solutions of methylcellulose. Macromol Chem Phys 210:211–216
170. Harrington WF, Rao NV (1970) Collagen structure in solution. I. Kinetics of helix regeneration in single-chain gelatins. Biochemistry 9:3714–3724
171. Eagland D, Pilling G, Wheeler RG (1974) Studies of the collagen fold formation and gelation in solutions of a monodisperse α gelatin. Faraday Discuss 57:181–200
172. Michon C, Cuvelier G, Launay B (1993) Concentration dependence of the critical viscoelastic properties of gelatin at the gel point. Rheol Acta 32:94–103
173. Kobayashi K, Huang C, Lodge TP (1999) Thermoreversible gelation of aqueous methylcellulose solutions. Macromolecules 32:7070–7077
174. Stolin AM, Merzhanov AG, Malkin AYa (1979) Non-isothermal phenomena in polymer engineering and science: a review-2. Non-isothermal phenomena in polymer deformation. Polym Eng Sci 19:1074–1080
175. Takahashi M, Shimazaki M, Yamamoto J (2001) Thermoreversible gelation and phase separation in aqueous methyl cellulose solutions. J Polym Sci B 39:91–100
176. Guigo N, Sbirrazzuoli N, Vyazovkin S (2012) Gelation on heating of supercooled gelatin solutions. Macromol Rapid Commun 33:698–702
177. Zhuravlev E, Schmelzer JWP, Wunderlich B, Schick C (2011) Kinetics of nucleation and crystallization in poly(ε-caprolactone) (PCL). Polymer 52:1983–1997
178. Dranca I, Vyazovkin S (2009) Thermal stability of gelatin gels: effect of preparation conditions on the activation energy barrier to melting. Polymer 50:4859–4867
179. te Nijenhuis K (1981) Investigation into the ageing process in gels of gelatin/water systems by the measurement of their dynamic moduli—Part II: mechanism of the ageing process. Colloid Polym Sci 259:1017–1026
180. Teramoto A (2001) Cooperative conformational transitions in linear macromolecules undergoing chiral perturbations. Prog Polym Sci 26:667–720
181. Smeller L (2002) Pressure-temperature phase diagrams of biomolecules. Biochim Biophys Acta 1595:11–29
182. Lumry R, Eyring H (1954) Conformation changes of proteins. J Phys Chem 58:110–120

183. Lepock JR, Ritchie KP, Kolios MC, Rodahl AM, Heinz KA, Kruuv J (1992) Influence of transition rates and scan rate on kinetic simulations of differential scanning calorimetry profiles of reversible and irreversible protein denaturation. Biochemistry 31:12706–12712
184. Sanchez-Ruiz JM (1992) Theoretical analysis of Lumry-Eyring models in differential scanning calorimetry. Biophys J 61:921–935
185. Vyazovkin S, Vincent L, Sbirrazzuoli N (2007) Thermal denaturation of collagen analyzed by isoconversional method. Macromol Biosci 7:1181–1186
186. Wright NT, Humphrey JD (2002) Denaturation of collagen via heating: an irreversible rate process. Annu Rev Biomed Eng 4:109–128
187. Bischof JC, He XM (2005) Thermal stability of proteins. Ann NY Acad Sci 1066:1–22
188. Weir CE (1949) Effect of temperature on the volume of leather and collagen in water. J Res Nat Bur Stand 42:17–32
189. Wright NT (2003) On a relationship between the Arrhenius parameters from thermal damage studies. J Biomed Eng 125:300–304
190. Jacques SL (2006) Ratio of entropy to enthalpy in thermal transitions in biological tissues. J Biomed Opt 11:041108-1–041108-7
191. Miles CA, Ghelashvili M (1999) Polymer-in-a-box mechanism for the thermal stabilization of collagen molecules in fibers. Biophys J 76:3243–3252
192. Miles CA, Burjanadze TV, Bailey AJ (1995) The kinetics of the thermal denaturation of collagen in unrestrained rat tail tendon determined by differential scanning calorimetry. J Mol Biol 245:437–446
193. Liu W, Li G (2010) Non-isothermal kinetic analysis of the thermal denaturation of type I collagen in solution using isoconversional and multivariate non-linear regression methods. Polym Degrad Stab 95:2233–2240
194. Xia Z, Calderon-Colon X, Trexler M, Elisseeff J, Guo Q (2012) Thermal denaturation of type I collagen vitrified gels. Thermochim Acta 527:172–179
195. Budrugeac P, Cucos A (2013) Application of Kissinger, isoconversional multivariate nonlinear regression methods for evaluation of the mechanism and kinetic parameters of phase transitions of type I collagen. Thermochim Acta 565:241–252
196. Liu W, Tian Z, Li C, Li G (2014) Thermal denaturation of fish collagen in solution: a calorimetric and kinetic analysis. Thermochimica Acta 581:32–40
197. Cao X, Wang Z, Liu Y, Wang C, Tian Y (2010) Effect of additive on the thermal denaturation of lysozyme analyzed by isoconversional method. Acta Chim Sinica 68:194–198
198. Cao X, Tian Y, Wang Z, Liu Y, Wang C (2014) Protein denaturation kinetic processes of a simple and a complex reaction mechanism analyzed by an iso-conversional method. J Therm Anal Calorim 117:1489–1495
199. Istrate D, Popescu C, Moller M (2009) Non-isothermal kinetics of hard α-keratin thermal denaturation. Macromol Biosci 9:805–812
200. Cao X, Li J, Yang X, Duan Y, Liu Y, Wang C (2008) Nonisothermal kinetic analysis of the effect of protein concentration on BSA aggregation at high concentration by DSC. Thermochim Acta 467:99–106

Chapter 4
Chemical Processes

4.1 Introduction

Why do I like chemistry? Why do you like apples?—by virtue of our sensations. It's all the same thing. Deeper than that men will never penetrate.

Ivan Turgenev, Fathers and Children.

The processes of transitions between the phases considered in Chap. 3 are both diverse and complex. Nevertheless, they cannot compare in the diversity and complexity with chemical reactions. Generally, all phase transitions boil down to spatial rearrangement of molecules, atoms, or ions that remain essentially unchanged. Chemical reactions go much further; they destroy the chemical bonds between the atoms, changing the reactant molecules to the molecules of reaction products.

When a chemical reaction is stimulated thermally, it rarely occurs in a single step, yielding a single set of reaction products. This is because heat is not a very selective reaction stimulus. Rising temperature increases the amplitude of vibration of all chemical bonds in a molecule. Once the amplitude reaches a critical size for a bond of a particular strength, the bond breaks. However, the respective level of thermal energy would also be sufficient to break a somewhat stronger bond, although with a somewhat lower probability. For example, when heated to sufficiently high temperature, an ethanol molecule would break its carbon–carbon bond first because it has the lowest (~370 kJ mol^{-1} [1]) dissociation enthalpy of all bonds in the molecule. However, the same temperature would be sufficient to break the carbon–oxygen bond whose dissociation enthalpy is about 380 kJ mol^{-1} [1]. Therefore, the thermal decomposition of ethanol would occur via at least two steps that compete with each other:

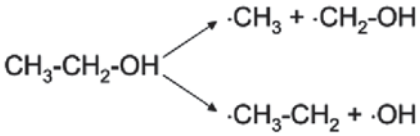

S. Vyazovkin, *Isoconversional Kinetics of Thermally Stimulated Processes,*
DOI 10.1007/978-3-319-14175-6_4

In addition to their tendency to involve multiple steps, the thermally stimulated reactions tend to involve multiple phases. For instance, the thermal decomposition of solid calcium carbonate produces solid- and gas-phase products:

$$CaCO_{3(s)} \rightarrow CaO_{(s)} + CO_{2(g)}.$$

Ammonium nitrate can be decomposed in the solid phase:

$$NH_4NO_{3(s)} \rightarrow NH_{3(g)} + HNO_{3(g)},$$

when heated below its meting temperature, and in the liquid phase:

$$NH_4NO_{3(l)} \rightarrow NH_{3(g)} + HNO_{3(g)},$$

when heated above the melting temperature. During the thermal liquid-state polymerization, the forming polymer product can undergo a phase transition from liquid to glass (when the process temperature is below the glass transition temperature) or from liquid to crystal (when the process temperature is below the melting temperature).

These are just a few examples that demonstrate the wealth of the phase and reaction situations in which thermally stimulated reactions can occur. This complicates the reaction kinetics to the degree when each chemical reaction has some unique kinetic features. Nevertheless, even in this situation, one can use isoconversional methods to identify some general features and, therefore, get a hint at the reaction mechanisms. In the following sections of this chapter, we discuss the application of isoconversional methods to the three largest classes of chemical reactions: polymerization and cross-linking, degradation of polymers, and decomposition of solids.

Unlike in the case of phase transitions, the application of the isoconversional methods to chemical reactions is several decades old. As already mentioned in Chap. 2, the history of isoconversional methods starts by Kujirai and Akahira's [2] application of the isothermal isoconversional method to the thermal degradation of natural fibers. It was successfully continued by the inventors of nonisothermal isoconversional methods. Friedman [3] applied his method to the thermal degradation of a phenolic plastic, and Ozawa [4] used his method on the thermal degradation of nylon 6 and the thermal decomposition of calcium oxalate. In the area of polymerization and cross-linking, the first application appears to date back to the work of Barton [5], who proposed a simplified version of the Friedman method and applied it to the reaction of epoxy–amine curing.

4.2 Polymerization and Cross-Linking

See plastic Nature working to this end,
The single atoms each to other tend,
Attract, attracted to, the next in place,
Form'd and impell'd its neighbour to embrace.
Alexander Pope, An Essay on Man

4.2.1 Background to Polymerization

Polymerization is a process of linking of small molecules (monomers) into a long molecular chain (polymer). In many monomers, polymerization can be initiated by increasing temperature giving rise to the so-called thermal polymerization. The process is initiated by bond breaking in a monomer molecule (M) that gives rise to highly reactive free radical species (M·). The latter can then react with the monomer yielding a macroradical that starts the growth of a polymer chain:

$$\mathrm{M}\cdot + \mathrm{M} \rightarrow \mathrm{MM}\cdot$$

$$\mathrm{MM}\cdot + \mathrm{M} \rightarrow \mathrm{MMM}\cdot$$

The mechanism can be summarized as follows:

$$\mathrm{M}_n\cdot + \mathrm{M} \overset{k_\mathrm{p}}{\rightarrow} \mathrm{M}_{n+1}\cdot, \tag{4.1}$$

where k_p is the rate constant of propagation.

Polymer chain propagation can be reversible:

$$\mathrm{M}_n\cdot + \mathrm{M} \underset{k_\mathrm{dp}}{\overset{k_\mathrm{p}}{\Leftrightarrow}} \mathrm{M}_{n+1}\cdot, \tag{4.2}$$

with the reverse process being depropagation. To occur spontaneously, the process of polymerization has to be exothermic, which is unavoidable because of a dramatic decrease in the entropy that accompanies polymerization. As for any exothermic process, an increase in temperature shifts equilibrium toward reactants, i.e., the monomer (4.2). At a certain temperature, the rate constants of propagation and depropagation (k_dp) become equal. At this point, a change in the Gibbs free energy,

$$\Delta G = -RT \ln K = -RT \ln\left(\frac{k_\mathrm{p}}{k_\mathrm{dp}}\right), \tag{4.3}$$

becomes zero so that polymerization would reach equilibrium. This brings about the concept of ceiling temperature, i.e., the temperature above which a monomer cannot

polymerize. Below this temperature, the equilibrium constant, *K,* is larger than 1. Then ΔG is negative and polymerization proceeds spontaneously.

In its simplest form, the kinetics of radical polymerization includes several steps [6]. The chief step is propagation of the polymer chain, whose rate according to Eq. 4.1 is proportional to the concentrations of the monomer and radical species as follows:

$$r_p = k_p[M][M\cdot]. \tag{4.4}$$

The radicals are produced in the initiation step:

$$M + M \xrightarrow{k_i} 2M\cdot. \tag{4.5}$$

The step is written as a bimolecular reaction because it normally has a significantly lower energy barrier than unimolecular bond breaking. The rate of bimolecular initiation is:

$$r_i = 2k_i[M]^2. \tag{4.6}$$

On the other hand, the radicals are consumed in the termination step:

$$M\cdot + M\cdot \xrightarrow{k_t} 2M. \tag{4.7}$$

The rate of termination is:

$$r_t = 2k_t[M\cdot]^2. \tag{4.8}$$

Under the steady-state conditions, $r_i = r_t$ so that the concentration of radicals with account of both the initiation and termination steps can be expressed as:

$$[M\cdot] = \left(\frac{k_i}{k_t}\right)^{\frac{1}{2}}[M]. \tag{4.9}$$

The substitution of Eq. 4.9 into Eq. 4.4 yields the overall rate of polymerization [6]:

$$r_p = k_p\left(\frac{k_i}{k_t}\right)^{\frac{1}{2}}[M]^2 = k_{ef}[M]^2. \tag{4.10}$$

Equation 4.10 is essential for understanding the meaning of effective activation energy of polymerization. This value is obtainable by taking the logarithmic derivative of k_{ef} :

$$E_{\mathrm{ef}} = -R\left(\frac{\mathrm{d}\ln k_{\mathrm{ef}}}{\mathrm{d}T^{-1}}\right) = E_{\mathrm{p}} + (E_{\mathrm{i}} - E_{\mathrm{t}})/2. \tag{4.11}$$

Equation 4.11 clearly suggests that the activation energy of polymerization is a composite value that involves a combination of the activation energies for propagation (E_{p}), initiation (E_{i}), and termination (E_{t}).

Polymerization is usually performed in the presence of an initiator such as benzoyl peroxide or azobis(isobutyronitrile). These are compounds that readily produce radical species (R·) on heating to moderate temperatures. The presence of an initiator (I) changes the initiation step (Eq. 4.5) to:

$$\mathrm{I} \xrightarrow{k_{\mathrm{i}}} 2\mathrm{R}\cdot. \tag{4.12}$$

As a result, the propagation and termination steps change as well:

$$\mathrm{RM}_n\cdot + \mathrm{M} \xrightarrow{k_{\mathrm{p}}} \mathrm{RM}_{n+1}\cdot \tag{4.13}$$

$$\mathrm{RM}_n\cdot + \mathrm{RM}_m\cdot \xrightarrow{k_{\mathrm{t}}} \mathrm{RM}_{n+m}\mathrm{R}. \tag{4.14}$$

By using the same reasoning as above, one can arrive at the rate equation for polymerization in the presence of an initiator that has the following form:

$$r_{\mathrm{p}} = k_{\mathrm{p}}\left(\frac{k_{\mathrm{i}}}{k_{\mathrm{t}}}\right)^{\frac{1}{2}}[\mathrm{M}][\mathrm{I}]^{\frac{1}{2}} = k_{\mathrm{ef}}[\mathrm{M}][\mathrm{I}]^{\frac{1}{2}}. \tag{4.15}$$

Because k_{ef} in Eq. 4.15 is identical to that in Eq. 4.10, the effective activation energy for polymerization in the presence of an initiator can also be expressed by Eq. 4.11, although the key difference is that the E_{i} value would then be the activation energy for degradation of the initiator (Eq. 4.12) rather than the monomer (Eq. 4.5).

With regard to the three steps involved in the aforementioned mechanism, one may expect that at the early stages, before the steady state sets in, the polymerization kinetics is determined by initiation. Then the effective activation energy would be that of the initiation step. Once the steady state is established, it would change to the value determined by Eq. 4.11.

Of course, the three-step kinetic model cannot represent adequately the full complexity of the polymerization kinetics. For example, it misses entirely the effects of diffusion on the kinetics. The effects become increasingly important as the polymer chains grow and the reaction medium becomes progressively more viscous, slowing down the molecular mobility. One such effect is known as the Trommsdorff [7] and Norrish [8] effect. It is detected as dramatic acceleration of the polymerization rate that takes place upon attaining some advanced degree of polymerization. It was

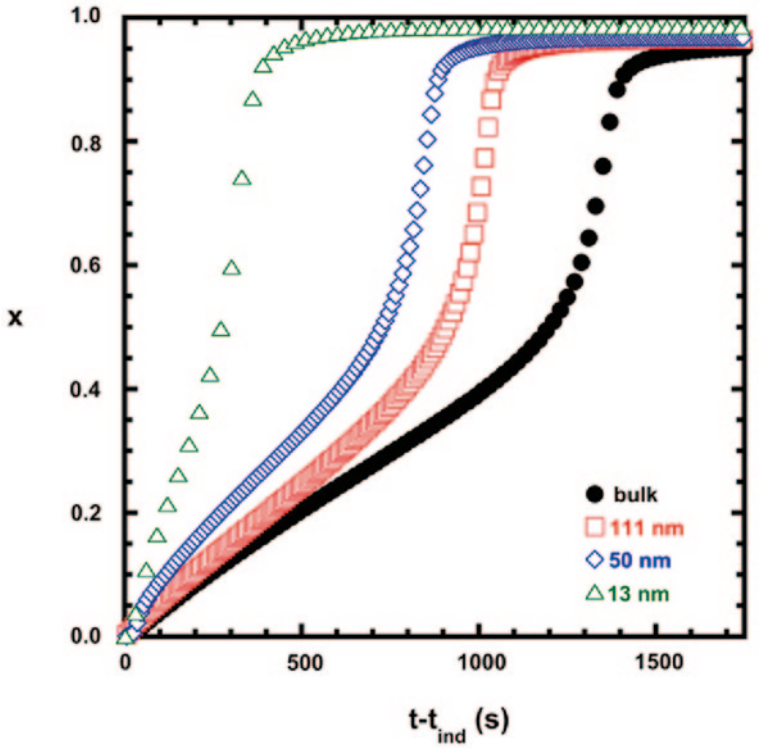

Fig. 4.1 Evolution of conversion during isothermal (80 °C) polymerization of methyl methacrylate in bulk and in hydrophilic nanopores of different diameter (13, 50, and 111 nm). (Reproduced from Zhao and Simon [10] with permission of Elsevier)

originally observed in the polymerization of methyl methacrylate and explained [7–9] by deceleration of the termination step (4.7). Indeed, an increase in viscosity of the medium first of all affects large molecules (i.e., macroradicals) that would take longest time to diffuse toward each other before they react.

An example of the Trommsdorff–Norrish effect is seen in Fig. 4.1 that displays some kinetic data [10] on the polymerization of methyl methacrylate in bulk and nanopores. The initial stages of polymerization demonstrate the decelerating, i.e., reaction-order type of kinetics (see Fig. 1.5). However, when the conversion reaches ~0.4, the rate suddenly accelerates, revealing a sharp increase in conversion.

The rate acceleration due to the Trommsdorff–Norrish effect should affect the effective activation energy. The trend can be predicted roughly from Eq. 4.11. Since the contribution of the termination step to the overall rate of polymerization becomes negligibly small relative to the two other steps, we can expect the E_t term to vanish. This means that the Trommsdorff–Norrish effect should be expected to cause an increase in the effective activation energy of polymerization.

The Trommsdorff–Norrish effect is not the only diffusion effect encountered during polymerization. As the molecular weight of the forming polymer rises and the reaction medium turns more and more viscous, the reaction system can vitrify, i.e., turn from the liquid to glassy state. This happens when the glass transition temperature of the monomer–polymer mixture rises above the polymerization temperature. When polymerization starts ($\alpha = 0$), the glass transition temperature of the reacting system is the same as that of the monomer, $T_{g,m}$. When it is finished ($\alpha = 1$), the glass transition temperature of the reacting system becomes that of the polymer, $T_{g,p}$. At any intermediate conversion, the value of T_g can be approximated by the Fox equation [11]:

$$\frac{1}{T_g} = \frac{1-\alpha}{T_{g,m}} + \frac{\alpha}{T_{g,p}}. \tag{4.16}$$

The resulting variation of the glass transition temperature of the reacting system as a function of conversion from monomer to polymer is shown in Fig. 4.2. An important conclusion arising from this temperature versus conversion diagram is that if polymerization is carried out at a temperature below the glass transition temperature of the final polymer, the system would vitrify at some $\alpha < 1$, i.e., before reaching complete polymerization. From the standpoint of the polymerization kinetics, this is a dramatic event. Since the molecular mobility in the glassy state is practically frozen, polymerization virtually stops at α of vitrification.

Incomplete polymerization due to vitrification is readily detectable calorimetrically under isothermal conditions. If the amount of heat released during polymerization increases systematically with increasing polymerization temperature and tends to some ultimate value, it is a good indication that the reacting system vitrifies before reaching complete conversion of a monomer to the polymer. Figure 4.3 provides a typical example of incomplete conversion in isothermal polymerization

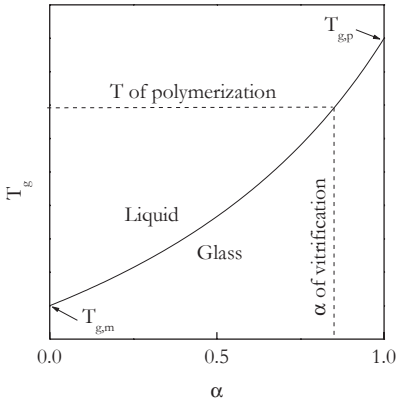

Fig. 4.2 The *solid line* separates the liquid and glassy states of a reacting system "monomer → polymer." When T_g reaches the temperature of isothermal polymerization, the system vitrifies before reaching complete conversion

of 2-hydroxyethyl methacrylate [12]. The glass transition temperature of poly(2-hydroxyethyl methacrylate) is reported [13, 14] to be around 90 °C. That is, all polymerization runs in Fig. 4.3 are conducted below the glass transition temperature of the polymer product. The lower the polymerization temperature falls below the glass transition temperature of the polymer, the smaller the conversion at which the reacting system vitrifies. If at 80 °C the systems vitrifies at $\alpha \sim 0.9$, at 50 °C the α value of vitrification is around 0.75. These results are obviously consistent with the general trend shown in Fig. 4.2.

It should be noted that vitrification of a reaction system introduces significant complications into the polymerization kinetics. Examples of such complications are discussed later. At this point, it should be mentioned that in most of polymerizing systems the isothermal kinetic measurements have to be performed at temperatures below the glass transition temperature of the polymer product. This is because above this temperature polymerization is too fast to follow with regular experimental techniques as differential scanning calorimetry (DSC). For example, it is seen from Fig. 4.3 that at 80 °C the process is completed in less than 10 min. Increasing temperature above 90 °C, which is approximately the glass transition temperature of the polymer, would reduce the completion time to a few minutes. For a typical DSC instrument, this would be insufficient time to equilibrate before taking the measurements that would deem the latter impossible.

It is much simpler to avoid vitrification when performing kinetic measurements under nonisothermal conditions. Simple heating at a constant heating rate may result in three different situations with respect to vitrification during polymerization. They are illustrated in Fig. 4.4 (curves 1, 2, and 3). When heating occurs at a slow heating rate, at some extent of conversion (point A on curve 1 in Fig. 4.4), the glass transition temperature of the monomer–polymer system may rise above the sample temperature. At this point, the system would vitrify causing polymerization to slow down dramatically or practically stop. However, if temperature continues to rise, it will ultimately reach the $T_{g,p}$ value. Then the glassy system would convert back to the liquid state and polymerization would resume. A similar process may occur at

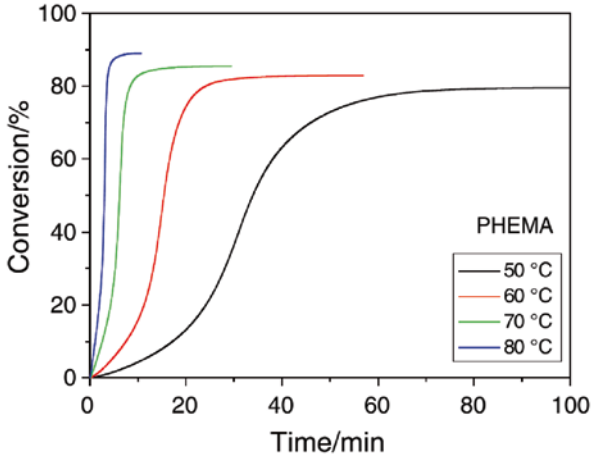

Fig. 4.3 Isothermal polymerization of 2-hydroxyethyl methacrylate at different temperatures. (Reproduced from Achilias [12] with permission of Springer)

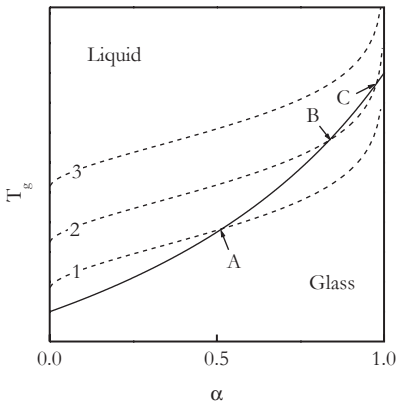

Fig. 4.4 The *solid line* separates the liquid and glassy states (see Fig. 4.2). Polymerization is performed under rising temperature conditions. *Dashed lines* 1, 2, and 3 represent variation of sample temperature at successively faster heating rates. *Points* A, B, and C represent conversions and temperatures of transition between the liquid and glass phases

some intermediate heating rate (curve 2 in Fig. 4.4). Just as in the previous situation, the system vitrifies at some intermediate extent of reaction (point B). However, at some point (point C), the rise of the sample temperature outruns the rise of the glass transition temperature of the monomer–polymer system. At this point, the system would devitrify promoting further polymerization. Finally, the third situation (curve 3 in Fig. 4.4) occurs at faster heating rates. That would be the heating rates at which the sample temperature rises faster than the glass transition temperature of the monomer–polymer system. Then, the whole polymerization process would take place in the liquid state without vitrification.

Even if vitrification does not happen, the kinetics of the later stages of polymerization is likely to be limited by the process of diffusion. However, vitrification makes the transition from a kinetic to diffusion regime more evident. At any rate, the transition between the two regimes can usually be detected as a change in the effective activation energy of the polymerization process. The change is easy to understand if we consider a typical bimolecular reaction (e.g., a monomer and radical) as a sequence of two steps:

$$\mathrm{A} + \mathrm{B} \overset{k_D}{\rightarrow} \mathrm{A} \cdots \mathrm{B} \overset{k_R}{\rightarrow} \mathrm{AB} \tag{4.17}$$

Before the species A and B can react and form the product AB, they have to approach each other at sufficiently close distance and assume a proper reaction orientation. This is accomplished through molecular motion, i.e., diffusion. The rate of this process is determined by the diffusion rate constant k_D. Once the species accomplish an appropriate reaction situation, a chemical reaction takes place. Its rate is determined by the reaction rate constant, k_R.

At the initial stages of the process (4.17), the viscosity of the reaction medium is low and molecular mobility is fast. Under this circumstance, k_D is likely to be significantly larger than k_R so that the rate of the whole process is determined by the slowest step which is the chemical reaction. It means that the effective activation

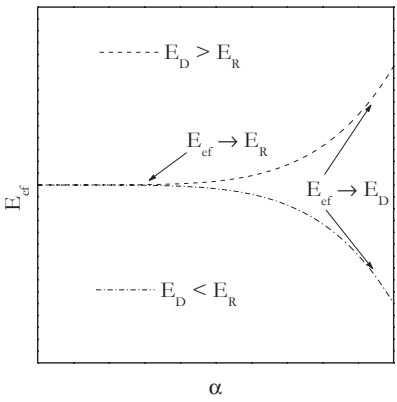

Fig. 4.5 A change from kinetic to diffusion regime is accompanied by a change in the effective activation energy of polymerization

energy of the initial stages should be close to the activation energy of the chemical reaction, E_R (Fig. 4.5). As polymerization advances, the molecular weight of the polymer product increases and viscosity of the reaction medium rises. This slows down the molecular mobility, and at some point the rate of diffusion would drop below the rate of the chemical reaction. That is, k_D would become smaller than k_R. Again, the overall process rate still would be limited by the slowest step, which at this stage of the process is diffusion. The further the process progresses into diffusion regime, the closer the effective activation energy approaches the activation energy of diffusion (Fig. 4.5). Note that the respective dependencies of the effective activation energy on conversion have been previously obtained [15] for a process involving two consecutive reactions.

It should be emphasized that, as shown in Fig. 4.5, a transition from a kinetic to diffusion regime can be accompanied by either decrease or increase in the effective activation energy. A particular type of dependence is defined by the relative values of E_R and E_D. If E_D is larger than E_R, the dependence increases. However, it decreases when E_D is smaller than E_R. Generally, the E_D values for diffusion of molecules inside a polymer can take on values from a rather wide range. To be more specific, the experimentally measured E_D values have been reported [16, 17] to be as small as 10 and as large as 160 kJ mol^{-1}. One of the key factors that define the magnitude of E_D is the size of the diffusing molecule. Generally, the larger the diffusing molecule the bigger the activation energy of its diffusion is. Therefore, if the process rate in the diffusion regime is determined by diffusion of large molecules such as polymer chains or their long segments, the E_D value is likely to be larger than E_R. On the other hand, when the rate is limited by diffusion of small molecules such as a monomer or a short segment of a polymer chain, the E_D value can be expected to be smaller than E_R.

4.2.2 Isoconversional Treatment of Polymerization

Because polymerization produces a significant amount of heat, the kinetics of the process is convenient to follow by means of DSC. The application of an

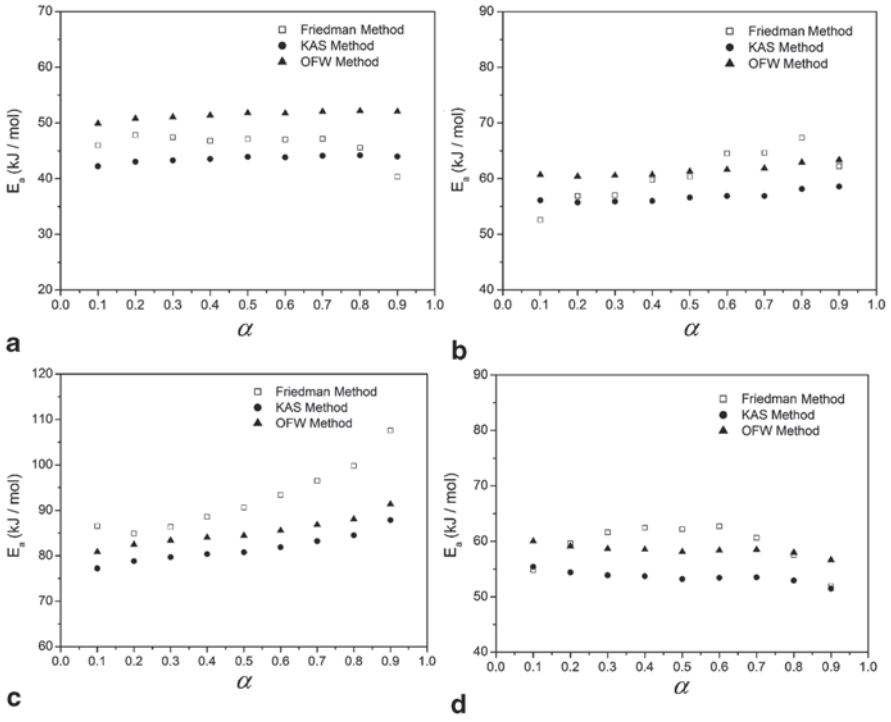

Fig. 4.6 The E_α dependencies obtained for polymerization of ε-caprolactone by isoconversional methods of Friedman, Kissinger–Akahira–Sunose (*KAS*), and Ozawa and Fynn and Wall (*OFW*). The initiators used are: (**a**) Ti(IV)*n*-propoxide, (**b**) Ti(IV)*n*-butoxide, (**c**) Ti(IV)*tert*-butoxide, (**d**) Ti(IV)2-ethylhexoxide. (Reproduced from Meelua et al. [18] with permission of Springer)

isoconversional method to DSC data yields a certain type of the E_α versus α dependencies that can be interpreted in terms of the reaction mechanisms discussed in the previous section. Let us consider some examples of the dependencies reported in the literature.

In the simplest case, the effective activation energy can be found practically invariable throughout polymerization. An example of such behavior has been reported [18] for ring-opening polymerization of ε-caprolactone initiated by a series of titanium (IV) alkoxides. As seen in Fig. 4.6, the application of isoconversional methods results in obtaining the E_α values that remain nearly constant as ε-caprolactone is converted to poly(ε-caprolactone). It is noteworthy that the activation energies differ by more than 30 kJ mol^{-1} depending on the initiator. Apparently, the observed difference in the E_α values is due to the difference in the activation energy of initiation (E_i) in Eq. 4.11. Surprisingly, the dependence of the activation energy on conversion does not show any changes associated with a transition from a kinetic to diffusion regime. However, it should not be entirely unexpected if one considers the temperature of polymerization relative to the temperatures of the glass transition and melting of poly(ε-caprolactone). Polymerization of ε-caprolactone commences above 150 °C [18]. This temperature is significantly higher than $T_g = -64$ °C and

$T_m = 69$ °C of poly(ε-caprolactone) [19]. It means that the process takes place in the melt, whose temperature is well above the polymer melting point. Under such conditions, the reacting system is likely to have very low viscosity so that the whole process of polymerization occurs in the kinetic regime, i.e., $k_D \gg k_R$ in Eq. 4.17. In other words, the E_α values determined for this process are the values of the chemical reaction.

A transition from a kinetic to diffusion regime is commonly found in the systems that vitrify during polymerization. As already explained, this would be the case of either isothermal polymerization at temperatures below the glass transition temperature of the polymer product (Fig. 4.2) or nonisothermal polymerization at relatively slow heating rates (Fig. 4.4). For example, the application of an isoconversional method to the data on isothermal polymerization of 2-hydroxyethyl methacrylate (Fig. 4.3) gives rise to the conversion dependence of the effective activation energy shown in Fig. 4.7. The kinetics of the initial stages of the polymerization ($\alpha < 0.2$) occurs in the kinetic mode, as normally is the case of all polymerization reactions. It is frequently found that the largest values of E_α are estimated at $\alpha \to 0$. This is because the activation energy of initiation is typically larger than that of propagation and termination. Therefore, in the early stages, before the steady-state regime sets in, $E_{\alpha \to 0}$ is close to E_i. Once the steady-state regime becomes operative, E_α drops to the value defined by Eq. 4.11. Note that, for the reactions of polymerization, $E_p - E_t/2$ is usually about 10–20 kJ mol^{-1} (see, for example, the E_p and E_t data found in Stevens [20]). If the activation energy of initiation of polymerization of 2-hydroxyethyl methacrylate is about 100 kJ mol^{-1} ($E_{\alpha \to 0}$), then upon reaching the

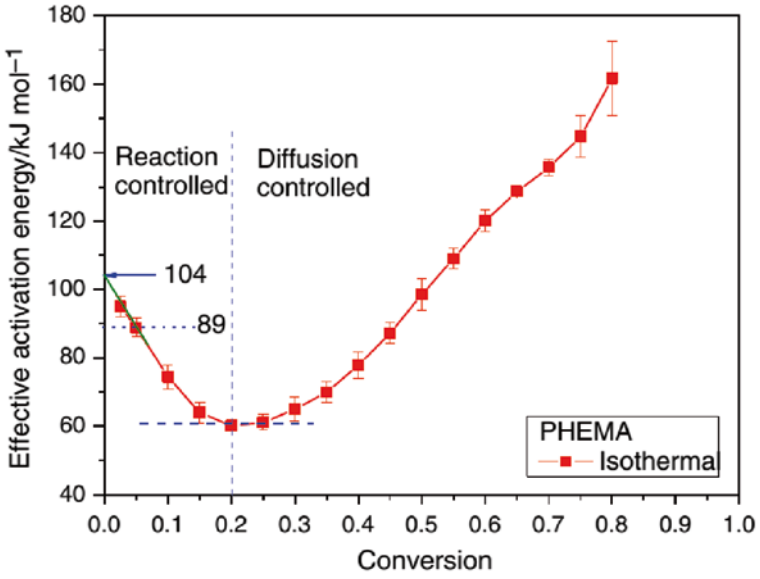

Fig. 4.7 E_α dependence for isothermal polymerization of 2-hydroxyethyl methacrylate (data in Fig. 4.3). (Reproduced from Achilias [12] with permission of Springer)

steady state E_α should drop (see Eq. 4.11) to about 60–70 kJ mol^{-1}, which is approximately E_α at $\alpha = 0.2$ in Fig. 4.7.

As polymerization progresses further, the rate control changes from a kinetic to diffusion regime as reflected in the E_α dependence that begins to climb up to the larger values of the activation energy past $\alpha = 0.2$ (Fig. 4.7). The increasing character of the dependence indicates (see Fig. 4.5) that the rate is limited by the mobility of large molecules or long segments of the polymer chains. Note that diffusion control becomes operative long before the reaction system vitrifies. As seen from Fig. 4.3, complete vitrification of the reaction system depends on temperature and occurs roughly at $\alpha = 0.7$. It is important to realize that the primary cause of a change from kinetic to diffusion control is an increase in viscosity that may or may not lead to vitrification.

It should also be kept in mind that, if it occurs, vitrification is smeared over a wide range of conversions because of the molecular weight distribution of the forming polymer product. This is illustrated in Fig. 4.8 that presents a dependence of the glass transition temperature on the number average molecular weight of polystyrene (PS) [11]. If styrene is polymerized at 80 °C, the forming PS can be expected to vitrify when M_n exceeds the value, for which T_g is 80 °C. The respective M_n is ~9000 g mol^{-1}. However, when the number average molecular weight of PS is 9000 g mol^{-1}, there are significant fractions of the polymer that have smaller and larger M_n values. The distribution of the molecular weights is equivalent to the distribution of the glass transition temperatures (Fig. 4.8). It means that vitrification would start with the fractions of higher molecular weight as soon as their T_g rises above the temperature of polymerization. At the same time, the polymer chains of lower molecular weight would still possess the liquid-state mobility and continue to grow until T_g of most of polymer fractions reaches the temperature of polymerization that would lead to vitrification of the whole reaction mixture.

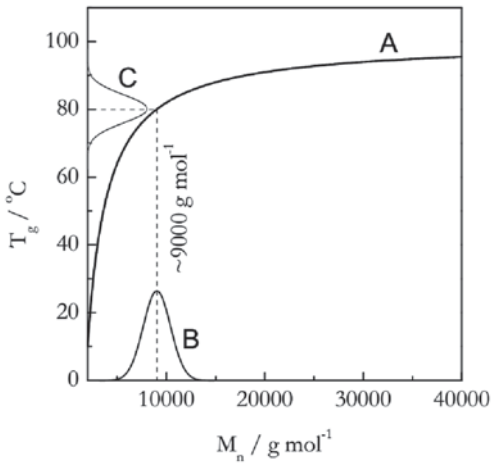

Fig. 4.8 Curve A is dependence of the glass transition temperature of the molecular weight of polystyrene ($T_g \approx 100\,°C - 1.8\ 10^5/M_n$) [11]. $T_g = 80\,°C$ corresponds to $M_n \sim 9000$ g mol^{-1}. *Curves* B and C represent respective distributions in M_n and T_g

Not only does vitrification occur throughout a range of conversions, but it also occurs at some finite rate. Therefore, it is possible to picture a situation when vitrification can be delayed or avoided when the polymerization temperature is raised sufficiently fast. It has been claimed [21] that such an effect is observed during the polymerization of *p*-xylylene. When analyzing DSC polymerization data collected in a wide range of the heating rates, the authors discovered that the Friedman plots (Fig. 4.9a) show a break for the heating rates above 10 K min^{-1}. It is especially distinct at larger values of α.

Separate analysis of the slower and faster heating rates by the differential method of Friedman [3] and the integral method of Vyazovkin [22] resulted in the E_α plots presented in Fig. 4.9b. The initial parts ($\alpha < 0.2$) of the dependencies do not show significant difference for the two ranges of the heating rates. $E_{\alpha \to 0}$ for the slow heating rates is somewhat larger than for the faster ones perhaps indicating a larger contribution of the initiation step. However, both dependencies merge at $\alpha \sim 0.2$ where the E_α value becomes practically identical with activation energy 36 kJ mol^{-1} reported [23] for polymerization of *p*-xylylene in hexane and toluene solutions. Nevertheless, a substantial difference is observed at higher conversions when polymerization switches from a kinetic to diffusion regime. The E_α dependence increases for slow heating rates and decreases for the faster ones. Note that at all heating rates used polymerization proceeded below the glass transition temperature of poly(*p*-xylylene), which is 13 °C [19]. That is, the reaction system should normally vitrify under such conditions (see Fig. 4.4). To explain the difference of the diffusion regimes, the authors [21] suggest that vitrification occurs only at slower heating rates. At faster heating rates, the sample temperature increases faster than the glass transition temperature of the reacting mixture so that polymerization proceeds without vitrification. Ultimately, the difference in the E_α dependencies is explained by the difference in the viscous conditions of the reaction medium.

4.2.3 Background to Cross-Linking

Cross-linking links polymer chains together giving rise to a polymer network. Cross-linking can be either physical or chemical. Physical cross-linking occurs via weak bonds (e.g., hydrogen or van der Waals bonds). Examples of such cross-linking are discussed in Sect. 3.10 dealing with physical gels. Chemical cross-linking involves the formation of strong covalent or ionic bonds. Cross-linked polymers form two important classes of polymeric materials: elastomers and thermosets. An elastomer is a cross-linked polymer above its glass transition temperature. A good example of an elastomer is vulcanized rubber, which is polyisoprene or polybutadiene covalently cross-linked with sulfur. A thermoset is a cross-linked polymer below its glass transition temperature.

In this section, we focus on the cross-linking that leads to the formation of thermoset materials because this is one of the most common thermal processes whose kinetics is routinely measured by DSC. A more technical name used most frequently for this process is curing. Among a variety of thermoset materials [24, 25], the

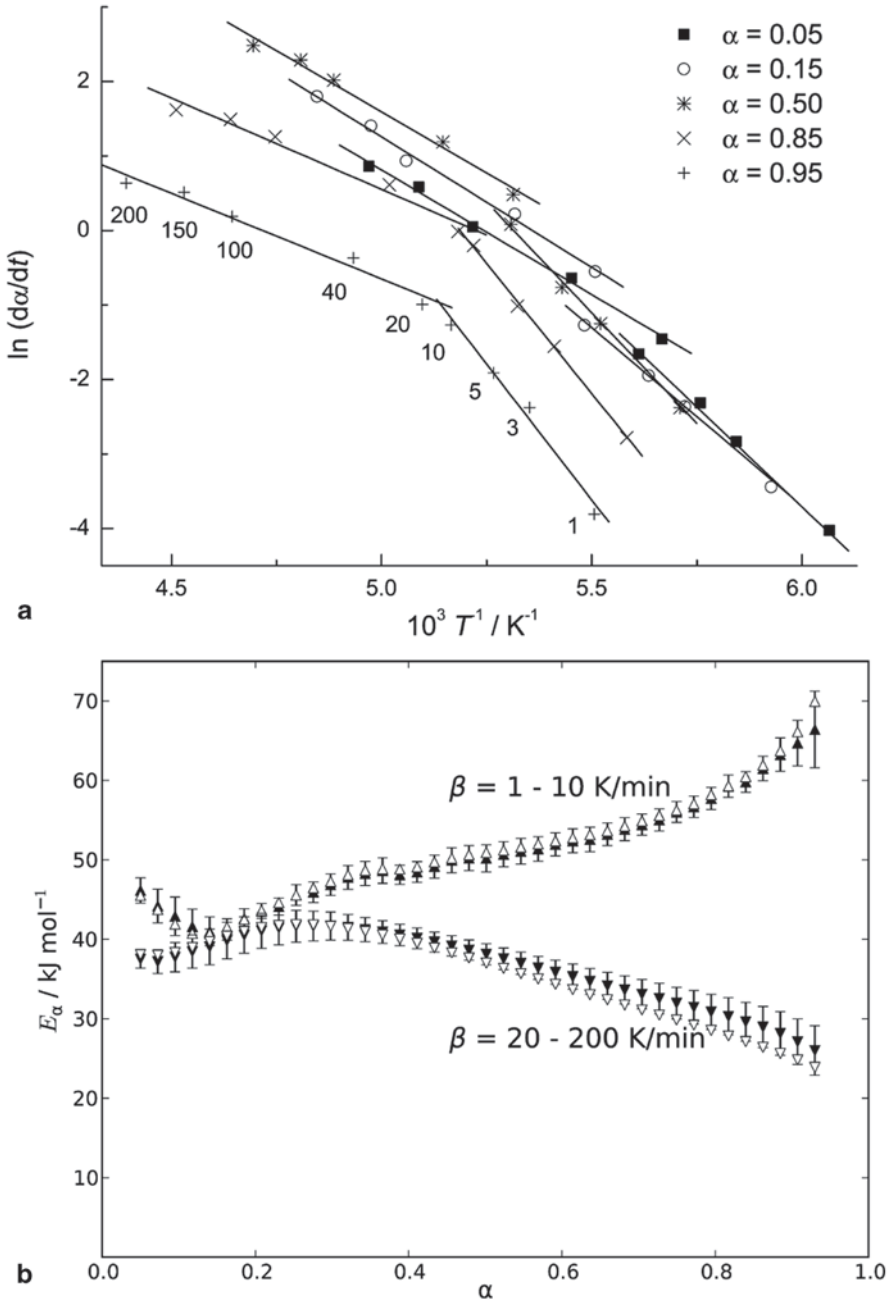

Fig. 4.9 Polymerization kinetics of p-xylylene. **a** Friedman plots at different conversions. *Numbers by the points* represent the heating rates used; **b** E_α dependencies estimated by the methods of Friedman (*solid* symbols) and Vyazovkin (*open* symbols). (Reproduced from Streltsov et al. [21] with permission of Elsevier)

epoxy-based ones appear to be the most versatile and common. An ubiquitous epoxy compound used in thermoset materials is diglycidyl ether of bisphenol A (DGEBA) or 2,2-bis(4-glycidyloxyphenyl)propane:

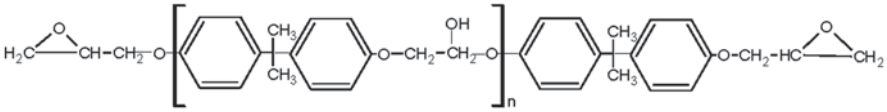

The value of *n* determines viscosity and the glass transition temperature of the DGEBA precursor so that at ambient temperature it can be either low-viscosity liquid or solid [24]. The compound is usually copolymerized with organic anhydrides or amines. The epoxy–amine polymerization includes several steps. The first is a primary amine reaction:

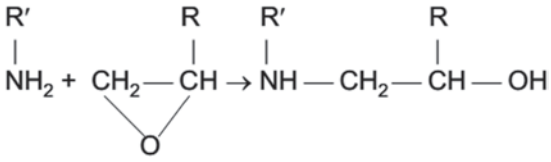

(4.18)

It is followed by a secondary amine reaction:

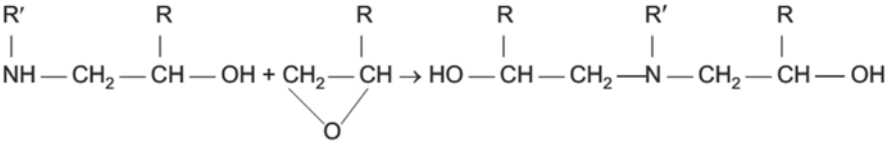

(4.19)

If DGEBA is reacted with a monoamine, reactions 4.18 and 4.19 would produce a linear polymer. A diamine should be used to form a network.

The rate of the secondary amine addition is generally slower than that of the primary one. The ratio of the rate constants for the secondary and primary amine reaction is reported [26–29] to be around 0.1–0.6. It means that the early stages of epoxy–amine curing are typically dominated by the primary amine addition. The primary amine groups become largely consumed close to 50% cure (i.e., $\alpha = 0.5$) and the secondary amine reaction (4.19) becomes dominant [30]. However, it proceeds in competition with etherification:

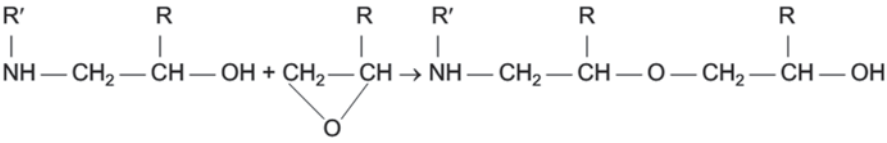

(4.20)

A contribution of etherification increases with temperature and may become dominant at $\alpha > 0.8$ [30]. Last but not least, at higher temperatures, DGEBA is capable of homopolymerization:

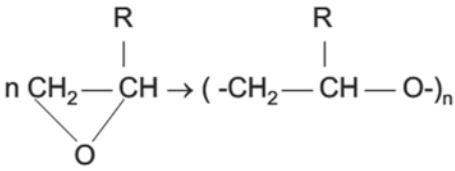

(4.21)

This reaction can be catalyzed by tertiary amines, and this type of species is formed as a product of reaction 4.19.

One of the popular models used to describe the kinetic of epoxy–amine curing is the model of Sourour and Kamal [31]. The model assumes that the process is initiated by uncatalyzed epoxy ring opening, which is promoted by hydrogen-bond donor molecules. This reaction is characterized by the rate constant k_1. Once this reaction takes place, it produces hydroxyl groups that catalyze epoxy ring opening, i.e., the process becomes autocatalytic. The rate constant for this catalyzed step is k_2. According to the Sourour–Kamal model, the process rate is describable by the following equation:

$$\frac{\mathrm{d}\alpha}{\mathrm{d}t} = (k_1 + \alpha k_2)(1-\alpha)(B-\alpha), \tag{4.22}$$

where B is the initial ratio of diamine equivalents to epoxide equivalents. The model does not make any distinction between the primary and secondary amine reaction and is only applicable when the process is not complicated by diffusion.

The Sourour–Kamal model can be used to predict the isoconversional activation energy by substituting the rate from Eq. 4.22 into 4.23:

$$E_\alpha = -R\left[\frac{\partial \ln(\mathrm{d}\alpha/\mathrm{d}t)}{\partial T^{-1}}\right]_\alpha = \frac{k_1 E_1 + \alpha k_2 E_2}{k_1 + \alpha k_2}. \tag{4.23}$$

It follows from Eq. 4.23 that at $\alpha \to 0$, $E_\alpha \to E_1$; i.e., at the lowest extents of conversion, E_α should yield an estimate for the activation energy of the uncatalyzed reaction. However, when $\alpha \to 1$, the E_α value does not generally approach E_2, but the weight average of E_1 and E_2 with k_1 and k_2 being the weights. In other words, at $\alpha \to 1$, E_α would approach E_2 only when the rate constant for the uncatalyzed reaction is much smaller than the one for the catalyzed reaction, i.e., when $k_1 << k_2$.

A similar autocatalytic model has been proposed by Kamal [32]. The model is based on the following equation:

$$\frac{\mathrm{d}\alpha}{\mathrm{d}t} = (k_1 + \alpha^m k_2)(1-\alpha)^n, \tag{4.24}$$

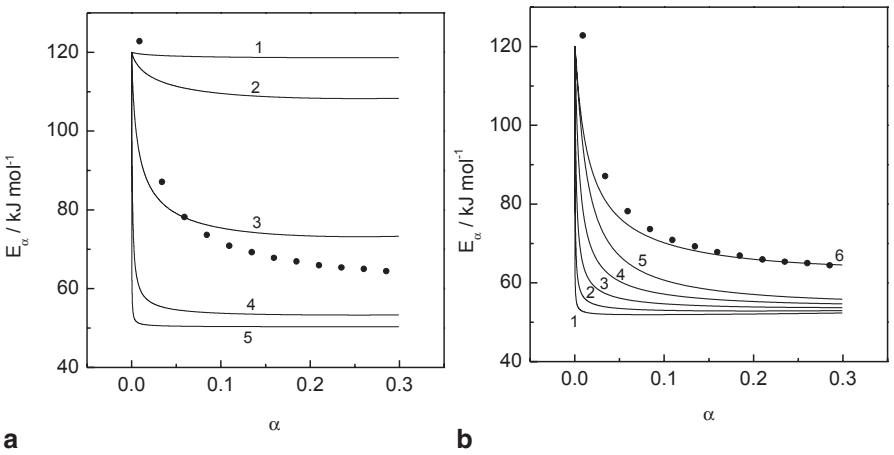

Fig. 4.10 Fitting Eqs. 4.23 (**a**) and 4.25 (**b**) to the E_α dependence for epoxy–amine curing data (*circles*). $E_1 = 120$ kJ mol^{-1}, $E_2 = 50$ kJ mol^{-1}, and $A_2 = 10^6$ min^{-1}. In **a**, *lines* represent different values of A_1: 1, 10^{18}; 2, 10^{17}; 3, 10^{16}; 4, 10^{15}; and 5, 10^{14} min^{-1}. In **b**, $A_1 = 10^{15}$ min^{-1} and *lines* represent different values of m: 1, 0.7; 2, 0.9; 3, 1.1; 4, 1.3; and 5, 1.5. *Line 6* represents $m = 1.3$ and $E_2 = 53$ kJ mol^{-1}. (Reproduced from Vyazovkin and Sbirrazzuoli [35] with permission of ACS)

where the exponents m and n are adjustable parameters. Although Eq. 4.24 is more flexible than 4.22, it is known [33, 34] to have numerical stability problems when fitted to the cure rate data. The isoconversional activation energy predicted from Eq. 4.24 has the following form:

$$E_\alpha = \frac{k_1 E_1 + \alpha^m k_2 E_2}{k_1 + \alpha^m k_2}. \tag{4.25}$$

It is easy to recognize that Eq. 4.25 predicts the same type of the E_α dependence as Eq. 4.23. That is, at the lowest extents of conversion ($\alpha \to 0$), E_α tends to the activation energy of the uncatalyzed reaction. If the catalyzed reaction is much faster than the uncatalyzed one, the value of E_α would approach the activation energy of the uncatalyzed reaction at $\alpha \to 1$.

Figure 4.10 demonstrates the ability of Eqs. 4.23 and 4.25 to reproduce the experimental E_α dependence estimated [35] for an epoxy–amine reaction. As seen from the graph **a,** Eq. 4.23 does not reproduce well the actual E_α dependence. Regardless of the A_1 value, the model dependence deviates significantly from the experimental one. On the other hand, the presence of an extra adjustable parameter m in Eq. 4.25 allows the actual E_α dependence to be reproduced quite well.

According to Eqs. 4.23 and 4.25, the type of E_α dependence is determined by a relation between E_1 and E_2. Since a catalytic action is typically associated with a decrease in the activation energy, one can expect E_2 to be generally smaller than

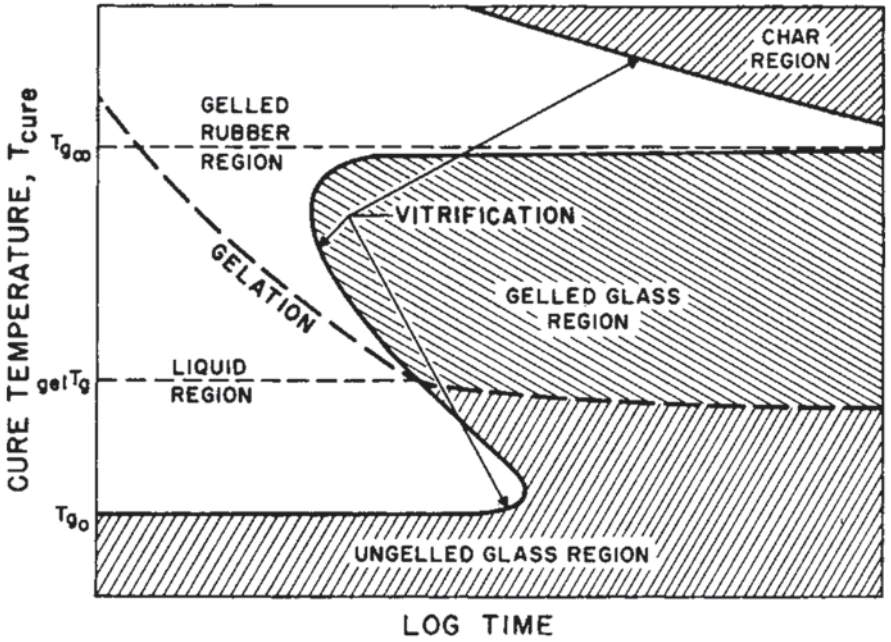

Fig. 4.11 Time–temperature–transformation diagram of a curing system. (Reproduced from Enns and Gillham [37] with permission of Wiley)

E_1. For an epoxy–amine reaction, this conjecture is supported by density functional theory calculations [36]. They suggest that the straight bimolecular reaction between epoxy and amine has a rather large barrier of ~110 kJ mol^{-1}. A markedly lower barrier (~85 kJ mol^{-1}) is estimated for the "self-promoted" reaction that involves two amine molecules, of which one forms a hydrogen bond with the epoxide oxygen and another participates in nucleophilic attack on the epoxide carbon. In terms of the aforementioned models (Eq. 4.22 or 4.24), this would be the uncatalyzed reaction promoted by a hydrogen-bond donor molecule. On the other hand, the catalyzed reaction that involves the formation of a hydrogen bond between the epoxide oxygen and the hydroxyl group (product of reaction 4.18) followed by nucleophilic addition of the amine to the epoxy carbon has the energy barrier of ~70 kJ mol^{-1}. The fact that E_1 is generally larger than E_2 suggests that epoxy–amine curing should be characterized commonly by decreasing E_α dependencies similar to that shown in Fig. 4.10. However, this is not always the case and many of these reactions barely show any variation in E_α in their initial stages.

As curing progresses to more advanced stages, the reaction medium undergoes two important microscopic changes: gelation and vitrification. The behavior of a curing system can be understood in the frameworks of a time–temperature–transformation (TTT) cure diagram [37] shown in Fig. 4.11. Gelation takes place when

a cross-linking system turns into a single infinite network. At this point, the system loses its ability flow. Theoretically [6], gelation occurs at a certain extent of cure that depends only on the functionality of the monomers. It was mentioned earlier that an epoxy–amine system would form a network when DGEBA is reacted with a diamine. The functionality of DGEBA is two because it has two reactive epoxy groups, and that of diamine is four because it has four reactive hydrogens. The theoretical value of the extent of cure at gelation, α_{gel}, is [6]:

$$\alpha_{gel} = \left(\frac{1}{(f_A - 1)(f_E - 1)}\right)^{1/2} = \left(\frac{1}{(4-1)(2-1)}\right)^{1/2} = 0.577, \tag{4.26}$$

where f_A and f_E are the respective functionalities of the amine and epoxy.

As discussed in Sect. 4.2.1, vitrification occurs when the glass transition temperature of the forming product (i.e., network in the present case) reached the temperature of the reaction system. In accord with the TTT diagram (Fig. 4.11), the phenomena of gelation and vitrification are independent from each other. If curing is performed at a temperature above $T_{g,0}$ (the glass transition temperature of the epoxy monomer) but below ${}_{gel}T_g$ (temperature at which gelation and vitrification occur simultaneously), the system would turn from liquid to glass without gelation. However, if curing is conducted above ${}_{gel}T_g$ but below $T_{g,\infty}$ (the glass transition temperature of the fully cured epoxy), the liquid system would first transform into a gel and then into a glass. Finally, if a curing system is maintained above $T_{g,\infty}$, it will gel without vitrification.

The TTT diagram can be recast in simpler temperature versus conversion form similar to that shown in Fig. 4.2. To do this, one needs to track the evolution of the glass transition temperature of a curing system as a function of conversion. This can be done by means of the modified DiBenedetto equation [38, 39]:

$$T_g = T_{g,0} + \frac{\lambda\alpha(T_{g,\infty} - T_{g,0})}{1-(1-\lambda)\alpha}, \tag{4.27}$$

where λ is a fit parameter. The actually measured [40] values of T_g at different values of α for an epoxy–amine curing system are shown in Fig. 4.12. It is seen that the glass transition temperature rises quickly with the progress of cross-linking and that the trend is well described by Eq. 4.27.

The T_g line from Eq. 4.27 limits the region of vitrification in the temperature versus conversion diagram (Fig. 4.13). Relative to the diagram for regular linear polymerization (Fig. 4.2), the diagram for cross-linking reveals the presence of a new phase, gel. The latter exists at conversions above α_{gel} (Eq. 4.26) and temperatures above T_g (Eq. 4.27).

Unlike the progress of linear polymerization, the progress of curing is difficult to characterize straightforwardly in terms of the average molecular weight and steady-state viscosity. As soon as a curing system gels, the steady-state viscosity turns

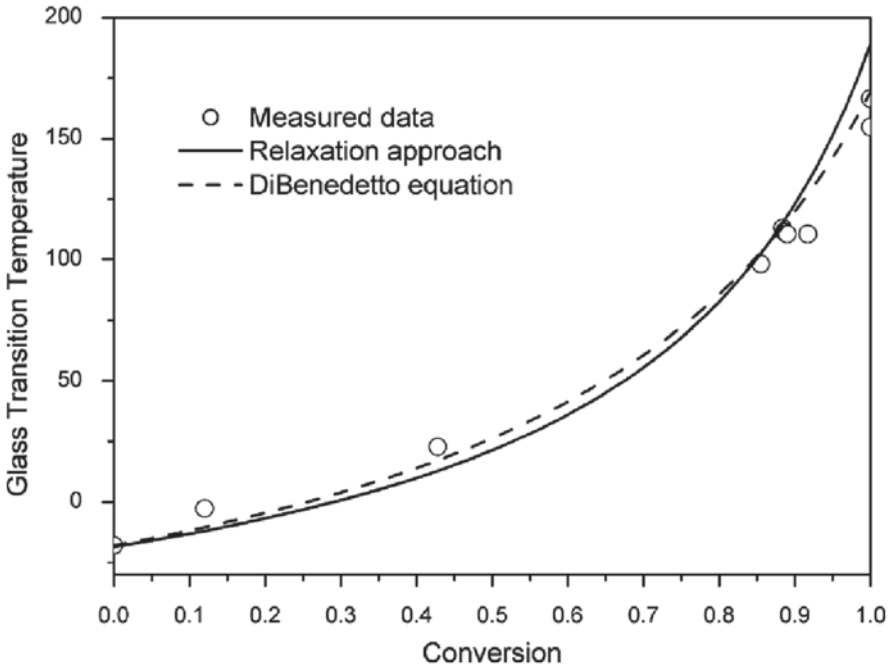

Fig. 4.12 Increase in the glass transition temperature with the extent of conversion in a curing epoxy–amine system. (Reproduced from Schawe [40] with permission of Elsevier)

to infinity because the system stops flowing. Also, the average molecular weight loses its meaning because all individual chains are cross-linked into one network or, in other words, into one macromolecule, whose molar mass effectively tends to infinity. However, curing continues, which means that there is some increase in the

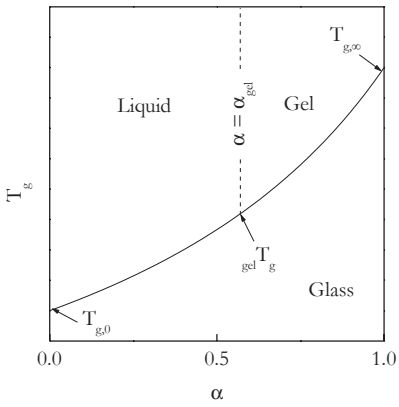

Fig. 4.13 The *dashed line* (Eq. 4.26) separates the liquid and gel states of a curing system. Below the *solid line* (Eq. 4.27), the system is in the glassy state

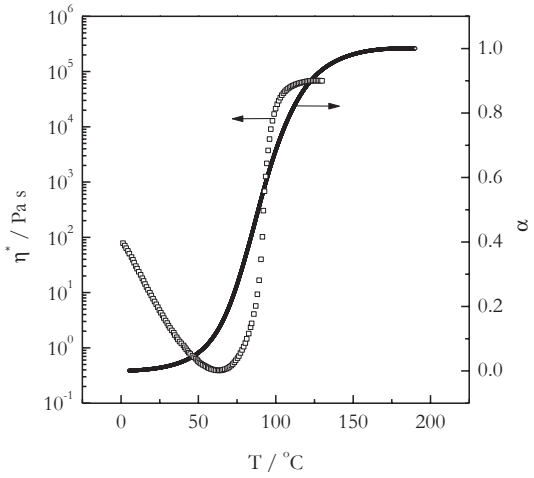

Fig. 4.14 Experimentally measured temperature dependencies of the extent of cure and dynamic viscosity for an epoxy–amine system cured at the heating rate of 2 °C min^{-1}. *Solid line* represents the extent of cure estimated from DSC data at the same heating rate. (Reproduced from Vyazovkin and Sbirrazzuoli [41] with permission of Wiley)

molecular weight of individual polymer branches. There also is some local short-range flow that can be measured in terms of dynamic viscosity [11], η^*. The latter can be used to follow the molecular mobility of the reaction medium throughout the whole process of cross-linking.

Figure 4.14 demonstrates a variation of the dynamic viscosity throughout the process of epoxy–amine curing under nonisothermal conditions [41]. The initial stages of the process ($\alpha < 0.2$) demonstrate a trivial decrease of the reactant viscosity with increasing temperature. Under isothermal conditions, this stage would be characterized by a very minor increase in viscosity. At later stages, an increase in viscosity due to cross-linking outweighs its decrease due to increasing temperature so that the overall effect is an increase in viscosity. The rising viscosity is reflective of retardation of the molecular mobility, which is the process that ultimately causes a change in the rate control from a kinetic to diffusion regime.

Despite the fact that a curing system undergoes a dramatic decrease in mobility at gelation, it is generally believed [24,37] that this process does not cause a transition from a kinetic to diffusion regime. It is certainly possible that the dramatic decrease in translational mobility of the network formed may not affect the local mobility of the dangling branches and monomer molecules so that they continue to react without any significant retardation. The commonly accepted view [24,25,37] is that a transition to a diffusion regime is associated with vitrification. Nevertheless, one cannot ignore the cases when such a transition has been detected [42–44] well before vitrification.

To model a transition from a kinetic to diffusion regime, one needs to introduce a diffusion term into the basic rate equation (1.1). The term can be introduced either as a multiplicand or as an addend. The following rate equation [37]:

$$\frac{d\alpha}{dt} = k(T) f(\alpha) \varphi(\eta) \tag{4.28}$$

introduces the diffusion term as a multiplicand $\varphi(\eta)$, where η is viscosity. The latter obviously involves dependencies on both temperature and molecular weight [37]. A more practically convenient approach is to introduce a multiplicand term that depends on temperature and conversion [45]:

$$\frac{\mathrm{d}\alpha}{\mathrm{d}t} = k(T) f(\alpha) \varphi(\alpha, T). \tag{4.29}$$

Variants of this approach are discussed by van Assche et al. [45] and by Schawe [40].

An alternative approach is to make use of the addition of kinetic resistances [46, 47] (Eq. 1.20) and introduce a diffusion term, $k_{\mathrm{D}}(T,\alpha)$, as an addend:

$$\frac{1}{k_{\mathrm{ef}}} = \frac{1}{k(T)} + \frac{1}{k_{\mathrm{D}}(T,\alpha)}. \tag{4.30}$$

The term can be introduced in the form of a diffusion rate constant with separable contributions of temperature and conversion [35]:

$$k_{\mathrm{D}}(T,\alpha) = D_0 \exp\left(\frac{E_{\mathrm{D}}}{RT} + B\alpha\right), \tag{4.31}$$

where D_0 is the preexponential factor, E_{D} the activation energy of diffusion, and B is a constant that accounts for a change in the conditions of diffusion due to the progress of cross-linking. A similar type of equation is used to describe the temperature dependence of viscosity in a system undergoing reactive polymerization [48].

Essentially, the $B\alpha$ term in Eq. 4.31 introduces the effective variable activation energy of diffusion:

$$E_{\mathrm{D,ef}} = E_{\mathrm{D}} + B\alpha RT. \tag{4.32}$$

There are a number of factors that may cause the activation energy of diffusion to vary during the process of curing. For example, it is known that the activation energy of diffusion of gases in rubber increases with the degree of cross-linking [49]. On the other hand, it is also known that for the same small molecule diffusant the activation energy is smaller when diffusion occurs in the glassy state than when it takes place in the liquid (rubbery) state of a polymer [17,49, 50].

From Eq. 4.30, the effective rate constant for the cross-linking kinetics accompanied by diffusion is as follows:

$$k_{\mathrm{ef}} = \frac{k(T)k_{\mathrm{D}}(T,\alpha)}{k(T)+k_{\mathrm{D}}(T,\alpha)}. \tag{4.33}$$

Equation 4.33 can further be used to derive the isoconversional activation energy in the usual manner:

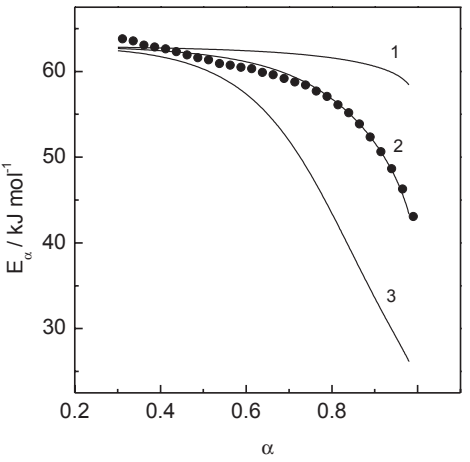

Fig. 4.15 Fitting the experimental E_α dependence for epoxy–amine curing data (*circles*) by Eq. 4.34. *Solid lines* are plotted for $E=63$ and $E_D=20$ kJ mol^{-1} and different values of B: −2 (1), −4 (2), and −6 (3). (Reproduced from Vyazovkin and Sbirrazzuoli [35] with permission of ACS)

$$E_\alpha = -R\left(\frac{\partial \ln k_{ef}}{\partial T^{-1}}\right)_\alpha = \frac{k(T)E_D + k_D(T,\alpha)E}{k(T) + k_D(T,\alpha)}, \tag{4.34}$$

where E_D and E, respectively, are the activation energies of diffusion and chemical reaction, e.g., catalyzed epoxy–amine reaction. Depending on the sign of B in Eq. 4.31, the E_α dependence can either decrease ($B<0$) or increase ($B>0$). As discussed earlier (Sect. 4.2.1), one can expect the E_α dependence to decrease when the rate becomes limited by the diffusion of small molecules such as a monomer or a short segment of a polymer chain. The increasing dependence should be expected when the process becomes determined by the diffusion of large molecules such as polymer chains or their long segments. Figure 4.15 provides an example of an epoxy–amine reaction that demonstrates a transition from a kinetic to diffusion regime accompanied by a decrease in E_α. It is seen that the aforementioned model (Eqs. 4.30, 4.31, and 4.34) is capable of adequately reproducing the actual variation in the effective activation energy.

It should be mentioned that vitrification during cross-linking is not the sole reason for diffusion control. The latter generally becomes operating when the characteristic time of relaxation, τ, of the reaction medium exceeds markedly the characteristic time of the reaction itself. The diffusion rate constant in a viscous medium can be expressed as [41]:

$$k_D = \frac{1}{\tau} = C\exp\left(\ln T - \frac{E_\eta}{RT}\right), \tag{4.35}$$

where C is the preexponential factor and E_η is the activation energy of viscous flow. Unlike Eq. 4.31 that describes a complex variation of k_D with T and α, Eq. 4.35 describes a simple increase of the diffusion rate constant with temperature. This

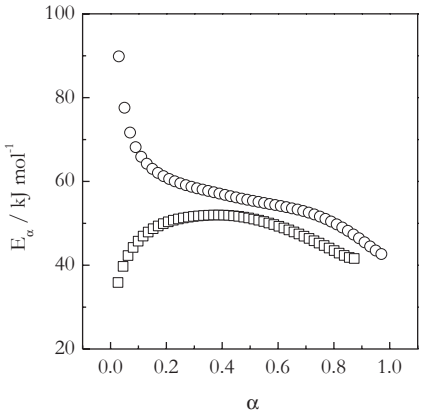

Fig. 4.16 The E_α dependencies for epoxy–amine cure under nonisothermal (*circles*) and isothermal (*squares*) conditions. Nonisothermal runs performed at 1–4 °C min^{-1}, isothermal at 80–120 °C. The viscosity data for this reaction are shown in Fig. 4.14. (Adapted from Vyazovkin and Sbirrazzuoli [41] with permission of Wiley)

increase is a consequence of the trivial decrease of viscosity with temperature, which can only occur in the early stages of cross-linking (e.g., $\alpha < 0.2$ in Fig. 4.14). Then following the same line of thought as above (Eqs. 4.30, 4.33, and 4.34), we can derive the effective activation energy as follows [41]:

$$E_{\text{ef}} = \frac{(E_\eta + RT)k + Ek_{\text{D}}}{k + k_{\text{D}}} \approx \frac{E_\eta k + Ek_{\text{D}}}{k + k_{\text{D}}}, \tag{4.36}$$

Considering that most of cures are typically conducted at moderate temperatures ($T < 200$ °C), the RT term in 4.36 is less than 4 kJ mol^{-1} and can be neglected relative to the E_η value which is quite large (50–90 [51–53] kJ mol^{-1}) in epoxy systems.

Equation 4.36 suggests that if at lower temperatures the reaction system has high viscosity so that $k_{\text{D}} << k$, the process of curing would start in a diffusion regime and its effective activation energy would be close to the activation energy of viscous flow. However, as temperature rises and viscosity decreases, the process would change from a diffusion to kinetic regime. Again, all this should be expected to happen in the initial stages of the nonisothermal cure process before viscosity starts to increase quickly due to an increase in the molecular weight of the polymer product (e.g., $\alpha > 0.2$ in Fig. 4.14).

An example of diffusion control in the initial stages of nonisothermal cure in an epoxy–amine system [41] is shown in Fig. 4.16. The phenomenon manifests itself in the form of a decreasing E_α dependence at $\alpha < 0.2$. For this system, at $\alpha < 0.2$, viscosity undergoes a significant decrease (Fig. 4.14), and the respective value of E_η estimated from the viscosity data is 80 kJ mol^{-1}. This value is practically the same value as E_α at the initial cure stages, which is predicted by the model (Eqs. 4.35 and 4.36). Note that no decrease in E_α is observed in the same region for an isothermal cure. This is because the effect is associated exclusively with a decrease in viscosity but under isothermal conditions the viscosity of a curing system can only increase.

4.2.4 Isoconversional Treatment of Cross-Linking

The kinetics of cross-linking (curing) is most commonly studied by DSC, although other techniques such as Fourier transform infrared (FTIR) spectroscopy, thermomechanical analysis (TMA), dynamic mechanical analysis (DMA), etc. are also used occasionally. The application of an isoconversional method to any type of data is only a matter of appropriate transformation of the property measured into the extent of conversion. However, a comparison of isoconversional activation energies as well as of other kinetic parameters obtained by different experimental techniques must be done with care. For example, the mechanical techniques (TMA, DMA) detect the reaction progress through a change in the mechanical properties of the whole bulk sample. Such global changes do not necessarily occur at the same time as some local molecular changes that are detectable by DSC or FTIR. The difference in the kinetics measured by mechanical techniques from one side and calorimetric and spectroscopic techniques from another side has been reported by Ramis et al. [54, 55]. Some of the results [55] of that work are illustrated in Fig. 4.17. It is seen that DSC and FTIR techniques yield very similar E_α dependencies that, however, deviate quite noticeably from the dependence estimated by TMA. On the other hand, there appear to be consistency of the E_α dependencies produced by two mechanical techniques: TMA and DMA [54].

Another important aspect of the isoconversional treatment of cross-linking data is related to practical evaluation of incomplete cure data collected under isothermal conditions. As discussed earlier, when curing is performed isothermally below $T_{g,\infty}$ the system would vitrify and the reaction would stop at some ultimate conversion $\alpha_T < 1$. The conversion α_T decreases with decrease in the curing temperature. It is the same effect as the one observed for linear polymerization (Figs. 4.2 and 4.3). In this situation, the question arises what value of α one should use in isoconversional computations: the absolute or relative value. The absolute value runs from 0 to dif-

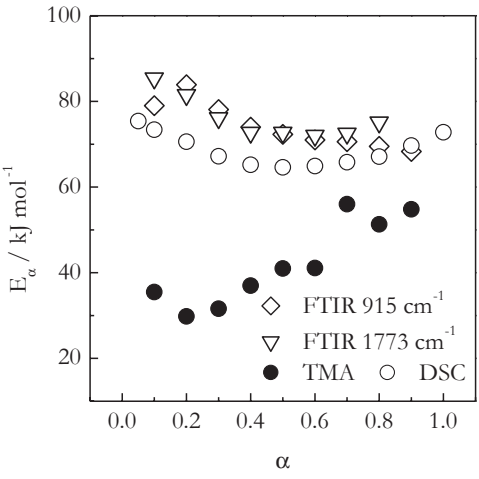

Fig. 4.17 Isoconversional activation energies for curing of DGEBA and γ-butyrolactone estimated by different techniques [55]. FTIR measurement at 915 and 1773 cm^{-1} [1] represent changes in epoxy and γ-butyrolactone, respectively

ferent values of α_T at different temperatures. It can be converted to the relative value by dividing the absolute α over α_T. The relative α would then run from 0 to 1.

It has been demonstrated [56] that the correct approach is to the use the relative values of conversion. It is explained easily by assuming that cure obeys, for example, a reaction-order model, $f(\alpha)=(1-\alpha)^n$. To adjust this model to conditions of incomplete cure, the model needs to be modified as:

$$f(\alpha)=(\alpha_T-\alpha)^n. \tag{4.37}$$

This adjustment is necessary to secure the fact that when cure reaches its ultimate conversion α_T at a given temperature, $f(\alpha)$ and, thus, the reaction rate turns to zero. As discussed in Chap. 1 (Eqs. 1.12 and 1.13), the derivative of the reaction rate at a constant conversion is equal to the activation energy:

$$E_\alpha=-R\left[\frac{\partial \ln(\mathrm{d}\alpha/\mathrm{d}t)}{\partial T^{-1}}\right]_\alpha=-R\left[\frac{\partial \ln k(T)}{\partial T^{-1}}\right]_\alpha-R\left[\frac{\partial \ln f(\alpha)}{\partial T^{-1}}\right]_\alpha, \tag{4.38}$$

because the second term in the right-hand side of Eq. 4.38 is zero. However, if one is to use the absolute conversion for estimating the activation energy, then the reaction model in Eq. 4.38 would have to take the form that contains α_T, such as in Eq. 4.37. Then, the second term in Eq. 4.39

$$E_\alpha=-R\left[\frac{\partial \ln k(T)}{\partial T^{-1}}\right]_\alpha-R\left[\frac{\partial \ln(\alpha_T-\alpha)}{\partial T^{-1}}\right]_\alpha \tag{4.39}$$

is no longer zero because α_T depends on temperature.

That is, the use of the absolute values of α would result in estimating the E_α values distorted by the temperature dependence of α_T in the second term of Eq. 4.39. Needless to say, exactly the same issue would arise when using any other $f(\alpha)$ model as long as it is adjusted to the condition of incomplete cure. On the other hand, transforming the absolute conversions for incomplete cure to the relative ones would change α_T in Eq. 4.37 to 1 that would make the second term in Eq. 4.39 zero and, thus, would produce undistorted values of E_α. The systematic error in E_α caused by using the absolute conversions increases as α approaches α_T and can be quite significant as illustrated in Fig. 4.18 for simulated data [56]. Significant differences in E_α estimated by using absolute and relative conversions are also found for experimental data [56–58].

In the beginning of Sect. 4.2.3, we discuss briefly that in a kinetic regime the initial portions of the E_α dependence are likely to be descending that follows from the model Eqs. 4.22 and 4.24 as long as E_1 for the uncatalyzed reaction is larger than E_2 for the catalyzed reaction. However, this is not a general rule. The E_α values at the smallest conversions (i.e., at $\alpha\to 0$) are determined by the activation energy of initiation that can be larger or smaller depending on the mechanism. For example, the activation energy of initiation of epoxy ring opening can depend strongly on how this process is catalyzed. An instructive example is provided in Fig. 4.19 that

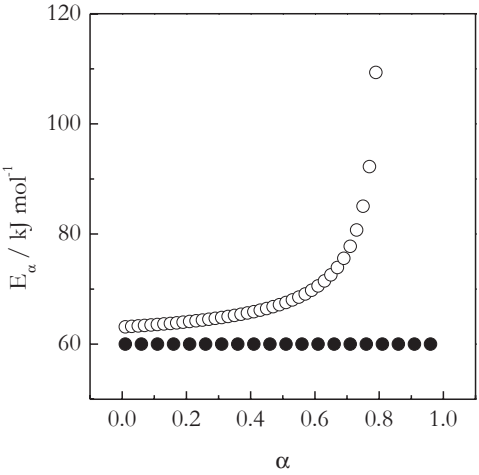

Fig. 4.18 Activation energies derived from the simulated data (E=60 kJ mol^{-1}). The values derived by using the absolute and relative extents of cure are shown, respectively, as *open* and *solid* symbols. (Adapted from Vyazovkin and Sbirrazzuoli [56] with permission of Wiley)

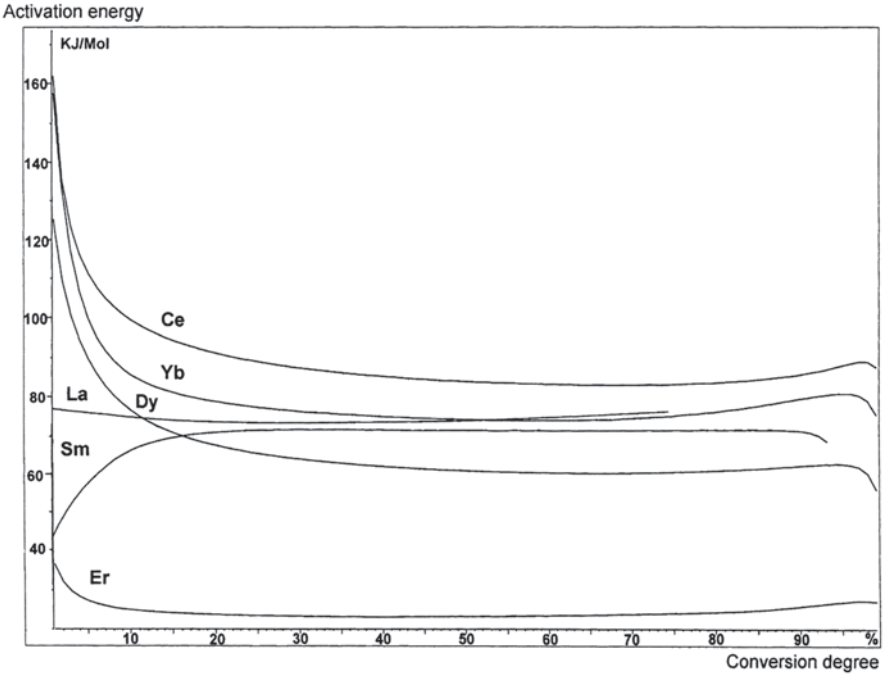

Fig. 4.19 E_α dependencies for polymerization of DGEBA initiated by various lanthanide triflates. (Reproduced from Castell et al. [59] with permission of Elsevier)

presents data on the polymerization of DGEBA in the presence of various lanthanide triflates [59]. By comparing the E_α values at $\alpha \to 0$, we can see that the activation energy of initiation by triflates of Ce, Yb, and Dy are significantly larger than the activation energy of propagation (practically constant E_α at $\alpha > 0.3$). On the

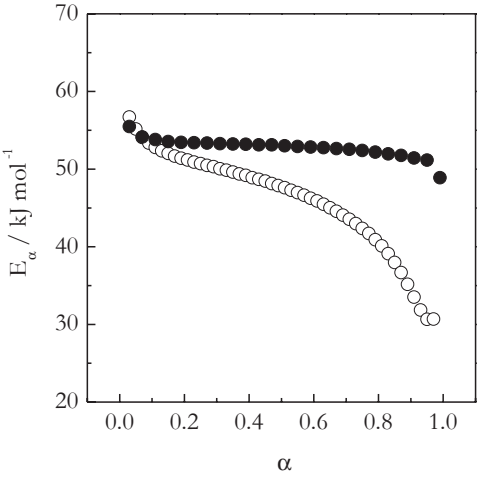

Fig. 4.20 Activation energy as a function of conversion for reaction between DGEBA and PDA (*open circles:* stoichiometric ratio, *solid circles:* excess of amine). (Adapted from Sbirrazzuoli et al. [60] with permission of Wiley)

other hand, for initiation by Sm triflate, the activation energy is significantly smaller than that of propagation, and for La triflate it is about the same for initiation and propagation.

No distinct decrease in the E_α values is seen in the initial stages of curing DGEBA with 1,3-phenylene diamine [60] (PDA; Fig. 4.20). Apparently, for this process, the activation energy of initiation is similar to that of propagation. This is confirmed by performing the same reaction with the fivefold excess of amine over the stoichiometric amount. Under the stoichiometric conditions, the DGEBA to amine ratio is such that the DGEBA and amine blocks alternate forming a polymer chain. When the amount of amine exceeds significantly the stoichiometric one, the DGEBA blocks would be mostly capped by amine blocks and, thus, would not be capable to build the polymer chain. In this situation, the activation energy of the whole process should be similar to the activation energy of initiation. As seen in Fig. 4.20, the respective E_α value is practically constant (~55 kJ mol^{-1}) throughout the whole process.

The system with excess of amine cannot produce a cross-linked polymer so that the reaction system cannot develop high viscosity and vitrify, which, in its turn, prevents a transition from a kinetic to diffusion regime. The absence of this transition is the chief reason why the E_α values at larger conversions remain unchanged. However, the transition occurs in the stoichiometric system (Fig. 4.20). In it, the initial E_α values are similar to those for the nonstoichiometric system that indicates that both systems have the same initiation process. As cross-linking progresses, the viscosity of the reacting system rises and the effective activation energy of curing decreases.

Dynamic rheology measurements (Fig. 4.21) shed light on physical changes taking place in the stoichiometric system throughout cross-linking [60]. The system gels at about 123 °C as detected by the point of intersection of the storage and loss modulus curves. According to the DSC measurements, it happens at conversion of

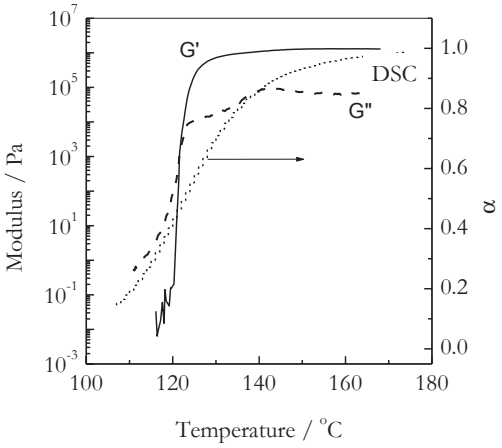

Fig. 4.21 Evolution of the storage (G') and loss (G'') moduli during curing of the DGEBA–PDA system at 2 °C min^{-1}. The *curve* denoted "DSC" represents the conversion of curing as estimated by integration of the DSC curve measured at 2 °C min^{-1}. (Reproduced from Sbirrazzuoli et al. [60] with permission of Wiley)

~0.53. The value is quite close to the theoretical $\alpha_{gel}=0.577$ (Eq. 4.26). At about 145 °C, the storage modulus reaches the so-called glassy plateau. This is the point when the reacting system is completely vitrified. The respective conversion is ~0.9. Of course, vitrification does not occur instantaneously at this point. It starts at some conversion past gelation (i.e., $\alpha \sim 0.53$) and finishes at $\alpha \sim 0.9$. Note that this is the region where the E_α values drop most quickly (Fig. 4.20). Clearly, the decrease in the effective activation energy of cure correlates with dramatic changes in viscosity of the reaction system.

It should be stressed that isoconversional calculations of the activation energy is not the only way to obtain insights into the kinetics and mechanisms of the cross-linking process. Estimating the preexponential factors by using the techniques discussed in Sect. 2.2 can also be of value. For example, Alzina et al. [61] have discovered that the reaction of curing between DGEBA and PDA can be accelerated by adding organically modified montmorillonite clay. The acceleration manifests itself as a shift of the reaction to lower temperature when clay is present (Fig. 4.22). The E_α dependencies for curing in these two systems are shown in Fig. 4.23. Surprisingly, the system containing montmorillonite demonstrates larger activation energy than the system without it. Generally, when the reaction rate accelerates, one should expect the activation energy to decrease.

Another reason of the reaction rate acceleration can be an increase in the value of the preexponential factor. The ln$A$ values estimated by using the compensation effect (Sect. 2.2.2) are displayed in Fig. 4.23. Indeed, the preexponential factors for the system containing montmorillonite are greater than for system without it. Therefore, the acceleration arises from entropic (steric) rather than enthalpic reasons. Conversion of the E_α dependencies to the dependencies of E_α versus T allowed Alzina et al. to fit data to Eq. 4.25 and determine the Arrhenius parameters of the uncatalyzed (A_1 and E_1) and catalyzed (A_2 and E_2) reactions. The parameters are shown in Table 4.1. The noteworthy result is that the ratio A_1/A_2 has more than doubled in the presence of montmorillonite. The likely explanation of the effect is improving the efficiency of reaction collisions for the curing reaction on the clay surface [61].

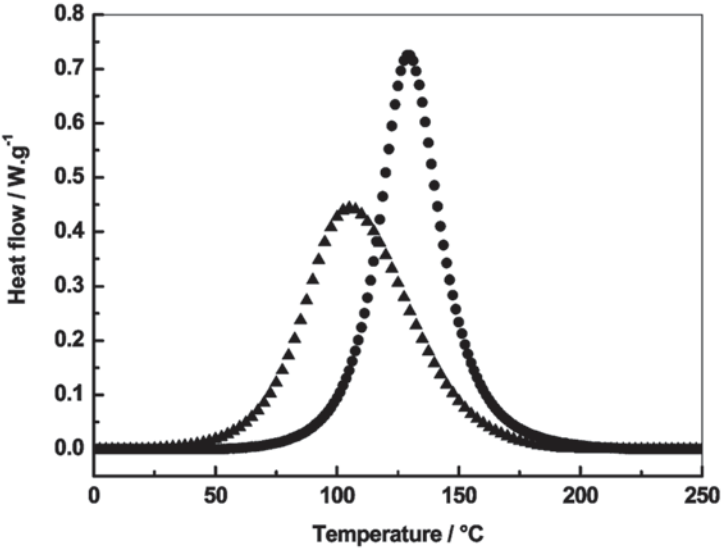

Fig. 4.22 DSC curves for curing reaction between DGEBA and PDA with (*triangles*) and without (*circles*) organically modified montmorillonite clay. (Reproduced from Alzina et al. [61] with permission of ACS)

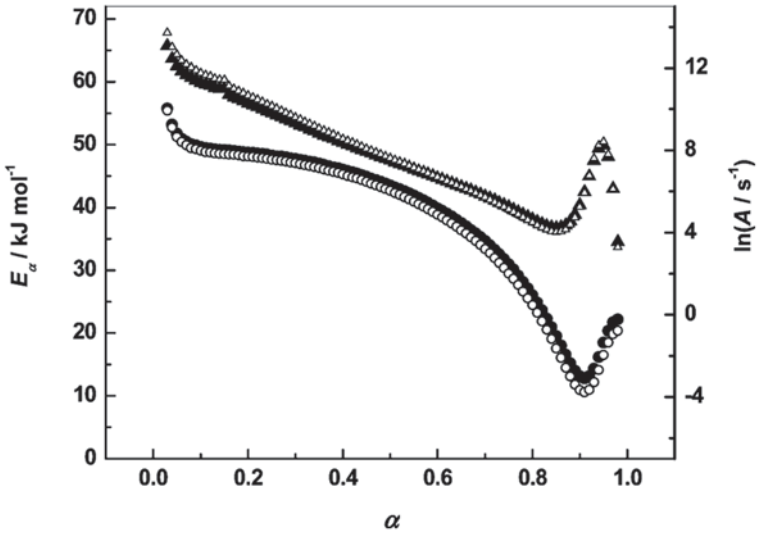

Fig. 4.23 Dependencies of the activation energy (*solid symbols*) and preexponential factor (*open symbols*) on conversion for the DGEBA/PDA system without (*circles*) and with (*triangles*) montmorillonite. (Reproduced from Alzina et al. [61] with permission of ACS)

Table 4.1 Kinetic parameters obtained [61] by fitting the E_α versus T dependencies to Eq. 4.25

	A_1/A_2	E_1/kJ mol^{-1}	E_2/kJ mol^{-1}	m
DGEBA/PDA	41.5	69.8	45.2	1.1
DGEBA/PDA/MMT	88.8	75.9	52.9	1.1

DGEBA diglycidyl ether of bisphenol A, *MMT* montmorillonite, *PDA* 1,3-phenylene diamine

4.3 Thermal and Thermo-oxidative Degradation of Polymers

It is a fire that burns to Destruction.

Job 31:12

4.3.1 Background

Polymers are the most versatile materials known to humankind. Because of this versatility, the application area of polymers is enormous. Numerous applications involve exposure of polymers to elevated temperatures. Elevated temperatures are also used when polymers are processed by molding, extrusion, coating, etc. To make a solid polymer pliable, one should turn it to the liquid state that is accomplished by heating well above its temperature of the glass transition and/or melting. Exposure to heat ultimately leads to breaking chemical bonds that hold together the atoms in a polymer chain. Scission of the polymer chain leads to degradation of the polymer material. If degradation is caused by heat alone without the presence of oxygen (or other oxidant), it is referred to as thermal degradation or pyrolysis. The presence of an oxidizing atmosphere usually accelerates thermal degradation and the respective process is called thermo-oxidative degradation.

From a thermodynamic standpoint, the thermal stability of a polymer can be characterized by the ceiling temperature, T_c, which is the temperature above which the polymer would degrade spontaneously to the monomer. In this case, degradation is a process reverse to polymerization (see Eq. 4.2):

$$\mathrm{M}_{n+1}\cdot \underset{k_\mathrm{p}}{\overset{k_\mathrm{dp}}{\Leftrightarrow}} \mathrm{M}_n\cdot + \mathrm{M}. \tag{4.40}$$

The degradation mechanism represented by Eq. 4.40 is referred to as depolymerization, or depropagation, or unzipping. Being opposite to polymerization, the process is endothermic, which means that an increase in temperature favors the forward process. At some temperature, the rate constants of depropagation and propagation become equal so that degradation attains equilibrium. Then, a change in the Gibbs free energy

$$\Delta G = \Delta H - T\Delta S = -RT \ln\left(\frac{k_{dp}}{k_p}\right) \tag{4.41}$$

becomes zero. Therefore, the ceiling temperature can be defined as the ratio:

$$T_c = \frac{\Delta H}{\Delta S}. \tag{4.42}$$

The concept of the ceiling temperature has limited use in estimating the thermal stability of polymers. It assumes that polymer degradation occurs via simple depolymerization; i.e., polymer is converted into its monomer. However, there are a few polymers (e.g., poly(α-methylstyrene); poly(methyl methacrylate), PMMA; polytetrafluoroethylene; polymethacrylonitrile) that degrade predominately to the monomer when heated. In addition to depolymerization, there are two other major mechanisms of degradation: side-group scission and random chain scission [62]. Side-group scission involves splitting off pendant groups without breaking the main chain. Examples of side-group scission include elimination of hydrogen chloride from poly(vinyl chloride), acid from poly(vinyl ester), and alkene from poly(alkyl acrylate). Random chain scission refers to breaking the polymer chain in random places that yields a variety of low molecular weight products, including the monomer. Thermal degradation of polyethylene (PE) and polypropylene (PP) are examples of this mechanism. Most of the time, the thermal degradation occurs via a combination of depolymerization and random chain scission. Obviously, if a polymer degrades by a mechanism other than depolymerization, the aforementioned equilibrium (4.40) becomes impossible and the ceiling temperature loses its meaning.

The kinetics of degradation by depolymerization can be described in the simplest case by using the same approach as the one used earlier for polymerization. Depolymerization is the process reverse to polymerization:

$$\mathrm{MM}\cdot \xrightarrow{k_{dp}} \mathrm{M} + \mathrm{M}\cdot. \tag{4.43}$$

Its rate is:

$$r_{dp} = k_{dp}[\mathrm{MM}\cdot]. \tag{4.44}$$

The process starts by initiation:

$$\mathrm{MM} \xrightarrow{k_i} \mathrm{MM}\cdot, \tag{4.45}$$

whose rate is:

$$r_i = k_i[\mathrm{MM}]. \tag{4.46}$$

The radicals produced in steps 4.43 and 4.45 can be consumed by termination:

$$\mathrm{M}\cdot + \mathrm{M}\cdot \xrightarrow{k_t} 2\mathrm{M}. \tag{4.47}$$

The rate of the termination step is:

$$r_t = 2k_t[\mathrm{M}\cdot]^2. \tag{4.48}$$

Under the steady-state conditions, the rates of initiation and termination are equal that allows the concentration of radicals to be expressed as:

$$[\mathrm{MM}\cdot] = \left(\frac{k_i}{2k_t}\right)^{\frac{1}{2}} [\mathrm{MM}]^{\frac{1}{2}}. \tag{4.49}$$

The substitution of Eq. 4.49 into Eq. 4.44 gives the overall rate of depolymerization:

$$r_{dp} = k_{dp}\left(\frac{k_i}{2k_t}\right)^{\frac{1}{2}} [\mathrm{MM}]^{\frac{1}{2}} = k_{ef}[\mathrm{MM}]^{\frac{1}{2}}. \tag{4.50}$$

Equation 4.50 can now be used to derive the effective activation energy of polymer degradation in the usual manner:

$$E_{ef} = -R\left(\frac{\mathrm{d}\ln k_{ef}}{\mathrm{d}T^{-1}}\right) = E_{dp} + (E_i - E_t)/2. \tag{4.51}$$

The significance of Eq. 4.51 is that it demonstrates that even when the thermal degradation of a polymer occurs by simple depolymerization, the activation energy of the process is a complex value that involves a combination of the activation energies for depropagation (E_{dp}), initiation (E_i), and termination (E_t).

The mechanism of thermo-oxidative degradation involves the same initiation step as thermal degradation (4.45). The macroradical propagates by forming peroxide, which abstracts a proton from the polymer yielding hydroperoxide and a new macroradical:

$$\mathrm{MM}\cdot + \mathrm{O_2} \rightarrow \mathrm{MMO_2}\cdot \tag{4.52}$$

$$\mathrm{MMO_2}\cdot + \mathrm{MMH} \rightarrow \mathrm{MMOOH} + \mathrm{MM}\cdot. \tag{4.53}$$

Termination of the radical species occurs by recombination to inert products, P:

$$2\mathrm{MM}\cdot \text{ or } 2\mathrm{MMO_2}\cdot \text{ or } \mathrm{MM}\cdot + 2\mathrm{MMO_2}\cdot \rightarrow \mathrm{P}. \tag{4.54}$$

It is usually postulated [63] that decomposition of the macromolecular peroxide is a rate-limiting step in the overall kinetics of thermo-oxidative degradation of polymers. The single oxygen–oxygen bond has a moderate dissociation enthalpy of ~150 [1] kJ mol^{-1} that can provide an estimate for the activation energy of monomolecular decomposition:

$$\mathrm{MMOOH} \rightarrow \mathrm{MMO}\cdot + \cdot\mathrm{OH}. \tag{4.55}$$

However, the bimolecular decomposition reaction

$$2\mathrm{MMOOH} \rightarrow \mathrm{MMO}\cdot + \mathrm{MMOO}\cdot + \mathrm{H_2O} \tag{4.56}$$

encounters an even lower energy barrier, which is the reason why the activation energy of decomposition of organic peroxides is usually found to be around 100 kJ mol^{-1} [62, 64]. Therefore, despite the numerous steps involved in thermo-oxidative degradation, oxidative conditions have a "simplifying effect" [62] on degradation, and the process is commonly found to have the activation energy close to 100 kJ mol^{-1} for many polymers.

4.3.2 Isoconversional Treatment

During thermal and thermo-oxidative degradation, polymer chains break forming lower molecular weight products. The volatile products escape from a degrading polymer that results in the mass loss of the polymer sample. For this reason, the polymer degradation kinetics is convenient to follow by means of thermogravimetric analysis (TGA).

The application of an isoconversional method to the thermal degradation of many vinyl polymers yields a somewhat common type of the E_α dependence. Some of such typical dependencies are presented in Fig. 4.24 for degradation of PE, PP, PS, and polyvinylpyrrolidone (PVP) [65, 66]. It is seen that the earliest stages of degradation ($\alpha \rightarrow 0$) are characterized by lower activation energies. However, as degradation progresses, the activation energy rises and tends to level off at around 200–250 kJ mol^{-1}.

The lower energy stages of degradation are associated with initiation of the process on the defects of polymer structure or so-called weak links [62, 67, 68]. These include branch points as well as peroxide and hydroperoxide groups that are formed during polymerization in the presence of oxygen. Head-to-head groups and unsaturated vinylidene end groups that result from bimolecular radical termination are also examples of such weak links.

The presence of weak links significantly lowers the thermal stability of a polymer. For example, the thermal stability of PS increases markedly if the polymer does not contain the head-to-head links [69]. Another example is PMMA, whose thermal degradation is initiated at vinylidene end groups formed during regular

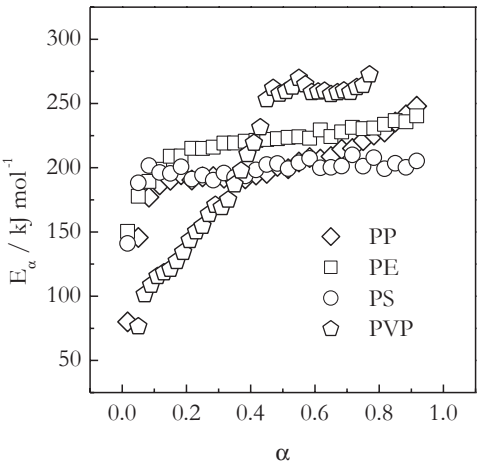

Fig. 4.24 Dependencies of the activation energy on conversion for thermal degradation of several polymers. (Adapted from Peterson et al. [65] and Jablonsky et al. [66] with respective permission of Wiley and Elsevier)

radical polymerization. Hu and Chen [70] have synthesized PMMA with different end groups: –S–$(CH_2)_{11}$–CH_3 (PMMA–R_{12}), –S–$(CH_2)_2$–COOH (PMMA–COOH), and –S–$(CH_2)_2$–OH (PMMA–OH) and compared the thermal degradation of these polymers with regular PMMA polymerized with AIBN as initiator (PMMA–AIBN) and PMMA polymerized with AIBN but in the presence of *n*-dodecanethiol as a chain transfer agent (PMMA–C_t). The TGA data indicate (Fig. 4.25) that regular PMMA–AIBN degrades in two steps, whereas the first step does not seem to be

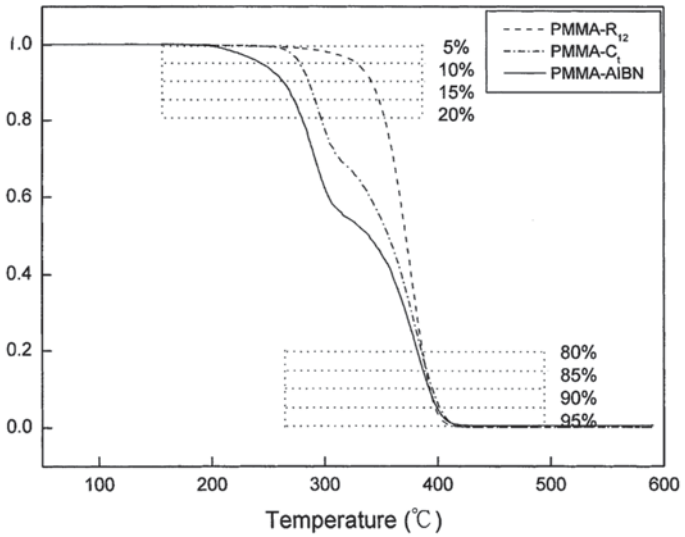

Fig. 4.25 Mass loss (TGA) curves obtained at 20 °C min^{-1} for the thermal degradation of PMMA having different end groups. The vertical axis is a fraction of the initial mass. The *dotted lines* demonstrate the extents of conversion which were used to estimate the activation energies (Fig. 4.26). (Reproduced from Hu and Chen [70] with permission of Elsevier)

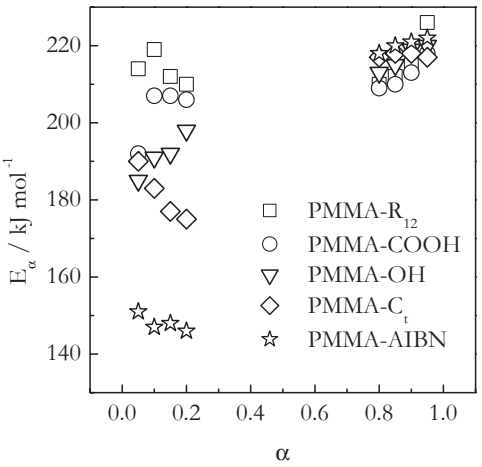

Fig. 4.26 Activation energies as a function of conversion estimated by an isoconversional method from the mass loss data for thermal degradation of PMMA having different end groups. (Data from Hu and Chen [70])

present in the degradation of PMMA–R_{12}. Also, the degradation temperature for the latter has increased by ~90 °C relative to the former. It should be noted that the first step in the degradation of PMMA is associated with the presence of weak links (see Peterson [71] and references therein). Obviously, the introduction of more stable end groups significantly increases the thermal stability of PMMA. The increase in stability is reflected in the values of the effective activation energy estimated by an isoconversional method. As seen in Fig. 4.26, the identity of the end group affects dramatically the activation energy of the initial stages of the thermal degradation of PMMA. If for regular PMMA–AIBN $E_{\alpha\to 0}$ is ~150 kJ mol^{-1}, for PMMA–R_{12} it is over 200 kJ mol^{-1}.

Note that the effect of weak links is limited to the initial stages of polymer degradation (Figs. 4.24 and 4.26). Once all weak links broke giving way to initiation, further initiation is only possible by breaking regular bonds that have higher energy. As a result, the activation energy rises to the plateau value that can be estimated by using Eq. 4.51. As noted earlier, $E_p - E_t/2$ in Eq. 4.11 is about 10–20 kJ mol^{-1} so that in the steady state the effective activation energy of polymerization is about 10–20 kJ mol^{-1} larger than $E_i/2$. Following the same reasoning, we can obtain an estimate for the effective activation energy of degradation in accord with Eq. 4.51. Instead of E_p, Eq. 4.51 has E_{dp}. The two values differ by the enthalpy of polymerization. For vinyl polymers, the heat of polymerization is roughly 65 ± 8 kJ/mol of monomer [6]. With regard of this, $E_{dp} - E_t/2$ in Eq. 4.51 should be about 75–85 kJ mol^{-1}. Then the effective activation energy of polymer degradation in the steady state should be 75–85 kJ mol^{-1} greater than half the activation energy of initiation, which can estimated as the enthalpy of dissociation a carbon–carbon bond. Depending on the molecular structure, this enthalpy varies around 280–340 kJ mol^{-1} [62]. Then half of this value (i.e., 140–170 kJ mol^{-1}) plus 75–85 kJ mol^{-1} would give us an estimate for the activation energy of degradation somewhere in the range of 210–260 kJ mol^{-1}. This estimate agrees fairly well with the plateau E_α values found for the actual thermal degradation of different polymers (Figs. 4.24 and 4.26).

A study of the kinetics of thermo-oxidative degradation may involve some problems specific to the process of oxidation. For example, the initial stages of thermo-oxidative degradation may be accompanied by a mass gain due to some accumulation of the oxidation products. This typically occurs when thermo-oxidative degradation is studied at very slow heating rates and can be avoided by ramping temperature at a faster rate [72]. Another problem is securing the saturation of the polymer sample with oxygen, which is not difficult to accomplish by using very thin polymer samples of low mass under large excess of oxygen [73].

Typically, the presence of oxygen accelerates the thermal degradation of polymers. Relative to regular thermal degradation in an inert atmosphere, thermo-oxidative degradation can start at 100–200 °C lower temperature. The dramatic decrease in thermal stability under oxidative conditions is reflected in a dramatic decrease in the activation energy of the process. Examples of the application of an isoconversional method to thermo-oxidative degradation of several polymers are given in Fig. 4.27. The respective E_α dependencies show little variation with the extent of conversion. For PS, PE, and PP, the mean E_α values fall within the range 80–120 kJ mol^{-1}. These values are consistent with activation energies of decomposition of organic hydroperoxides. As discussed earlier (Sect. 4.3.1), this process usually plays the role of the rate-limiting step in the thermo-oxidative degradation of many polymers.

Of course, not all thermo-oxidative degradations have the same rate-limiting step. For example, as seen in Fig. 4.27, PMMA has markedly larger activation energy of thermo-oxidative degradation than PP, PS, and PE. This is not surprising because oxygen has a very different effect on PMMA than on other polymers. It actually stabilizes PMMA. In the presence of oxygen, thermal degradation of PMMA starts at temperature ~50 °C higher than under inert atmosphere [71]. The decelerating effect of oxygen is illustrated in Fig. 4.28 that presents mass loss data measured while periodically switching the gas atmosphere between air and nitrogen. It is seen that a switch from air to nitrogen causes an increase in the slope of the mass loss curve

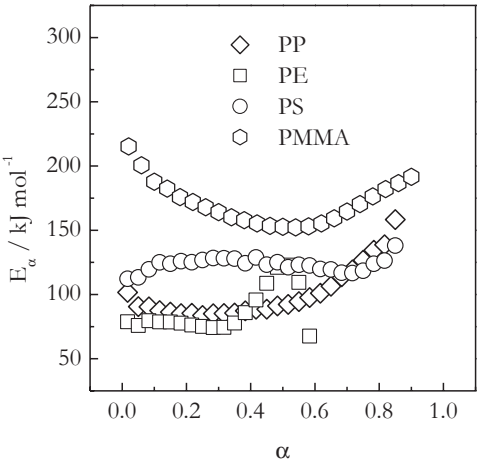

Fig. 4.27 Dependencies of the activation energy on conversion for thermo-oxidative degradation of several polymers. (Adapted from Peterson et al. [65] and Peterson et al. [71] with respective permission of Wiley and ACS)

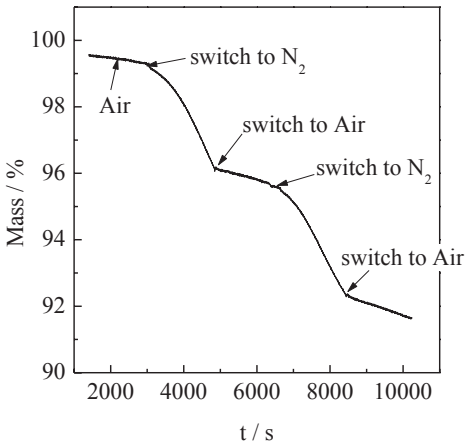

Fig. 4.28 TGA curve showing the effect of switching of gaseous atmospheres between air and nitrogen on the thermal degradation of PMMA at 200 °C. (Reproduced from Peterson et al. [71] with permission of ACS)

or, in other words, acceleration of the degradation rate. A switch from nitrogen to air obviously causes the opposite effect. The effect is explained [71] by the formation of thermally stable radical species that suppress the process of depolymerization.

Isoconversional analysis of the polymer degradation kinetics is frequently limited to estimating a dependence of the effective activation energy on conversion. By comparing the values of the activation energy, one can obtain quick insights into the origins of thermal stability changes due to modification of polymeric materials. For example, cross-linking of a polymer can increase significantly its thermal stability that is reflected in an increase of the activation energy [74]. The enhancement of thermal stability can also be accomplished by addition nanoparticles, i.e., by converting polymers to nanocomposites [75–79].

For example, relative to virgin PS, the thermal and thermo-oxidative degradation of PS-clay nanocomposites can occur at tens of degrees higher temperature [80]. Slowing down of the respective degradation kinetics reveals itself in markedly increasing effective activation energy of the process. An example of this effect is shown in Fig. 4.29 that compares the isoconversional activation energies for virgin PS and several PS–clay nanocomposites [81]. The nanocomposite containing 1 wt.% of clay is PS brush on exfoliated clay that was synthesized by surface-initiated polymerization. The nanocomposites containing 3 and 5 wt. % of clay are intercalated clay materials that were prepared by in situ polymerization of styrene in the presence of organically modified clay. It is seen that the activation energy of thermal degradation is greater in any of the composites than in virgin PS, although the exfoliated system may be somewhat more effective in raising the activation energy than the intercalated one.

Although the activation energy of thermal degradation is a major reason that determines thermal stability, it is not the only reason. A change in thermal stability or, more generally, a change in the reaction rate may be associated with a change in the preexponential factor. In fact, a change in the preexponential factor appears to be the primary cause of deceleration [82] as well as acceleration [10, 83, 84] of chemical reactions when they are confined to nanopores. Also, thermal stability

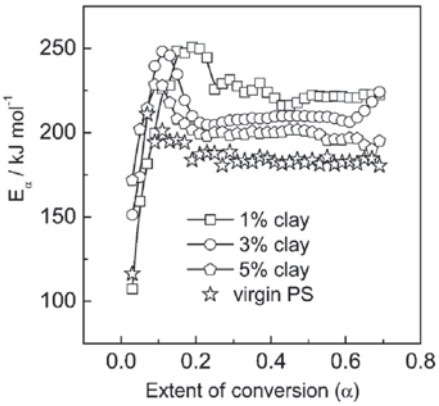

Fig. 4.29 E_α dependencies for thermal degradation of virgin PS and PS–clay nanocomposites containing different percentages of clay. The 1% clay system is exfoliated, and 3 and 5% are intercalated systems. (Reproduced from Vyazovkin et al. [81] with permission of ACS)

may change because of a change in the reaction mechanism and, thus, a change in the reaction model. The degradation mechanism changes can be caused by various factors, one of which is the introduction of nanoparticles [85–87]. For example, the PS–clay (5 wt.%) nanocomposite prepared by ultrasound-assisted solution mixing has demonstrated a significant increase in the degradation temperature relative to virgin PS [88]. Nevertheless, the isoconversional activation energy for the thermal decomposition of the nanocomposite has been found to be markedly lower than that for virgin PS. Further analysis has revealed that the process in the nanocomposite is described by a lower value of the preexponential factor and different reaction model [90]. Apparently, these two are the reasons for the enhanced thermal stability of this particular nanocomposite.

At any rate, performing kinetic analysis beyond estimating the E_α dependence can be beneficial in figuring out what components of the kinetic triplet are linked to the observed changes in the thermal stability of a polymer. For instance, isotactic PS (iPS) is more thermally stable than regular atactic PS (aPS) [89]. Isoconversional treatment of TGA data on the thermal degradation of these two polymers yields the E_α dependencies depicted in Fig. 4.30. The E_α values for both polymers are practically independent of α. On average, the activation energies for iPS are about 10 kJ mol^{-1} larger than those for aPS. Obviously, larger activation energy is consistent with larger thermal stability observed experimentally. By using the compensation effect, as discussed in Sect. 2.2, one can also evaluate the conversion dependence of the preexponential factor. The resulting dependencies are presented in Fig. 4.31. Clearly, for the thermal degradation of iPS, the $\ln A_\alpha$ values are greater than for the thermal degradation of aPS. However, larger preexponential factor means a faster process and, therefore, lower thermal stability. That is, an increase in the preexponential factor diminishes the process deceleration associated with an increase in the activation energy.

No less important is to figure out how the reaction model for iPS can affect the thermal stability of this polymer relative to that of aPS. However, this particular task faces an important general issue of the applicability of the commonly used

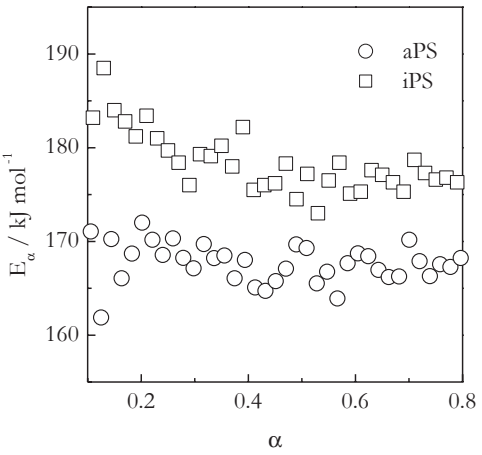

Fig. 4.30 E_α dependencies for the thermal degradation of isotactic polystyrene (iPS) and atactic polystyrene (aPS). (Adapted from Chen et al. [89] with permission of Wiley)

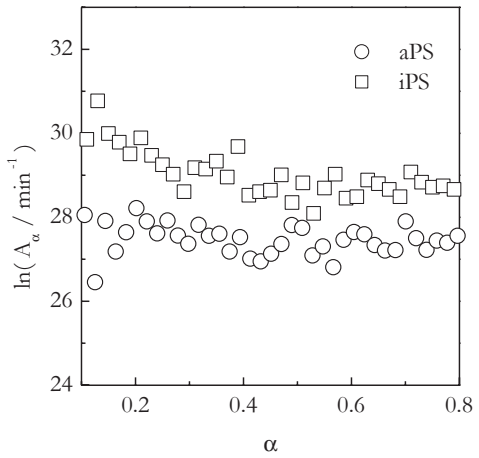

Fig. 4.31 lnA_α dependencies for the thermal degradation of isotactic polystyrene (iPS) and atactic polystyrene (aPS). (Adapted from Chen et al. [89] with permission of Wiley)

reaction models (Table 1.1) to the process of polymer degradation. The issue is due to the fact that these models were derived for processes that involve solids, whereas thermal degradation of the majority of polymers takes place in the liquid state. By way of illustration, the model of a contracting sphere assumes that a reactant is a solid spherical particle, which decreases in size throughout the process of decomposition. This can be a reasonable assumption when the reactant is a solid powder, but not so when the reactant is bulk liquid. Therefore, when the solid-state reaction models are applied to liquid-state polymer degradation, they rather play a role of interpolating functions than physically meaningful models. That is why one should be careful in assigning a physical meaning when polymer degradation data are found to fit one of these models, unless the model is similar to one of the homogeneous kinetics models. For example, the Mampel model is identical with the first-order reaction model. As an alternative to the solid-state models, one can use the truncated

Sestak–Berggren model (Eq. 2.32) that provides enough flexibility to fit most of the types of the $f(\alpha)$ dependencies.

With regard to physically meaningful models, we should mention a work of Sanchez-Jimenez et al. [90], who have found a way of converting the random scission model of polymer degradation [91] to the convenient $f(\alpha)$ form. The original work by Simha and Wall [91] describes the kinetics of bond breaking as:

$$\frac{dx}{dt} = k(T)(1-x), \tag{4.57}$$

where x is the fraction of broken bonds. Since not every broken bond produces a volatile fragment, x is not equal to the extent of conversion of polymer to volatile fragments, α. These two values are related to each other as [91]:

$$1-\alpha = (1-x)^{L-1}\left[1+x\frac{(N-L)(L-1)}{N}\right], \tag{4.58}$$

where N is the initial degree of polymerization and L is the number of monomer units in the shortest chain fragment that does not evaporate before being degraded. By assuming that normally $L \ll N$, Sanchez-Jimenez et al. [90] simplify Eq. 4.58 to 4.59:

$$\alpha = 1-(1-x)^{L-1}[1+x(L-1)], \tag{4.59}$$

and take its derivative with respect to time:

$$\frac{d\alpha}{dt} = L(L-1)(1-x)^{L-2}x\frac{dx}{dt}. \tag{4.60}$$

Replacing dx/dt with the right-hand side of Eq. 4.57 yields:

$$\frac{d\alpha}{dt} = k(T)L(L-1)(1-x)^{L-1}x. \tag{4.61}$$

Comparing Eq. 4.61 with the regular rate equation (Eq. 1.1) suggests that everything but $k(T)$ in the right-hand side is $f(\alpha)$. Thus, $f(\alpha)$ for random scission must have the following form:

$$f(\alpha) = L(L-1)(1-x)^{L-1}x. \tag{4.62}$$

Equation 4.62 does not provide an analytical form of $f(\alpha)$ dependence on α as the models considered earlier (Table 1.1) do. In general, this dependence can be found in numerical form by substituting the same values of x and L in Eqs. 4.59 and 4.62. An analytical expression for $f(\alpha)$ was determined by fitting numerical dependencies of $f(\alpha)$ on α to an approximating equation of the following form:

Table 4.2 Parameters of Eq. 4.63 obtained [90] by its fitting to numerical $f(\alpha)$ data for equation of random scission

Code	L	c	n	m
L2	2	1.204	1.119	0.4
L3	3	2.080	1.057	0.396
L4	4	2.929	1.039	0.394
L5	5	3.767	1.030	0.391
L6	6	4.597	1.024	0.389
L7	7	5.422	1.020	0.388
L8	8	6.242	1.017	0.386

$$f(\alpha) = c\alpha^m (1-\alpha)^n. \tag{4.63}$$

Table 4.2 collects the fit parameters of Eq. 4.63.

The aforementioned approach has been tested by using data on the thermal degradation of poly(butylene terephthalate) (PBT), the polymer that degrades via random scission. Figure 4.32 presents the $f(\alpha)$ plots reduced to $\alpha = 0.5$ for experimental data as well as some theoretical models, including the models of random scission (L2 and L8) and some solid-state reaction models. Clearly, the random scission models provide much better fit to the experimental data than any of the solid-state reaction models that makes a good case for the viability of the derived $f(\alpha)$ models of random scission.

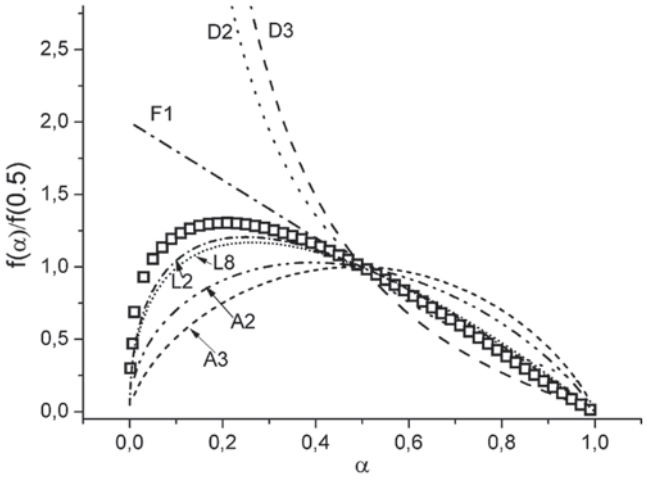

Fig. 4.32 Comparison of the $f(\alpha)$ data for the thermal degradation of PBT (*points*) against theoretical models (*lines*). L2 and L8 represent the random scission models with L equal to 2 and 8, respectively. (Reproduced from Sanchez-Jimenez et al. [90] with permission of Elsevier)

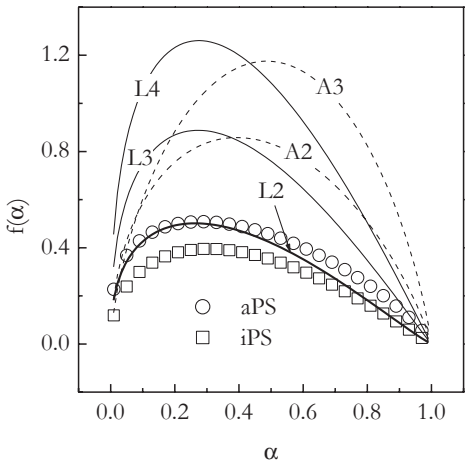

Fig. 4.33 Thermal degradation data for atactic polystyrene (aPS) and isotactic polystyrene (iPS) as compared against the random scission (L2, L3, L4) and Avrami–Erofeev (A2, A3) models

We can now try to use this approach to see whether the thermal degradation data for iPS and aPS are consistent with the random scission model. As seen in Fig. 4.33, the experimental $f(\alpha)$ data show a maximum that means that we deal with an autocatalytic type of kinetics (see Sect. 1.1). This type of kinetics is consistent with the random scission models. Among the solid-state reaction models (Table 1.1, Fig. 1.4), the kinetics of this type is represented by the Avrami–Erofeev models. All these models are depicted in Fig. 4.33. It is obvious that the Avrami–Erofeev models cannot reproduce the degradation kinetics of either iPS or aPS. The problem is not so much the significant difference in the absolute values of $f(\alpha)$. This difference can always be diminished by multiplying $f(\alpha)$ by some constant that can then be compensated by dividing the preexponential factor by the same constant. The problem is that the Avrami–Erofeev models have a maximum at significantly larger α than the actual thermal degradation data. On the other hand, the random scission models reveal their maximum at practically the same α as the actual data. The L2 model provides the best match among the random scission models. Undoubtedly, the thermal degradation kinetics of either iPS or aPS can be described quite well by the random scission models. This conclusion is in agreement with the earlier work on the thermal degradation of aPS by Sanchez-Jimenez et al. [88].

The data presented in Fig. 4.33 can also help us to answer the earlier question of how the reaction model for iPS can affect the thermal stability of this polymer relative to that of aPS. It is easy to see that the absolute values of $f(\alpha)$ for iPS are smaller than those for aPS. In other words, the reaction model for iPS indicates that the degradation rate of this polymer is slower than that of aPS. Overall, the fact that iPS has a somewhat larger thermal stability than aPS is associated with two components of the kinetic triplet: the activation energy and the reaction model.

4.4 Thermal Decomposition of Solids

...and nothing can hide itself from Thy heat
Saint Augustine, The Confessions of St. Augustine

4.4.1 Background

Solid substances are very diverse. They can be made of atoms, ions, or molecules and can exist in the crystalline or amorphous form. However, when it comes to the thermal decomposition of solids, the solid usually means [92–95] an ionic crystalline compound. This is the largest class of solid compounds that on heating can decompose before they melt. Therefore, the thermal decomposition of most of ionic solids can proceed entirely in the solid state at least in some temperature region. This is in contrast to molecular solids whose solid structure is held together by weak van der Waals forces that break easily on heating causing a solid to melt. As a result, the thermal decomposition of molecular solids typically occurs in the liquid state. As discussed in Sect. 4.3, most of polymers, being molecular solids, undergo thermal degradation in the liquid state.

Ionic solids in which the cation is a metallic ion usually decompose to form at least one solid and one gaseous product in accord with the following general equation:

$$A_s \rightarrow B_s + C_g. \tag{4.64}$$

Equation 4.64 suggests that the solid reactant A transforms directly into the solid product B or, in other words, the new phase B grows inside the reactant phase A. The process is reminiscent of the solid–solid phase transitions discussed in Sect. 3.8, except that in decomposition the phases obviously have different molecular compositions. As discussed in Chap. 3, the formation of new phases is treated customarily in terms of nucleation. In the area of the thermal decomposition of solids, the concept of nucleation was introduced by MacDonald and Hinshelwood [96]. The general idea is that the solid product B appears in the form of individual nuclei that successively grow on the surface of the solid reactant *A*. This concept has given rise to a multitude of the reaction kinetics models, some of which are listed in Table 1.1. An overview of these models is given elsewhere [93, 94, 97].

For thermolysis, equations for the critical nucleus size and the free energy barrier to nucleation were derived by Jacobs and Tompkins [98]. Their approach is similar to the traditional approach to the nucleation kinetics of phase transitions (see Sect. 3.5). They start by assuming that the free energy of the formation of the spherical nucleus of the solid reaction product B is determined by the sum of the volume and surface free energies:

$$\Delta G = m\Delta G_B + 4\pi r^2\sigma, \tag{4.65}$$

where ΔG_B is the volume free energy per molecule, m is the number of molecules in the nucleus, r is the nucleus radius, and σ is what Jacobs and Tompkins called the strain energy per unit area. This is the energy associated with the local deformation of the lattice due to the difference in the molecular volumes of A and B. Instead of using the radius as a variable, Jacobs and Tompkins employ the number of molecules, which is linked to the radius as:

$$m = \frac{4\pi r^3}{3V_m}, \tag{4.66}$$

where V_m is the volume of a molecule. Then Eq. 4.65 turns into Eq. 4.67:

$$\Delta G = m\Delta G_B + (36\pi V_m^2)^{\frac{1}{3}} m^{\frac{2}{3}}\sigma. \tag{4.67}$$

From the condition of ΔG maximum, the critical nucleus size is:

$$m^* = -36\pi V_m^2 \left(\frac{2\sigma}{3\Delta G_B}\right)^3. \tag{4.68}$$

Substitution of m^* into Eq. 4.67 yields the height of the free energy barrier:

$$\Delta G^* = \frac{16\pi V_m^2 \sigma}{3(\Delta G_B)^2}. \tag{4.69}$$

Jacobs and Tompkins did not introduce temperature dependence into ΔG^*. However, this can be easily done by assuming that at some temperature T_0 the product phase B can be at equilibrium with reactant phase A. Then one can follow the usual reasoning (Eqs. 3.37 and 3.38) to arrive at an equation that establishes a temperature dependence of the free energy barrier height:

$$\Delta G^* = \frac{16\pi V_m^2 \sigma T_0^2}{3(\Delta H_B)^2 (T - T_0)^2} = \frac{Z}{(\Delta T)^2}, \tag{4.70}$$

where Z is a constant that collects all parameters that can be considered temperature independent and $\Delta T = T - T_0$ is superheating. The temperature dependence of the nucleation rate for the product phase B is obtained by substituting the resulting ΔG^* into the Fisher–Turnbull [99] equation (Eq. 3.42) that yields:

$$w(T) = w_0 \exp\left[\frac{-Z}{RT(\Delta T)^2}\right] \exp\left(\frac{-E_D}{RT}\right). \tag{4.71}$$

From Eq. 4.71, one can derive the effective activation energy for nucleation of the product phase as follows:

$$E = -R\frac{\mathrm{d}\ln w(T)}{\mathrm{d}T^{-1}} = E_{\mathrm{D}} + Z\left[\frac{1}{(\Delta T)^2} + \frac{2T}{(\Delta T)^3}\right]. \tag{4.72}$$

The temperature dependence of E that follows from Eq. 4.72 is similar to that found for the solid–solid phase transition from a low-temperature phase II to a high-temperature phase I on heating above the equilibrium temperature T_0 (Fig. 3.50). That is, at temperatures just above T_0 (i.e., when ΔT is close to zero), the effective energy of the formation of the product phase may be quite large. However, as temperature continues to rise, the E value would decrease toward the activation energy of diffusion (E_{D}) of the product molecules as they self-assemble into a crystalline lattice.

It should be stressed that the nucleation model of Jacobs and Tompkins applies only to the physical aspect of the reaction 4.64. It describes the process of self-assembly of randomly formed individual molecules of B into a nucleus of the phase B. The model does not account for the chemical aspect of the reaction, i.e., the fact that the formation of individual molecules of B requires breaking bonds in the reactant A. Therefore, the application of this model is limited primarily to the induction period of thermal decomposition. The presence of a distinct induction period in the integral kinetic curves measured under isothermal conditions (Fig. 1.5 and Sect. 1.1) is an indication that the process rate is limited by slow nucleation. In agreement with the predictions of Eq. 4.72, the nucleation activation energies derived from the induction periods are sometimes estimated to be significantly larger [100, 101] than the activation energy of further stages of thermal decomposition.

The meaning of the equilibrium temperature T_0 as well as of the effective activation energies estimated beyond the induction period can be understood when considering the chemical aspect of thermal decomposition. Many of thermal decompositions are endothermic and reversible. Common examples include the thermal decomposition of carbonates, oxides, hydrates, and sulfates. The general equation of reversible decomposition can be written as:

$$\mathrm{A_s} \underset{k_2}{\overset{k_1}{\Leftrightarrow}} \mathrm{B_s} + \mathrm{C_g}, \tag{4.73}$$

where k_1 and k_2 are the rate constants of the forward and reverse reaction. Because the activities of pure solid phases are taken to be 1, the equilibrium constant of such a process is:

$$K = P_{0,\mathrm{C}}, \tag{4.74}$$

where $P_{0,\mathrm{C}}$ is the equilibrium partial pressure of the gaseous product C. Since the equilibrium constant depends on temperature in accord with the van't Hoff equation, Eq. 4.74 can be rewritten as:

$$\ln P_0 = D - \frac{\Delta H_r}{RT}, \tag{4.75}$$

where ΔH is the enthalpy of reaction (4.73) and D is a constant. Equation 4.75 links pressure and temperature at which all three phases, i.e., A_s, B_s, and C_g, can coexist in equilibrium.

A well-studied example of reversible decomposition is the thermal decomposition of calcium carbonate:

$$CaCO_{3(s)} \Leftrightarrow CaO_{(s)} + CO_{2(g)}. \tag{4.76}$$

A temperature dependence of the equilibrium pressure of carbon dioxide for the decomposition of calcium carbonate [102] is presented in Fig. 4.34. Fitting the dependence to Eq. 4.75 yields the following equation:

$$\ln[P_{0,CO_2}(\text{Pa})] = 29.18 - \frac{20590}{T}. \tag{4.77}$$

The straight line set up by Eq. 4.77 correlates pressure and temperature at which $CaCO_{3(s)}$, $CaO_{(s)}$, and $CO_{2(g)}$ are at equilibrium with each other. Above this line, calcium carbonate remains thermally stable, whereas below it the compound would decompose to calcium oxide and carbon dioxide. While largely simplified, this thermodynamic model allows one to introduce an important notion of the equilibrium temperature as the temperature, at which the equilibrium pressure of the gaseous product rises above its partial pressure. For instance, according to the Keeling curve [103], the concentration of carbon dioxide in atmospheric air has been steadily growing over decades and currently is about 400 ppm that makes its partial pressure at ambient conditions around 40 Pa. This is several orders of magnitude

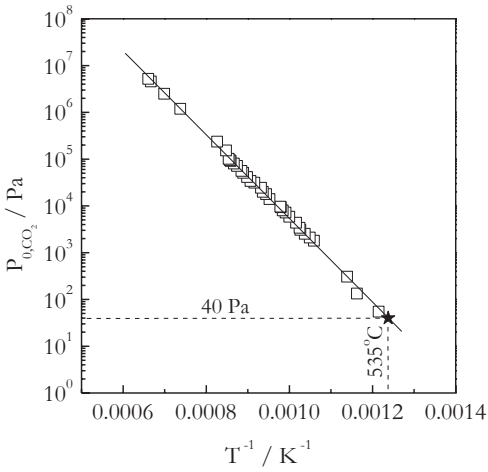

Fig. 4.34 Temperature dependence of the equilibrium pressure of CO_2 for reaction 4.76. (Data from Lide [102])

larger than the equilibrium pressure of carbon dioxide estimated from Eq. 4.77 for ambient temperature that prevents the thermal decomposition of calcium carbonate. To decompose calcium carbonate, one has to raise the equilibrium pressure above 40 Pa that is accomplished by raising the temperature above $T_0 \approx 535\,°C$. Then calcium carbonate would start converting to carbon dioxide and calcium oxide. An alternative way to initiate decomposition would be to decrease the partial pressure of carbon dioxide below its equilibrium value at a given temperature. This is accomplished experimentally by performing reversible decompositions in vacuum. It should be noted that the effect of the partial pressure on the thermal decomposition of calcium carbonate as well as of a gaseous product on other reversible decompositions can be quite drastic. As seen from Fig. 4.35, performing thermal decomposition of this compound in vacuum and in carbon dioxide atmospheres causes the decomposition temperature to shift by some 300 °C [104].

The pressure of the gaseous product affects not only the decomposition temperature of the solid reactant (e.g., Fig. 4.35) but the effective activation energy of the process as well. Zawadzki and Bretsznajder [105] reported the earliest example of a dramatic increase in the activation energy of the thermal decomposition of calcium carbonate with increasing pressure of carbon dioxide. Their data are depicted in Fig. 4.36. It is seen that increasing the carbon dioxide pressure from 130 to 6000 Pa causes the E value to rise about eight times from ~190 to 1500 kJ mol^{-1}.

The dramatic increase in the effective activation energy with increasing pressure of a gaseous reaction product has been rationalized by means of a model proposed by Pawlyutschenko and Prodan [106] and presented here. They start by assuming that the rate of the forward reaction is proportional to the solid surface area, S:

$$v_1 = k_1 S. \tag{4.78}$$

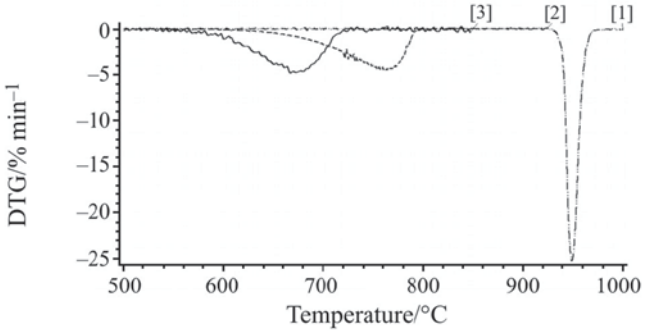

Fig. 4.35 Differential thermogravimetric curve for the thermal decomposition of calcium carbonate at 8 °C min^{-1} in the atmosphere of vacuum (*solid line* [3]), argon (*dashed line* [2]), and carbon dioxide (*dashed dot dot line* [1]). (Reproduced from Sanders and Gallagher [104] with permission of Springer)

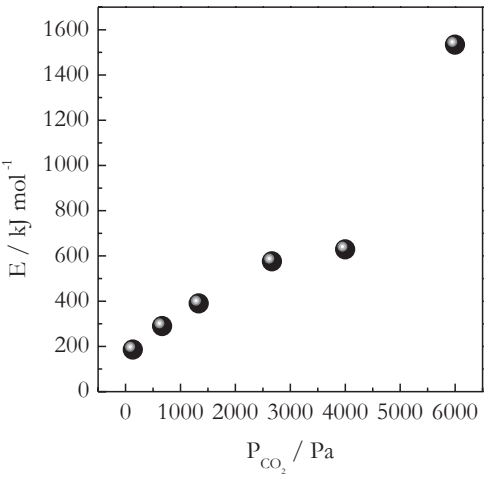

Fig. 4.36 The effective activation energy of the reversible thermal decomposition of $CaCO_3$ increases with increase in the pressure of CO_2. (Data from Zawadzki and Bretsznajder [105])

The rate of the reverse reaction is also proportional to n(P), which is the amount of C_g adsorbed on B_s at given pressure P:

$$v_2 = k_2 S n(P). \tag{4.79}$$

Then the overall rate of decomposition is:

$$v = k_{ef} S = v_1 - v_2 = k_1 S - k_2 S n(P), \tag{4.80}$$

where k_{ef} is the effective rate constant of the overall process. At the equilibrium pressure, P_0, the rates of the forward and reverse reactions are equal so that:

$$k_1 = k_2 n(P_0). \tag{4.81}$$

By substituting Eq. 4.81 into 4.80, they obtain:

$$k_{ef} = k_2 [n(P_0) - n(P)]. \tag{4.82}$$

The dependence of the adsorbed amount on pressure can be expressed in the form similar to the Freundlich isotherm [1]:

$$n(P) = KP^m, \tag{4.83}$$

where m is a fit parameter ($0 < m \leq 1$) and K has a meaning of the adsorption equilibrium constant, whose temperature dependence is defined by the van't Hoff equation:

$$K = L \exp\left(\frac{-\Delta H_{ad}}{RT}\right), \tag{4.84}$$

where L is a constant and ΔH_{ad} is the adsorption enthalpy. In their turn, the rate constants k_{ef} and k_2 have the Arrhenius temperature dependence. Therefore, Eq. 4.82 can be written as:

$$k_{ef} = A_2 \exp\left(\frac{-E_2}{RT}\right)\left[L \exp\left(\frac{-\Delta H_{ad}}{RT}\right)\left(P_0^m - P^m\right)\right]. \tag{4.85}$$

Normally, the pressure of C_g is maintained constant in kinetic experiments that means that the P^m term is constant and independent of temperature. However, the equilibrium pressure is temperature dependent in accord with Eq. 4.75. Considering this dependence, the effective activation energy of the process can be determined as follows:

$$E_{ef} = -R\left(\frac{\mathrm{d}\ln k_{ef}}{\mathrm{d}T^{-1}}\right) = E_2 + \Delta H_{ad} + m\Delta H_r \frac{P_0^m}{P_0^m - P^m}. \tag{4.86}$$

Equation 4.86 is the result obtained by Pawlyutschenko and Prodan [106]. It should be noted that if one replaces the Freundlich isotherm with the Langmuir isotherm [1] at lower pressure that would be equivalent to using $m=1$ in Eq. 4.83. Then Eq. 4.86 for E_{ef} would take the following form:

$$E_{ef} = E_2 + \Delta H_{ad} + \Delta H_r \frac{P_0}{P_0 - P}, \tag{4.87}$$

which allows one to arrive at the same conclusions as Eq. 4.86 but without the need for guessing the value of m.

At any rate, the third term in the right-hand side of Eq. 4.86 (and 4.87) determines the dependence of the effective activation energy of reversible decomposition on pressure. It is clear that when P is maintained slightly below the equilibrium value P_0 the third term tends to infinity and so does the value of E_{ef}. A physically meaningful value of E_{ef} can only be obtained when the gaseous pressure is maintained markedly below the equilibrium pressure, i.e., when the reaction is run in vacuum. Then P can be neglected relative to P_0 so that the pressure term $P_0/(P_0-P)$ becomes approximately equal to 1 and the pressure dependence of the effective activation energy vanishes. Figure 4.37 demonstrates the dynamics of decreasing the pressure term as a function of the gaseous product pressure. The dependencies suggest that the pressure dependence of E_{ef} should practically vanish when the gaseous product pressure is at least ten times lower than the equilibrium pressure.

Another important conclusion that can be drawn from Eqs. 4.87 and 4.86 is that one may not need to use vacuum to eliminate the pressure dependence of the effective activation energy. Alternatively, one can run a reaction at ambient pressure but at temperatures significantly above the equilibrium temperature. Such conditions can be relatively easy to realize when thermal decomposition is studied under nonisothermal conditions because they allow one to stretch the temperature range of a study to significantly higher temperatures than those covered by isothermal

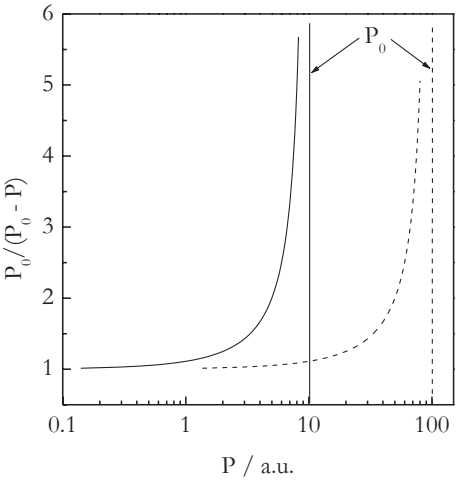

Fig. 4.37 Dependence of the pressure term in Eq. 4.87 on the gaseous product pressure. The *vertical lines* denote the values of the equilibrium pressure

runs. The situation is illustrated in Fig. 4.38 for decomposition of calcium carbonate under ambient pressure of carbon dioxide, i.e., 40 Pa. When the temperature rises, so does the equilibrium pressure in accord with Eq. 4.77. As illustrated in Fig. 4.34, decomposition would start when temperature rises above 535 °C and the equilibrium pressure above 40 Pa. Because at this point P_0 is yet very close to P, the pressure term in Eq. 4.87 is large so that the effective activation energy at the initial stages of decomposition can also be expected to be unusually large. However, as temperature continues to rise causing continuous increase of the equilibrium pressure, the pressure term becomes progressively smaller. This means that at some later stages of decomposition the pressure dependence of the effective activation energy should vanish. As mentioned before, the pressure dependence practically vanishes when the equilibrium pressure is at least ten times larger than the gaseous product pressure. Figure 4.38 shows that this is accomplished at temperatures above

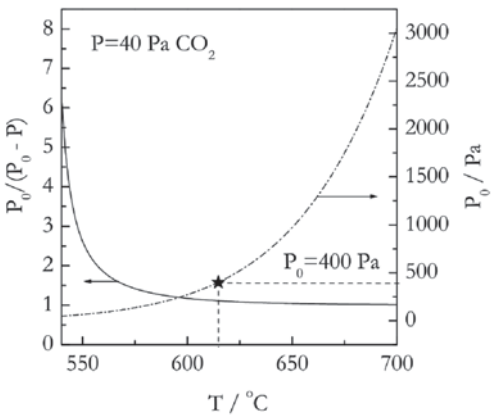

Fig. 4.38 Decrease of the pressure term (*solid line*) with increasing temperature at constant pressure (40 Pa) of the gaseous product. The equilibrium pressure (*dashed dotted line*) increases with temperature in accord with Eq. 4.77

~615 °C, i.e., when P_0 rises above 400 Pa. These conclusions have direct relevance for isoconversional analysis of reversible thermal decompositions studied under nonisothermal conditions. They suggest that the E_α dependencies estimated for this type of processes can be expected to have unusually large values at low conversions (i.e., $\alpha \to 0$). However, as α increases, the E_α values should be expected to decrease until reaching some plateau value.

The aforementioned discussion explains the conditions under which one can eliminate the pressure dependence of the effective activation energy of reversible thermal decomposition. Let us note that even if such conditions are accomplished, the effective activation energy would still be a composite value that involves the activation energy of the reverse reaction as well as the reaction and adsorption enthalpies (Eqs. 4.86 and 4.87). Nevertheless, the effective activation energy of reversible decomposition studied under vacuum is frequently interpreted as the activation energy of the forward reaction. For such an interpretation to be reasonable, the rate of the forward reaction should exceed significantly the rate of the reverse reaction. Note that in Eq. 4.87 the sum of the activation energy of the reverse reaction (E_2) and the reaction enthalpy (ΔH_r) gives an estimate for the activation energy of the forward reaction (E_1; Fig. 4.39). The adsorption enthalpy enters Eqs. 4.86 and 4.87 only because the rates of adsorption and the reverse reaction are not considered to be significantly slower than the rate of the forward reaction. The rates of adsorption and the reverse reaction can be significantly decelerated by effectively removing the gaseous product. This is accomplished by applying vacuum or fast purge with an inert gas at ambient pressure.

Another important factor in slowing down the rates of adsorption and the reverse reaction is increasing temperature. First, increasing temperature depresses adsorption. Adsorption is an exothermic process and, thus, disfavored by increasing temperature. The effect is especially strong in the case of chemisorption that is characterized by large negative values of the adsorption enthalpy [1]. For example, the enthalpy of adsorption of carbon dioxide on calcium oxide is about −200 kJ mol^{-1}

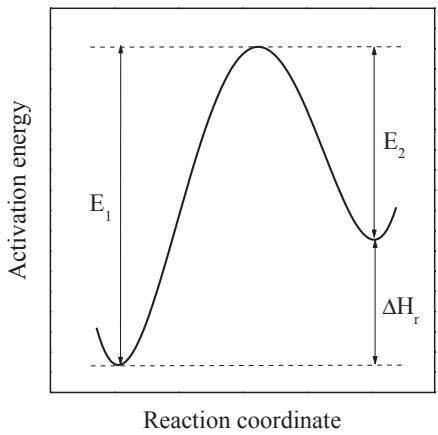

Fig. 4.39 Activation energy diagram for a reversible endothermic process

[107]. Second, increasing temperature accelerates the forward and reverse reaction to a different degree. As seen in Fig. 4.40, the process having a steeper Arrhenius plot has a larger increase in the rate constant per the same increase in temperature. To put it differently, the same increase in temperature would accelerate more the process having larger activation energy. In the case of an endothermic reversible process, it means that the forward reaction would be accelerated more than the reverse reaction because the activation energy for the former is always larger than for the latter (Fig. 4.39).

Let us assume that temperature increases from T_1 to T_2. In accord with the Arrhenius equation (Eq. 1.2), the resulting increase in the rate constant is proportional to the activation energy as follows:

$$\Delta \ln k = \ln k(T_2) - \ln k(T_1) = \frac{-E}{R}\left(\frac{1}{T_2} - \frac{1}{T_1}\right). \tag{4.88}$$

Then the difference between the increases in the respective rate constants for the forward and reverse reaction is:

$$\Delta \ln k_1 - \Delta \ln k_2 = \frac{-E_1 + E_2}{R}\left(\frac{1}{T_2} - \frac{1}{T_1}\right) = \frac{-\Delta H_r}{R}\left(\frac{1}{T_2} - \frac{1}{T_1}\right). \tag{4.89}$$

Equation 4.89 suggests that the acceleration of the forward reaction relative to the reverse one is proportional to the process enthalpy. It means that the larger the enthalpy of reversible decomposition the easier it is to reach the temperature region in which the rate of the forward reaction is significantly faster than that of the reverse reaction.

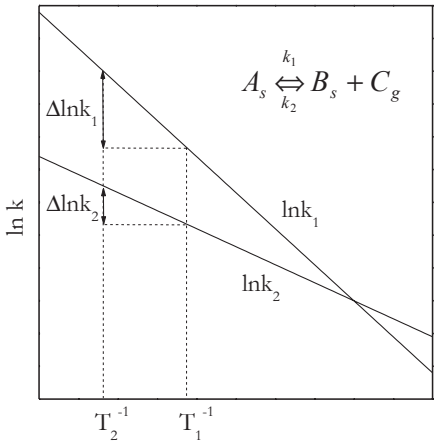

Fig. 4.40 Arrhenius plots for the forward ($\ln k_1$) and reverse ($\ln k_2$) reactions of reversible decomposition (Eq. 4.73). $\Delta \ln k$ represents the respective acceleration of these two reactions due to an increase in temperature from T_1 to T_2

4.4.2 Isoconversional Treatment

According to Eq. 4.64, the mass of a solid product B_s is less than the mass of a solid reactant A_s by the mass of released gas C_g. The decrease in mass that accompanies thermal decomposition of solids is usually large enough to be accurately measured by TGA. The use of this technique is the most common way of measuring the kinetics of thermal decomposition.

Calcium carbonate appears to be the compound whose thermal decomposition has been studied most frequently. In 1987, Maciejewski and Reller [108] published a statistical distribution of 168 values of the activation energy reported for this process (Fig. 4.41). The values range from 100 to over 300 kJ mol^{-1}, with absolute majority of the values falling in a somewhat narrower range: 170 and 250 kJ mol^{-1}. The wide spread of the values was proposed [108] to be due to the effect of experimental conditions on the reversible decomposition. Although this effect is undeniable (see, for example, Fig. 4.36), the method by which the kinetic triplets were estimated is just as important. The authors did not comment what fraction of the values was estimated by using single-heating-rate methods that are presently known [109–113] to be computationally flawed and, thus, generally incapable of producing reliable kinetic triplets.

Considering that the single-heating-rate methods had been dominating the field until the beginning of the twenty-first century, one can safely infer that a great many numbers presented in Fig. 4.41 are no more than computational mishaps. This in-

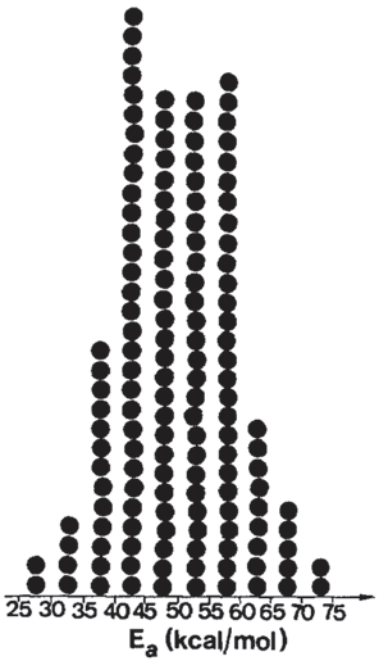

Fig. 4.41 Statistical distribution of the literature values for the activation energy of the thermal decomposition of calcium carbonate. Each *dot* represents an individual literature value. (Reproduced from Maciejewski and Reller [108] with permission of Elsevier)

ference is supported by the fact that the application of isoconversional methods to the thermal decomposition of calcium carbonate tends to produce rather consistent values of the activation energy. Figure 4.42 presents five E_α dependencies estimated form four different data sets obtained under nonisothermal conditions in the atmosphere of flowing nitrogen [110, 114–116]. Except the data of Elder [114], the E_α values do not show any significant variation with α and practically all of them fit within 10% of 190 kJ mol^{-1}, which is obviously a much narrower range than the one seen in Fig. 4.41.

The application of isoconversional methods to the isothermal decomposition of calcium carbonate under nitrogen flow also yields the E_α values that do not practically vary with α and that average to 186 kJ mol^{-1} [117]. The value is certainly within the limits for the nonisothermal values. Isoconversional treatment of the constant rate thermal analysis data (temperature is varied to maintain the process rate constant) on decomposition of calcium carbonate performed under vacuum ($4 \cdot 10^{-3}$ Pa) has also yielded nearly constant E_α values [118]. The latter average to 224 kJ mol^{-1}. Keeping in mind that a confidence interval for an individual E_α value is rarely less than 10% of the value, the difference between the activation energies respectively obtained under vacuum and nitrogen (Fig. 4.42) is hardly significant.

Considering that the thermal decomposition of calcium carbonate under nitrogen flow does not demonstrate consistently descending E_α dependencies, we can suppose that the pressure term has a negligible contribution to the effective activation energy of the process under such conditions. Apparently, it is easy for this process to reach the temperature range when the rate of the forward reaction becomes much faster than that of the reverse reaction. As discussed earlier, this is expected for reversible processes having larger reaction enthalpy. For the thermal decomposition of calcium carbonate, this value is 178 kJ mol^{-1} [93]. Even larger enthalpies are reported [93] for decomposition of strontium (235 kJ mol^{-1}) and barium (269 kJ mol^{-1}) carbonates. Incidentally, isoconversional analysis of the ther-

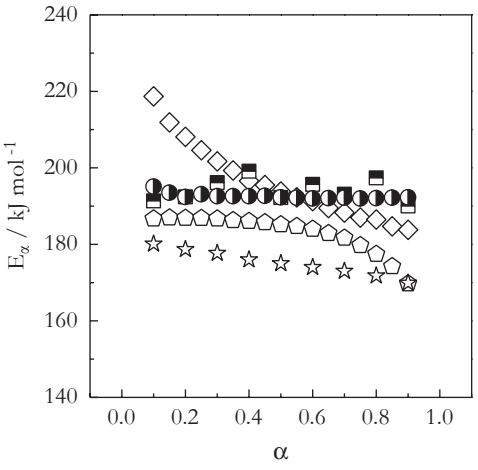

Fig. 4.42 Isoconversional activation energies for the nonisothermal decomposition of calcium carbonate under nitrogen. (The data are from Elder [114] (*diamonds*), Tan et al. [116] (*pentagons*, data are courtesy of Guanglei Tan), Gao et al. [115] (*stars*). *Half-filled symbols* correspond to the same data set [110] processed by the differential (*squares,* data are courtesy of Alan Burnham) and integral method (*circles,* data of Sergey Vyazovkin))

mal decomposition of strontium carbonate measured under a flow of nitrogen also demonstrates a practically constant value of E_α (~220 kJ mol^{-1}) at $\alpha < 0.5$ [119].

The situation appears quite different for another class of reversible processes: the thermal dehydration of crystal hydrates. The enthalpies for dehydration are quite small, mostly under 60 kJ mol^{-1} [93]. This is markedly less than the enthalpies for decomposition of carbonates (from 70 to 270 kJ mol^{-1}) and sulfates (from 190 to 790 kJ mol^{-1}) [93]. The most studied thermal dehydration is that of calcium oxalate monohydrate. The enthalpy of this process is only 38 kJ mol^{-1} [120]. It obviously means that the difference in the activation energies of the forward and reverse processes is quite small. Therefore, an increase in temperature of dehydration should not be very efficient in accomplishing the situation when the rate of the forward reaction becomes significantly faster than that of the reverse one. In other words, unless the process is run in high vacuum, the contribution of the pressure term is not likely to be negligible.

Figure 4.43 demonstrates the results of application of isoconversional methods to four different samples [22, 114, 121, 122] of calcium oxalate monohydrate dehydrated nonisothermally under a flow of nitrogen. The resulting E_α dependencies are consistently descending. This agrees well with the afore-discussed effect of the pressure term on the effective activation energy that should reveal itself in large E_α values at low conversions that should gradually drop to some plateau value as temperature and conversion increase. Descending E_α dependencies have also been reported [123, 124] for the nonisothermal dehydration of lithium sulfate monohydrate in the atmosphere of flowing nitrogen. Depending on the sample type and other conditions, the drop in E_α with increasing α has been as much as 140 and as little as 20 kJ mol^{-1}.

Although pressure and temperature are the key factors that control the kinetics of reversible decompositions, there are a number of other factors that may play an important role. For example, attaining global equilibrium can be complicated by

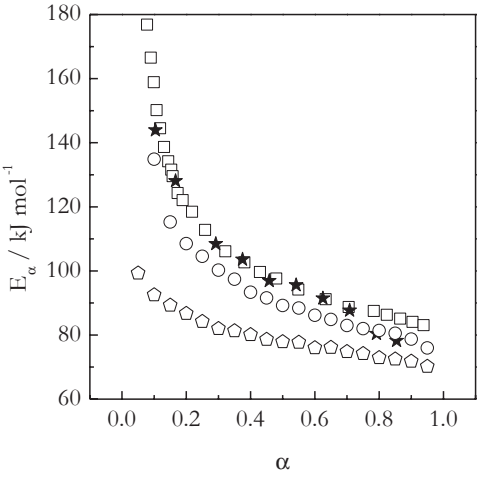

Fig. 4.43 E_α dependencies for the thermal dehydration of calcium oxalate monohydrate under nitrogen. (Data from Masuda et al. [122], *squares*; Urbanovici and Segal [121], *stars*; Vyazovkin [22], *circles*; and Elder [114], *pentagons*)

temporary local equilibria that occur in the vicinity of the solid surface. The effect can be especially strong when the solid reactants or products have a large surface area. This is quite common in porous solids or fine powders. In these systems, gaseous products can participate multiple times in reverse and forward reactions before they permanently leave the solid phase. Local equilibria may also depend on the type of a purge gas, its flow rate, and the way it is delivered to the sample. In addition, they may be affected by size and shape of the sample pans. The removal of gaseous products is much more efficient from the pans of smaller height and larger diameter. The bottom line is that the general trends discussed earlier provide but general guidelines for understanding the kinetics of reversible decomposition. Nevertheless, the effects actually observed can be diminished or enhanced by a variety of specific factors that should also be taken into consideration.

Reactivity of solids is strongly affected by imperfections or defects of the crystalline lattice that are naturally formed during synthesis and processing. The most drastic imperfection of any crystalline lattice is its surface. The structure of the surface is unavoidably different from that of the bulk. The surface layer species (atoms, ions, molecules) are surrounded by and, thus, bound to fewer neighbors than their bulk counterparts. To satisfy uncompensated chemical bonds, the surface species undergo drastic spatial rearrangements [125]. A vivid example is the bond-length contraction, i.e., shortening the interlayer spacing between the topmost and the second layer. The resulting surface tension imposes significant stress on chemical bonds of the surface layer species. Significant stress is concentrated also in other lattice defects (kinks, ledges, dislocations, etc.) primarily located on the surface. The mechanically stressed species included in the structural defects possess higher energy and are more reactive.

The respective increase in the reactivity can be formalized by using the kinetic theory of the strength of solids developed by Zhurkov [126, 127]:

$$\tau = \tau_0 \exp\left(\frac{E - a\sigma}{RT}\right), \tag{4.90}$$

where τ is the lifetime of a solid, τ_0 is the preexponential factor, E is the activation energy required to break a chemical bond, σ is the mechanical stress, and a is the coefficient that characterizes conversion of the stress to energy. While developed to describe the mechanical fracture of solids, the theory sets forth an important idea of coupling two different reaction stimuli, thermal and mechanical. They are respectively represented by two different components of the overall effective activation energy, E and $a\sigma$, in Eq. 4.90. Clearly, the larger the stress, the smaller the overall energy barrier and the faster a solid breaks or decomposes. The stress term lowers the energy barrier by increasing the energy of the solid reactant.

Because the surface is the most defective part of a solid, an increase in the surface area generally increases the reactivity of solid reactants. The surface to volume ratio is increased effectively by decreasing the size of solid reactant particles. Typically, it takes a significant change in the particle size to reveal its effect on the rate and activation energy of decomposition. For example, a decrease in the average par-

ticle size of potassium iodate from ~140 to 70 μm causes about 5% increase in the rate constants and no systematic change in the isoconversional activation energy of decomposition [128]. Nevertheless, the effect on the rate and activation energy can be quite dramatic when the particle size is reduced significantly, especially to nanometer dimensions. This is illustrated in Fig. 4.44 that presents the isoconversional values of the activation energy estimated for the thermal decomposition of calcium carbonate nanoparticles [129]. It is seen that for decomposition of the larger-size (~88 nm) nanoparticles the E_α values are practically independent of α and average to ~180 kJ mol^{-1} that is quite similar to what is observed (Fig. 4.42) for decomposition of regular microparticles. However, as the particle size is brought down to 36 nm, the effective activation energy drops below 140 kJ mol^{-1}.

The defects of the crystalline structure can be induced by mechanical treatment of solid reactants, e.g., by grinding. The stress field produced by mechanical treatment is relaxed by the solid via a number of pathways that include the release of heat, creation of new surface, accumulation of the crystalline lattice defects, polymorphic transitions, amorphization, and chemical reactions [130]. The creation of a new surface is possible as long as solid particles continue to break. As the particles approach a certain minimum size, the solid undergoes a transition from the brittle to ductile state and, as a result, can only undergo plastic deformation [131]. The latter gives rise to various crystalline defects that include dislocations as well as vacancies and interstitial ions in the crystalline lattice [130].

It is important to recognize that the phase transitions and chemical reactions can be initiated by simple manual grinding [132, 133]. Thus, one should be mindful of this ubiquitous procedure as a factor affecting the reactivity of a solid. The use of a more intense mechanical treatment such as high-energy ball milling can lead to the massive creation of defects, which is the purpose of mechanical activation of solids. This activation usually results in a significant decrease in the activation energy of the reaction involving the solids [130]. An illustration of this effect is the thermal

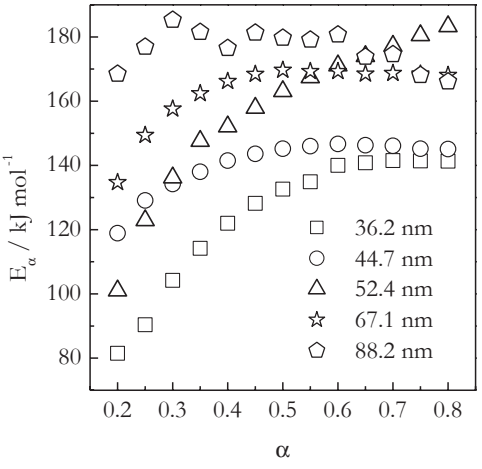

Fig. 4.44 Isoconversional activation energies for the thermal decomposition of calcium carbonate powders of different particle size ([129])

decomposition of the mineral alunite, whose chemical formula is $KAl_3(SO_4)_2(OH)_6$. Alunite decomposes in two consecutive steps that respectively represent dehydration and desulfation [134]. Figure 4.45 compares the E_α dependencies estimated for both processes in regular and mechanically activated alunite. It is seen that the activation energy of either dehydration or desulfation is much lower in the mechanically activated sample.

Solids can also be activated by exposure to different types of electromagnetic radiation, including visible and ultraviolet light as well as X- and γ-rays. Interaction of the radiation photons with ionic solids leads to bond breaking and the creation of various defects in the crystalline lattice [135]. As a result, the solid almost universally becomes more reactive and the activation energy of decomposition drops [92–94]. By way of example, Fig. 4.46 demonstrates the effect of pretreatment of

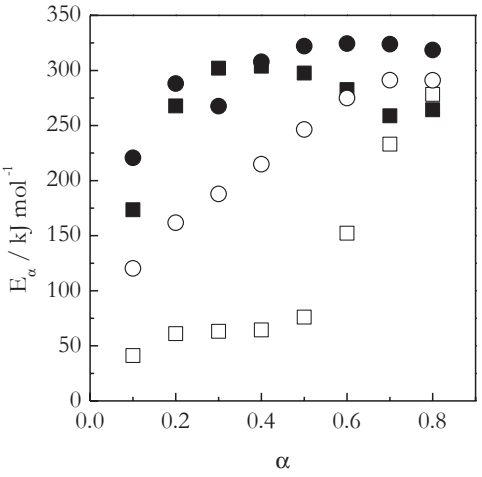

Fig. 4.45 The E_α dependencies estimated by an isoconversional method for the thermal decomposition of alunite [134]. *Solid symbols* correspond to regular (not activated) sample, and *open symbols* to the sample mechanically activated by high energy ball milling. *Squares* and *circles,* respectively, represent dehydration and desulfation steps

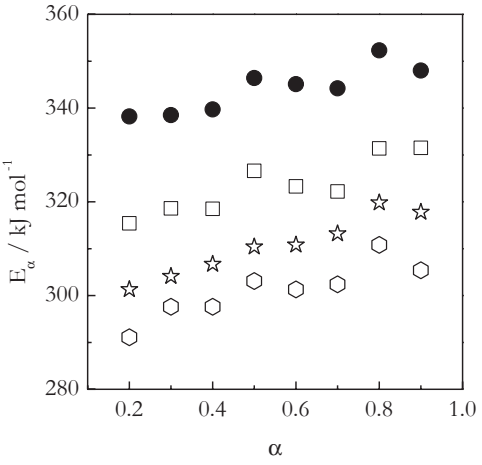

Fig. 4.46 Isoconversional activation energies determined for the thermal decomposition of strontium nitrate [136]. *Solid symbols* represent the untreated sample. *Open symbols* correspond to the samples exposed to different doses of ^{60}Co γ-radiation (*squares:* 0.5 MGy; *stars:* 1.5 MGy; *hexagons:* 2.5 MGy)

strontium nitrate with γ-radiation on the isoconversional activation energy of the thermal decomposition of this compound [136]. As typically is the case, the irradiated samples demonstrate lower activation energy than the untreated ones. The activation energy obviously decreases with increase in the radiation dose.

The reactivity of a solid may also be affected by its phase state. Many solids can exist in more than one crystalline form (polymorph; see Sect. 3.8). In this case, a solid compound can be thermally decomposed in different crystalline forms as long as the temperature of the transition between two polymorphs lies within the decomposition temperature range of the compound. It is also possible when a crystalline compound can be prepared in the form of stable and metastable polymorphs that can exist in the temperature range of decomposition. Although solid polymorphs of the same compound have the same molecular composition, they have different crystalline lattices and thus different distances between the atoms. A change in the interatomic distances may affect appreciably the chemical bond strength and, thus, the chemical reactivity of a solid.

For example, ferrous oxalate dihydrate ($FeC_2O_4 \cdot 2H_2O$) can be prepared in the form of α- and β- polymorphs. Dehydration of the α-polymorph has been found [137] to occur at ~15 °C higher temperature relative to the β-polymorph. The application of an isoconversional method to the dehydration data indicates (Fig. 4.47) that in the α-polymorph the process occurs with larger average activation energy (133 ± 7 kJ mol^{-1}) than in the β-polymorph (117 ± 4 kJ mol^{-1}). Further kinetic analysis has demonstrated [137] that the reaction models and preexponential factors are also respectively different for the two polymorphs.

Another important phase change that can occur during decomposition of solids is melting. Normally, melting causes acceleration of decomposition. Bawn [138] proposed that the acceleration may be associated with the fact that the activation energy of the liquid-state process is smaller than that for the solid-state process. The reasoning was as follows [138]: Considering that the temperature dependence of the reaction rate obeys the Arrhenius equation, one can write:

$$\ln \frac{k_l}{k_s} = \ln \frac{A_l}{A_s} + \frac{E_s - E_l}{RT}, \tag{4.91}$$

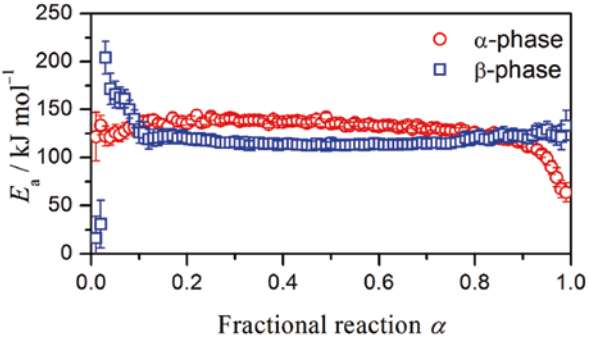

Fig. 4.47 Dependence of the activation energy on conversion for the thermal dehydration of the α- and β- polymorphs of ferrous oxalate dihydrate. (Reproduced from Ogasawara and Koga [137] with permission of ACS)

where the subscripts l and s represent, respectively, the liquid- and solid-state processes. Then the difference between E_s and E_l should be equal to the enthalpy of melting, ΔH_m. Assuming that $A_l \approx A_s$ and taking into account that for many organic solids ΔH_m is about 5 kcal mol^{-1}, the ratio of k_l/k_s at 100 °C should be expected to be around 800.

However, one should take notice of two important facts [138]. First is that the experimentally measured k_l/k_s ratios are commonly found to be no more than a few decades. Second, the E_s and E_l values are frequently determined to be insignificantly different, as should be expected considering the typically small values of ΔH_m. Extensive recent work [139] on the thermal decomposition of solid explosives also suggests that the E_s and E_l values are usually equal within the experimental error limits. An example of isoconversional evaluation of the activation energies for the solid- and liquid-state process is a study of the thermal decomposition of hexanitrostilbene [140]. At slow heating rates ($\leq$0.4 °C min^{-1}), the process can be carried out below the melting point of the compound, i.e., in the solid state, whereas at faster heating rates ($\geq$2.5 °C min^{-1}) it takes place in the liquid state. The application of an isoconversional method to the solid-state decomposition yields activation energy around 200 kJ mol^{-1}. For the liquid-state process, the isoconversional activation energy appears to be only marginally smaller than this value.

It should be kept in mind that when the activation energy decreases significantly in the liquid state, it can be a sign of change in the reaction mechanism. For instance, unimolecular decomposition can become bimolecular. Also, the acceleration does not have to be linked uniquely to a decrease in the energy barrier. The rate increase can be associated with an increase in the frequency of intermolecular collisions and, thus, with a larger value of the preexponential factor in the liquid state. Last but not least, the reaction does not have to accelerate on transition from the solid to liquid state. As a matter of fact, there are many reactions that proceed faster in the solid than liquid state [141, 142]. Ultimately, the size and sign of the effect of the phase transition on the reaction rate depends on the reaction mechanism.

A good example of a reaction whose rate remains practically unaffected by a phase transition is the thermal decomposition of ammonium nitrate [143]. The compound melts at 169.5 °C [102] and can be decomposed isothermally below and above this temperature, i.e., in the solid and liquid state, respectively. Isoconversional analysis of the isothermal data on solid- and liquid-state decomposition yields the E_α dependencies displayed in Fig. 4.48. It is seen that for the most part of the process the activation energies for the solid- and liquid-state decomposition are nearly identical. Of course, one cannot expect any significant difference in the E_s and E_l values because the enthalpy of ammonium nitrate melting is only 6.4 kJ mol^{-1} [144]. Further kinetic analysis suggests [143] that in both liquid and solid state the decomposition obeys the same reaction model, which is the model of a contracting cylinder (N12 in Table 1.1). The rate constants estimated for the liquid- and solid-state process fall on a single Arrhenius plot presented in Fig. 4.49. The respective values of the activation energy and preexponential factor are: $E = 92 \pm 6$ kJ mol^{-1} and $\log(A/\text{min}^{-1}) = 9.0 \pm 0.6$. That is, both liquid- and solid-state decomposition of ammonium

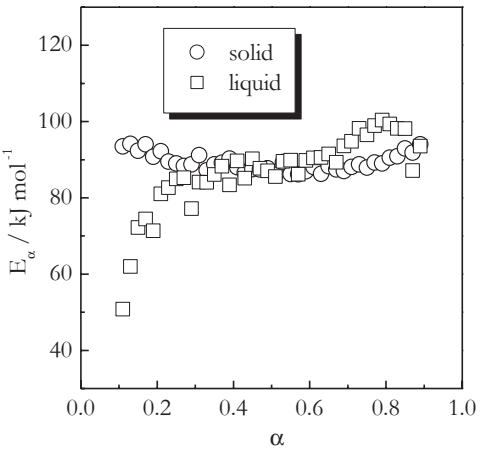

Fig. 4.48 Isoconversional activation energies evaluated for isothermal decomposition of ammonium nitrate in the solid and liquid states. (Adapted from Vyazovkin et al. [143] with permission of ACS)

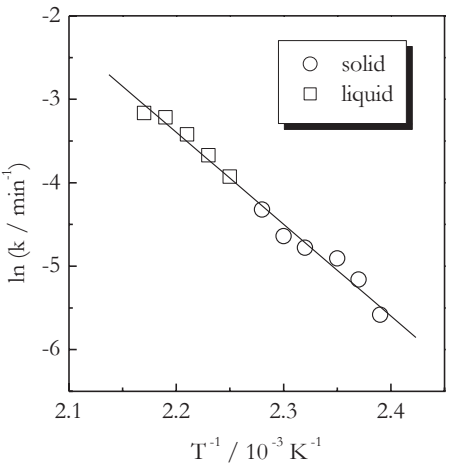

Fig. 4.49 Single Arrhenius plot fits both solid- and liquid-state data on the thermal decomposition of ammonium nitrate. (Adapted from Vyazovkin et al. [143] with permission of ACS)

nitrate are described by the same kinetic triplet. Note that under nonisothermal conditions the process starts in the solid but ends in the liquid state. However, melting that occurs in the initial stages of the process does not affect the isoconversional values of the activation energy. They remain practically constant throughout the process and average to 93 ± 1 kJ mol^{-1} [143].

The absence of a difference in the kinetic triplets for the liquid- and solid-state decomposition of ammonium nitrate appears to be due to the fact that the process follows the mechanism of dissociative sublimation/vaporization [143]. In the solid state, the rate of this process is determined by the surface to volume ratio of solid particles. Melting of the particles turns them into droplets but the surface to volume ratio remains practically the same. Therefore, the process rate remains unaffected by melting.

References

1. Atkins P, de Paula J (2010) Physical chemistry, 9th edn. W.H. Freeman, New York
2. Kujirai T, Akahira T (1925) Effect of temperature on the deterioration of fibrous insulating materials. Sci Papers Inst phys chem Res Tokyo 2:223–252
3. Friedman HL (1964) Kinetics of thermal degradation of char-forming plastics from thermogravimetry. Application to a phenolic plastic. J Polym Sci Part C 6:183–195
4. Ozawa T (1965) A new method of analyzing thermogravimetric data. Bull Chem Soc Jpn 38:1881–1886
5. Barton JM (1973) Monitoring the curing reaction of an aromatic amine/epoxide resin system by differential scanning salorimetry (DSC): determination and significance of the activation energy. Makromol Chem 171:247–251
6. Flory P (1969) Principles of polymer chemistry. Cornell University Press, Ithaca
7. Trommsdorff E, Kohle H, Lagally P (1948) Zur Polymerisation des Methacrylsauremethylesters. Makromol Chem 1:169–198
8. Norrish RGW, Smith RR (1942) Catalysed polymerization of methyl methacrylate in the liquid phase. Nature 150:336–337
9. Schulz GV, Harborth G (1947) Uber den Mechanismus des explosiven Polymerisations-verlaufes des Methacrylsauremethylesters. Makromol Chem 1:106–139
10. Zhao H, Simon SL (2011) Methyl methacrylate polymerization in nanoporous confinement. Polymer 52:4093–4098
11. Sperling LH (2001) Introduction to physical polymer science, 3rd edn. Wiley, New York
12. Achilias DS (2014) Investigation of the radical polymerization kinetics using DSC and mechanistic or isoconversional methods. J Therm Anal Calorim 116:1379–1386
13. Verhoeven J, Schaeffer R, Bouwstra JA, Junginger HE (1989) The physico-chemical characterization of poly (2-hydroxyethyl methacrylate-co-methacrylic acid: 2. Effect of water, PEG 400 and PEG 6000 on the glass transition temperature. Polymer 30:1946–1950
14. Caykara T, Ozyurek C, Kantoglu O, Erdogan B (2003) Thermal behavior of poly(2-hydroxyethyl methacrylate-maleic acid) networks. Polym Degrad Stabil 80:339–343
15. Vyazovkin S (1994) Conversion dependence of activation energy for model DSC curves of consecutive reactions. Thermochim Acta 236:1–13
16. Pace RJ, Datyner A (1979) Statistical mechanical model for diffusion of simple penetrants in polymers. II. Applications—nonvinyl polymers. J Polym Sci Polym Phys Ed 17:453–464
17. Pace RJ, Datyner A (1979) Statistical mechanical model for diffusion of simple penetrants in polymers. III. Applications—vinyl and related polymers. J Polym Sci Polym Phys Ed 17:465–476
18. Meelua W, Molloy R, Meepowpan P, Punyodom W (2012) Isoconversional kinetic analysis of ring-opening polymerization of ε-caprolactone: steric influence of titanium(IV) alkoxides as initiators. J Polym Res 19:9799 (article number)
19. Wunderlich B (2005) Thermal analysis of polymeric materials. Springer, Berlin
20. Stevens MP (1999) Polymer chemistry, 3rd edn. Oxford University Press, New York
21. Streltsov DR, Buzin AI, Dmitryakov PV, Bessonova NP, Kamasa P, Ivanov DA, Chvalun SN (2013) A study of p-xylylene polymerization kinetics by isoconversional analysis. Thermochim Acta 573:175–180
22. Vyazovkin S (2001) Modification of the integral isoconversional method to account for variation in the activation energy. J Comput Chem 22:178–183
23. Errede LA, Gregorian RS, Hoyt JM (1960) The chemistry of xylylenes.VI. The polymerization of p-xylylene. J Am Chem Soc 82:5218–5223
24. Prime RB (1997) Thermosets. In: Turi EA (ed) Thermal characterization of polymeric materials, 2nd edn, vol 2. Academic Press, San Diego, pp 1380–1763
25. Hale A (2002) Thermosets. In: Cheng SZD (ed) The handbook of thermal analysis & calorimetry, vol 3: applications to polymers and plastics. Elsevier, Amsterdam, pp 295–354
26. Verchere D, Sautereau H, Pascault JP, Riccardi CC, Moschiar SM, Williams RJJ (1990) Buildup of epoxycycloaliphatic amine networks. Kinetics, vitrification, and gelation. Macromolecules 23:725–731

27. St. John NA, George GA (1992) Cure kinetics and mechanisms of a tetraglycidyl-4,4′-diaminodiphenylmethane/diaminodiphenylsulphone epoxy resin using near i.r. spectroscopy. Polymer 33:2679–2688
28. Mijovic J, Fishbain A, Wijaya J (1992) Mechanistic modeling of epoxy-amine kinetics. 1. Model compound study. Macromolecules 25:979–985
29. Mijovic J, Wijaya J (1994) Reaction kinetics of epoxy/amine model systems. The effect of electrophilicity of amine molecule. Macromolecules 27:7589–7600
30. Cole KC, Hechler JJ, Noel D (1991) A new approach to modeling the cure kinetics of epoxy amine thermosetting resins. 2. Application to a typical system based on bis[4-(diglycidylamino) phenyl]methane and bis(4-aminophenyl) sulfone. Macromolecules 24:3098–3110
31. Sourour S, Kamal MR (1976) Differential scanning calorimetry of epoxy cure: isothermal cure kinetics. Thermochim Acta 14:41–59
32. Kamal MR (1974) Thermoset characterization for moldability analysis. Polym Eng Sci 14:231–239
33. Vyazovkin S, Sbirrazzuoli N (1999) Kinetic methods to study isothermal and nonisothermal epoxy-anhydride cure. Macromol Chem Phys 200:2294–2303
34. Zvetkov VL, Krastev RK, Paz-Abuin S (2010) Is the Kamal's model appropriate in the study of the epoxy-amine addition kinetics? Thermochim Acta 505:47–52
35. Vyazovkin S, Sbirrazzuoli N (1996) Mechanism and kinetics of epoxy-amine cure studied by differential scanning calorimetry. Macromolecules 29:1867–1873
36. Ehlers JE, Rondan NG, Huynh LK, Pham H, Marks M, Truong TN (2007) Theoretical study on mechanisms of the epoxy-amine curing reaction. Macromolecules 40:4370–4377
37. Enns JB, Gillham JK (1983) Time-temperature-transformation (TTT) cure diagram: modeling the cure behavior of thermosets. J Appl Polym Sci 28:2567–2591
38. DiBenedetto AT (1987) Prediction of the glass transition temperature of polymers: a model based on the principle of corresponding states. J Polym Sci Part B Polym Phys 26:1949-l969
39. Pascault JP, Williams RJJ (1990) Glass transition temperature versus conversion relationships for thermosetting polymers. J Polym Sci Part B Polym Phys 28:85–95
40. Schawe JEK (2002) A description of chemical and diffusion control in isothermal kinetics of cure kinetics. Thermochim Acta 388:299–312
41. Vyazovkin S, Sbirrazzuoli N (2000) Effect of viscosity on the kinetics of initial cure stages. Macromol Chem Phys 201:199–203
42. Riccardi CC, Adabbo HE, Williams RJJ (1984) Curing reaction of epoxy resins with diamines. J Appl Polym Sci 29:2481–2492
43. Simon SL, Gillham JK (1993) Cure kinetics of a thermosetting liquid dicyanate ester monomer/High-T, polycyanurate material. J Appl Polym Sci 47:461–485
44. Sbirrazzuoli N, Vyazovkin S, Mititelu A, Sladic C, Vincent L (2003) A study of epoxy-amine cure kinetics by combining isoconversional analysis with temperature modulated DSC and dynamic rheometry. Macromol Chem Phys 204:1815–1821
45. Van Assche G, Swier S, van Mele B (2002) Modeling and experimental verification of the kinetics of reacting polymer systems. Thermochim Acta 388:327–341
46. Frank-Kamenetskii DA (1969) Diffusion and heat transfer in chemical kinetics, 2nd edn. Plenum Press, New York
47. Rabinowitch E (1937) Collision, co-ordination, diffusion and reaction velocity in condensed systems. Trans Faraday Soc 33:1225–1233
48. Stolin AM, Merzhanov AG, Malkin AYa (1979) Non-isothermal phenomena in polymer engineering and science: a review-2. Non-isothermal phenomena in polymer deformation. Polym Eng Sci 19:1074–1080
49. Stannet V (1968) Simple gases. In: Crank J, Park GS (eds) Diffusion in polymers. Academic Press, London, pp 41–73
50. Barrie JA (1968) Water in polymers. In: Crank J, Park GS (eds) Diffusion in polymers. Academic Press, London, pp 259–313
51. Lee WI, Loos AC, Springer GS (1982) Heat of reaction, degree of cure, and viscosity of Hercules 3501-6 resin. J Compos Mater 16:510–520

52. Cheng KC, Chiu WY, Hsieh KH, Ma CCM (1994) Chemorheology of epoxy resin. Part I. Epoxy resin cured with tertiary amine. J Mater Sci 29:721–727
53. Cheng KC, Chiu WY, Hsieh KH, Ma CCM (1994) Chemorheology of epoxy resin. J Mater Sci 29:887–893
54. Ramis X, Cadenato A, Morancho JM, Salla JM (2003) Curing of a thermosetting powder coating by means of DMTA, TMA and DSC. Polymer 44:2067–2079
55. Ramis X, Salla JM, Mas C, Mantecon A, Serra A (2004) Kinetic study by FTIR, TMA, and DSC of the curing of a mixture of DGEBA resin and γ-butyrolactone catalyzed by ytterbium triflate. J Appl Polym Sci 92:381–393
56. Vyazovkin S, Sbirrazzuoli N (2000) Kinetic analysis of isothermal cures performed below the limiting glass transition temperature. Macromol Rapid Commun 21:85–90
57. Salla JM, Ramis X (1996) Comparative study of the cure kinetics of an unsaturated polyester resin using different procedures. Polym Eng Sci 36:835–851
58. Roman F, Calventus Y, Colomer P, Hutchinson JM (2013) Isothermal curing of polymer layered silicate nanocomposites based upon epoxy resin by means of anionic homopolymerisation. Thermochim Acta 574:98–108
59. Castell P, Galia M, Serra A, Salla JM, Ramis X (2000) Study of lanthanide triflates as new curing initiators for DGEBA. Polymer 41:8465–8474
60. Sbirrazzuoli N, Vyazovkin S, Mititelu A, Sladic C, Vincent L (2003) A study of epoxy-amine cure kinetics by combining isoconversional analysis with temperature modulated DSC and dynamic rheometry. Macromol Chem Phys 204:1815–1821
61. Alzina C, Sbirrazzuoli N, Mija A (2010) Hybrid nanocomposites: advanced nonlinear method for calculating key kinetic parameters of complex cure kinetics. J Phys Chem B 114:12480–12487
62. Flynn JH (2002) Polymer degradation. In: Cheng SZD (ed) The handbook of thermal analysis & calorimetry, vol 3: applications to polymers and plastics. Elsevier, Amsterdam, pp 587–651
63. Reich L, Stivala SS (1971) Elements of polymer degradation. McGraw-Hill, New York
64. Reich L, Stivala SS (1969) Autoxidation of hydrocarbons and polyolefins. M Dekker, New York
65. Peterson JD, Vyazovkin S, Wight CA (2001) Kinetics of the thermal and thermoxidative degradation of polystyrene, polyethylene and polypropylene. Macromol Chem Phys 202:775–784
66. Jablonski AE, Lang AJ, Vyazovkin S (2008) Isoconversional kinetics of degradation of polyvinylpyrrolidone used as a matrix for ammonium nitrate stabilization. Thermochim Acta 474:78–80
67. Madorsky SL (1964) Thermal degradation of organic polymers. Interscience Publishers, New York
68. Grassie N, Scott G (1985) Polymer degradation and stabilization. Cambridge University Press, Cambridge
69. Howell BA, Chaiwong K (2009) Thermal stability of poly(styrene) containing no head-to-head units. J Therm Anal Calorim 96:219–223
70. Hu YH, Chen CY (2003) The effect of end groups on the thermal degradation of poly(methyl methacrylate). Polym Degrad Stabil 82:81–88
71. Peterson JD, Vyazovkin S, Wight CA (1999) Kinetic study of stabilizing effect of oxygen on thermal degradation of poly(methyl methacrylate). J Phys Chem B 103:8087–8092
72. Prime RB, Bair HE, Vyazovkin S, Gallagher PK, Riga A (2009) Thermogravimetric analysis. In: Menczel JD, Prime RB (eds) Thermal analysis of polymers, fundamentals and applications. Wiley, New York, pp 241–317
73. Vyazovkin S, Chrissafis K, Di Lorenzo ML, Koga N, Pijolat M, Roduit B, Sbirrazzuoli N, Suñol JJ (2014) ICTAC kinetics committee recommendations for collecting experimental thermal analysis data for kinetic computations. Thermochim Acta 590:1–23
74. Krongauz VV, Ling MTK (2009) Photo-crosslinked acrylates degradation kinetics. J Therm Anal Calorim 96:715–725

75. Leszczynska A, Njuguna J, Pielichowski K, Banerjee JR (2007) Polymer/montmorillonite nanocomposites with improved thermal properties Part I. Factors influencing thermal stability and mechanisms of thermal stability improvement. Thermochim Acta 453:75–96
76. Leszczynska A, Njuguna J, Pielichowski K, Banerjee JR (2007) Polymer/montmorillonite nanocomposites with improved thermal properties Part II. Thermal stability of montmorillonite nanocomposites based on different polymeric matrixes. Thermochim Acta 454:1–22
77. Pavlidou S, Papaspyrides CD (2008) A review on polymer–layered silicate nanocomposites. Progr Polym Sci 33:1119–1198
78. Chrissafis K, Bikiaris D (2011) Can nanoparticles really enhance thermal stability of polymers? Part I: an overview on thermal decomposition of addition polymers. Thermochim Acta 523:1–24
79. Bikiaris D (2011) Can nanoparticles really enhance thermal stability of polymers? Part II: an overview on thermal decomposition of polycondensation polymers. Thermochim Acta 523:25–45
80. Vyazovkin S, Dranca I, Fan X, Advincula R (2004) Degradation and relaxation kinetics of polystyrene-clay nanocomposite prepared by surface initiated polymerization. J Phys Chem B 108:11672–11679
81. Chen K, Wilkie CA, Vyazovkin S (2007) Nano-confinement revealed in degradation and relaxation studies of two structurally different polystyrene-clay systems. J Phys Chem B 111:12685–12692
82. Yancey B, Vyazovkin S (2014) Venturing into kinetics and mechanism of nanoconfined solid-state reactions: trimerization of sodium dicyanamide in nanopores. Phys Chem Chem Phys 16:11409–11416
83. Li Q, Simon SL (2008) Curing of bisphenol M dicyanate ester under nanoscale constraint. Macromolecules 41:1310–1317
84. Koh YP, Simon SL (2011) Kinetic study of trimerization of monocyanate ester in nanopores. J Phys Chem B 115:925–932
85. Jang BN, Wilkie CA (2005) The thermal degradation of polystyrene nanocomposite. Polymer 46:2933–2942
86. Chen K, Susner MA, Vyazovkin S (2005) Effect of the brush structure on the segradation mechanism of polystyrene-clay nanocomposite. Macromol Rapid Commun 26:690–695
87. Chen K, Vyazovkin S (2006) Mechanistic differences in degradation of polystyrene and polystyrene-clay nanocomposite: thermal and thermo-oxidative degradation. Macromol Chem Phys 207:587–595
88. Sanchez-Jimenez PE, Perez-Maqueda LA, Perejon A, Criado JM (2012) Nanoclay nucleation effect in the thermal stabilization of a polymer nanocomposite: a kinetic mechanism change. J Phys Chem C 116:11797–11807
89. Chen K, Harris K, Vyazovkin S (2007) Tacticity as a factor contributing to the thermal stability of polystyrene. Macromol Chem Phys 208:2525–2532
90. Sanchez-Jimenez PE, Perez-Maqueda LA, Perejon A, Criado JM (2010) A new model for the kinetic analysis of thermal degradation of polymers driven by random scission. Polym Degrad Stabil 95:733–739
91. Simha R, Wall LA (1952) Kinetics of chain depolymerization. J Phys Chem 56:707–715
92. Young DA (1966) Decomposition of solids. Pergamon, Oxford
93. Brown ME, Dollimore D, Galwey AK (1980) Reactions in the solid state. Elsevier, Amsterdam
94. Glawey AK, Brown ME (1999) Thermal decomposition of ionic solids. Elsevier, Amsterdam
95. Stern KH (2000) High temperature properties and thermal decomposition of inorganic salts with oxyanions. CRC Press, Boca Raton
96. MacDonald JY, Hinshelwood CN (1925) The formation and growth of silver nuclei in the decomposition of silver oxalate. J Chem Soc 128:2764–2771
97. Khawam A, Flanagan DR (2006) Solid-state kinetic models: basics and mathematical fundamentals. J Phys Chem B 110:17315–17328

98. Jacobs PWM, Tompkins FC (1955) Classification and theory of solid reactions. In: Garner WE (ed) Chemistry of the solid state. Butterworth, London, pp 184–212
99. Turnbull D, Fisher JC (1949) Rate of nucleation in condensed systems. J Chem Phys 17:71–73
100. Devlin GJ, Herley PJ (1986) Thermal decomposition and dehydration of magnesium perchlorate hexahydrate. Thermochim Acta 104:159–178
101. Koga N, Kimizu T (2008) Thermal decomposition of indium(III) hydroxide prepared by the microwave-assisted hydrothermal method. J Am Ceram Soc 91:4052–4058
102. Lide DR (ed) (2002) CRC handbook of chemistry and physics, 83rd edn. CRC Press, Boca Raton
103. https://scripps.ucsd.edu/programs/keelingcurve/. Accessed Nov 2014
104. Sanders JP, Gallagher PK (2005) Kinetic analyses using simultaneous TG/DSC measurements. Part II: decomposition of calcium carbonate having different particle sizes. J Therm Anal Calorim 82:659–664
105. Zawadzki J, Bretsznajder S (1935) Über das Temperaturinkrement der Reaktionsgeschwindigkeit bei Reaktionen vom Typus: $A_{fest} = B_{fest} + C_{Gas}$. Z Elektrochem Angew Phys Chem 41:215–223
106. Pawlutschenko MM, Prodan EA (1965) Kristallisationsvorgange in der thermischen zersetzung fester stoffe. In: Schwab GM (ed). Reactivity of solids, 5th International symposium of the reactivity of solids, Munich, 2–8 Aug 1964. Elsevier, Amsterdam, pp 409–421
107. Beruto D, Botter R, Searcy AW (1984) Thermodynamics and kinetics of carbon dioxide chemisorption on calcium oxide. J Phys Chem 88:4052–4055
108. Maciejewski M, Reller A (1987) How (un)reliable are kinetic data of reversible solid-state decomposition processes? Thermochim Acta 110:145–152
109. Vyazovkin S, Wight CA (1999) Model-free and model-fitting approaches to kinetic analysis of isothermal and nonisothermal data. Thermochim Acta 340/341:53–68
110. Brown ME, Maciejewski M, Vyazovkin S, Nomen R, Sempere J, Burnham A, Opfermann J, Strey R, Anderson HL, Kemmler A, Keuleers R, Janssens J, Desseyn HO, Li CR, Tang TB, Roduit B, Malek J, Mitsuhashi T (2000) Computational aspects of kinetic analysis. Part A: the ICTAC kinetics project-data, methods and results. Thermochim Acta 355:125–143
111. Maciejewski M (2000) Computational aspects of kinetic analysis. Part B: the ICTAC kinetics project—the decomposition kinetics of calcium carbonate revisited, or some tips on survival in the kinetic minefield. Thermochim Acta 355:145–154
112. Vyazovkin S (2000) Computational aspects of kinetic analysis. Part C: the ICTAC kinetics project—the light at the end of the tunnel? Thermochim Acta 355:155–163
113. Burnham AK (2000) Computational aspects of kinetic analysis. Part D: the ICTAC kinetics project—multi-thermal–history model-fitting methods and their relation to isoconversional methods. Thermochim Acta 355:165–170
114. Elder JP (1998) The "E-ln(A)-f(α)" triplet in non-isothermal reaction kinetics analysis Thermochim Acta 318:229–238
115. Gao Z, Amasaki I, Nakada M (2002) A description of kinetics of thermal decomposition of calcium oxalate monohydrate by means of the accommodated R_n model. Thermochim Acta 385:95–103
116. Tan G, Tang D, Mua T, Xu C, Wang D, Wang Q (2014) The validity of nonlinear isoconversional method in the kinetic analysis of calcium carbonate decomposition under isothermal and non-isothermal conditions. Thermochim Acta 585:21–24
117. Budrugeac P (2011) An iterative model-free method to determine the activation energy of heterogeneous processes under arbitrary temperature programs. Thermochim Acta 523:84–89
118. Koga N, Criado JM (1998) The influence of mass transfer phenomena on the kinetic analysis for the thermal decomposition of calcium carbonate by constant rate thermal dnalysis (CRTA) under vacuum. Int J Chem Kinet 30:737–744
119. Han Y, Chen H, Liu N (2011) New incremental isoconversional method for kinetic analysis of solid thermal decomposition. J Therm Anal Calorim 104:679–683

120. Rejai B, Gonzalez RD (1990) The formation of supported bimetallic catalysts I. The measurement of enthalpies of gas-solid reactions using differential scanning calorimetry. J Catal 123:98–112
121. Urbanovici E, Segal E (1985) On the changes of the activation energy with the conversion degree in non-isothermal kinetics. Thermochim Acta 94:399–408
122. Masuda Y, Ito Y, Ito R, Iwata K (1986) Kinetic study of the thermal dehydration of calcium oxalate monohydrate. Thermochim Acta 99:205–215
123. Huang J, Gallagher PK (1991) Influence of water vapor on the thermal dehydration of $Li_2SO_4 \cdot H_2O$. Thermochim Acta 192:35–45
124. Tanaka H, Koga N, Sestak J (1992) Thermoanalytical kinetics for solid state reactions as exemplified by the thermal dehydration of $Li_2SO_4 \cdot H_2O$. Thermochim Acta 203:203–220
125. Somorjai GA (1994) Introduction to surface chemistry and catalysis. Wiley, New York
126. Zhurkov SN (1965) Kinetic concept of the strength of solids. Int J Fract Mech 1:311–322
127. Zhurkov SN (1984) Kinetic concept of the strength of solids. Int J Fract 26:295–307
128. Muraleedharan K (2012) Thermal decomposition kinetics of potassium iodate. Part I. The effect of particle size on the rate and kinetics of decomposition. J Therm Anal Calorim 109:237–245
129. Cui Z, Xue Y, Xiao L, Wang T (2013) Effect of particle size on activation energy for thermal decomposition of nano-$CaCO_3$. J Comput Theor Nanosci 10:1–4
130. Boldyrev VV (2006) Mechanochemistry and mechanical activation of solids. Russ Chem Rev 75:177–189
131. Kendall K (1978) The impossibility of comminuting small particles by compression. Nature 272:710–711
132. Takacs L (2013) The historical development of mechanochemistry. Chem Soc Rev 42:7649–7659
133. Boldyreva E (2013) Mechanochemistry of inorganic and organic systems: what is similar, what is different? Chem Soc Rev 42:7719–7738
134. Kucuk F, Yildiz K (2006) The decomposition kinetics of mechanically activated alunite ore in air atmosphere by thermogravimetry. Thermochim Acta 448:107–110
135. Jacobs PWM, Tompkins FC (1955) The action of light on solids. In: Garner WE (ed) Chemistry of the solid state. Butterworth, London, pp 57–90
136. Culas S, Samuel J (2013) γ-Irradiation effects on the non-isothermal decomposition of strontium nitrate by model-free and model-fitting methods. Radiat Phys Chem 86:90–95
137. Ogasawara H, Koga N (2014) Kinetic modeling for thermal dehydration of ferrous oxalate dihydrate polymorphs: a combined model for induction period—surface reaction—phase boundary reaction. J Phys Chem A 118:2401–2412
138. Bawn CEH (1955) Decomposition of organic solids. In: Garner WE (ed) Chemistry of the solid state. Butterworth, London, pp 254–267
139. Manelis GB, Nazin GM, Rubtsov YuI, Strunin VA (2003) Thermal decomposition and combustion of explosives and propellants. Taylor & Francis, London
140. Rieckmann Th, Volker S, Lichtblau L, Schirra R (2001) Investigation on the thermal stability of hexanitrostilbene by thermal analysis and multivariate regression. Chem Eng Sci 56:1327–1335
141. Pincock RE (1969) Reactions in frozen systems. Acc Chem Res 2:97–103
142. Tanaka K, Toda F (2000) Solvent-free organic synthesis. Chem Rev 100:1025–1074
143. Vyazovkin S, Clawson JS, Wight CA (2001) Thermal dissociation kinetics of solid and liquid ammonium nitrate. Chem Mater 13:960–966
144. Keenan AG (1956) The cryoscopic heat of fusion of ammonium nitrate. J Phys Chem 60:1356–1361

Chapter 5
Epilogue

Since no one knows the future, who can tell someone else what is to come?

Ecclesiastes 8:7

To conclude the book I would like to share some thoughts on the present status of the isoconversional kinetics and its future progress and challenges. Without a doubt, isoconversional methods currently present the major computational technique for exploring the kinetics of thermally stimulated processes. It should be noted that isoconversional methods started making a significant impact only about a decade ago. A descriptive picture can be obtained by comparing the numbers of citations to the three most popular isoconversional methods [1–4] with the three most popular single-heating rate methods [5–7]. The numbers shown in Fig. 5.1a indicate that the community started to prefer the isoconversional methods to the single-heating-rate ones only past 2004. Apparently, the change was inspired by the results of the International Confederation of Thermal Analysis and Calorimetry (ICTAC) 2000 Kinetic Project that officially recognized the deficiency of the single-heating-rate kinetic analyses [8–11].

The data also indicate (Fig. 5.1a) that the gap between the isoconversional and single-heating-rate methods is growing, although not fast enough. For example, when considering the six aforementioned highly popular methods, the citations to the single-heating-rate methods presently appear to be about one third of the total number of the citations (Fig. 5.1b). The actual fraction may be somewhat smaller because there are a number of newer isoconversional methods not included in the estimate. Nonetheless, it is quite unsettling to realize that 20–30 % of kinetic results reported in the current literature are still produced by single-heating-rate methods which are known to be flawed computationally and incapable of producing reliable kinetic data. While not exactly a problem of the isoconversional kinetics, the thermal analysis community at large definitely faces a challenge to convince the remaining devotees of the single-heating-rate methods to abandon their atavistic ways.

It is no secret that nowadays most of the isoconversional kinetics computations are conducted by the integral methods. Analysis of the literature citations to the integral isoconversional methods reveals another curious detail. The majority of workers prefer to use computationally outdated methods of Ozawa [2] and Flynn

S. Vyazovkin, *Isoconversional Kinetics of Thermally Stimulated Processes,*
DOI 10.1007/978-3-319-14175-6_5

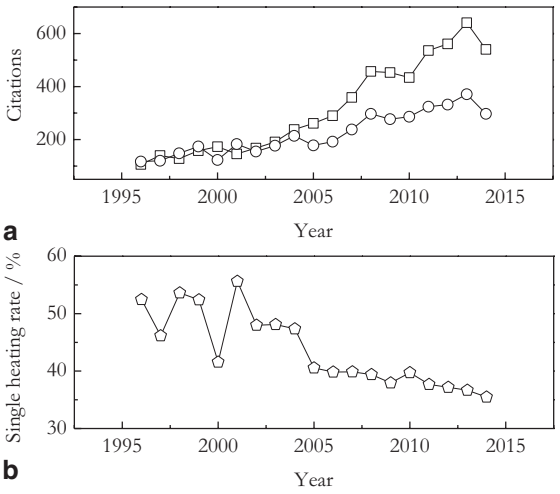

Fig. 5.1 **a** Number of citations to the three most popular single heating rate methods [5–7] (*circles*) and three most popular isoconversional methods [1–4] (*squares*) **b** Fraction of citations to the single heating rate methods [5–7]. Here and in Figures 5.2 and 5.3 the citations are found by using the Scopus database. For 2014, the citations represent first ten month of the year

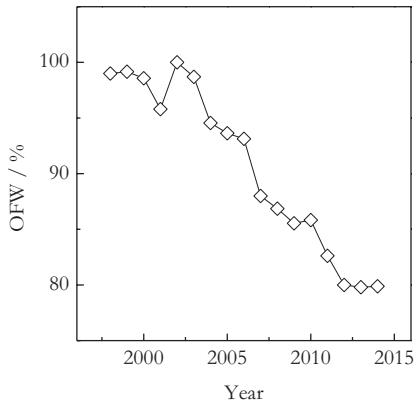

Fig. 5.2 Fraction of citations to the methods of Ozawa and Flynn and Wall (*OFW*)

and Wall [3, 4] to significantly more accurate methods discussed in Sect. 2.1.2. It is even more surprising that these crude methods are preferred to the methods of Starink [12] and of Kissinger–Akahira–Sunose [13] that are just as simple computationally but yield markedly more accurate results. Analysis of the citation data for these four methods is shown in Fig. 5.2. It is seen that among these four methods the fraction of Ozawa and Flynn–Wall methods steadily decreases but still remains at remarkably high 80%. The need for broader use of the more accurate methods was strenuously emphasized in the ICTAC 2011 recommendations [14]. Certainly, further efforts are required to promote modern integral methods.

Closely related is the problem of promoting the isoconversional methods that can properly account for variation in the activation energy and are applicable to arbitrary

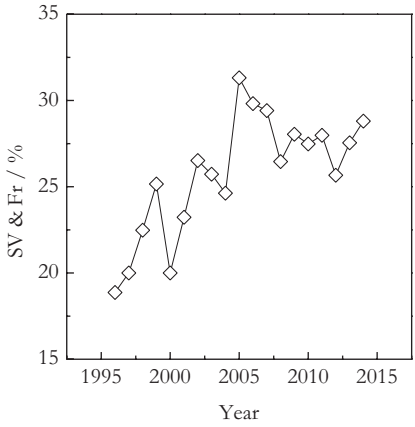

Fig. 5.3 Fraction of citations to the methods of Friedman (*Fr*) and Vyazovkin (*SV*)

temperature programs, including cooling. This is accomplishable by employing the good old method of Friedman as well as flexible integral methods (Sect. 2.1.2). Again, we can estimate the use of such methods by analyzing the literature citations. Of the flexible integral methods, so far only the Vyazovkin method [15] has generated significant number of citations. The fraction of citations to the Vyazovkin and Friedman methods among the total number of citations to these two methods and the four rigid integral methods (Ozawa, Flynn–Wall, Kissinger–Akahira–Sunose, and Starink) is still less than one third (Fig. 5.3). Although in many situations the use of the Friedman and flexible integral methods may not be necessary, it is important to continue reiterating the message of the ICTAC 2011 recommendations [14] that in certain cases it is mandatory. Such cases include the situations when data collected on cooling as well as when the sample temperature deviates significantly from the program temperature.

However important, the problems associated with computations only partially determine the progress of the isoconversional kinetics. For the most part, the progress has been and will be defined by searching and finding the links between the variation of the effective activation energy and the process mechanism. In this book, I have given many examples of how such links can be established for a variety of physical and chemical processes. In the area of chemical processes, such links have been explored successfully for years. On the other hand, the isoconversional kinetics of physical processes (phase transitions) is yet largely unchartered territory. That is why much of my effort in this book has been focused on this particular topic. Although this field is full of theoretical and experimental challenges, I believe that in the future, the kinetic exploration of physical processes will provide the biggest contribution to the progress of the isoconversional kinetics.

References

1. Friedman HL (1964) Kinetics of thermal degradation of char-forming plastics from thermogravimetry. Application to a phenolic plastic. J Polym Sci Part C 6:183–195
2. Ozawa T (1965) A new method of analyzing thermogravimetric data. Bull Chem Soc Jpn 38:1881–1886
3. Flynn JH, Wall LA (1966) A quick, direct method for the determination of activation energy from thermogravimetric data. J Polym Sci B, Polym Lett 4:323–328
4. Flynn JH, Wall LA (1966) General treatment of the thermogravimetry of polymers. J Res Nat Bur Stand Part A 70:487–523
5. Freeman ES, Carroll B (1958) The application of thermoanalytical techniques to reaction kinetics. J Phys Chem 62:394–397
6. Horowitz HH, Metzger G (1963) A new analysis of thermogravimetric traces. Anal Chem 35:1464–1468
7. Coats AW, Redfern JP (1964) Kinetic parameters from thermogravimetric data. Nature 201:68–69
8. Brown ME, Maciejewski M, Vyazovkin S, Nomen R, Sempere J, Burnham A, Opfermann J, Strey R, Anderson HL, Kemmler A, Keuleers R, Janssens J, Desseyn HO, Li CR, Tang TB, Roduit B, Malek J, Mitsuhashi T (2000) Computational aspects of kinetic analysis. Part A: the ICTAC kinetics project-data, methods and results. Thermochim Acta 355:125–143
9. Maciejewski M (2000) Computational aspects of kinetic analysis. Part B: the ICTAC kinetics project—the decomposition kinetics of calcium carbonate revisited, or some tips on survival in the kinetic minefield. Thermochim Acta 355:145–154
10. Vyazovkin S (2000) Computational aspects of kinetic analysis. Part C: the ICTAC kinetics project—the light at the end of the tunnel? Thermochim Acta 355:155–163
11. Burnham AK (2000) Computational aspects of kinetic analysis. Part D: the ICTAC kinetics project—multi-thermal–history model-fitting methods and their relation to isoconversional methods. Thermochim Acta 355:165–170
12. Starink MJ (2003) The determination of activation energy from linear heating rate experiments: a comparison of the accuracy of isoconversion methods. Thermochim Acta 404:163–176
13. Akahira T, Sunose T (1971) Method of determining activation deterioration constant of electrical insulating materials. Res Report Chiba Inst Technol (Sci Technol) 16:22–31
14. Vyazovkin S, Burnham AK, Criado JM, Pérez-Maqueda LA, Popescu C, Sbirrazzuoli N (2011) ICTAC kinetics committee recommendations for performing kinetic computations on thermal analysis data. Thermochim Acta 520:1–19
15. Vyazovkin S (2001) Modification of the integral isoconversional method to account for variation in the activation energy. J Comput Chem 22:178–183

Index

S.Vyazovkin, *Isoconversional Kinetics of Thermally Stimulated Processes*,
DOI 10.1007/978-3-319-14175-6